




5-2012

A Novel Imaging System for Automatic Real-Time 3D Patient-Specific Knee Model Reconstruction Using Ultrasound RF Data

Rimon Adel Messiha Tadross
rtadross@utk.edu

Follow this and additional works at: https://trace.tennessee.edu/utk_graddiss

 Part of the [Bioimaging and Biomedical Optics Commons](#), [Biomedical Devices and Instrumentation Commons](#), and the [Systems and Integrative Engineering Commons](#)

Recommended Citation

Tadross, Rimon Adel Messiha, "A Novel Imaging System for Automatic Real-Time 3D Patient-Specific Knee Model Reconstruction Using Ultrasound RF Data. " PhD diss., University of Tennessee, 2012.
https://trace.tennessee.edu/utk_graddiss/1354

This Dissertation is brought to you for free and open access by the Graduate School at TRACE: Tennessee Research and Creative Exchange. It has been accepted for inclusion in Doctoral Dissertations by an authorized administrator of TRACE: Tennessee Research and Creative Exchange. For more information, please contact trace@utk.edu.

To the Graduate Council:

I am submitting herewith a dissertation written by Rimon Adel Messiha Tadross entitled "A Novel Imaging System for Automatic Real-Time 3D Patient-Specific Knee Model Reconstruction Using Ultrasound RF Data." I have examined the final electronic copy of this dissertation for form and content and recommend that it be accepted in partial fulfillment of the requirements for the degree of Doctor of Philosophy, with a major in Biomedical Engineering.

Mohamed R. Mahfouz, Major Professor

We have read this dissertation and recommend its acceptance:

Richard D. Komistek, William R. Hamel, Aly E. Fathy, and Ray C. Wasielewski (Courtesy Member)

Accepted for the Council:

Carolyn R. Hodges

Vice Provost and Dean of the Graduate School

(Original signatures are on file with official student records.)

**A Novel Imaging System for Automatic Real-Time
3D Patient-Specific Knee Model Reconstruction
Using Ultrasound RF Data**

A Dissertation Presented for the

Doctorate of Philosophy

Degree

The University of Tennessee, Knoxville

Rimon Adel Messiha Tadross

May 2012

Copyright © 2012 by Rimón Adel Messiha Tadross

All rights reserved.

Acknowledgements

I would like to thank Dr. Mohamed Mahfouz for his guidance and support throughout my work on this dissertation, and throughout my graduate studies. Additionally, I would like to thank him for giving me the opportunity to work in the Center for Musculoskeletal Research (CMR) laboratory at the University of Tennessee as a graduate research assistant where I gained great experience in the field of biomedical engineering. I would like also to thank all my colleagues at the CMR for their great cooperation during my work at the CMR, and especially for their tremendous help in performing the cadaveric experiments, and the manual segmentation of the MRI/CT scans. I would also like to convey my appreciation to Dr. Richard Komistek for his encouragement and support throughout the course of this work. I also would like to thank Dr. Ray Wasielewski and the staff of Minimally Invasive Orthopedics (MIO) in Columbus, Ohio for their enormous assistance in the preparation and performance of the clinical study. Finally, I would like to greatly thank my father Adel Messiha, and my mother Afaf Aziz for their immense support.

Abstract

This dissertation introduces a novel imaging method and system for automatic real-time 3D patient-specific knee model reconstruction using ultrasound RF data. The developed method uses ultrasound to transcutaneously digitize a point cloud representing the bone's surface. This point cloud is then used to reconstruct 3D bone model using deformable models method.

In this work, three systems were developed for 3D knee bone model reconstruction using ultrasound RF data. The first system uses tracked single-element ultrasound transducer, and was experimented on 12 knee phantoms. An average reconstruction accuracy of 0.98 mm was obtained. The second system was developed using an ultrasound machine which provide real-time access to the ultrasound RF data, and was experimented on two cadaveric distal femurs, and proximal tibia. An average reconstruction accuracy of 0.976 mm was achieved. The third system was developed as an extension of the second system, and was used for clinical study of the developed system further assess its accuracy and repeatability. A knee scanning protocol was developed to scan the different articular surfaces of the knee bones to reconstruct 3D model of the bone without the need for bone-implanted motion tracking reference probes. The clinical study was performed on six volunteers' knees. Average reconstruction accuracy of 0.88 mm was achieved with 93.5% repeatability.

Three extensions to the developed system were investigated for future work. The first extension is 3D knee injection guidance system. A prototype for the 3D injection guidance system was developed to demonstrate the feasibility of the idea. The second

extension in a knee kinematics tracking system using A-mode ultrasound. A simulation framework was developed to study the feasibility of the idea, and to find the best number of single-element ultrasound transducers and their spatial distribution that yield the highest kinematics tracking accuracy. The third extension is 3D cartilage model reconstruction. A preliminary method for cartilage echo detection from ultrasound RF data was developed, and experimented on the distal femur scans of one of the clinical study's volunteers to reconstruct a 3D point cloud for the cartilage.

Table of Contents

Chapter 1	Introduction.....	1
1.1	Significance.....	1
1.2	Literature Review.....	5
1.3	Fundamental Contributions.....	12
1.4	Dissertation Outline	13
Chapter 2	Introduction to Ultrasound.....	14
Chapter 3	Bone Morphing	20
3.1	Introduction.....	20
3.2	Knee Bones Statistical Deformable Models	23
3.2.1	Atlas Dataset	23
3.2.2	Knee Bones Principal Component Analysis (PCA).....	27
3.2.3	Knee Bones' Morphology Variation Analysis.....	34
3.2.4	Knee Bones Atlases Analysis	39
3.3	Bone Morphing Methods	52
3.3.1	Powell's Direction Set Optimization Morphing	56
3.3.2	Linear Least Squares Morphing.....	61
3.3.3	Hybrid Morphing	68
Chapter 4	3D Knee Model Reconstruction Using Single-Element Ultrasound	
Transducer	72
4.1	System Setup.....	72
4.1.1	Ultrasound Transducer and Pulser/Receiver.....	72

4.1.2	Data Acquisition System.....	74
4.1.3	Motion Tracking System.....	75
4.1.4	Imaging Software.....	79
4.2	Tracked A-Mode Ultrasound Probe Calibration.....	80
4.3	Bone Echo Detection and Point Cloud Reconstruction	83
4.3.1	Bone Echo Detection	83
4.3.2	Bone Echoes Registration (Point Cloud Reconstruction).....	87
Chapter 5	3D Knee Model Reconstruction Using Ultrasound RF Data.....	89
5.1	Imaging System Setup	89
5.1.1	Ultrasound Machine, and Transducer	89
5.1.2	Motion Tracking System.....	91
5.1.3	Imaging Software.....	94
5.2	Tracked Linear Ultrasound Probe 3D Calibration	95
5.3	Knee Scanning Protocol.....	98
5.4	Bone Echo Detection and Point Cloud Reconstruction	102
5.4.1	Automatic Extraction of Bone Contours from Ultrasound RF Data.....	102
5.4.2	Bone Contours Registration.....	114
Chapter 6	Clinical Study.....	119
6.1	Imaging System Setup	119
6.1.1	Ultrasound Machine, and Transducer	119
6.1.2	Motion Tracking System.....	121
6.1.3	Imaging Software.....	124

6.2	Tracked Linear Ultrasound Probe Calibration	125
6.3	Patient's Knee Scanning Setup	126
6.4	Patient's Knee Scanning Protocol.....	128
Chapter 7	Results.....	134
7.1	Single-Element Transducer System's Phantoms Experiments Results.....	134
7.1.1	Point Cloud Reconstruction	134
7.1.2	3D Bone Model Reconstruction (Bone Morphing)	136
7.2	Ultrasound RF Data System Cadavers' Experiments Results	143
7.3	Ultrasound RF Data Imaging System's Clinical Study Results	148
Chapter 8	Future Work	156
8.1	System Enhancement, Accuracy Improvement, and Inclusion of other Joints.....	156
8.2	3D Knee Injection Guidance.....	159
8.3	Knee Kinematics Tracking Using A-Mode Ultrasound.....	164
8.4	Cartilage Model Reconstruction	173
Chapter 9	Appendix.....	178
9.1	Knee Bones Atlas Analysis.....	179
9.1.1	Female Distal Femur.....	179
9.1.2	Male Distal Femur	181
9.1.3	Female Proximal Tibia.....	183
9.1.4	Male Proximal Tibia	185
9.2	Bone Morphing Analysis	187
9.2.1	Direction Set Method.....	187

9.2.2	Linear Least Squares Method	197
9.2.3	Hybrid Method.....	205
9.3	Single-Element Ultrasound Transducer-Based Systems' Phantom Results ...	213
9.3.1	Reconstructed Point Clouds Results	213
9.3.2	3D Model Reconstruction Results	237
9.4	Ultrasound RF Data System Cadavers' Experiments Results	243
9.4.1	First Cadaver's Distal Femur	243
9.4.2	First Cadaver's Proximal Tibia.....	244
9.4.3	Second Cadaver's Distal Femur.....	245
9.5	Ultrasound RF Data Imaging System's Clinical Study Results	246
9.5.1	Volunteer's Knee 1	249
9.5.2	Volunteer's Knee 2	255
9.5.3	Volunteer's Knee 3	261
9.5.4	Volunteer's Knee 4	267
9.5.5	Volunteer's Knee 5	273
9.5.6	Volunteer's Knee 6	279
	References	286

List of Tables

Table 3.1 Accumulated variances for the gender-specific knee bones atlas.....	29
Table 3.2 Accumulated variances for the non-gender specific knee bones atlases	30
Table 7.1 Mean number of points in the acquired point clouds, and the mean RMS error between the 75 th percentile filtered point clouds and their reference models.....	136
Table 7.2 Mean reconstruction RMS errors (in mm) for the three morphing methods using the point clouds with 1 mm density.	140
Table 7.3 3D model reconstruction errors (in mm) between the reconstructed models using the developed ultrasound RF data system, and the CT-segmented models for the scanned cadavers' bones.	147
Table 7.4 3D model reconstruction average (Avg.), and root mean square (RMS) errors (in mm) for the 3 trials for the distal femur and proximal tibia 3D model reconstruction for the 6 volunteers' knees (Vol. 1 to Vol. 4 refers to the four volunteers). The Body Mass Index (BMI) for the volunteers is shown in the last column.....	152
Table 7.5 Mean (μ), standard deviation (σ) for the average (Avg.), and root mean square (RMS) errors (in mm), and their relative standard deviation (σ/μ) for the three trials for the three trials for the distal femur and proximal tibia 3D model reconstruction for the 6 volunteers' knees. The BMI for the volunteers is shown in the last column.	153
Table 7.6 Ultrasound speed for the water and different soft tissue types in the knee [17].	155

List of Figures

Figure 1.1 Overview of the ultrasound-based image guided system developed by Barrat et. al for 3D patient-specific model reconstruction of the femur [13]	5
Figure 1.2 The color maps for the mean reconstruction error (compared with the reference models) for the 6 cadaveric femurs used by Barrat et. al in their experiments for 3D patient-specific model reconstruction of the femur [13]	7
Figure 1.3 Snapshot for the scanning of the cadaveric knee using the tracked ultrasound probe by Kilian et. al. [15]	8
Figure 1.4 The point cloud reconstructed for the cadaveric distal femur scanned in the experiment performed by Kilian et. al. [15]	9
Figure 1.5 Color maps for the error between the reconstructed 3D models of the cadaveric distal femur (scanned by first (a, b), , and second (c) operator) using ultrasound, and the 3D model reconstructed by bone morphing using a point cloud digitized over the dissected cadaveric femur, by Kilian et. al. [15].....	9
Figure 3.1 Histogram of the models' mean inter-vertices distance for the female distal femur models with an average of 2.66 mm.....	25
Figure 3.2 Histogram of the models' mean inter-vertices distance for the male distal femur models with an average of 2.32 mm.....	25
Figure 3.3 Histogram of the models' mean inter-vertices distance for the female proximal tibia models with an average of 1.76 mm	26
Figure 3.4 Histogram of the models' mean inter-vertices distance for the male proximal tibia models with an average of 2 mm	26

Figure 3.5 Accumulated variance versus the number of principal components for the gender-specific female distal femur atlas	31
Figure 3.6 Accumulated variance versus the number of principal for the gender-specific male distal femur atlas	31
Figure 3.7 Accumulated variance versus the number of principal components for the gender-specific female proximal tibia atlas	32
Figure 3.8 Accumulated variances versus the number of principal components for the gender-specific male distal femur atlas.....	32
Figure 3.9 Accumulated variances versus the number of principal components for the non gender-specific distal femur atlas	33
Figure 3.10 Accumulated variances versus the number of principal components for the non gender-specific proximal tibia atlas	33
Figure 3.11 Histogram of the mean RMS errors between the female distal femur models, and their jack-knife mean models with mean RMS error of 1.6 mm, and maximum RMS error of 3.54 mm.....	34
Figure 3.12 Histogram of the mean RMS errors between the male distal femur models, and their jack-knife mean models with mean RMS error of 1.87 mm and maximum RMS error of 5.33 mm.....	35
Figure 3.13 Histogram of the mean RMS errors between the female proximal tibia models, and their jack-knife mean models with mean RMS error of 1.52 mm and maximum RMS error of 3.42 mm.....	35

Figure 3.14 Histogram of the mean RMS errors between the male proximal tibia models, and their jack-knife mean models with mean RMS error of 1.9 mm and maximum RMS error of 5.03 mm.....	36
Figure 3.15 Color map for the mean distance error between the female distal femur models, and their jack-knife mean models	37
Figure 3.16 Color map for the standard deviation of the distance error between the female distal femur models, and their jack-knife mean models	37
Figure 3.17 Color map for the mean distance error between the male distal femur models, and their jack-knife mean models	37
Figure 3.18 Color map for the standard deviation of the distance error between the male distal femur models, and their jack-knife mean models	38
Figure 3.19 Color map for the mean distance error between the female proximal tibia models, and their jack-knife mean models	38
Figure 3.20 Color map for the standard deviation of the distance error between the female proximal tibia models, and their jack-knife mean models	38
Figure 3.21 Color map for the mean distance error between the male proximal tibia models, and their jack-knife mean models	38
Figure 3.22 Color map for the standard deviation of the distance error between the female proximal tibia models' vertices, and their jack-knife mean models	39
Figure 3.23 Mean RMS errors versus the number of principal components for the projection-reconstruction process using the jack-knife (blue) and non jack-knife (red) gender-specific female distal femur atlases.	43

Figure 3.24 Mean RMS errors versus the number of principal components for the projection-reconstruction process using the jack-knife (blue) and non jack-knife (red) gender-specific male distal femur atlases.	44
Figure 3.25 Mean RMS errors versus the number of principal components for the projection-reconstruction process using the jack-knife (blue) and non jack-knife (red) gender-specific female proximal tibia atlases.	44
Figure 3.26 Mean RMS errors versus the number of principal components for the projection-reconstruction process using the jack-knife (blue) and non jack-knife (red) gender-specific male proximal tibia atlases.	45
Figure 3.27 Mean RMS error versus the number of principal components for the projection-reconstruction process using gender-specific (red) and non gender- specific (blue) jack-knife female distal femur atlases.....	46
Figure 3.28 Mean RMS errors versus the number of principal components for the projection-reconstruction process using gender-specific (red) and non gender- specific (blue) jack-knife male distal femur atlases.....	47
Figure 3.29 Mean RMS errors versus the number of principal components for the projection-reconstruction process using gender-specific (red) and non gender- specific (blue) jack-knife female proximal tibia atlases.	47
Figure 3.30 Mean RMS errors versus the number of principal components for the projection-reconstruction process using gender-specific (red) and non gender- specific (blue) jack-knife male proximal tibia atlases.	48

Figure 3.31 Mean, minimum, and maximum RMS errors versus the number of principal components for the projection-reconstruction process using jack-knife gender-specific female distal femur atlases.	50
Figure 3.32 Mean, minimum, and maximum RMS errors versus the number of principal components for the projection-reconstruction process using jack-knife gender-specific male distal femur atlases.	50
Figure 3.33 Mean, minimum, and maximum RMS errors versus the number of principal components for the projection-reconstruction process using jack-knife gender-specific female proximal tibia atlases.	51
Figure 3.34 Mean, minimum, and maximum RMS errors versus the number of principal components for the projection-reconstruction process using jack-knife gender-specific male proximal tibia atlases.	51
Figure 3.35 Unreduced point clouds for a female distal femur, showing the anterior side (left), the condyles (middle), and the posterior side (right)	53
Figure 3.36 4-mm reduced point cloud for a female distal femur, showing the anterior side (left), the condyles (middle), and the posterior side (right).....	53
Figure 3.37 8-mm reduced point cloud for a female distal femur, showing the anterior side (left), the condyles (middle), and the posterior side (right).....	54
Figure 3.38 16-mm reduced point cloud for a female distal femur, showing the anterior side (left), the condyles (middle), and the posterior side (right).....	54
Figure 3.39 32-mm reduced point cloud for a female distal femur, showing the anterior side (left), the condyles (middle), and the posterior side (right).....	54

Figure 3.40 Unreduced point clouds for a female proximal tibia, showing the anterior side (left), the tibial plateau (middle), and the posterior side (right)	55
Figure 3.41 4-mm reduced point clouds for a female proximal tibia, showing the anterior side (left), the tibial plateau (middle), and the posterior side (right)	55
Figure 3.42 8-mm reduced point clouds for a female proximal tibia, showing the anterior side (left), the tibial plateau (middle), and the posterior side (right)	55
Figure 3.43 16-mm reduced point clouds for a female proximal tibia, showing the anterior side (left), the tibial plateau (middle), and the posterior side (right).....	56
Figure 3.44 32-mm reduced point clouds for a female proximal tibia, showing the anterior side (left), the tibial plateau (middle), and the posterior side (right).....	56
Figure 3.45 Mean RMS errors vs number of principal components for the female distal femur morphing using the Direction Set method and gender-specific jack-knife atlases	59
Figure 3.46 Mean RMS errors vs number of principal components for the female distal femur morphing using the Direction Set method and gender-specific jack-knife atlases.....	59
Figure 3.47 Mean RMS errors vs number of principal components for female proximal tibia morphing using Direction Set method and gender-specific jack-knife atlases	60
Figure 3.48 Mean RMS errors vs number of principal components for male proximal tibia morphing using the Direction Set method using gender specific jack-knife atlases	60

Figure 3.49 Mean RMS errors vs number of principal components for female distal femur morphing using the linear least squares method using gender specific jack-knife atlases	66
Figure 3.50 Mean RMS errors vs number of principal components for male distal femur morphing using the linear least squares method and gender specific jack-knife atlases	66
Figure 3.51 Mean RMS errors vs number of principal components for female proximal tibia morphing using linear least squares method and gender specific jack-knife atlases	67
Figure 3.52 Mean RMS errors vs number of principal components for male proximal tibia morphing using linear least squares method using gender specific jack-knife atlases	67
Figure 3.53 Mean RMS errors versus the number of principal components for the female distal femur reconstruction using the hybrid morphing method for the unreduced, 4 mm, 8 mm, and 16 mm reduced models' point clouds using gender-specific jack-knife atlases.....	70
Figure 3.54 Mean RMS errors versus the number of principal components for the male distal femur reconstruction using the hybrid morphing method for the unreduced, 4 mm, 8 mm, and 16 mm reduced models' point clouds using gender-specific jack-knife atlases.....	70
Figure 3.55 Mean RMS errors vs the number of principal components for the female proximal tibia morphing using the hybrid morphing method for the unreduced, 4	

mm, 8 mm, and 16 mm reduced models' point clouds using gender-specific jack-knife atlases..... 71

Figure 3.56 Mean RMS errors vs the number of principal components for the male proximal tibia morphing using the hybrid morphing method for the unreduced, 4 mm, 8 mm, and 16 mm reduced models' point clouds using gender-specific jack-knife atlases..... 71

Figure 4.1 The A-mode ultrasound transducer (left), and the 5072 pulser/receiver (Olympus NDT) used in the developed single-element ultrasound transducer-based 3D knee model reconstruction system. 73

Figure 4.2 The impulse response (left) for the ultrasound transducer used in the system, and its frequency spectrum (right) generated during the transducer test performed by the vendor using a water tank and a rigid reflector (Olympus NDT). 73

Figure 4.3 Octopus CompuScope (Gage Inc, Lockport, IL) data acquisition PCI card used in the developed single-element ultrasound transducer-based 3D knee model reconstruction system..... 74

Figure 4.4 The developed single-element ultrasound transducer-based 3D knee model reconstruction system's setup showing the OptoTrak3020 (Northern Digital Inc (NDI), Ontario, Canada) tracking system, the phantom scanning, and the developed imaging software during one of the phantom experiments..... 78

Figure 4.5 A snapshot for a phantom scanning experiment showing the distal femur phantom and the tracked A-mode ultrasound probe during the scanning process. .. 79

Figure 4.6 A snapshot for the developed imaging software, for 3D knee model reconstruction using single-element ultrasound transducer, during scanning of a phantom. It shows the reconstructed 3D point cloud for a distal femur phantom and one of the ultrasound A-mode (RF) signals with the initial echo (red dot) reflected by transducer-water interface, and the bone echo (white dot) reflected by the bone-water interface.....	80
Figure 4.7 The tracked single-element (A-mode) ultrasound probe showing the optical motion tracking probe, the A-mode ultrasound transducer rigidly attached to it, the optical probe's local coordinate frame (<i>OP</i>) and the calibration parameters	81
Figure 4.8 An ultrasound RF signal showing the two main echoes, which are the main bang echo (red dot) and the bone echo (white dot).....	84
Figure 4.9 An ultrasound echo signal showing the main bang, bone echo, and an off-axis echo.	85
Figure 4.10 An ultrasound echo signal showing the main bang echo, bone echo, and multiple reverberation echoes	85
Figure 5.1 SonixRP ultrasound machine (Ultrasonix Inc, British Columbia, Canada) used in the second developed patient-specific 3D knee model reconstruction system.....	90
Figure 5.2 Polaris Spectra optical motion tracking system (Northern Digital Inc (NDI), Ontario, Canada) used in the second developed imaging system; showing the infrared camera, and the control unit	92
Figure 5.3 Active and passive motion tracking probes for the Polaris Spectra optical motion tracking system (Northern Digital Inc (NDI), Ontario, Canada).....	93

Figure 5.4 Polaris Spectra tracking volume (Northern Digital Inc (NDI), Ontario, Canada)	
.....	93
Figure 5.5 A snapshot of the developed imaging software during scanning of a cadaveric distal femur, showing a B-mode ultrasound image, the bone contour extracted from the ultrasound raw RF data, and the reconstructed point cloud while being reconstructed.	95
Figure 5.6 The tracked linear ultrasound probe used in the developed system, showing the collected calibration measurements, and the calculated calibration parameters.....	98
Figure 5.7 Dissected cadaver's knee showing the different ultrasound-visible regions of the patella, distal femur, and proximal tibia at 90 degrees flexion	100
Figure 5.8 Fluoroscopic images of a volunteer's knee [26] at different flexion angles starting from full extension (1) to deep knee bend (6). The images show the different articular bone surfaces of the knee visible to ultrasound at different flexion angles	101
Figure 5.9 An ultrasound B-mode image of a cadaver's distal femoral groove (top), example ultrasound RF signals (middle), and the automatically extracted bone contour overlaid on the reconstructed B-mode image (bottom)	103
Figure 5.10 Flowchart for the process of automatic bone contour extraction from ultrasound RF data	104
Figure 5.11 Sample RF signals (in blue) from the ultrasound frame in Figure 5.9, and their moving power envelopes (in red). The detected echoes are shown in green for the detected bone-echoes, and in cyan for the other echoes	106

- Figure 5.12 Two ultrasound B-mode images (top), and the extracted bone contour from their RF data overlaid on the B-mode images (bottom). The unfiltered contours are shown in red, and the median-filtered contours, to filter the outlier echoes, are shown in yellow 109
- Figure 5.13 Sample ultrasound B-mode images (top) for frames with partial bone contour segments, showing the extracted contour from their RF data overlaid on the B-mode images (middle), and the contour's local standard deviation with the threshold line (bottom). The true bone contour segments are shown in green, while the filtered out noise contour segments are shown in red 112
- Figure 5.14 Sample ultrasound B-mode images (top) for the case of frames with no bone contour, and the extracted contour from their RF data overlaid on the B-mode images (middle), and the contour's local standard deviation with the threshold line (bottom). The entire extracted contour (red) was detected as noise since no segment in it satisfied the continuity and the minimum-length conditions..... 113
- Figure 5.15 Flowchart for the contours registration and bone model reconstruction process..... 116
- Figure 5.16 An anterior distal femur's partial point cloud (top left), and the partial point cloud aligned to the atlas' mean model (top right). A medial partial point cloud is shown aligned to the mean model (bottom left), and the integrated point cloud after combining the anterior, medial and lateral partial point clouds for the distal femur (bottom right) 118

Figure 6.1 The SonixTOUCH ultrasound machine (Ultrasonix Inc, British Columbia, Canada) used in the clinical study, showing the magnet of the driveBay electromagnetic tracking system (Ascension Inc) fixed to an articulating arm.....	120
Figure 6.2 The DriveBay (Ascension Inc, Burlington, VT) electromagnetic tracking system used in the clinical study, showing the control unit (left), and the magnet (right)	122
Figure 6.3 The 800 mm (left), 180 mm (middle), and 130 mm (right) electromagnetic motion tracking sensors (Ascension Inc, Burlington, VT)	122
Figure 6.4 Schematics for the magnet, a model for the 800 mm sensor, and micro sensors (the 130 mm, and 180 mm sensors), showing their coordinate frames of reference (Ascension Inc, Burlington, VT)	123
Figure 6.5 Position noise versus range (distance to the magnet's center) comparison for the 90 mm, 130 mm, 180 mm and 800 mm Sensors (Ascension Inc, Burlington, VT)	123
Figure 6.6 Tracking volume for the mid range magnet used in the clinical study system (Ascension Inc, Burlington, VT)	124
Figure 6.7 Snapshot of the developed imaging software used in the clinical study, showing a reconstructed 3D point cloud for a distal femur, and one of the automatically extracted contours with the bone contour segment (green), and the rejected non-bone contour segments (red).	125

- Figure 6.8 Deep, and 90° knee bend leg holders with a volunteer's leg attached to it in the position used for scanning of the anterior, medial, and lateral regions of the distal femur, and proximal tibia bones. 127
- Figure 6.9 Full extension leg holder with a volunteer's leg attached to it in the position for the scanning of the posterior region of distal femur, and proximal tibia bones 128
- Figure 6.10 Scanning protocol for the anterior distal femur region scan, showing the axial scanning of the lateral (a), medial (b), and anterior (c) areas of the distal femur as well as the medial (d), and lateral (e) condyles. The trochlear groove is scanned transversally (f). 131
- Figure 6.11 Scanning protocol for the posterior distal femur region scan, showing the axial scanning of the lateral condyle (a), medial condyle (b), and posterior distal femoral shaft (c) areas of the distal femur 132
- Figure 6.12 Scanning protocol for the anterior proximal tibia region scan, showing the axial scanning of the lateral (a), and medial areas of the proximal tibia (b). 132
- Figure 6.13 Scanning protocol for the posterior proximal tibia region scan, showing the transverse scanning of the posterior areas of the tibial condyles and intercondylar area (a), and the axial scanning of the posterior area of the proximal tibia shaft (b). 133
- Figure 7.1 Mean RMS distance error color maps for the female distal femurs reconstructed using the Direction Set method with maximum error of 2.49 mm (a), the linear least squares method with maximum error of 2.46 mm (b), and for the male distal femurs reconstructed using the Direction Set method with maximum

error of 2.38 mm (c), and the linear least squares method with maximum error of 2.35(d). 141

Figure 7.2 Mean RMS distance error color maps for the female proximal tibias reconstructed using the Direction Set method with maximum error of 2.7 mm (a), the linear least squares method with maximum error of 2.1 mm (b), and for the male proximal tibias reconstructed using the Direction Set method with maximum error of 2.89 mm (c), and the linear least squares method with maximum error of 3.2 (d). 142

Figure 7.3 A picture for the one of the cadaveric experiments showing the developed imaging system running on the SonixRP ultrasound machine 143

Figure 7.4 Ultrasound B-mode image (left), reconstructed by applying Hilbert transform to the ultrasound RF data, for a different regions of a cadaveric knee, and the extracted bone contour from the RF data overlaid on the B-mode image (right)... 145

Figure 7.5 A snapshot from scanning the anterior distal femur of a volunteer's knee ... 149

Figure 7.6 A snapshot from scanning the anterior proximal tibia of a volunteer's knee 150

Figure 7.7 A snapshot from scanning of the posterior distal femur of a volunteer's knee 150

Figure 7.8 A snapshot from scanning of posterior proximal tibia of a volunteer's knee. 151

Figure 8.1 Example for the latest ultrasound-based needle guidance systems (Ultrasonix Inc) using the electromagnetic tracking system (Ascension Inc) to track the needle's motion and project it on the ultrasound image. It shows the two cases when the

needle is in the image plane (left), and when the needle is out of the image plane, i.e. the needle is not in the ultrasound image (right)..... 160

Figure 8.2 A schematic comparison between the traditional 2D and the 3D ultrasound-based injection guidance, showing a schematic of a patient's knee while being injected (left), the 2D ultrasound-based injection guidance (center), and the 3D injection guidance with the visualized 3D joint bone models and real-time tracked needle (right). 160

Figure 8.3 Flowchart for the proposed 3D joint injection guidance system, showing the process flow starting from the scanning of the joint, then automatic real-time 3D bones models reconstruction, then volume reconstruction (for soft tissue visualization), then injection planning, and finally injection execution and needle guidance. 161

Figure 8.4 A picture taken for the developed 3D injection guidance prototype while experimenting it in injection planning (no injection was performed) for a volunteering surgeon, showing the reconstructed 3D models of the knee bones (distal femur, and proximal tibia), and the 3D model of the needle, while being tracked, showing its position and orientation relative to the knee bones..... 163

Figure 8.5 Flowchart for fluoroscopy-based kinematics tracking of the knee. Fluoroscopy images copied from the work in [26], and modified for illustration in the flowchart. 165

Figure 8.6 Schematic for the ultrasound-based knee kinematics tracking system, showing the femoral, and tibial braces that host the single-element ultrasound transducers. 166

Figure 8.7 A flowchart for the A-mode ultrasound based kinematics tracking simulation	172
Figure 8.8 Sample raw ultrasound RF signals (in blue), and their processed versions (in red) below them, showing the detected bone echoes (green dots), and cartilage echoes (red dots), and the other detected non-bone non-cartilage echoes (cyan dots)	175
Figure 8.9 Two examples for bone (in green) and cartilage (red) contours extracted using the ultrasound RF data overlaid on their B-mode images, for two frames of one of the clinical study volunteers' femoral condyle scans. The cartilage is the hypoechoic region lying between the bone and cartilage contours.	176
Figure 8.10 The reconstructed 3D cartilage point cloud, showing the outer (red), and inner (green) cartilage surfaces of the distal femur of the 3 rd trial for the 1 st volunteer's knee of the clinical study. The cartilage's inner surface point cloud is itself the bone's surface point cloud. Three views of the point cloud are shown; superior view(top), inferior view(middle), and side view(bottom)	177
Figure 9.1 Mean, maximum, and minimum RMS errors for the models projection-reconstruction using gender-specific, jack-knife atlas for the female distal femur	179
Figure 9.2 Mean, maximum, and minimum RMS errors for the model projection-reconstruction using gender-specific, non jack-knife atlas for the female distal femur	179

Figure 9.3 Mean, maximum, and minimum RMS errors for the models projection-reconstruction using non gender-specific, jack-knife atlas for the female distal femur	180
Figure 9.4 Mean, maximum, and minimum RMS errors for the projection-reconstruction using non gender-specific, non jack-knife atlas for the female distal femur	180
Figure 9.5 Mean, maximum, and minimum RMS errors for the models projection-reconstruction using gender-specific, jack-knife atlas for the male distal femur ...	181
Figure 9.6 Mean, maximum, and minimum RMS errors for the models projection-reconstruction using gender-specific, non jack-knife atlas for the male distal femur	181
Figure 9.7 Mean, maximum, and minimum RMS errors for the models projection-reconstruction using non gender-specific, jack-knife atlas for the male distal femur	182
Figure 9.8 Mean, maximum, and minimum RMS errors for the models projection-reconstruction using non gender-specific, non jack-knife atlas for the male distal femur	182
Figure 9.9 Mean, maximum, and minimum RMS errors for the models projection-reconstruction using gender-specific, jack-knife atlas for the female proximal tibia	183
Figure 9.10 Mean, maximum, and minimum RMS errors for the models projection-reconstruction using gender-specific, non jack-knife atlas for the female proximal tibia	183

Figure 9.11 Mean, maximum, and minimum RMS errors for the models projection- reconstruction using non gender-specific, jack-knife atlas for the female proximal tibia	184
Figure 9.12 Mean, maximum, and minimum errors for the models projection- reconstruction using non gender-specific, non jack-knife atlas for the female proximal tibia	184
Figure 9.13 Mean, maximum, and minimum RMS errors for the models projection- reconstruction using gender-specific, jack-knife atlas for the male proximal tibia	185
Figure 9.14 Mean, maximum, and minimum RMS errors for the models projection- reconstruction using gender-specific, non jack-knife atlas for the male proximal tibia	185
Figure 9.15 Mean, maximum, and minimum RMS errors for the models projection- reconstruction using non gender-specific, jack-knife atlas for the male proximal tibia	186
Figure 9.16 Mean, maximum, and minimum RMS errors for the models projection- reconstruction using non gender-specific, non jack-knife atlas for the male proximal tibia	186
Figure 9.17 Mean, maximum, and minimum RMS errors for the female distal femur morphing using the Direction Set method for the unreduced models' point clouds	187

Figure 9.18 Mean, maximum, and minimum RMS errors for the male distal femur morphing using the Direction Set method for the unreduced models' point clouds	187
Figure 9.19 Mean, maximum, and minimum RMS errors for the female proximal tibia morphing using the Direction Set method for the unreduced models' point clouds	188
Figure 9.20 Mean, maximum, and minimum RMS errors for the male proximal tibia morphing using the Direction Set method for the unreduced models' point clouds	188
Figure 9.21 Mean, maximum, and minimum RMS errors for the female distal femur morphing using the Direction Set method for the 4 mm reduced models' point clouds	189
Figure 9.22 Mean, maximum, and minimum RMS errors for the female proximal tibia morphing using the Direction Set method for the 4 mm reduced models' point clouds	189
Figure 9.23 Mean, maximum, and minimum RMS errors for the female proximal tibia morphing using the Direction Set method for the 4 mm reduced models' point clouds	190
Figure 9.24 Mean, maximum, and minimum RMS errors for the male proximal tibia morphing using the Direction Set method for the 4 mm reduced models' point clouds	190

Figure 9.25 Mean, maximum, and minimum RMS errors for the female distal femur morphing using the Direction Set method for the 8 mm reduced models' point clouds	191
Figure 9.26 an, maximum, and minimum RMS errors for the male distal femur morphing using the Direction Set method for the 8 mm reduced models' point clouds.....	191
Figure 9.27 Mean, maximum, and minimum RMS errors for the female proximal tibia morphing using the Direction Set method for the 8 mm reduced models' point clouds	192
Figure 9.28 Mean, maximum, and minimum RMS errors for the male proximal tibia morphing using the Direction Set method for the 8 mm reduced models' point clouds	192
Figure 9.29 Mean, maximum, and minimum RMS errors for the female distal femur morphing using the Direction Set method for the 16 mm reduced models' point clouds	193
Figure 9.30 Mean, maximum, and minimum RMS errors for the male distal femur morphing using the Direction Set method for the 16 mm reduced models' point clouds	193
Figure 9.31 Mean, maximum, and minimum RMS errors for the female proximal tibia morphing using the Direction Set optimization method for the 16 mm reduced models' point clouds	194

Figure 9.32 Mean, maximum, and minimum RMS errors for the male proximal tibia morphing using the Direction Set method for the 16 mm reduced models' point clouds	194
Figure 9.33 Mean, maximum, and minimum RMS errors for the female distal femur using the Direction Set method for the 32 mm reduced models' point clouds	195
Figure 9.34 Mean, maximum, and minimum RMS errors for the male distal femur using the Direction Set method for the 32 mm reduced models' point clouds	195
Figure 9.35 Mean, maximum, and minimum RMS errors for the female proximal tibia using the Direction Set method for the 32 mm reduced models' point clouds	196
Figure 9.36 Mean, maximum, and minimum RMS errors for the male proximal tibia using the Direction Set method for the 32 mm reduced models' point clouds	196
Figure 9.37 Mean, maximum, and minimum RMS errors for the female distal femur using the linear least squares method for the unreduced models' point clouds	197
Figure 9.38 Mean, maximum, and minimum RMS errors for the male distal femur using the linear least squares method for the unreduced models' point clouds	197
Figure 9.39 Mean, maximum, and minimum RMS errors for the female proximal tibia using the linear least squares method for the unreduced models' point clouds	198
Figure 9.40 Mean, maximum, and minimum RMS errors for the male proximal tibia using the linear least squares method for the unreduced models' point clouds	198
Figure 9.41 Mean, maximum, and minimum RMS errors for the female proximal tibia using the linear least squares method for the 4 mm reduced models' point clouds	199

Figure 9.42 Mean, maximum, and minimum RMS errors for the female proximal tibia using the linear least squares method for the 4 mm reduced models' point clouds using	199
Figure 9.43 Mean, maximum, and minimum RMS errors for the female proximal tibia using the linear least squares method for the 4 mm reduced models' point clouds	200
Figure 9.44 Mean, maximum, and minimum RMS errors for the male proximal tibia using the linear least squares method for the 4 mm reduced models' point clouds	200
Figure 9.45 Mean, maximum, and minimum RMS errors for the female distal femur using the linear least squares method for the 8 mm reduced models' point clouds	201
Figure 9.46 Mean, maximum, and minimum RMS errors for the female distal femur using the linear least squares method for the 8 mm reduced models' point clouds	201
Figure 9.47 Mean, maximum, and minimum RMS errors for the female proximal tibia using the linear least squares method for the 8 mm reduced models' point	202
Figure 9.48 Mean, maximum, and minimum RMS errors for the male proximal tibia using the linear least squares method for the 8 mm reduced models' point clouds	202
Figure 9.49 Mean, maximum, and minimum RMS errors for the female distal femur using the linear least squares method for the 16 mm reduced models' point clouds	203
Figure 9.50 Mean, maximum, and minimum RMS errors for the male distal femur using the linear least squares method for the 16 mm reduced models' point clouds	203

Figure 9.51 Mean, maximum, and minimum RMS errors for the female proximal tibia using the linear least squares method for the 16 mm reduced models' point clouds	204
Figure 9.52 Mean, maximum, and minimum RMS errors for the male proximal tibia using the linear least squares method for the 16 mm reduced models' point clouds Hybrid Morphing	204
Figure 9.53 Mean, maximum, and minimum RMS errors for the female distal femur using the hybrid method for the unreduced models' point clouds.....	205
Figure 9.54 Mean, maximum, and minimum RMS errors for the male distal femur using the hybrid method for the unreduced models' point clouds	205
Figure 9.55 Mean, maximum, and minimum RMS errors for the female proximal tibia using the hybrid method for the unreduced models' point clouds.....	206
Figure 9.56 Mean, maximum, and minimum RMS errors for the male proximal tibia using the hybrid method for the unreduced models' point clouds.....	206
Figure 9.57 Mean, maximum, and minimum RMS errors for the female distal femur using the hybrid method for the 4 mm reduced models' point clouds.....	207
Figure 9.58 Mean, maximum, and minimum RMS errors for the male distal femur using the hybrid method for the 4 mm reduced models' point clouds	207
Figure 9.59 Mean, maximum, and minimum RMS errors for the female proximal tibia using the hybrid method for the 4 mm reduced models' point clouds.....	208
Figure 9.60 Mean, maximum, and minimum RMS errors for the male proximal tibia using the hybrid morphing method for the 4 mm reduced models' point clouds ...	208

Figure 9.61 Mean, maximum, and minimum RMS errors for the female distal femur using the hybrid method for the 8 mm reduced models' point clouds.....	209
Figure 9.62 Mean, maximum, and minimum RMS errors for the male distal femur using the hybrid method for the 8 mm reduced models' point clouds	209
Figure 9.63 Mean, maximum, and minimum RMS errors for the female proximal tibia using the hybrid method for the 8 mm reduced models' point clouds.....	210
Figure 9.64 Mean, maximum, and minimum RMS errors for the male proximal tibia using the hybrid method for the 8 mm reduced models' point clouds.....	210
Figure 9.65 Mean, maximum, and minimum RMS errors for the female distal femur using the hybrid method for the 16 mm reduced models' point clouds.....	211
Figure 9.66 Mean, maximum, and minimum RMS errors for the male distal femur using the hybrid method for the 16 mm reduced models' point clouds	211
Figure 9.67 Mean, maximum, and minimum RMS errors for the female proximal tibia using the hybrid method for the 16 mm reduced models' point clouds.....	212
Figure 9.68 Mean, maximum, and minimum RMS errors for the male proximal tibia using the hybrid method for the 16 mm reduced models' point clouds.....	212
Figure 9.69 Point cloud for the ID_27_01 female distal femur phantom (left), and the point cloud overlaid on its reference model (right), with 6721 points and RMS error of 0.8 mm between the 75 th percentile filtered point cloud and the reference model	213
Figure 9.70 Histogram of the error between the point cloud and its reference model for the ID_27_01 female distal femur phantom with median error of 1.29 mm	213

- Figure 9.71 Point cloud for the ID_33_03 female distal femur phantom using (left), and the point cloud overlaid on its reference model (right), with 5322 points and RMS of 0.73 mm error between the 75th percentile filtered point cloud and the reference model..... 214
- Figure 9.72 Histogram of the error between the point cloud and its reference model for the ID_33_03 female distal femur phantom with median error of 1.14 mm 214
- Figure 9.73 Point cloud for the ID_37_23 female distal femur phantom (left), and the point cloud overlaid on its reference model (right) with 6624 points and RMS of 0.83 mm error between the 75th percentile filtered point cloud and the reference model..... 215
- Figure 9.74 Histogram of the error between the point cloud and its reference model for the ID_37_23 female distal femur phantom with median error of 1.4 mm 215
- Figure 9.75 Point cloud for the ID_39_01 female distal femur phantom using (left), and the point cloud overlaid on its reference model (right) with 6837 points and RMS error of 1 mm between the 75th percentile filtered point cloud and the reference model..... 216
- Figure 9.76 Histogram of the error between the point cloud and its reference model for the ID_39_01 female distal femur phantom with median error of 1.5 mm 216
- Figure 9.77 Point cloud for the ID_11_90 female distal femur phantom (left), and the point cloud overlaid on its reference model (right) with 7022 points and RMS error of 0.89 mm between the 75th percentile filtered point cloud and the reference model 217

- Figure 9.78 Histogram of the error between the point cloud and its reference model for the ID_11_90 female distal femur phantom with median error of 1.31 mm 217
- Figure 9.79 Point cloud for the ID_12_02 female distal femur phantom (left), and the point cloud overlaid on its reference model (right) with 7051 points and RMS error of 0.7 mm between the 75th percentile filtered point cloud and the reference model 218
- Figure 9.80 Histogram of the error between the point cloud and its reference model for the ID_12_02 female distal femur phantom with median error of 1.23 mm 218
- Figure 9.81 Point cloud for the ID_1_03 male distal femur phantom (left), and the point cloud overlaid on its reference model (right), with 5034 points and RMS error of 0.75 mm between the 75th percentile filtered point cloud and the reference model 219
- Figure 9.82 Histogram of the error between the point cloud and its reference model for the ID_1_03 male distal femur phantom with median error of 1.2 mm 219
- Figure 9.83 Point cloud for the ID_31_00 male distal femur phantom (left), and the point cloud overlaid on its reference model (right), with 5713 points and RMS error of 0.75 mm between the 75th percentile filtered point cloud and the reference model 220
- Figure 9.84 Histogram of the error between the point cloud and its reference model for the ID_31_00 male distal femur phantom with median error of 1.19 mm 220
- Figure 9.85 Point cloud for the ID_1_87 male distal femur phantom (left), and the point cloud overlaid on its reference model (right), with 6471 point and RMS error of 0.93 mm between the 75th percentile filtered point cloud and the reference model 221

Figure 9.86 Histogram of the error between the point cloud and its reference model for the ID_1_87 male distal femur phantom with median error of 1.54 mm	221
Figure 9.87 Point cloud for the ID_4_97 male distal femur phantom (left), and the point cloud overlaid on its reference model (right), with 7154 points and RMS of 0.86 mm error between the 75 th percentile filtered point cloud and the reference model.....	222
Figure 9.88 Histogram of the error between the point cloud and its reference model for the ID_4_97 male distal femur phantom with median error of 1.38 mm	222
Figure 9.89 Point cloud for the ID_11_97 male distal femur phantom (left), and the point cloud overlaid on its reference model (right), with 8183 points and RMS error of 0.63 mm between the 75 th percentile filtered point cloud and the reference model	223
Figure 9.90 Histogram of the error between the point cloud and its reference model for the ID_11_97 male distal femur phantom with median error of 1.15 mm	223
Figure 9.91 Point cloud for the ID_14_90 male distal femur phantom (left), and the point cloud overlaid on its reference model (right), with 6583 points and RMS error of 0.72 mm between the 75 th percentile filtered point cloud and the reference model	224
Figure 9.92 Histogram of the error between the point cloud and its reference model for the ID_14_90 male distal femur phantom with median error of 1.23 mm	224
Figure 9.93 Point cloud for the ID_39_01 female proximal tibia phantom (left), and the point cloud overlaid on its reference model (right), with 5767 points and RMS error of 0.85 mm between the 75 th percentile filtered point cloud and the reference model	225

- Figure 9.94 Histogram of the error between the point cloud and its reference model for the ID_39_01 female proximal tibia phantom with median error of 1.2 mm..... 225
- Figure 9.95 Point cloud for the ID_37_02 female proximal tibia phantom (left), and the point cloud overlaid on its reference model (right), with 4159 points and RMS error of 0.97 mm between the 75th percentile filtered point cloud and the reference model 226
- Figure 9.96 Histogram of the error between the point cloud and its reference model for the ID_37_02 female proximal tibia phantom with median error of 1.29 mm..... 226
- Figure 9.97 Point cloud for the ID_27_01 female proximal tibia phantom (left), and the point cloud overlaid on its corresponding model (right), with 5039 points and RMS error of 0.98 mm between the 75th percentile filtered point cloud and the reference model..... 227
- Figure 9.98 Histogram of the error between the point cloud and its reference model for the ID_27_01 female proximal tibia phantom with median error of 1.27 mm..... 227
- Figure 9.99 Point cloud for the ID_12_02 female proximal tibia phantom (left), and the point cloud overlaid on its reference model (right), with 5248 points and RMS error of 0.6 mm between the 75th percentile filtered point cloud and the reference model 228
- Figure 9.100 Histogram of the error between the point cloud and its reference model for the ID_12_02 female proximal tibia phantom with median error of 1.05 mm..... 228
- Figure 9.101 Point cloud for the ID_11_90 female proximal tibia phantom (left), and the point cloud overlaid on its reference model (right), with 4887 points and RMS error

of 0.94 mm between the 75th percentile filtered point cloud and the reference model
 229

Figure 9.102 Histogram of the error between the point cloud and its reference model for
 the ID_11_90 female proximal tibia phantom with median error of 1.28 mm..... 229

Figure 9.103 Point cloud for the ID_33_03 female proximal tibia phantom (left), and the
 point cloud overlaid on its reference model (right), with 6163 points and RMS error
 of 0.85 mm between the 75th percentile filtered point cloud and the reference model
 230

Figure 9.104 Histogram of the error between the point cloud and its reference model for
 the ID_33_03 female proximal tibia phantom with median error of 1.17 mm..... 230

Figure 9.105 Point cloud for the ID_1_03 male proximal tibia phantom (left), and the
 point cloud overlaid on its of 0.94 mm model (right), with 5711 points and RMS
 error of 0.85 mm between the 75th percentile filtered point cloud and the reference
 model..... 231

Figure 9.106 Histogram of the error between the point cloud and its reference model for
 the ID_1_03 male proximal tibia phantom with median error of 1.18 mm..... 231

Figure 9.107 Point cloud for the ID_14_90 male proximal tibia phantom (left), and the
 point cloud overlaid on its reference model (right), with 7222 points and RMS error
 of 0.86 mm between the 75th percentile filtered point cloud and the reference model
 232

Figure 9.108 Histogram of the error between the point cloud and its reference model for
 the ID_14_90 male proximal tibia phantom with median error of 1.24 mm..... 232

- Figure 9.109 Point cloud for the ID_31_00 male proximal tibia phantom (left), and the point cloud overlaid on its reference model (right), with 8155 points and RMS error of 0.77 mm between the 75th percentile filtered point cloud and the reference model 233
- Figure 9.110 Histogram of the error between the point cloud and its reference model for the ID_31_00 male proximal tibia phantom with median error of 1.13 mm..... 233
- Figure 9.111 Point cloud for the ID_11_97 male proximal tibia phantom (left), and the point cloud overlaid on its reference model (right), with 5481 points and RMS error of 1 mm between the 75th percentile filtered point cloud and the reference model 234
- Figure 9.112 Histogram of the error between the point cloud and its reference model for the ID_11_97 male proximal tibia phantom with median error of 1.35 mm..... 234
- Figure 9.113 Point cloud for the ID_1_87 male proximal tibia phantom (left), and the point cloud overlaid on its reference model (right), with 4968 points and RMS error of 0.82 mm between the 75th percentile filtered point cloud and the reference..... 235
- Figure 9.114 Histogram of the error between the point cloud and its reference model for the ID_1_87 male proximal tibia phantom with median error of 1.27 mm..... 235
- Figure 9.115 Point cloud for the ID_4_97 male proximal tibia phantom (left), and the point cloud overlaid on its reference model (right), with 4346 points and RMS error of 0.8 mm between the 75th percentile filtered point cloud and the reference model 236
- Figure 9.116 Histogram of the error between the point cloud and its reference model for the ID_4_97 male proximal tibia phantom with median error of 1.21 mm..... 236

Figure 9.117 Reconstruction RMS errors vs. point cloud density (in mm) for the female (top), and male (bottom) distal femur phantoms using the linear least squares method.....	237
Figure 9.118 Reconstruction RMS errors vs. point cloud density (in mm) for the female (top), and male (bottom) proximal tibia phantoms using the linear least squares method.....	238
Figure 9.119 Reconstruction RMS errors vs. point cloud density (in mm) for the female (top), and male (bottom) distalfemur phantoms using the linear least squares method	239
Figure 9.120 Reconstruction RMS errors vs. point cloud density (in mm) for the female (top), and male (bottom) proximal tibia phantoms using the linear least squares method.....	240
Figure 9.121 Reconstruction RMS errors vs. point cloud density (in mm) for the female (top), and male (bottom) distal femur phantoms using the hybrid morphing method	241
Figure 9.122 Reconstruction RMS errors vs. point cloud density (in mm) for the female (top), and male (bottom) proximal tibia phantoms using the hybrid morphing method	242
Figure 9.123 Point cloud (left), point cloud overlaid on reconstructed model (middle), and reconstruction error color map (right) for the first cadaver's distal femur	243
Figure 9.124 Point cloud (left), point cloud overlaid on reconstructed model (middle), and reconstruction error color map (right) for the first cadaver's proximal tibia...	244

- Figure 9.125 Point cloud (left), point cloud overlaid on reconstructed model (middle), and reconstruction error color map (right) for the second cadaver's distal femur.. 245
- Figure 9.126 Point cloud (left), reconstructed model (middle), and error map (right) for volunteer's knee 1 distal femur, trial 1, with RMS of 0.84 mm and Avg. error of 0.64 mm 249
- Figure 9.127 Point cloud (left), reconstructed 3D model (middle), and reconstruction error color map (right) for volunteer's knee 1 distal femur, trial 2, with RMS of 0.94 mm and Avg. error of 0.74 mm 250
- Figure 9.128 Point cloud (left), reconstructed 3D model (middle), and reconstruction error color map (right) for volunteer's knee 1 distal femur, trial 3, with RMS of 1.04 mm and Avg. error of 0.8 mm 251
- Figure 9.129 Point cloud (left), reconstructed 3D model (middle), and reconstruction error map (right) for volunteer's knee 1 proximal tibia, trial 1, with RMS of 0.78 mm and Avg. error of 0.6 mm 252
- Figure 9.130 Point cloud (left), reconstructed 3D model (middle), and reconstruction error color map (right) for volunteer 1 proximal tibia, trial 2, with RMS of 0.79 mm and Avg. error of 0.62 mm..... 253
- Figure 9.131 Point cloud (left), reconstructed 3D model (middle), and reconstruction error color map (right) for volunteer's knee 1 proximal tibia, trial 3, with RMS of 0.96 mm and Avg. error of 0.75 mm 254

Figure 9.132 Point cloud (left), reconstructed 3D model (middle), and error map (right) for volunteer's knee 2 distal femur, trial 1, with RMS of 1 mm and Avg. error of 0.78 mm	255
Figure 9.133 Point cloud (left), reconstructed 3D model (middle), and reconstruction error color map (right) for volunteer's knee 2 distal femur, trial 2, with RMS of 1.09 mm and Avg. error of 0.85 mm	256
Figure 9.134 Point cloud (left), reconstructed 3D model (middle), and reconstruction error color map (right) for volunteer 2 distal femur, trial 3, with RMS of 0.95 mm and Avg. error of 0.72 mm.....	257
Figure 9.135 Point cloud (left), reconstructed 3D model (middle), and reconstruction error color map (right) for volunteer 2 proximal tibia, trial 1, with RMS of 1.2 mm and Avg. error of 0.98 mm.....	258
Figure 9.136 Point cloud (left), reconstructed 3D model (middle), and reconstruction error color map (right) for volunteer 2 proximal tibia, trial 2, with RMS of 0.91 mm and Avg. error of 0.71 mm.....	259
Figure 9.137 Point cloud (left), reconstructed 3D model (middle), and reconstruction error color map (right) for volunteer 2 proximal tibia, trial 1, with RMS of 0.95 mm and Avg. error of 0.72 mm.....	260
Figure 9.138 Point cloud (left), reconstructed model (middle), and error map (right) for volunteer's knee 3 distal femur, trial 1, with RMS of 1.18 mm and Avg. error of 0.93 mm	261

- Figure 9.139 Point cloud (left), reconstructed 3D model (middle), and reconstruction error color map (right) for volunteer's knee3 distal femur, trial 2, with RMS of 1.05 mm and Avg. error of 0.83 mm 262
- Figure 9.140 Point cloud (left), reconstructed 3D model (middle), and reconstruction error color map (right) for volunteer's knee 3 distal femur, trial 3, with RMS of 1.01 mm and Avg. error of 0.81 mm 263
- Figure 9.141 Point cloud (left), reconstructed 3D model (middle), and reconstruction error color map (right) for volunteer's knee 3 proximal tibia, trial 1, with RMS of 1.05 mm and Avg. error of 0.8 mm 264
- Figure 9.142 Point cloud (left), reconstructed 3D model (middle), and reconstruction error color map (right) for volunteer's knee 3 proximal tibia, trial 2, with RMS of 0.88 mm and Avg. error of 0.69 mm 265
- Figure 9.143 Point cloud (left), reconstructed 3D model (middle), and reconstruction error color map (right) for volunteer's knee 3 proximal tibia, trial 3, with RMS of 0.89 mm and Avg. error of 0.68 mm 266
- Figure 9.144 Point cloud (left), reconstructed model (middle), and error map (right) for volunteer's knee 4distal femur, trial 1, with RMS of 1.14 mm and Avg. error of 0.89 mm 267
- Figure 9.145 Point cloud (left), reconstructed 3D model (middle), and reconstruction error color map (right) for volunteer's knee 4, trial 2, distal femur with RMS of 1.17 mm and Avg. error of 0.92 mm 268

Figure 9.146 Point cloud (left), reconstructed 3D model (middle), and reconstruction error color map (right) for volunteer's knee 4 distal femur, trial 3, with RMS of 1.2 mm and Avg. error of 0.95 mm	269
Figure 9.147 Point cloud (left), reconstructed 3D model (middle), and reconstruction error color map (right) for volunteer's knee 4 proximal tibia, trial 1, with RMS of 0.94 mm and Avg. error of 0.75 mm	270
Figure 9.148 Point cloud (left), reconstructed 3D model (middle), and reconstruction error color map (right) for volunteer's knee4 proximal tibia, trial 2, with RMS of 0.87 mm and Avg. error of 0.68 mm	271
Figure 9.149 Point cloud (left), reconstructed 3D model (middle), and reconstruction error color map (right) for volunteer's knee 4 proximal tibia, trial 3, with RMS of 0.86 mm and Avg. error of 0.66 mm	272
Figure 9.150 Point cloud (left), reconstructed model (middle), and error map (right) for volunteer's knee5 distal femur, trial 1, with RMS of 1.19 mm and Avg. error of 0.96 mm	273
Figure 9.151 Point cloud (left), reconstructed 3D model (middle), and reconstruction error color map (right) for volunteer's knee 5 distal femur, trial 2, with RMS of 1.28 mm and Avg. error of 1.01 mm	274
Figure 9.152 Point cloud (left), reconstructed 3D model (middle), and reconstruction error color map (right) for volunteer's knee 5, trial 3, distal femur with RMS of 1.3 mm and Avg. error of 1.04 mm	275

Figure 9.153 Point cloud (left), reconstructed 3D model (middle), and reconstruction error color map (right) for volunteer's knee 5 proximal tibia, trial 1, with RMS of 1.3 mm and Avg. error of 1.08 mm	276
Figure 9.154 Point cloud (left), reconstructed 3D model (middle), and reconstruction error color map (right) for volunteer's knee 5 proximal tibia, trial 2, with RMS of 1.42 mm and Avg. error of 1.13 mm	277
Figure 9.155 Point cloud (left), reconstructed 3D model (middle), and reconstruction error color map (right) for volunteer's knee 5 proximal tibia, trial 3, with RMS of 1.49 mm and Avg. error of 1.2 mm	278
Figure 9.156 Point cloud (left), reconstructed model (middle), and error color map (right) for volunteer's knee 6 distal femur, trial 1, with RMS of 1.27 mm and Avg. error of 1 mm	279
Figure 9.157 Point cloud (left), reconstructed 3D model (middle), and reconstruction error color map (right) for volunteer's knee 6 distal femur, trial 2, with RMS of 1.17 mm and Avg. error of 0.92 mm	280
Figure 9.158 Point cloud (left), reconstructed 3D model (middle), and reconstruction error color map (right) for volunteer's knee 6 distal femur, trial 3, with RMS of 1.21 mm and Avg. error of 0.97 mm	281
Figure 9.159 Point cloud (left), reconstructed 3D model (middle), and reconstruction error color map (right) for volunteer's knee 6 proximal tibia, trial 1, with RMS of 1.61 mm and Avg. error of 1.27 mm	282

Figure 9.160 Point cloud (left), reconstructed 3D model (middle), and reconstruction error color map (right) for volunteer's knee 6 proximal tibia, trial 2, with RMS of 1.54 mm and Avg. error of 1.23 mm	283
--	-----

Figure 9.161 Point cloud (left), reconstructed 3D model (middle), and reconstruction error color map (right) for volunteer's knee 6 proximal tibia, trial 3, with RMS of 1.75 mm and Avg. error of 1.43 mm	284
--	-----

Scientific Terminology

cm	Centimeters
dB	Decibels
Hz	Hertz
GHz	Gigahertz
KHz	Kilohertz
MHz	Megahertz
mm	Millimeters
m/s	Meters per second
μ	Mean
σ	Standard Deviation

Acronyms

2D	Two Dimensional
3D	Three Dimensional
A-Mode	Amplitude Mode
API	Application Programming Interface
Avg.	Average
B-Mode	Brightness Mode
BMI	Body Mass Index
CT	Computed Tomography
CSP	Closest Surface Point
FDF	Female Distal Femur
FDM	Fused Deposition Modeling
FPT	Female Proximal Tibia
G-Specific	Gender-Specific
ICP	Iterative Closest Point
JK	Jack-Knife
MDF	Male Distal Femur
MPT	Male Proximal Tibia
MRI	Magnetic Resonance Imaging
NG-Specific	Non Gender-Specific

NJK	Non Jack-Knife
PCA	Principal Component Analysis
RF	Radio Frequency
RMS	Root Mean Square
SVD	Singular Value Decomposition
VIBE	Volumetric Interpolated Breath-Hold Examination

Chapter 1 Introduction

1.1 Significance

Joint pain is a major public health problem, responsible for significant costs and disability in the united states. Due at least in part to underlying osteoarthritis, the prevalence of joint pain is 46 million and increasing due to an aging population and an epidemic of increasing obesity [1]. Joint pain costs the healthcare system \$37 billion annually [1].

Depending on the degree of disability, joint pain can be treated with systemic (e.g. dietary supplements, prescription pain relievers and anti-inflammatory medications) and targeted (e.g. medication injections, surgical correction of underlying pathology and total joint replacement surgery) interventions. Within the targeted interventions segment, annually there are an estimated 10,000,000 patients receiving treatments of the knee, hip, spine and shoulder, including an estimated 505,000 knee, 280,000 hip and 42,000 shoulder arthroplasties.

Injections of expensive pre-arthroplasty substances (e.g. single dose visco-supplements, platelet rich plasma, stem cells, etc.) necessitate accurate injection into the joint space as studies have revealed injection inaccuracies ranging from 18-34% in the knee and 33-90% in the shoulder with similar missed injection rates in the hip [1]- [8].

By 2030, the number of knee and hip arthroplasties are projected to increase by 565% and 101% respectively[1]. For every joint replacement patient, there are an estimated 10 patients upstream in the care pathway creating a large symptomatic population that is projected to increase 40% by 2030 [1].

A major challenge for conservative management of joint pain is the lack of low cost, accurate, radiation-free joint imaging. A low-cost imaging modality to accurately visualize joints would represent a significant musculoskeletal innovation, moving diagnostic and treatment to lower-cost sites relative to MRI or fluoroscopy imaging. The site of care could move from the radiology suite to the physician's office. Today, only knee and shoulder injections and aspirations are office-based procedures, and then, only for skilled orthopedists. Improved joint visualization would enable treatment of other joints in the office. Improved visualization and resulting migration of many injections and aspirations to lower-cost settings ultimately by the non-orthopedist is attractive to third-party payers.

Ultrasound is widely accepted as a means to visualize the joint space, but not without limitations. Common imaging techniques are 2D and do not provide full insight of the joint space. X-Ray shows only joint space and little other bony anatomic data. Current ultrasound-based joint injection guidance systems provide orthopedic surgeons with a difficult to interpret 2D planar image of a limited area of the joint to be injected. Some surgeons use fluoroscopy to assist with the guidance, which can be harmful to both the patient and the surgeon due to the ionizing X-Ray radiation emitted. To limit the amount of radiation exposure, many surgeons do not keep the fluoroscopy machine active to track the needle while it is being inserted into the joint. Rather, they capture snapshots at different time intervals to obtain the location of the needle relative to the joint space.

Current imaging techniques are expensive, furthermore X-Ray based imaging systems (CT, X-Ray, and Fluoroscopy) expose patients to radiation[9]-[12]. Most

medical practices cannot afford fluoroscopic or MRI guided equipment, so almost all are facility or hospital based. Injections with these modalities are often more painful if multiple attempts are needed. Fluoroscopy exposes the patient to X-Ray radiation far in excess to conventional radiographs.

This work targets the development of a real-time knee imaging system for automatic reconstruction of patient-specific 3D models of the knee bones using ultrasound. This system utilizes ultrasound scans of the joint performed by the surgeon to reconstruct and register 3D models of the patient's actual bones. This new technology will enable additional office-based diagnostics and treatment planning innovations in orthopedics, which are :

1. An accurate low cost, radiation-free 3D joint injection guidance system that can provide the orthopedic surgeons with a 3D view of the bones, while leaving their hands free during the injection process. The injection guidance system can be extended to include the joint space by 3D visualization of the joint's volume or the more advanced approach of 3D reconstruction of soft tissue (cartilage, muscles, ligaments, and tendons) models.
2. A diagnostic bone and joint imaging system that allows the physician to optimize pre-operative planning by identifying additional 3D anatomical information that is of substantial value in understanding patient symptoms (e.g. size, shape, contours, osteophytes, joint space, and bone deformities).
3. Imaging system that allows precise patient-specific pre-operative 3D bone reconstructions will address the need for reduced instrument and implant hospital

inventory and ensure correct implant selection at surgery. Additionally, using the reconstructed patient-specific 3D models, the orthopedist can match the patient to the best fitting off the shelf implant. The 3D bone models can also be used by orthopedic implants manufacturers to create patient-specific implants.

4. 3D dynamic joint motion tracking (by tracking the bone not the outer surface of the joint) and analysis using ultrasound utilizing the reconstructed 3D patient-specific bones models.

1.2 Literature Review

Reconstruction of patient-specific 3D models of the bones has been widely investigated for the CT and MRI imaging modalities. However, the research of the use of ultrasound in the 3D patient-specific modeling of bones has not been widely investigated.

Barrat et. al, and Chan et. al. have researched the instantiation of femur and pelvis 3D models using B-mode ultrasound [13][14]. Figure 1.1 shows an overview of the ultrasound-based image guided system developed by Barrat et. al.

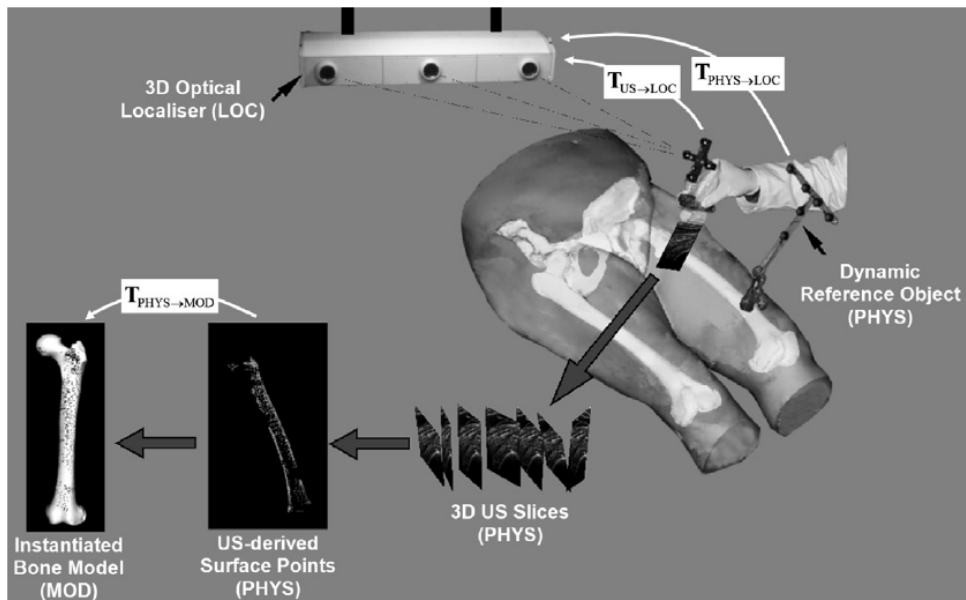


Figure 1.1 Overview of the ultrasound-based image guided system developed by Barrat et. al for 3D patient-specific model reconstruction of the femur [13]

They extracted the bone contours from B-Mode ultrasound images by manually selecting ten points on the bone's contour in each ultrasound image. These 10 points are then used to fit a cubic spline that represents the bone contour in segmented ultrasound image. They used the principal components analysis (PCA)-based statistical deformable models (SDM) to reconstruct patient-specific bones models. The first five principal

components were used to instantiate the patient-specific model. The statistical shape model (SSM) or atlas for the femur was built using 16 femur scans for male and female patients, while the pelvis atlas was built using ten scans for female patients. The ultrasound scans were collected from three cadavers. Optotrack 3020 optical tracking system (from Northern Digital Inc, Canada) was used for tracking the ultrasound probe's motion while being used in scanning. The accuracy of the optical tracking is 0.1-0.15 mm[24]. Reference tracking probes were implanted in the cadavers' bones to avoid the leg motions artifacts. They performed the experiments on three cadavers (three pelvises, and six femurs). A mean reconstruction RMS error of 4.15 mm was achieved for the six femurs, and 2.83 mm for the three pelvises. Figure 1.2 shows the mean reconstruction error color maps for the six cadaveric femoral models reconstructed. The reported scan time was 5-30 min to selectively acquire high quality ultrasound images that can be used for the 3D model reconstruction. The drawbacks of this work are:

- The ultrasound images were segmented manually.
- The ultrasound images had to be collected carefully to acquire high quality ultrasound images, which requires a skilled user and more acquisition time.
- A reference tracking probe implanted in the cadaver's knee was used, which makes the method highly invasive.
- Despite the high accuracy optical tracking system used (with 0.1 mm accuracy), and implanted reference probe (which prevents patient motion artifact), the achieved RMS error is 4.15 mm for the femoral model reconstruction.

- It did not focus on the articulating surfaces of the knee bones, and the scanning protocols or procedures required to image those articulating surface.

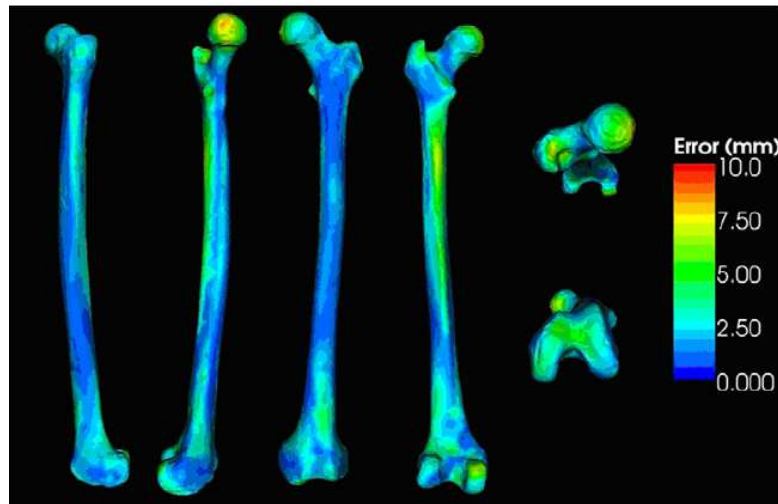


Figure 1.2 The color maps for the mean reconstruction error (compared with the reference models) for the 6 cadaveric femurs used by Barrat et. al in their experiments for 3D patient-specific model reconstruction of the femur [13]

Kilian et. al. investigated the reconstruction of the distal femur bone model using tracked B-mode ultrasound [15]. One cadaveric distal femur was used to test the developed system. An optical motion tracking system was used for the ultrasound probe's motion tracking. A reference optical tracking probe was implanted in the bone while being scanned to avoid motion artifacts in the collected scans, which makes the process an invasive process. They claim a scanning time of five minutes for the distal femur. Figure 1.3 shows a snapshot for the scanning of the cadaveric knee using the tracked ultrasound probe by Kilian et. al. [15]

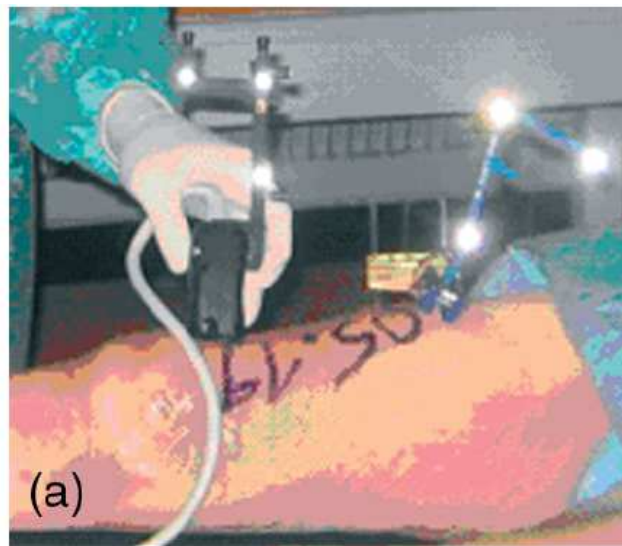


Figure 1.3 Snapshot for the scanning of the cadaveric knee using the tracked ultrasound probe by Kilian et. al. [15]

The reconstruction error was specified to be less than 1 mm without mentioning an exact error value, with local error values exceeding 2 mm at the trochlear groove and femoral condyles (the articulating surfaces of the distal femur). The error was calculated by comparing the 3D bone model created using the ultrasound and a 3D bone model created from bone morphing from a set of point digitized over the surface of the distal femur after dissecting the cadaver. They claim automatic segmentation of the B-mode images using active contours. The speed of the contour segmentation method was not mentioned. Figure 1.4 show a reconstructed point cloud for the cadaveric distal femur [15]. Figure 1.5 shows the distance error color map for the reconstructed 3D models of the cadaveric distal femur scanned by two operators in the experiments performed by Kilian et. al [15].



Figure 1.4 The point cloud reconstructed for the cadaveric distal femur scanned in the experiment performed by Kilian et. al. [15]

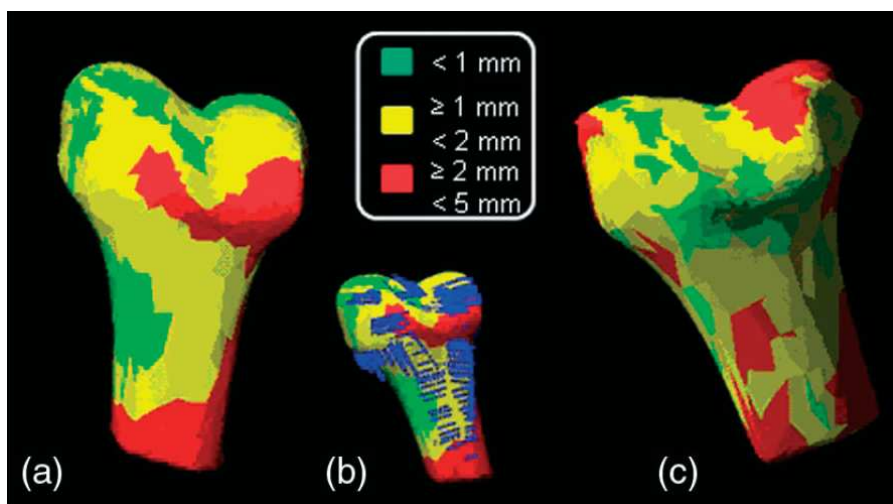


Figure 1.5 Color maps for the error between the reconstructed 3D models of the cadaveric distal femur (scanned by first (a, b), , and second (c) operator) using ultrasound, and the 3D model reconstructed by bone morphing using a point cloud digitized over the dissected cadaveric femur, by Kilian et. al. [15].

Two scanning methods were mentioned; the first was called single image scanning, where the operator has to scan through the bone until he/she find a clear ultrasound image of the bone interface then he/she press a pedal to make the imaging software acquire this

image and process it to extract the bone contour. It was mentioned this image selection process has to be performed at least six times to acquire a minimum of six images. The second scanning method is the continuous scanning, in which the operator scans the bone, and all the images are acquired by the software and processed to extract the bone contours. The drawbacks of this work are:

- A specific bone model reconstruction error value was not mentioned.
- The reconstruction error calculation was not performed against a segmented CT or MRI scans of the bone, but rather it was performed using a morphing-based reconstructed model, which makes the reported reconstruction error inaccurate.
- High error (greater than 2 mm) values reported at the clinically important bone articulating surfaces (distal condyles, and trochlear groove)
- The use of bone-implanted reference probe, which makes the process invasive.
- The B-mode images automatic segmentation method was not described, nor was its accuracy mentioned, and whether it is fast enough to be real-time or not.

Some research groups attempted the development of automatic segmentation methods for the bone contours from B-mode ultrasound images. Kumar et. al. used Bayesian probability model to segment bone contours in the ultrasound images of plastic bone immersed in water [16]. The features used in the Bayesian model were the intensity values and the reverberation. Processing time was five seconds per image, running on a 2.5 GHz Pentium 4 processor. Gonçalves et. al. experimented the snakes and the probabilistic methods for bone contours segmentation from B-mode ultrasound images. Both methods require manual selection of initialization points. The use of A-mode

ultrasound for intra-operative registration in computer aided orthopedic surgery for the skull [17]-[20], and knee [21] has also been investigated for the registration between the patient's surgical region of interest and the MRI/CT scans. It is also used for the registration process in the robotic surgeries.

In this work, an imaging system for the reconstruction of 3D knee models using ultrasound was developed to overcome the drawbacks of the mentioned previous work in this area, and provide an accurate, fully automated, real-time, noninvasive imaging system for 3D knee model reconstruction using ultrasound RF data.

1.3 Fundamental Contributions

The presented work in this dissertation was built using the knee bones statistical atlases developed in the center for musculoskeletal research (CMR) at the University of Tennessee. The cadaveric experiments were performed with the help of the anthropology department. The clinical study was prepared and performed in the Minimally invasive Orthopedics clinic, Columbus, Ohio. My fundamental contribution in this work are:

1. Developed a novel method for fully automated real-time patient-specific 3D bone model reconstruction using ultrasound RF data.
2. Developed a novel signal processing framework for ultrasound RF data processing for automatic real-time extraction of bone contours from ultrasound raw RF data frames.
3. Developed a knee scanning protocol and partial scans registration method for scanning the different articulating surfaces of the knee bones at different flexion angles without the need for invasive reference motion tracking probes implanted in the bones.
4. Developed a new method for 3D bone model reconstruction by morphing a template model to a point cloud acquired using tracked single-element ultrasound transducer.
5. Performed clinical study of the developed method and imaging system for patient-specific 3D knee model reconstruction using ultrasound RF data to evaluate its accuracy and repeatability.
6. Developed a simulation framework for knee kinematics tracking using single-element ultrasound transducers, which can be applied to other joints.

1.4 Dissertation Outline

Chapter 2 provides an introduction to ultrasound.

Chapter 3 discusses the statistical atlas used for the bone morphing, and its performance analysis. It also discusses the different morphing used and their accuracy and performance.

Chapter 4 discusses the developed system and method for 3D knee model reconstruction using single-element ultrasound transducer.

Chapter 5 presents the developed system and method for 3D knee model reconstruction using ultrasound RF data.

Chapter 6 presents the clinical study performed on the developed system and method for 3D knee model reconstruction using ultrasound RF data.

Chapter 7 presents the results for the phantom experiments of the single-element ultrasound transducer system. It also presents the cadaveric experiments, and the clinical study results for the 3D knee model reconstruction system using ultrasound RF data.

Chapter 8 presents the potential technologies that can be developed in future work, based on the developed 3D knee model reconstruction system using ultrasound RF data.

Chapter 2 Introduction to Ultrasound

Ultrasound is a pressure wave that travels through a medium with frequency greater than 20 KHz. Mechanical waves with frequency smaller than 20 KHz are audible sound waves. The ultrasound wave consists of compression and rarefaction regions in which the medium particles oscillate and transmit the mechanical energy through the medium. There are two types of ultrasound waves, these are:

- **Longitudinal Ultrasound Waves:** in which the direction of the propagation is the same direction of the particles displacement (oscillation). Example of this type of waves is the ultrasound waves in soft tissue, air, and water.
- **Transverse (Shear) Ultrasound Waves:** in which the direction of the propagation perpendicular to the particles displacement (oscillation). Example of this type of waves is the ultrasound waves in bones, and solids.

The speed of the ultrasound wave is equal to the product of the ultrasound frequency and the wavelength of the ultrasound wave:

$$c = \lambda f \quad (2.1)$$

Where f is the ultrasound frequency and λ is the wavelength. The frequency is dependent on the ultrasound transducer, while the wavelength depends on the medium, and changes with the change in the ultrasound speed in the medium.

The ultrasound speed is determined by the medium's compressibility (bulk modulus) K and density ρ as follows:

$$c = \frac{1}{\sqrt{\rho K}} \quad (2.2)$$

As the density of the medium increases, its compressibility decreases, but the decrease in the compressibility is a lot bigger than the increase in the density; therefore it dominates the effect on the ultrasound speed in the medium and results in increased ultrasound speed in the medium.

Every medium has its characteristic acoustic impedance denoted by Z . the medium's acoustic impedance is a function of the ultrasound velocity of the medium, and the density of the medium according to the following relation:

$$Z = \rho c \quad (2.3)$$

Where c is the ultrasound speed in the medium and ρ is the density of the medium. Since the ultrasound speed itself is a function of the density and compressibility of the medium, the acoustic impedance Z can be alternatively expressed in terms of the compressibility and density of the medium as follows:

$$Z = \sqrt{\frac{\rho}{K}} \quad (2.4)$$

The acoustic impedance can also alternatively expresses in terms of the local pressure and velocity of the medium particles as follows:

$$Z = \frac{p}{s} \quad (2.5)$$

Where s is the local velocity of the medium particles, and p is the local pressure exerted on the medium particles to produce the velocity s . this relation is similar to the electric impedance relation which is given by the following relation:

$$Z = \frac{V}{I} \quad (2.6)$$

Where V is the electric voltage (potential), and I is the produced current through the electric impedance.

The intensity I of the ultrasound beam is given by:

$$I = ps = \frac{p^2}{Z} \quad (2.7)$$

The ultrasound wave interacts with the medium in two different ways:

1. Reflection and Transmission: The reflection of the ultrasound wave occurs when the wave passes through two mediums with different acoustic impedances (having impedance mismatch). The amplitude reflection coefficient R_p (the percentage of the amplitude of the reflected pressure of the ultrasound wave) of the ultrasound wave is a function of the impedances of the two media as follows:

$$R_p = \frac{p_r}{p_i} = \frac{Z_2 - Z_1}{Z_2 + Z_1} \quad (2.8)$$

Where p_i is the incident pressure, and p_r is the reflected pressure. Z_1 , and Z_2 are the acoustic impedances of the first and second medium, respectively. The intensity reflection coefficient R_I is given by:

$$R_I = R_p^2 = \frac{(Z_2 - Z_1)^2}{(Z_2 + Z_1)^2} \quad (2.9)$$

The intensity transmission coefficient T_I is given by:

$$T_I = 1 - R_I^2 = \frac{4Z_1Z_2}{(Z_2 + Z_1)^2} \quad (2.10)$$

Therefore, as the impedance mismatch of a two medium interface increases, the reflectivity increases.

2. Attenuation: The energy of the ultrasound wave is dissipated as it travels through the medium. This energy dissipation results in attenuation to the ultrasound wave. This attenuated is carried out by two processes:

- **Absorption:** A portion of the ultrasound wave energy is transformed into heat energy and is absorbed by the medium. The rate of absorption is a linear function of the ultrasound frequency.
- **Scattering:** When the ultrasound wave hits particles with different impedance than the medium, and of size similar to the wavelength of the ultrasound wave, the particles act as an ultrasound source and radiate the ultrasound incident in spherical volume (in all directions). This results in weakening the main beam of the ultrasound wave.

The radiated ultrasound beam from the ultrasound crystal contains a main beam and side lobes. The divergence angle φ_d (measured from the line perpendicular to the transducer at its center, and the edge of the ultrasound beam) of the main beam is given by:

$$\varphi_d = \arcsin(1.22 \frac{\lambda}{D}) \quad (2.11)$$

Where D is the diameter of the ultrasound transducer, and λ is the wavelength of the ultrasound wave. The distance traveled by the ultrasound beam before it starts divergence is called the near field distance and is given by:

$$NFD = \frac{D^2}{4\lambda} \quad (2.12)$$

The ultrasound is used in two modes of operation:

- **Continuous:** The continuous ultrasound wave is a sinusoidal wave and its wave equation is given by:

$$P = P_0 \sin(2\pi ft + \phi) \quad (2.13)$$

Where P is the amplitude of the wave (pressure amplitude), P_0 is the maximum pressure amplitude, f is the wave frequency, t is the time, and ϕ is the phase of the wave. It is used in Doppler imaging and therapeutic ultrasound.

- **Pulsed (Pulse-Echo):** Pulse-echo ultrasound is the most widely used ultrasound imaging mode. It is used in the B-mode, M-mode, and pulsed Doppler imaging. It

consists of sending an ultrasound pulse, and then receives the reflected echoes at different tissue interfaces in the imaged specimen. The ultrasound pulse wave is ideally a decaying sinusoidal wave, and its wave equation is given by:

$$P = e^{-\frac{t}{\tau}} P_0 \sin(2\pi f t + \phi) \quad (2.14)$$

Where τ is the time constant of the decaying wave, and it depends on the damping of the ultrasound pulser generating the ultrasound pulse. Since most ultrasound transducers are wideband transducer (to generate a pulse with small pulse duration in order to achieve high axial resolution), the generated pulse contains a several frequencies instead of one single frequency as in the continuous ultrasound mode.

In this work, the pulse-echo ultrasound mode is used for the reconstruction of the point cloud representing the bone's surface.

Chapter 3 Bone Morphing

3.1 Introduction

Bone morphing is the process of reconstruction of 3D bone model by deforming a template bone model, which can be the bone atlas' mean model, to reconstruct the new 3D bone model. The model deformation is performed using an optimization algorithm which changes the shape of the template model to match the shape dictated by a morphing guide. This morphing guide is the available information for the bone morphing to create the new 3D model. The morphing guide can be any type of measurements or information about the bone to be modeled. The optimization error function measures the degree of fitting between the deforming model and the given measurements or information about the bone. The morphing process changes the shape of the template model to create a new model that maximizes the degree of fitting (or reduces the error) between the reconstructed model and the given measurement or information about the bone to be modeled.

In this work, the morphing (deformation) guide is a reconstructed point cloud representing the bone's surface. Since the bone's 3D model consists of thousands of vertices (4120 for the distal femur, and 4812 for the proximal tibia), and each vertex consists of three variables which are the x, y, and z coordinates of the vertex, which makes each model consists approximately of 12,000 variables. It is nearly impossible to perform the optimization on those 12,000 variables (the x, y, and z coordinates of the model's vertices) for every 3D bone model to be reconstructed.

In order to perform the optimization for the model's morphology, the 3D model needs to be represented by a limited number of variables that can be managed by an optimization algorithm. To overcome this problem, the 3D models are transformed into another domain which can approximate the model with fewer parameters. Several surface representation methods have been developed and studied. Fourier descriptors have been used for shape approximation [29], [30] in which Fourier transform is applied to the 3D model, and the model is approximated by the Fourier descriptors which capture the spatial frequency coefficients of the model's shape.

Another approach introduced by Cootes and Taylor[31] is statistical method that uses point distribution models (alternatively called statistical deformable models). Statistical deformable models method is based on the statistical analysis of a set of training models. For 3D bone surface representation, the training models are 3D models of bones to be represented. These bones' models can be obtained by scanning dry cadaveric bones using laser scanners or motion tracking systems. Another method of obtaining the training bone models is scanning dry cadaveric bones using computed tomography imaging (CT) or scanning patients/volunteers using CT or magnetic resonance imaging (MRI). These CT or MRI scans are then segmented (manually, semi-automatically, or automatically) to obtain the 3D bones' models. Principal component analysis (PCA) is then performed on the training set's models. The PCA transforms the models from the three-dimensional Cartesian coordinate space defined by the x, y, and z coordinates of the models vertices, to a new vector space called eigenspace. The unit vectors comprising this *eigenspace*, are the modes of variation of the morphology of the

training set's models. Each model of the training data set can then be represented as a linear combination of the eigenvectors plus the dataset's mean model. These eigenvectors are called the principal components, and consequently, their coefficients are called principal components coefficients. Any model outside the training dataset can be approximated by the dataset's mean model plus a linear combination of the principal components using different principal components' coefficients. The deformable models method has been extensively used for automatic segmentation of CT, and MRI scans for different body organs. It has also been used for reconstruction of 3D bones models from multi-planer X-Ray images[32]-[34], and from sparse point clouds acquired from the surface of the bone[35]-[37].

In this work, the statistical deformable models method was used for the reconstruction of the 3D surface models for the scanned knee bones, using the bones' surface point clouds reconstructed using ultrasound. In the following sections, the statistical deformable method will be described in more detail. The training datasets (alternatively referred to as atlases) will be presented with a detailed analysis for their 3D model representation capabilities. Then the bone morphing methods used in this work will be presented along with their performance and reconstruction accuracy analysis.

3.2 Knee Bones Statistical Deformable Models

3.2.1 Atlas Dataset

The knee bone atlases used in this work were created using a dataset of 444 dry femur (144 female, 304 male) and 422 dry tibia (119 female, and 303 male) bones, which were CT-scanned and segmented. Segmented bone models for each of the knee bones (femur, and tibia) were then used to create its statistical atlases. The first step in creating the statistical atlas for each bone's dataset is to establish anatomical correspondence between the individual models in each dataset; i.e. each vertex in each model in the dataset is anatomically corresponding to the same vertex in all the other models of the same dataset [38], and [39]. The output of the correspondence creation process is a set of 3D bone models M_i (where $i \in [1, N]$, N is the number of models in the dataset) having the same number of vertices, and every vertex v_j in any of the models corresponds (at the same anatomical location on the bone) to the vertex v_j' in the other models.

After the anatomical correspondence is established for all the 3D bone models of each femur, and tibia datasets, the distal portion of the femur and the proximal portion of the tibia bones are separated from the femur and tibia models. This is performed by creating a mean model for the models in each dataset, and then labeling the vertices in the distal femur portion of the mean distal femur, and the vertices in the proximal tibia portion of the tibia. The vertices corresponding to the mean model's labeled vertices are then extracted from each model in the dataset to create the distal femur or proximal tibia models. These separated distal femur and proximal tibia bones models maintains the anatomical correspondence established for the femur, and tibia models. These distal

femur and proximal tibia bone models were used throughout this work for the atlas analysis and 3D knee bone models reconstruction.

In order to study the density of the models' vertices, the average distance between each vertex and its neighbor vertices was calculated for each model of the atlases. This distance will be denoted as the model's inter-vertices distance and is calculated as follows:

Given a 3D model M_i with a set of vertices v_j , where $j \in [1, m]$, where m is the number of vertices in the model. The mean inter-vertices distance d_j for the vertex v_j is the mean distance between the vertex and its neighbor vertices and can be defined as follows:

$$d_j = \frac{1}{l} \sum_{i=1}^l \|v_j - v_i\| \quad (3.1)$$

Where v_i is the i^{th} neighbor vertex of the vertex v_j , and l is the number of neighbor vertices to the vertex v_j . The mean inter-vertices distance for the model M_i is the average of the inter-vertices distance for the model's vertices. Histograms of the models' mean inter-vertices distances are shown in Figure 3.1 through Figure 3.4 for the female distal femur, male distal femur, female proximal tibia, and male proximal tibia atlas models respectively. The average of the models' mean inter-vertices distances are 2.66 mm for the female distal femur, 2.32 mm for the male distal femur, 1.76 mm for the female proximal tibia, and 2 mm for the male proximal tibia datasets respectively.

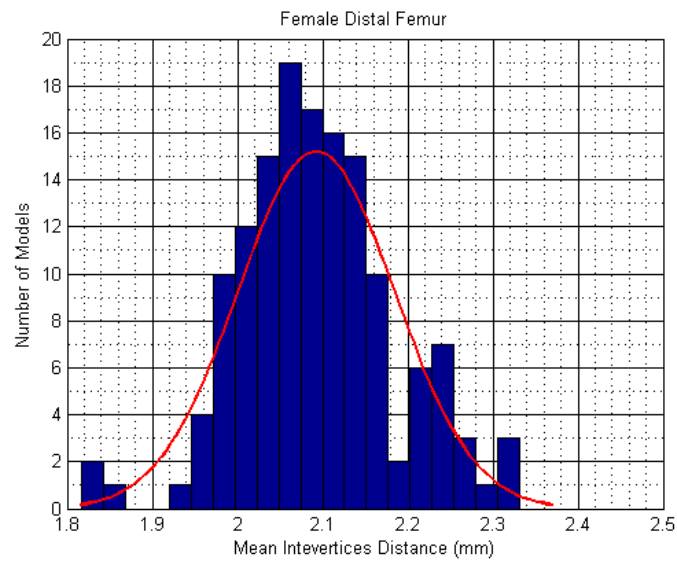


Figure 3.1 Histogram of the models' mean inter-vertices distance for the female distal femur models with an average of 2.66 mm

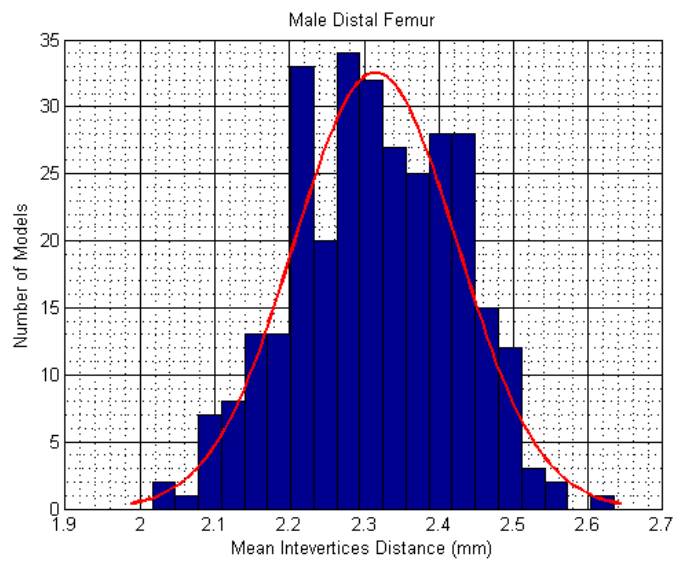


Figure 3.2 Histogram of the models' mean inter-vertices distance for the male distal femur models with an average of 2.32 mm

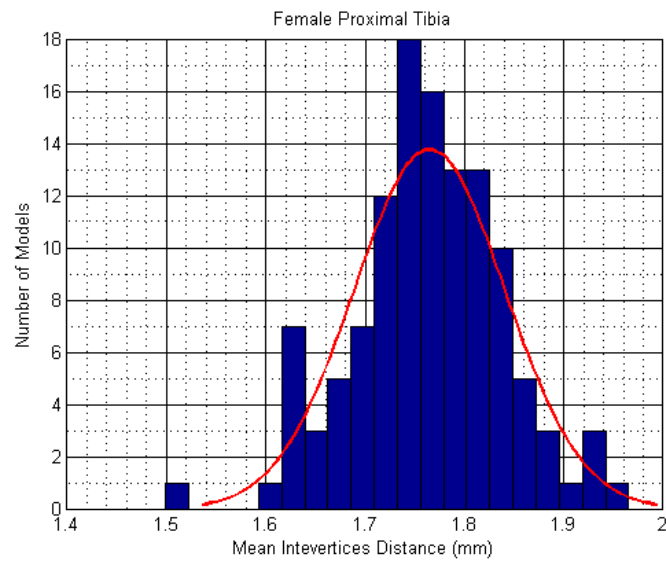


Figure 3.3 Histogram of the models' mean inter-verteces distance for the female proximal tibia models with an average of 1.76 mm

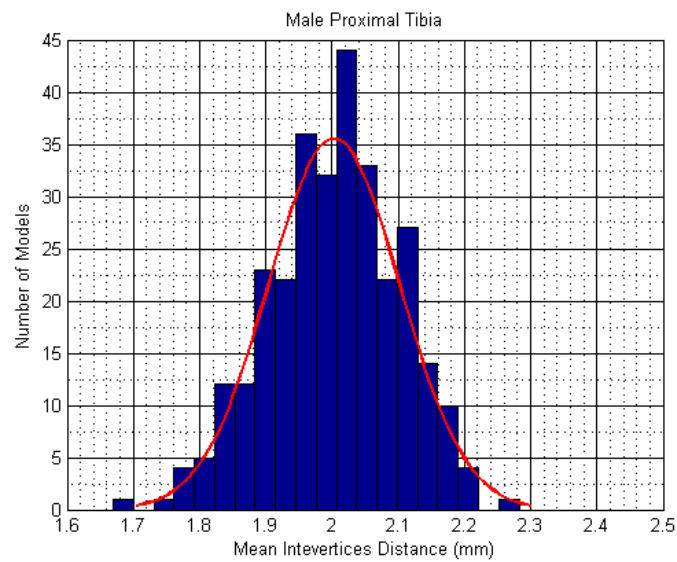


Figure 3.4 Histogram of the models' mean inter-verteces distance for the male proximal tibia models with an average of 2 mm

3.2.2 Knee Bones Principal Component Analysis (PCA)

Principal Component Analysis (PCA) was performed on each of the bone models datasets to extract the modes of variations of the bones' morphology which are represented by the eigenvectors generated by the PCA. These eigenvectors are alternatively called eigenbones or principal components, and they define the vector space for the bone morphology variations existing in the bone's dataset. Any bone model in the dataset used to perform the PCA can be expressed as a linear combination of the eigenbones plus the mean model of the dataset as follows:

$$M_{avg} = \frac{1}{N} \sum_{i=1}^N M_i \quad (3.2)$$

$$M_i = M_{avg} + \sum_{k=1}^L \alpha_{ik} U_k \quad \forall i \in [1, N] \quad (3.3)$$

Where M_{avg} is the mean model of the dataset, L is the dimensionality of the eigenspace (the number of eigenbones), and is equal to the number of models in the dataset N . U_k is the k^{th} eigenbone, and α_{ik} is the k^{th} shape descriptor or eigenbone's coefficient for the i^{th} model.

Furthermore, any new model M_{new} outside the dataset (used to perform the PCA) can be approximated by new values of the shape descriptors (eigenvectors coefficients) as follows:

$$M_{new} \simeq M_{avg} + \sum_{k=1}^W \alpha_k U_k \quad (3.4)$$

Where M_{new} is the new bone's model, α_k are the shape descriptors for the new model, U_k are the eigenvectors (principal components) of the atlas, and W is the number of principal components used in the model approximation, and $W \leq L$. The accuracy of the representation of a new model is directly proportional to the number of principal components W used for model representation and the number of models L of the dataset used for the PCA. The residual error or root mean square error (RMS) for the new model representation using the PCA shape descriptors is defined by:

$$\text{RMS} = \text{rms} \left[M_{new} - (M_{avg} + \sum_{k=1}^W \alpha_k U_k) \right] \quad (3.5)$$

Where the root mean square error (RMSE) of two models A, and B having the same number of vertices m is defined by:

$$\text{RMSE} = \text{rmse}(A - B) = \sqrt{\frac{\sum_{j=1}^m \|V_{Aj} - V_{Bj}\|^2}{m}} \quad (3.6)$$

Where m is the number of vertices in each model, V_{Aj} is the j^{th} vertex in model A, and similarly V_{Bj} is the j^{th} vertex in model B. Table 3.1., and Table 3.2 list the accumulated variances, as a percentage of the total dataset models morphology variance, carried by different principal components for the gender-specific atlases, and non gender-specific atlases respectively. Figure 3.5 through Figure 3.8 show plots for the accumulated variance versus the number of principal components for the gender-specific atlases. The plot of the accumulate variance versus the number of principal components for the non gender-specific atlases are shown in Figure 3.9 and Figure 3.10 for the distal femur and proximal tibia atlases respectively.

Table 3.1 Accumulated variances for the gender-specific knee bones atlas

PCs Count	Female	Male	Female	Male
	Distal Femur	DistalFemur	Proximal Tibia	Proximal Tibia
1	35	33.8	33.9	42.6
2	51.2	58.2	49.9	58.7
3	62.1	69.1	58.7	66
4	68.4	72.9	64.9	70.8
5	73.4	76.5	70.6	74.7
6	77.3	79.3	74.7	78.3
7	79.5	81.5	77.9	80.1
8	81.4	83.2	80.1	81.7
16	89.7	90.1	88.4	87.7
17	90.2	90.6	89	88.1
18	90.8	91.1	89.5	88.6
19	91.2	91.5	90.4	89
20	91.7	92.1	90.9	89.4
21	92.1	92.4	91.2	90.1
119	99.76	98.93	100	97.691
143	100	99.25		98.17
302		99.9987		100
303		100		

Table 3.2 Accumulated variances for the non-gender specific knee bones atlases

PC Count	Distal Femur	Proximal Tibia
1	37.6	59.5
2	61.9	70.3
3	72.3	75.5
4	75.9	79
5	79.2	81.9
6	81.7	84.4
7	83.5	85.7
8	85.1	86.9
9	86.1	87.7
10	87.1	88.4
11	88.1	89
12	88.8	89.5
13	89.5	89.9
14	90.1	90.3
421	99.986	100
447	100	

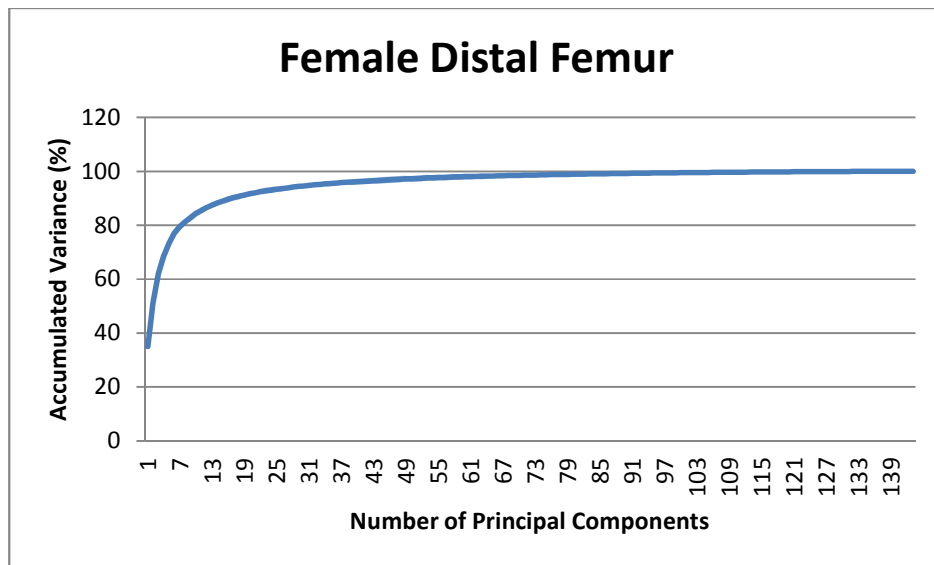


Figure 3.5 Accumulated variance versus the number of principal components for the gender-specific female distal femur atlas

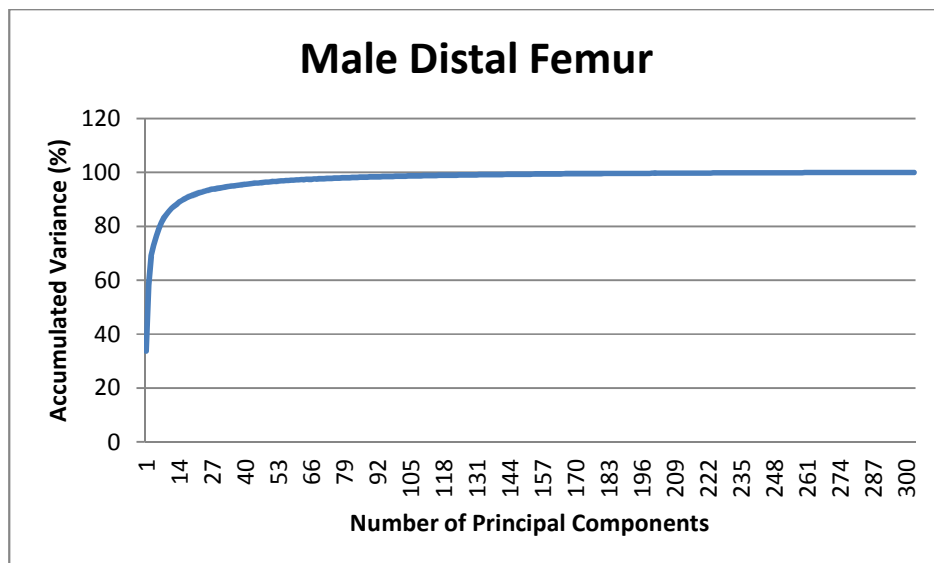


Figure 3.6 Accumulated variance versus the number of principal for the gender-specific male distal femur atlas

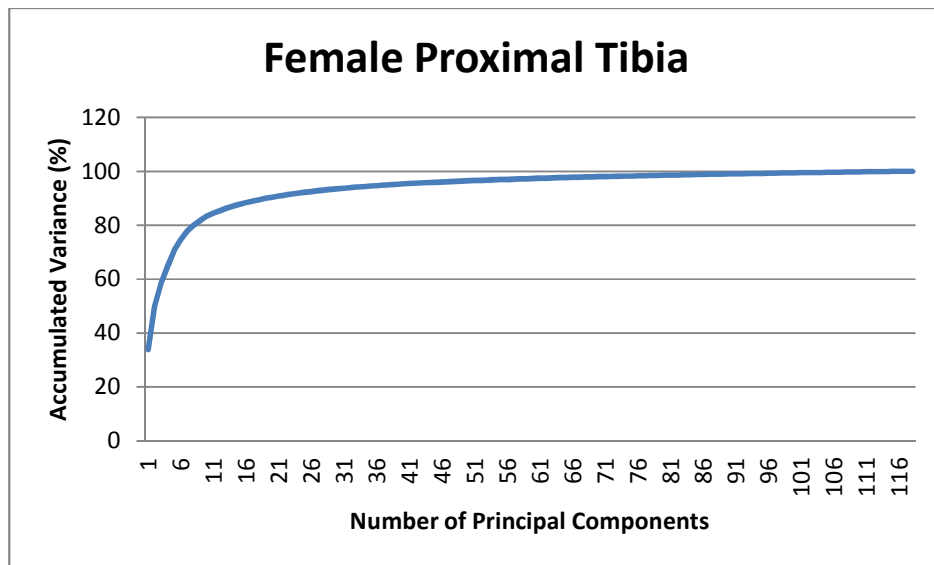


Figure 3.7 Accumulated variance versus the number of principal components for the gender-specific female proximal tibia atlas

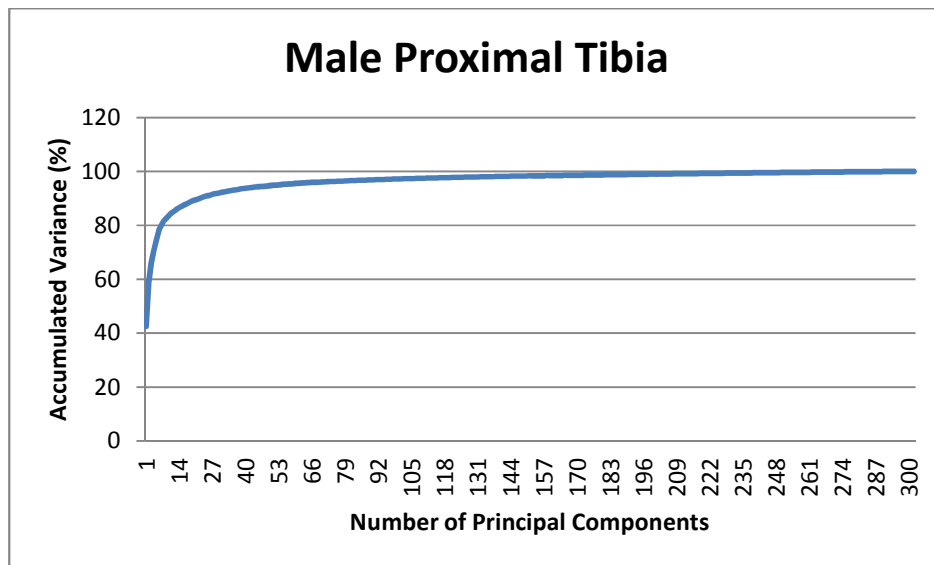


Figure 3.8 Accumulated variances versus the number of principal components for the gender-specific male distal femur atlas

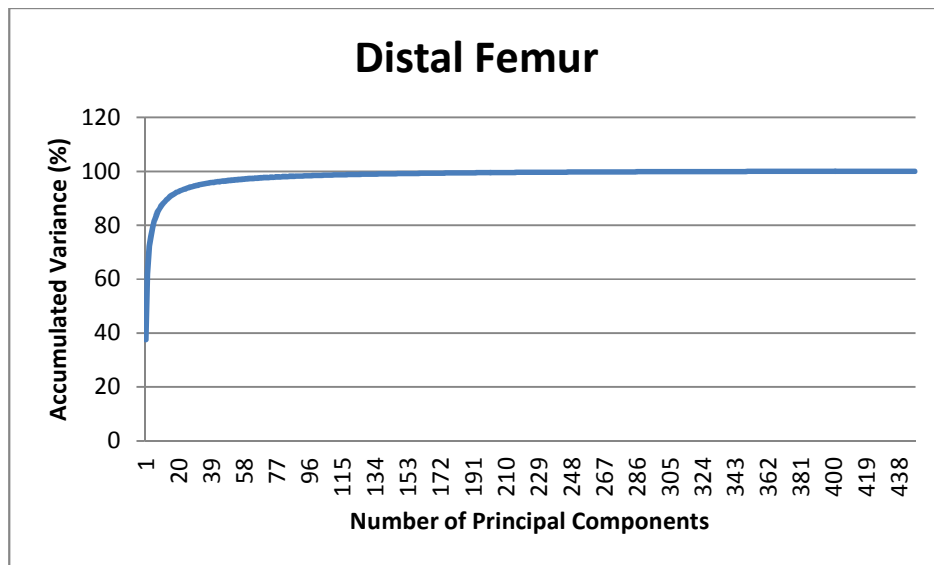


Figure 3.9 Accumulated variances versus the number of principal components for the non gender-specific distal femur atlas

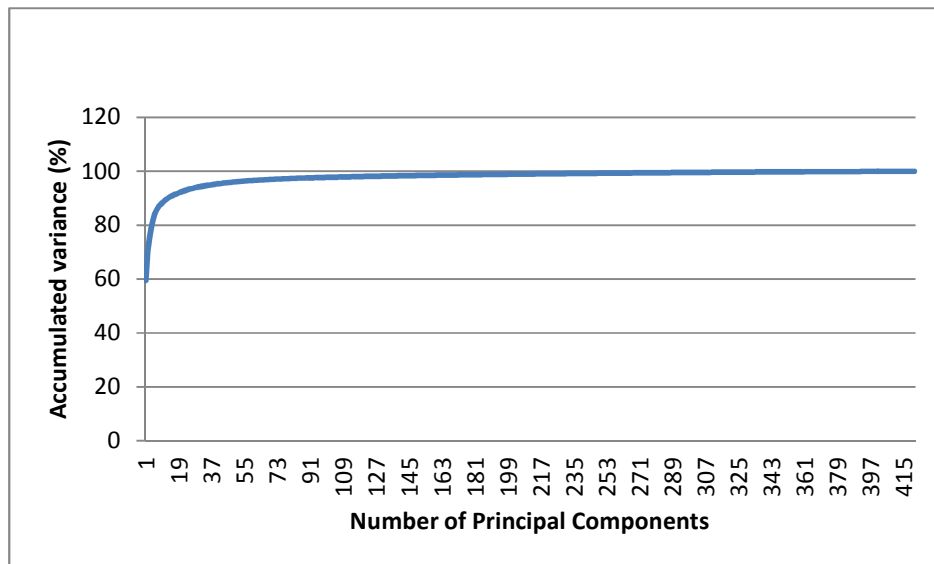


Figure 3.10 Accumulated variances versus the number of principal components for the non gender-specific proximal tibia atlas

3.2.3 Knee Bones' Morphology Variation Analysis

To study the morphology variation of the distal femur, and proximal tibia bones, the RMS distance error between each model in each of the bones' datasets (female and male distal femur, and proximal tibia) and their jack-knife mean model (the mean model calculated using all the models in the dataset except the model whose RMS error is calculated) was calculated, and histograms for these RMS errors were generated. Figure 3.11 through Figure 3.14 show the histograms for the RMS errors between the models and their jack-knife mean models for the female distal femur, male distal femur, female proximal tibia, and male proximal tibia, respectively. From examining the histograms, it can be concluded that the morphology variations is greater in the male datasets than the female datasets. This can be contributed to the larger numbers of models in the male datasets than the female datasets.

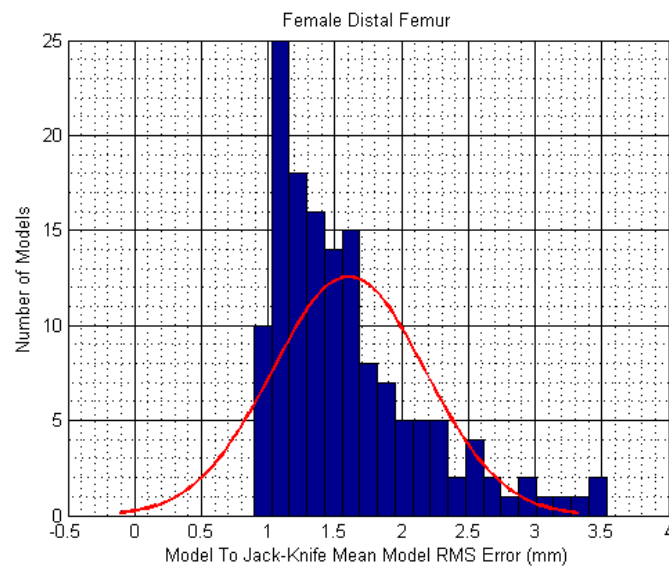


Figure 3.11 Histogram of the mean RMS errors between the female distal femur models, and their jack-knife mean models with mean RMS error of 1.6 mm, and maximum RMS error of 3.54 mm

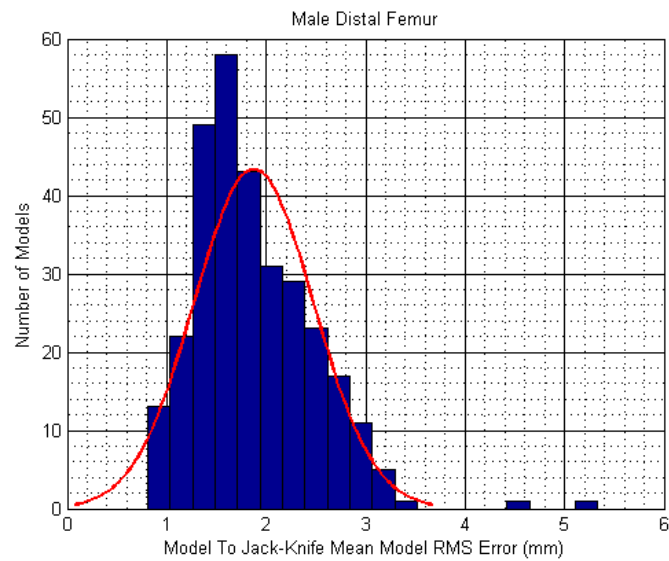


Figure 3.12 Histogram of the mean RMS errors between the male distal femur models, and their jack-knife mean models with mean RMS error of 1.87 mm and maximum RMS error of 5.33 mm

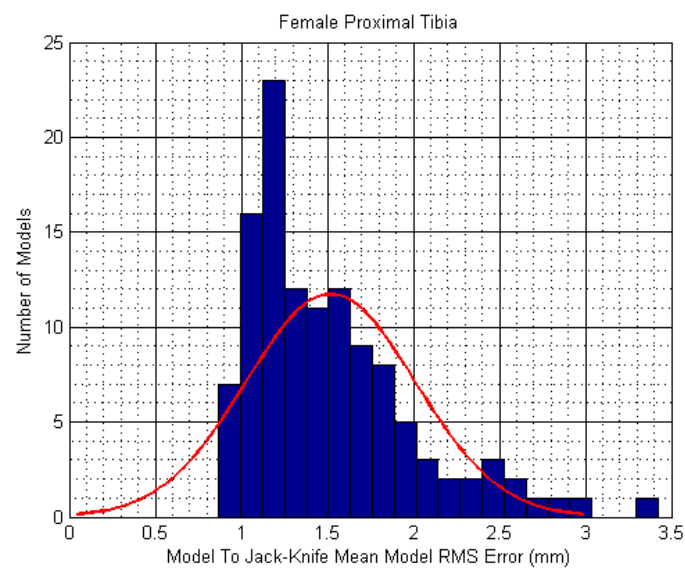


Figure 3.13 Histogram of the mean RMS errors between the female proximal tibia models, and their jack-knife mean models with mean RMS error of 1.52 mm and maximum RMS error of 3.42 mm

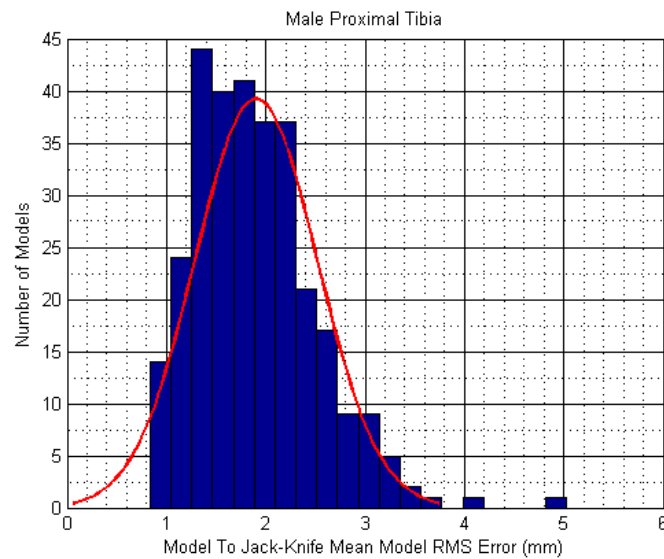


Figure 3.14 Histogram of the mean RMS errors between the male proximal tibia models, and their jack-knife mean models with mean RMS error of 1.9 mm and maximum RMS error of 5.03 mm

To examine the local morphology variations of the knee bones, the distance error between the vertices of each model in a dataset and their corresponding vertices in the jack-knife mean model were averaged over the models of the dataset, and a color map for these distance errors was generated for every dataset. Also, similar color maps were generated for the standard deviation of these distance errors. Figure 3.15, and Figure 3.16 show the color maps for the mean and standard deviations of distance errors between the models and their jack-knife mean models for the female distal femur. Similarly, Figure 3.17, and Figure 3.18 show the mean and standard deviation of the distance errors for the male distal femur. Figure 3.19, and Figure 3.20 show the mean and standard deviation of the distance errors for the female proximal tibia. Figure 3.21, and Figure 3.22 show the mean and standard deviation of the distance errors for the male proximal tibia.

Examining the color maps, it can be concluded that the female and male datasets (distal femur, or proximal tibia) show very similar variation distribution among the bones. However, the distal femur exhibits small variations at some areas and large variation in other areas, while the proximal tibia is characterized by more homogeneous distribution for the variations across bone surface.

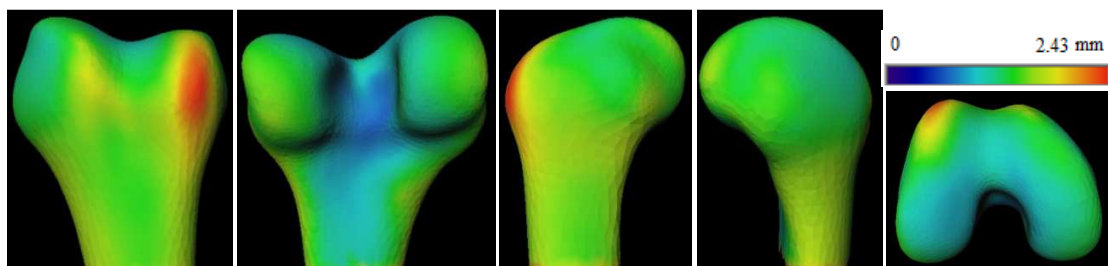


Figure 3.15 Color map for the mean distance error between the female distal femur models, and their jack-knife mean models

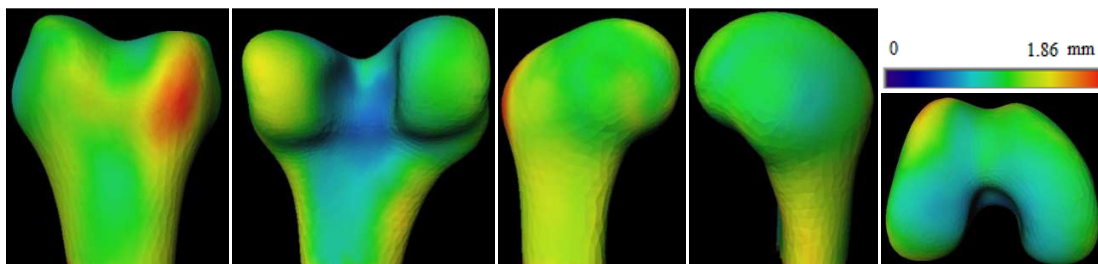


Figure 3.16 Color map for the standard deviation of the distance error between the female distal femur models, and their jack-knife mean models

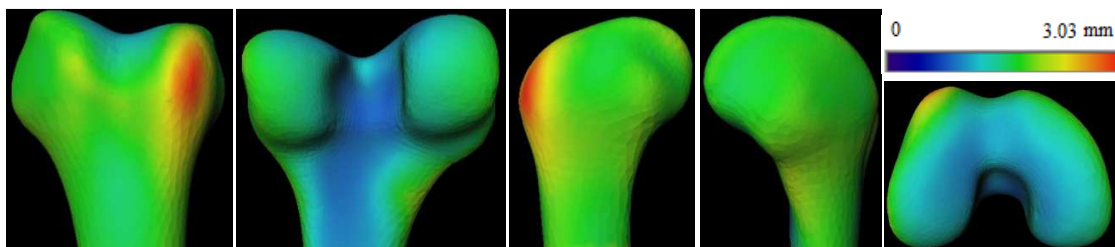


Figure 3.17 Color map for the mean distance error between the male distal femur models, and their jack-knife mean models

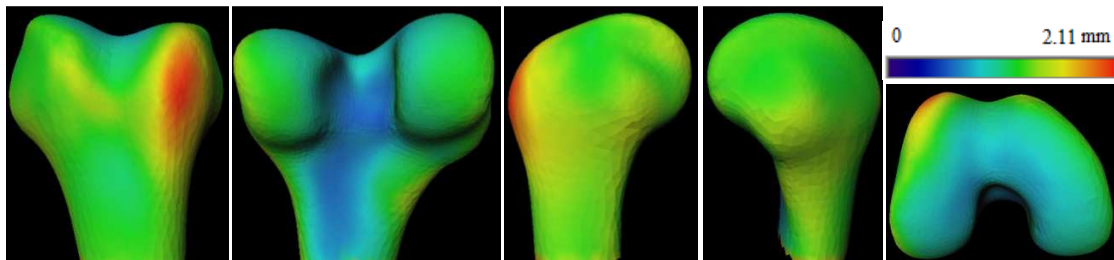


Figure 3.18 Color map for the standard deviation of the distance error between the male distal femur models, and their jack-knife mean models

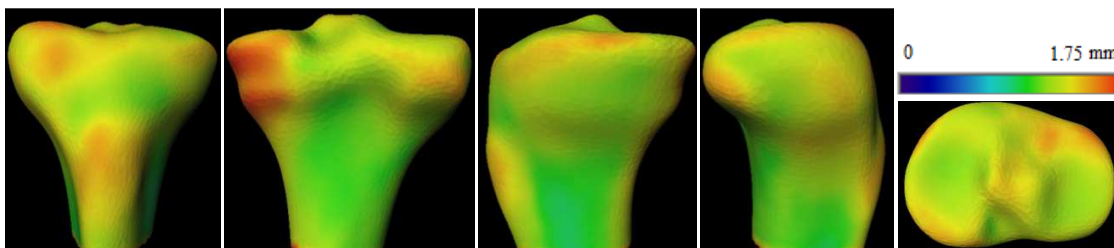


Figure 3.19 Color map for the mean distance error between the female proximal tibia models, and their jack-knife mean models

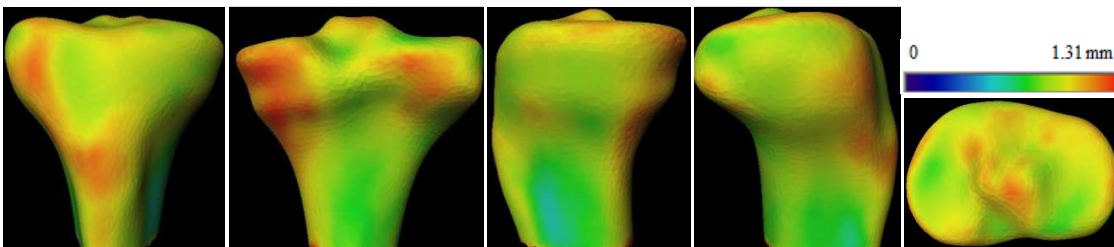


Figure 3.20 Color map for the standard deviation of the distance error between the female proximal tibia models, and their jack-knife mean models

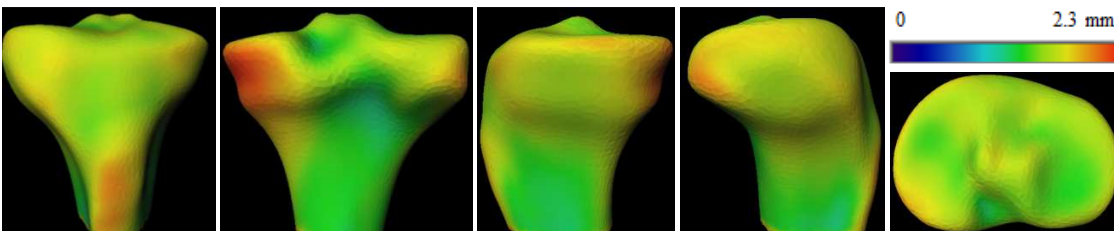


Figure 3.21 Color map for the mean distance error between the male proximal tibia models, and their jack-knife mean models

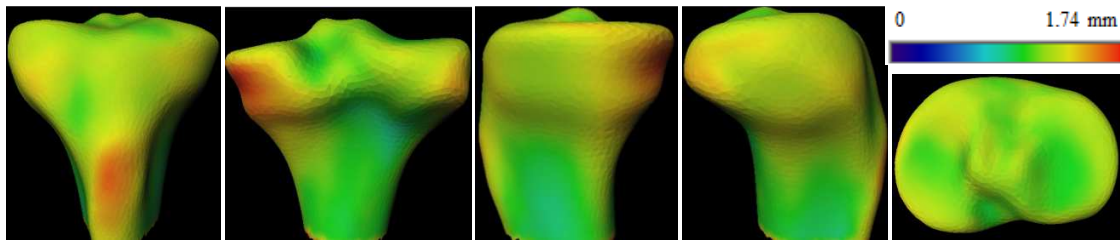


Figure 3.22 Color map for the standard deviation of the distance error between the female proximal tibia models' vertices, and their jack-knife mean models

3.2.4 Knee Bones Atlases Analysis

In previous work, the knee atlases were studied for gender, and ethnic difference [39], and [40]. In this work a similar study was performed on the knee bones PCA-based atlases (used in the developed systems) to analyze their capabilities in 3D of the knee bones morphology. Three different aspects of the PCA-based atlases of the knee bones were studied:

1. Bone morphology approximation capability.
2. Gender-specific morphology effect on atlas.
3. Effect of dimensionality reduction on bone's morphology representation.

In order to study these three features, the knee bones were divided into female and male datasets for each bone, i.e female distal femur, male distal femur, female proximal tibia, and male proximal tibia. For each dataset, principal component analysis was performed using jack-knife and non jack-knife methods. In the jack-knife (leave one out) method, PCA is performed on all the models of the dataset except one model. This jack-knife method produces a PCA-based statistical atlas for each model of the dataset, which is generated using all the models of the dataset except this specific model. The atlas

generated using this method contains the morphology information of all the models in the dataset except the model left out, which simulate the real-life situation when the atlas will be used to reconstruct a 3D model that was not included in the atlas dataset. While in the non jack-knife method, all the models in the dataset are used to generate one atlas. This method produces a PCA-based atlas that has the morphology information of all the dataset models encoded in its principal components.

Gender-specific and non-gender specific atlases were also generated (using jack-knife and non jack-knife methods). In the Gender-specific atlases, the models were grouped based of the bone type and gender, and then the PCA (jack-knife and non jack-knife) was performed on each group. While in the non gender-specific atlases, the bone models were grouped by bone type only, i.e. distal femur and proximal tibia, and the PCA (jack-knife and non jack-knife) was performed on each group. Therefore, four types of PCA-based atlases were generated for each bone type (distal femur, and proximal tibia) and gender (male and female) combination:

1. Gender-specific jack-knife atlas.
2. Gender-specific non jack-knife atlas.
3. Non gender-specific jack-knife atlas.
4. Non gender-specific non jack-knife atlas.

This results in 16 atlases, in which for the jack-knife atlas, each model in the dataset (for bone type, and gender combination) has its corresponding leave-on-out statistical atlas. The aforementioned features of the bone atlas were studied by projecting the bones models on the atlas' principal components and reconstructing the model again

using the principal components coefficients resulted from the projection process. This projection-reconstruction process was performed using different numbers of principal components that were chosen to be powers of 2, i.e 1, 2, 4, 8,...,N, where N is the maximum number of principal components in the atlas. This projection-reconstruction process was performed for each of the 16 atlases. For each atlas, the projection-reconstruction process was performed for each model, then the RMS error between the reconstructed model and the original model was calculated using the closest surface point method. The results for the projection-reconstruction process for the different 16 atlases, are presented in the appendix section 9.1

3.2.4.1 Bone Morphology Estimation Capability of the PCA-Based Statistical Atlas

In order to study the ability of the PCA-based atlas to approximate the morphology of a bone's model outside the atlas' dataset, the projection-reconstruction process was performed using jack-knife, and non jack-knife atlases. This process was performed on all distal femur, and proximal tibia (both males and females) models using the gender-specific atlases . Since the non jack-knife atlas is generated using all the models of the dataset, the morphology of the model being studied (projected and reconstructed) is encoded in the atlas' principal components; hence, the only error source in the non jack-knife projection-reconstruction process is the dimensionality reduction, i.e. using a subset of the principal components as opposed to using all the principal components to project and reconstruct the models.

On the other hand, the jack-knife atlas does not have the morphology of the model being studied encoded in its principal components, and therefore the projection of the

model on the jack-knife atlas' principal components and reconstruction of the model results in an estimation of the model's morphology. The model estimation using the jack-knife atlas is based on the morphology, of all the dataset models except the model being studied, encoded in the atlas' principal components. Therefore, comparing the mean RMS error for the projection-reconstruction process using the jack-knife atlas and the non jack-knife atlas, for each number of principal components used, shows the residual error resulting from the model's shape estimation performed by the atlas. Figure 3.23 through Figure 3.26 show the RMS errors for the projection-reconstruction process using the gender jack-knife and non jack-knife atlases for the female distal femur, male distal femur, female proximal tibia, and male proximal tibia respectively. The gender-specific atlases (jack-knife and non jack-knife) were arbitrarily chosen to be used for this comparison in order to keep the effect of gender-specific versus non gender specific factor constant during the comparison.

Comparing the jack-knife and the non-jack-knife RMS errors for each of the datasets shows that when a small number of principal components is used, the difference in the RMS error between the jack-knife and non jack-knife is small. This difference increases as the number of principal components used increases. This shows that when using small number of principal components, the dimensionality reduction effect is more prominent and is the main source of the residual error between the reconstructed and the original models. While, increasing the number of principal components used, the error of the model's morphology estimation becomes more prominent and the difference between

the RMS errors for the reconstruction using the jack-knife atlases becomes greater than the errors resulting from using the non jack-knife atlases.

Furthermore, by comparing the RMS errors for the male datasets to the female datasets, it can be shown that for the female datasets, the difference between the RMS errors resulting from using the jack-knife atlases and the errors resulting from using the non jack-knife atlases are greater than the ones for the male datasets. This can be attributed to the larger number of models in the male datasets than the female datasets. This reveals that the model's morphology estimation capability increases as the number of models included in creating the statistical atlas increases.

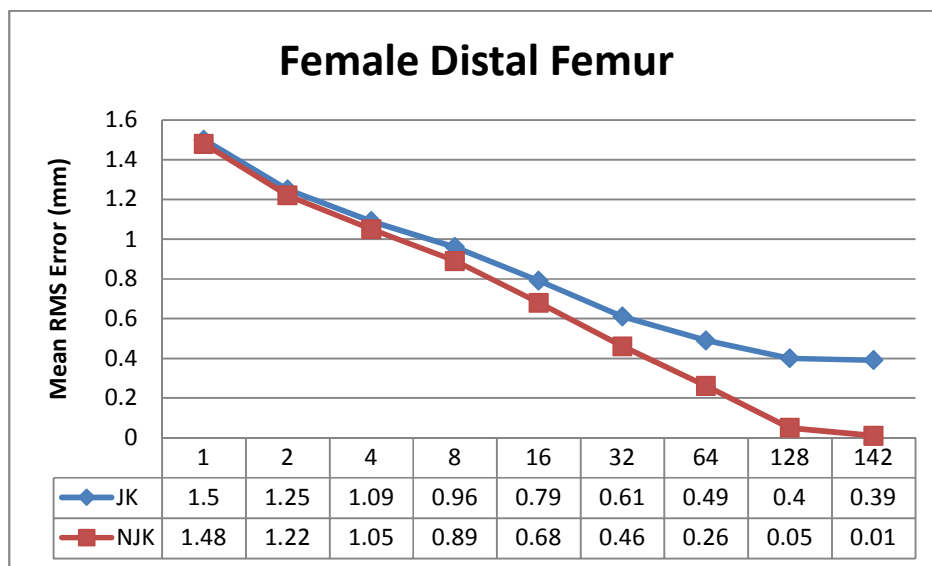


Figure 3.23 Mean RMS errors versus the number of principal components for the projection-reconstruction process using the jack-knife (blue) and non jack-knife (red) gender-specific female distal femur atlases.

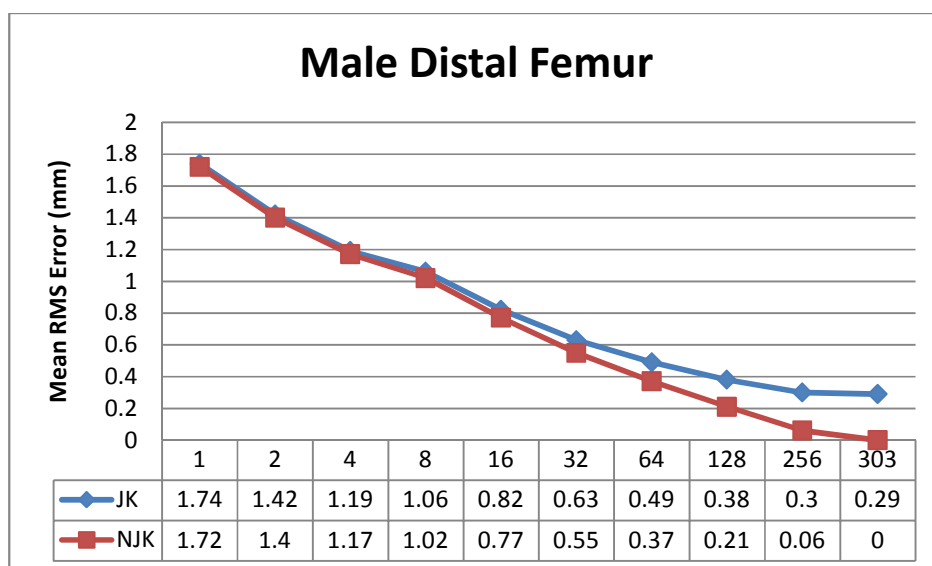


Figure 3.24 Mean RMS errors versus the number of principal components for the projection-reconstruction process using the jack-knife (blue) and non jack-knife (red) gender-specific male distal femur atlases.

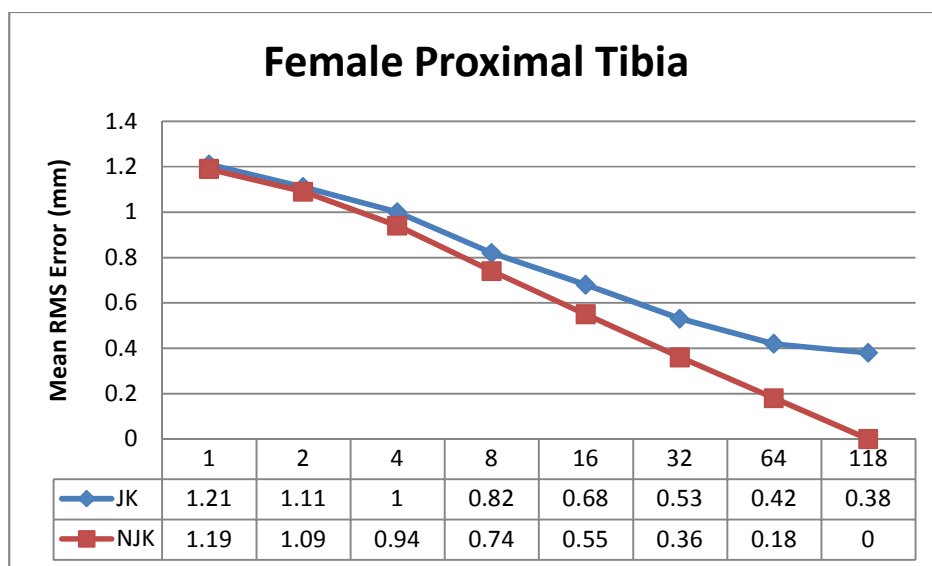


Figure 3.25 Mean RMS errors versus the number of principal components for the projection-reconstruction process using the jack-knife (blue) and non jack-knife (red) gender-specific female proximal tibia atlases.

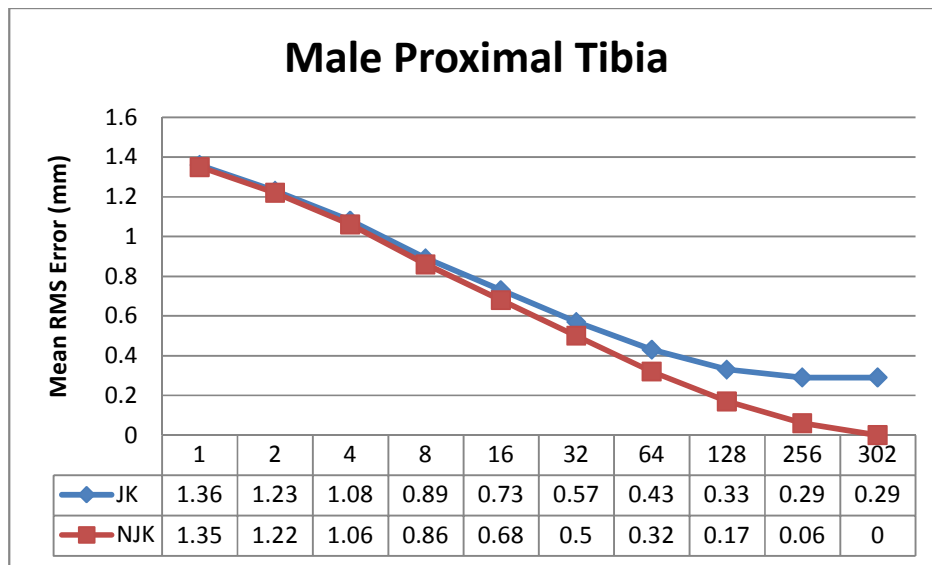


Figure 3.26 Mean RMS errors versus the number of principal components for the projection-reconstruction process using the jack-knife (blue) and non jack-knife (red) gender-specific male proximal tibia atlases.

3.2.4.2 Difference between gender-specific and non gender-specific atlases

To study the effect of gender-specific atlases versus non gender gender-specific atlases on the knee bones' morphology representation, the model projection-reconstruction process was performed on the bones' models using gender-specific and non gender-specific jack-knife atlases. The RMS errors between the reconstructed models and the original models were then calculated using the closest surface point method. Figure 3.27 through Figure 3.30 show the mean RMS errors for the projection-reconstruction process using gender-specific and non gender-specific jack-knife atlases for the female distal femur, male distal femur, female proximal tibia, and male proximal tibia respectively. Examining these RMS errors shows that there is a small-to-no difference between gender-specific and non gender-specific atlases in the morphology

representation of the distal femur, and proximal tibia bones. However, a small difference in the mean RMS errors between the gender-specific and non gender-specific female atlases is shown in Figure 3.27, and Figure 3.29. This small difference is attributed to the difference in the number of models incorporated in creating the gender-specific female atlases (144 for the female distal femur and 119 for the female proximal tibia) and the number of models used in generating the non gender-specific female atlases (which was 448 for the distal femur, and 422 for the proximal tibia). This difference results in a distributional difference of the morphology variance on the principal components. Therefore it can be concluded that there is no difference in morphology representation between gender-specific and non gender-specific atlases.

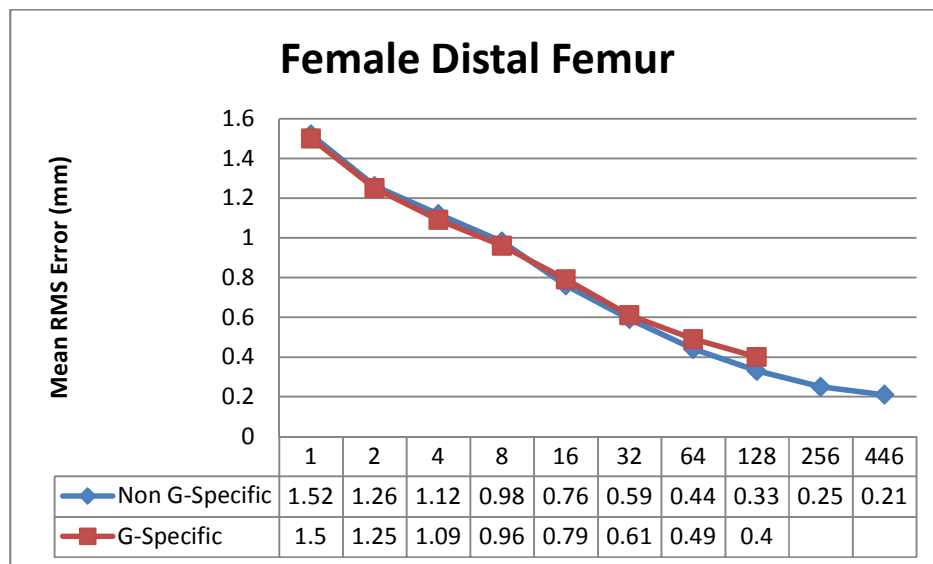


Figure 3.27 Mean RMS error versus the number of principal components for the projection-reconstruction process using gender-specific (red) and non gender-specific (blue) jack-knife female distal femur atlases.

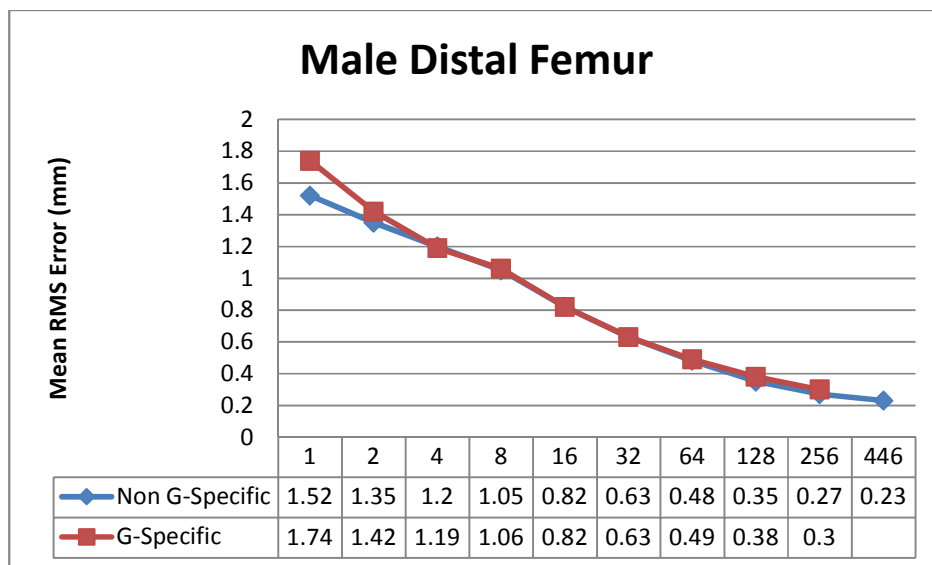


Figure 3.28 Mean RMS errors versus the number of principal components for the projection-reconstruction process using gender-specific (red) and non gender-specific (blue) jack-knife male distal femur atlases.

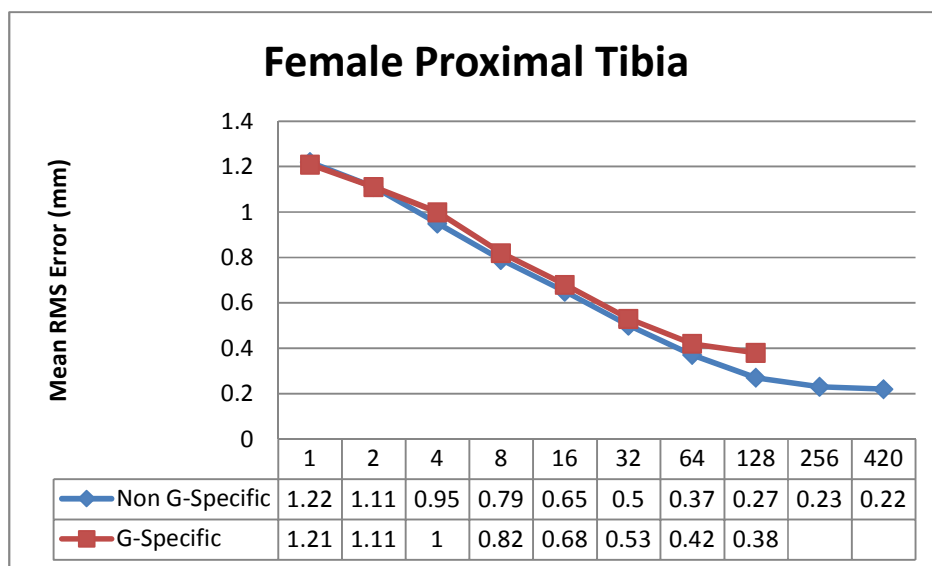


Figure 3.29 Mean RMS errors versus the number of principal components for the projection-reconstruction process using gender-specific (red) and non gender-specific (blue) jack-knife female proximal tibia atlases.

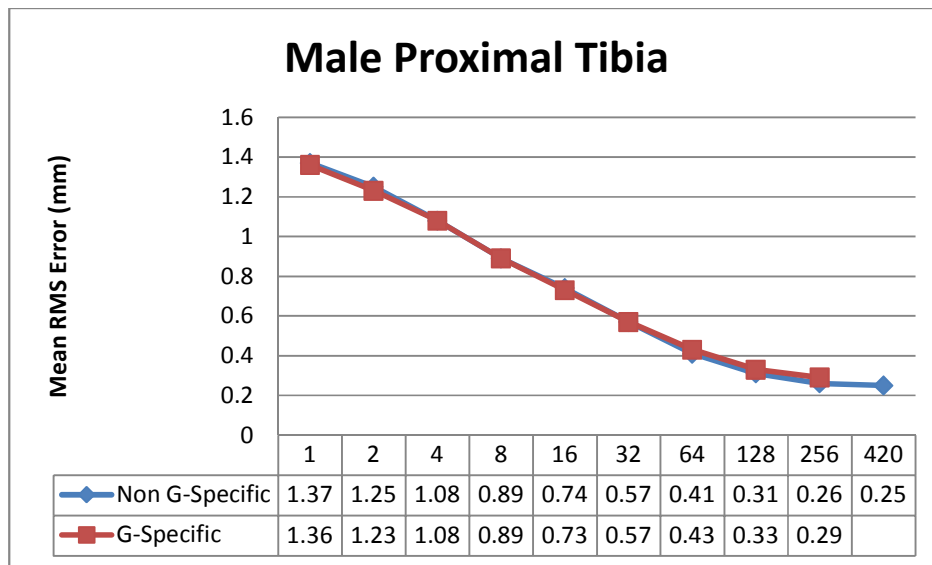


Figure 3.30 Mean RMS errors versus the number of principal components for the projection-reconstruction process using gender-specific (red) and non gender-specific (blue) jack-knife male proximal tibia atlases.

3.2.4.3 Effect of dimensionality reduction on bones' morphology representation

The most important feature of the PCA-based atlas is the dimensionality reduction, which enables approximating the 3D model with few parameters (the principal components coefficients) manageable by an optimization algorithm for instantiation of new 3D models. To study the effect of the dimensionality reduction on the representation of the 3D bone models, the projection-reconstruction process was performed on the atlases' models using different numbers of principal components, the same approach used in studying the previous features: increasing powers of two as the number of principal components used. The closest surface point method was utilized to calculate the residual RMS error between the reconstructed models and the original models. The jack-knife atlases were used to study the effect of the dimensionality reduction on the combined

effect of models' morphology estimation (due to using jack-knife atlases), and approximation (due to using subset of the principal components). Figure 3.31 through Figure 3.34 show the mean, maximum, and minimum projection-reconstruction RMS errors for the female distal femur, male distal femur, female proximal tibia, and male proximal tibia respectively using the gender-specific jack-knife atlases for different numbers of principal components.

The RMS errors graphs show that increasing the number of principal components (modes of variations) used in the model representation (estimation and approximation) results in an increase in the model representation. However, the slope of the change of the RMS error decreases by increasing the number of principal components, as the higher order principal component carries fewer variations than the lower order principal components. The slope of the RMS error reaches very small value (nearly zero) after 128 principal components, leading to the conclusion that adding more models to the atlas will not have a significant effect on the model representation accuracy.

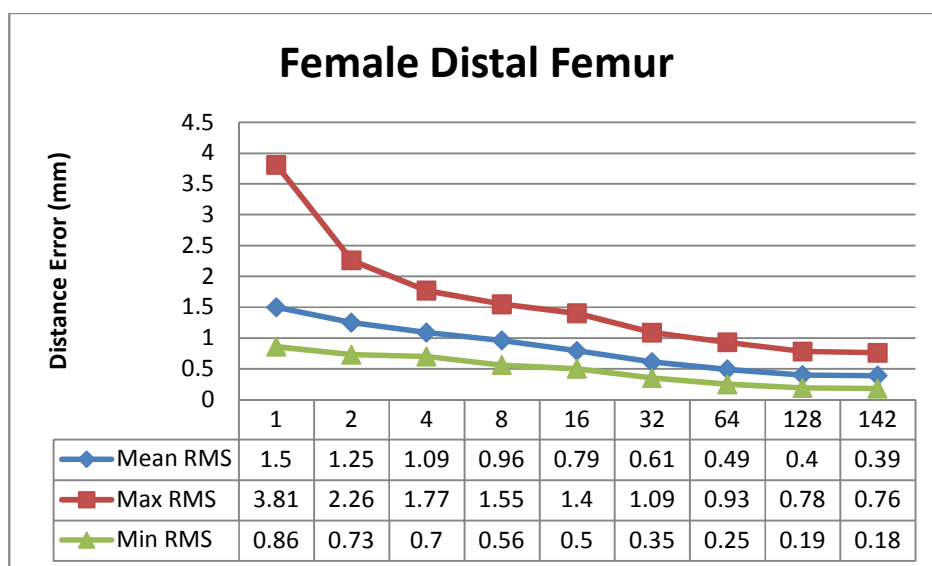


Figure 3.31 Mean, minimum, and maximum RMS errors versus the number of principal components for the projection-reconstruction process using jack-knife gender-specific female distal femur atlases.

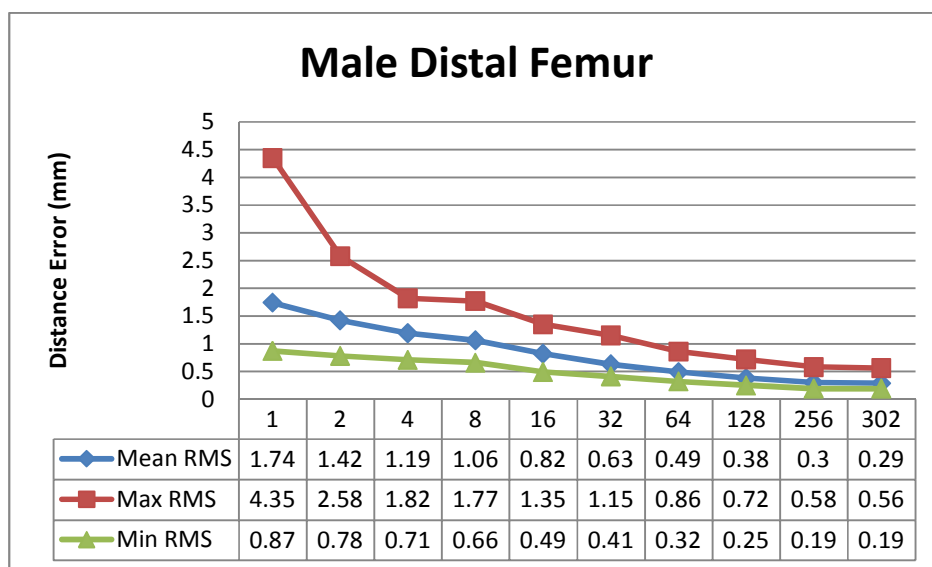


Figure 3.32 Mean, minimum, and maximum RMS errors versus the number of principal components for the projection-reconstruction process using jack-knife gender-specific male distal femur atlases.

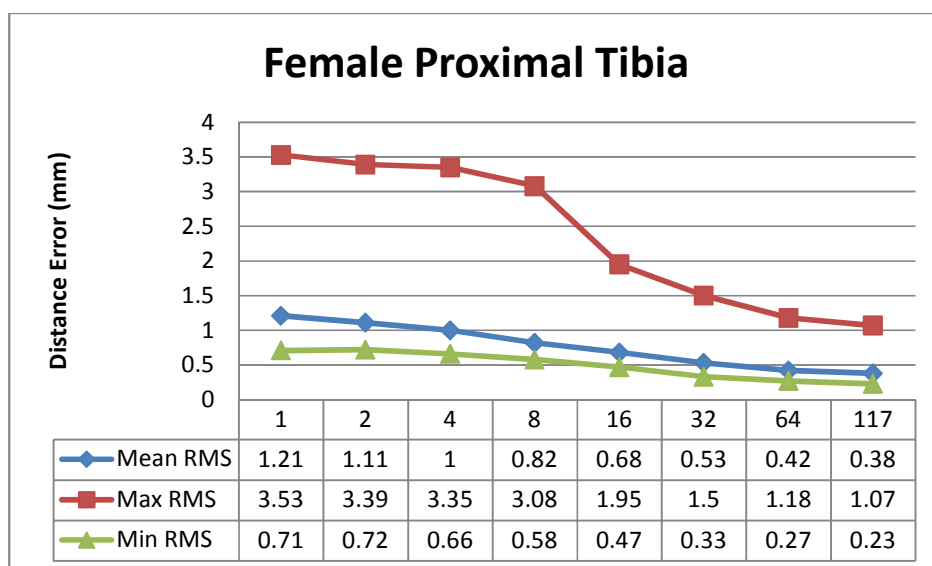


Figure 3.33 Mean, minimum, and maximum RMS errors versus the number of principal components for the projection-reconstruction process using jack-knife gender-specific female proximal tibia atlases.

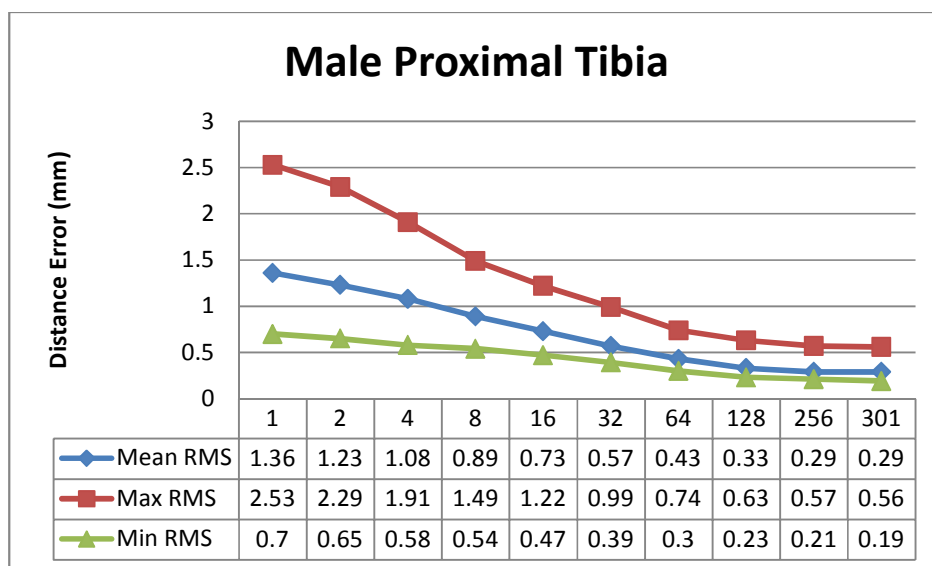


Figure 3.34 Mean, minimum, and maximum RMS errors versus the number of principal components for the projection-reconstruction process using jack-knife gender-specific male proximal tibia atlases.

3.3 Bone Morphing Methods

Three bone morphing methods have been investigated: the first is based on a numerical iterative optimization algorithm called Powell's Direction Set method [40]. The second morphing method is a linear least squares method that calculates the shape descriptors using closed-form solution [35]. A hybrid morphing method, which consists of applying the iterative morphing followed by the linear least squares morphing, was also investigated.

In order to study the performance and reconstruction accuracy of each morphing method, the vertices of the atlas models were used as the morphing guidance point clouds to reconstruct the 3D bones models from those point clouds. To study the effect of the point cloud density, different densities of the models' point clouds were used for performing 3D model reconstruction using the different morphing methods. For each model, the model's vertices was used as the unreduced point cloud, and this point cloud was reduced to different densities to obtain different point clouds with different densities for the same model. The reduced point clouds were obtained by reducing the number of points in the point cloud using an octree, where the octree leaves' size was specified to be 4, 8, 16, and 32 mm. The original models' point clouds (unreduced), had a mean inter-vertices distance (the mean distance between each vertex and its neighbor vertices) of approximately 2 mm as described in section 3.2.1. Figure 3.35 through Figure 3.39 show sample point clouds for a distal femur with 2 mm (unreduced), 4 mm, 8 mm, 16 mm, and 32 mm mean inter-vertices distance. Similarly, Figure 3.40 through Figure 3.44 show

sample point clouds for a proximal tibia with 2 mm (unreduced), 4 mm, 8 mm, 16 mm, and 32 mm inter-vertices distance.

The different point clouds (with different inter-vertices distances) were used to reconstruct the 3D models using the three morphing methods, and the reconstructed model was compared with the original model to calculate the root mean square error (RMS). In the following sections, the three morphing methods are presented, as well as the reconstruction accuracy analysis for each of them. The complete results of the models reconstruction using the three morphing methods results and the point clouds with different densities are presented in the appendix section 9.2

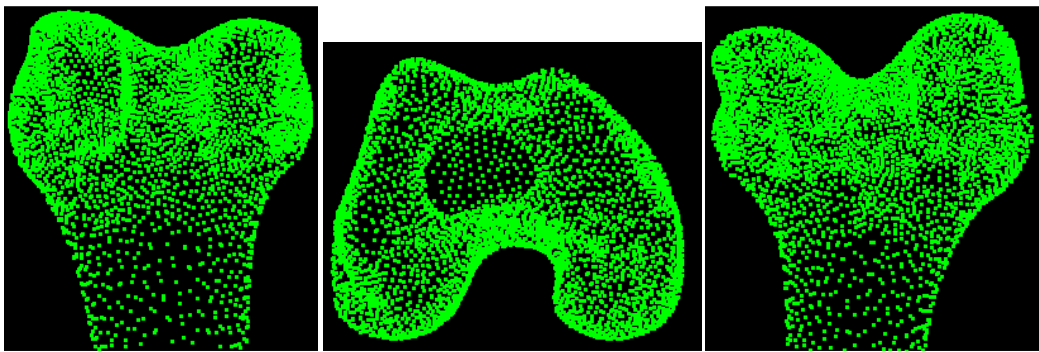


Figure 3.35 Unreduced point clouds for a female distal femur, showing the anterior side (left), the condyles (middle), and the posterior side (right)



Figure 3.36 4-mm reduced point cloud for a female distal femur, showing the anterior side (left), the condyles (middle), and the posterior side (right)

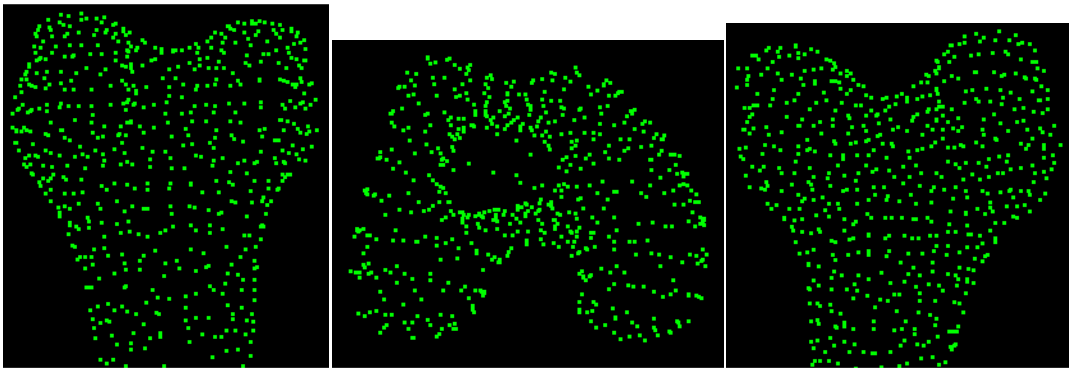


Figure 3.37 8-mm reduced point cloud for a female distal femur, showing the anterior side (left), the condyles (middle), and the posterior side (right)

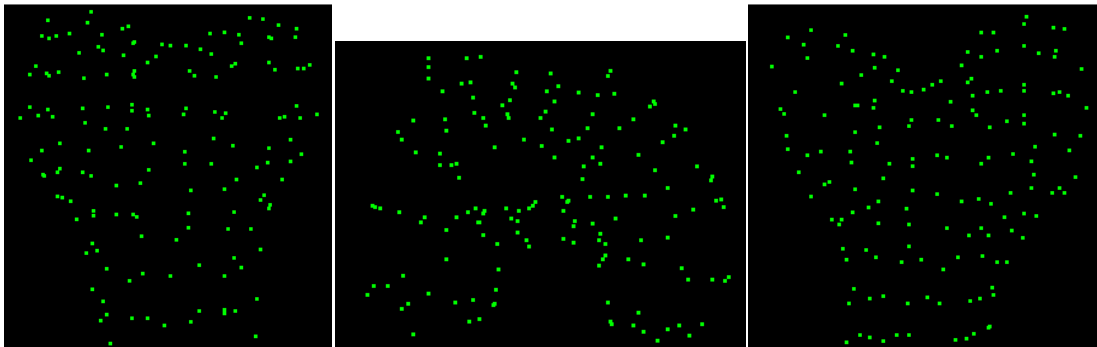


Figure 3.38 16-mm reduced point cloud for a female distal femur, showing the anterior side (left), the condyles (middle), and the posterior side (right)

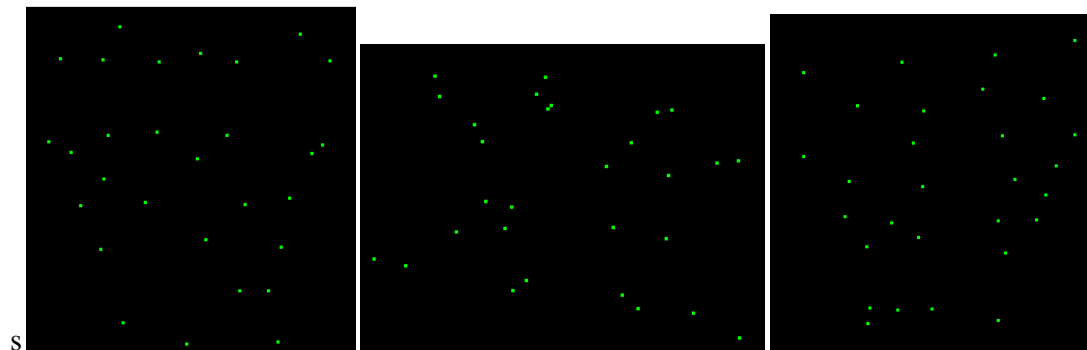


Figure 3.39 32-mm reduced point cloud for a female distal femur, showing the anterior side (left), the condyles (middle), and the posterior side (right)

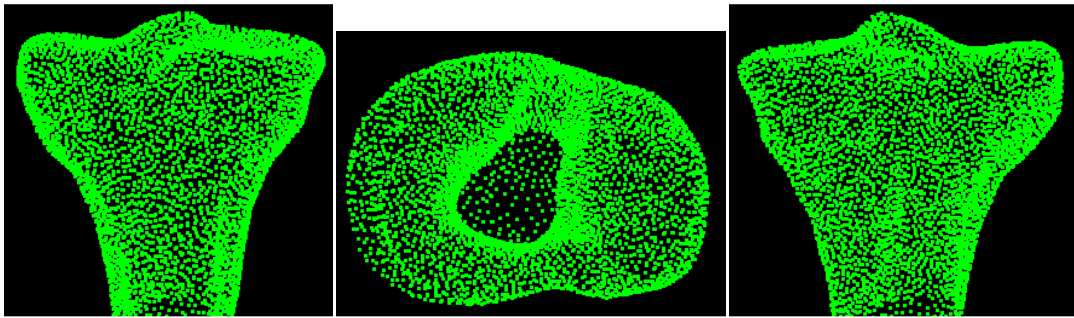


Figure 3.40 Unreduced point clouds for a female proximal tibia, showing the anterior side (left), the tibialplateue (middle), and the posterior side (right)

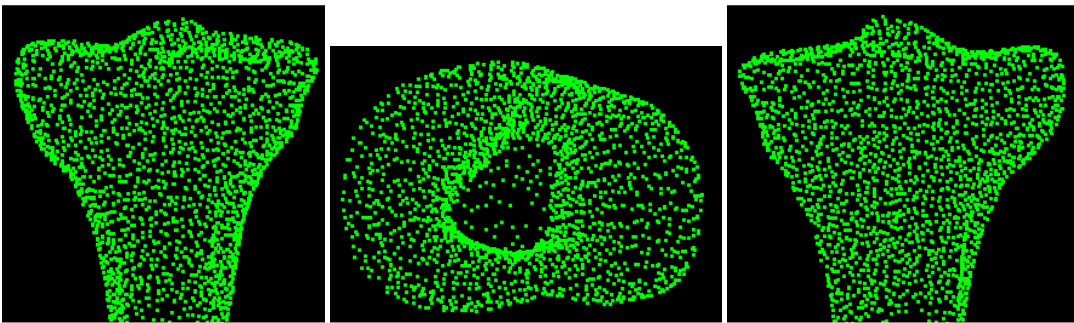


Figure 3.41 4-mm reduced point clouds for a female proximal tibia, showing the anterior side (left), the tibial plateau (middle), and the posterior side (right)

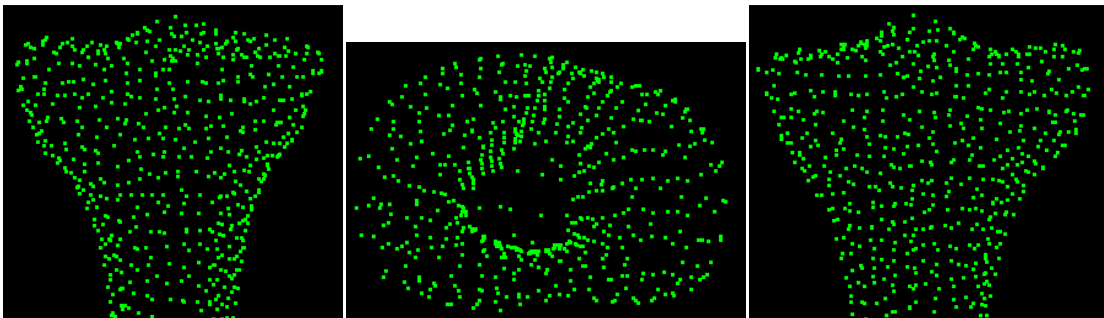


Figure 3.42 8-mm reduced point clouds for a female proximal tibia, showing the anterior side (left), the tibial plateau (middle), and the posterior side (right)

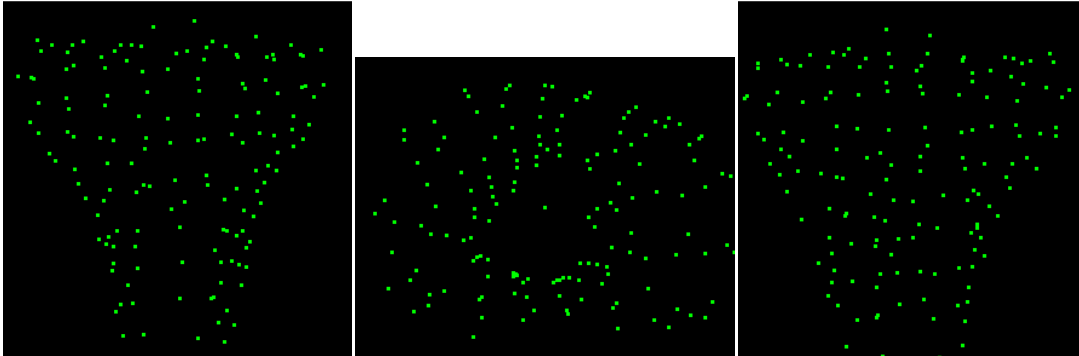


Figure 3.43 16-mm reduced point clouds for a female proximal tibia, showing the anterior side (left), the tibial plateau (middle), and the posterior side (right)

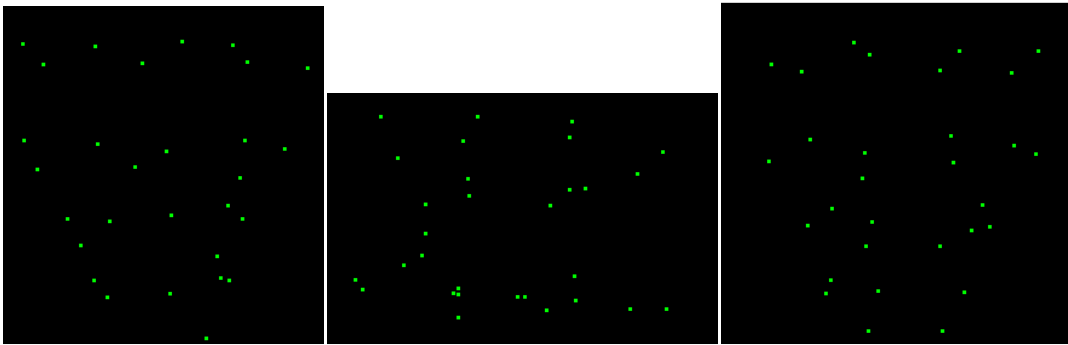


Figure 3.44 32-mm reduced point clouds for a female proximal tibia, showing the anterior side (left), the tibial plateau (middle), and the posterior side (right)

3.3.1 Powell's Direction Set Optimization Morphing

The first optimization method is an iterative method that searches the principal components vector space to find the minima of the error function to create a 3D bone model that best matches the bone's point cloud. Powell's Direction Set method [40] was used as for the shape descriptors (principal components coefficients) optimization. The directions used were the basis vectors of the eigenspace which are the eigenvectors (or principal components). The error function used was the root mean square error between the optimization-guiding point cloud and the model being morphed. The model under

morphing is represented by the shape descriptors, and thus the changes to the shape descriptors performed by the optimization algorithm creates a new model, as defined in (3.4), at every iteration of the optimization. The error E function is defined as follows:

Given a point cloud Q with n points, and a model M , being morphed, with l vertices. The set of closest vertices V in M to the points in the point cloud Q is defined as follows:

$$v_i = \underset{v_j \in M}{\operatorname{argmin}} \|v_j - q_i\| \quad \forall i \in [1, n], j \in [1, l] \quad (3.7)$$

Where v_i is the closest point in V to the point q_i in the point cloud Q . An octree was used to efficiently search for the closest points in the model's vertices to the point cloud points. The error E between the morphed model M and the point cloud Q is then defined as:

$$E = \|V - Q\|^2 \quad (3.8)$$

To study the performance of the Direction Set optimization-based morphing method in estimating the bone's morphology given a point cloud representing the bone's shape, the point clouds extracted from the datasets' models were used to reconstruct bones models using the gender-specific jack-knife atlases. To study the effect of the point cloud density on the morphing accuracy, different point cloud densities (as shown in Figure 3.35 through Figure 3.44) were used to reconstruct the bones models. Another factor included in this morphing accuracy evaluation, was the number of principal components (modes of variations) used in the bone morphology optimization. The closest

surface point based RMS error between the reconstructed models, and their reference original models was then calculated.

The detailed results for the accuracy study of Direction Set morphing method are presented in the appendix section 9.2.1. A comparison for the mean RMS reconstruction error for the Direction Set morphing method different point cloud densities as shown in Figure 3.45 through Figure 3.48 for the female distal femur, male distal femur, female proximal tibia, and male proximal tibia respectively. Examining these figures, it can be shown that decreasing the point cloud density results in an increase in the reconstruction RMS error. However, this increase in the reconstruction error is more significant for the 32 mm point clouds. The effect of the point cloud density is also decreased by decreasing the number of principal components used for the model morphing. This is due to the dominating effect of the decreased number of principal components used over the decreased point cloud. The maximum number of principal components used was limited to be 32, since this yield the highest reconstruction accuracy with reasonable processing time. The processing time for morphing one model using the 2-mm density point cloud was 2, and 14 minutes when using 32, and 64 principal components respectively on an Intel Core i7 2.3 GHz processor. The processing time dropped to 15-20 seconds when using the first 32 principal components with the 4-mm point cloud density. The difference in accuracy was below 0.08 mm for four experimented model reconstruction using 32, and 64 principal components.. The first 32 principal components carries 94.97%, 94.58%, 93.95%, and 92.5% for the female distal femur, male distal femur, female proximal tibia, and male proximal tibia atlases respectively.

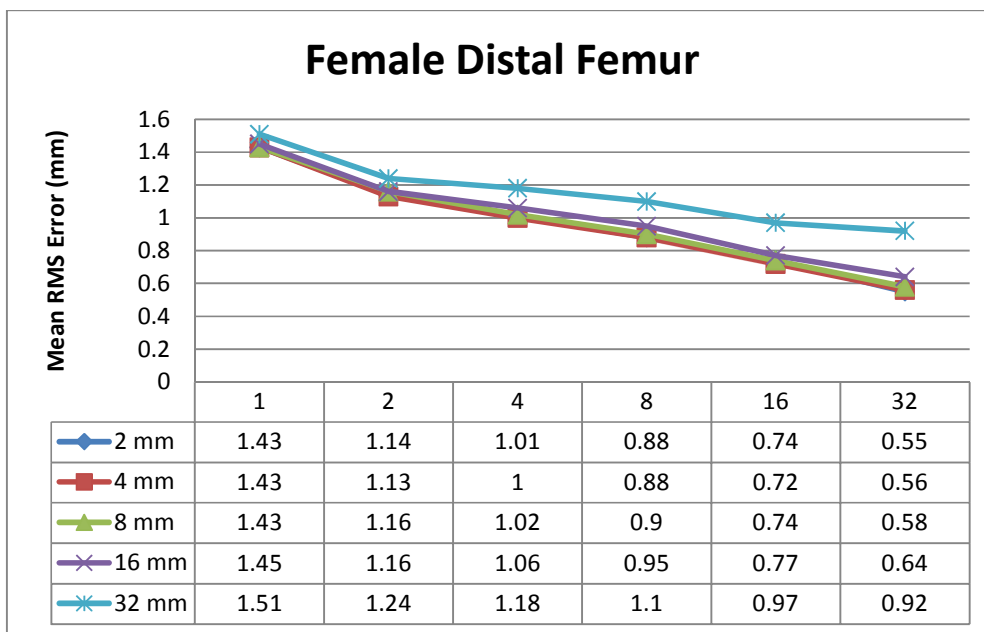


Figure 3.45 Mean RMS errors vs number of principal components for the female distal femur morphing using the Direction Set method and gender-specific jack-knife atlases

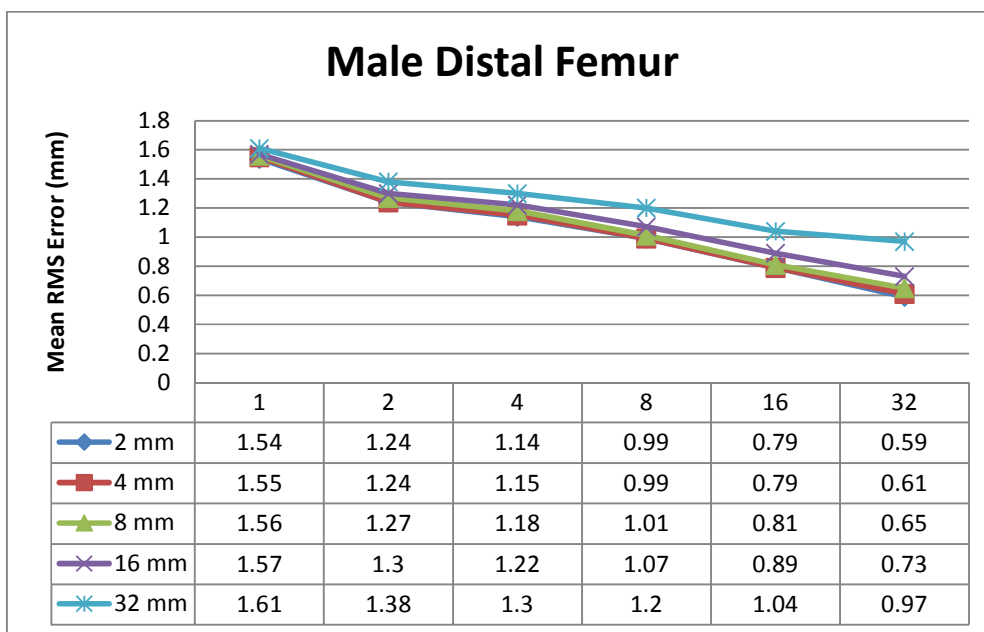


Figure 3.46 Mean RMS errors vs number of principal components for the male distal femur morphing using the Direction Set method and gender-specific jack-knife atlases

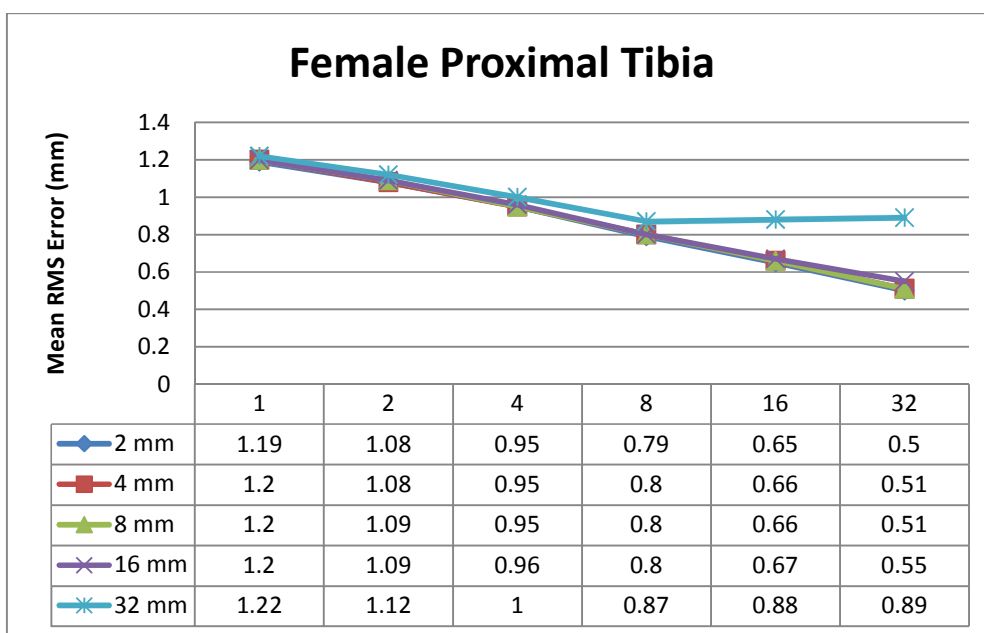


Figure 3.47 Mean RMS errors vs number of principal components for female proximal tibia morphing using Direction Set method and gender-specific jack-knife atlases

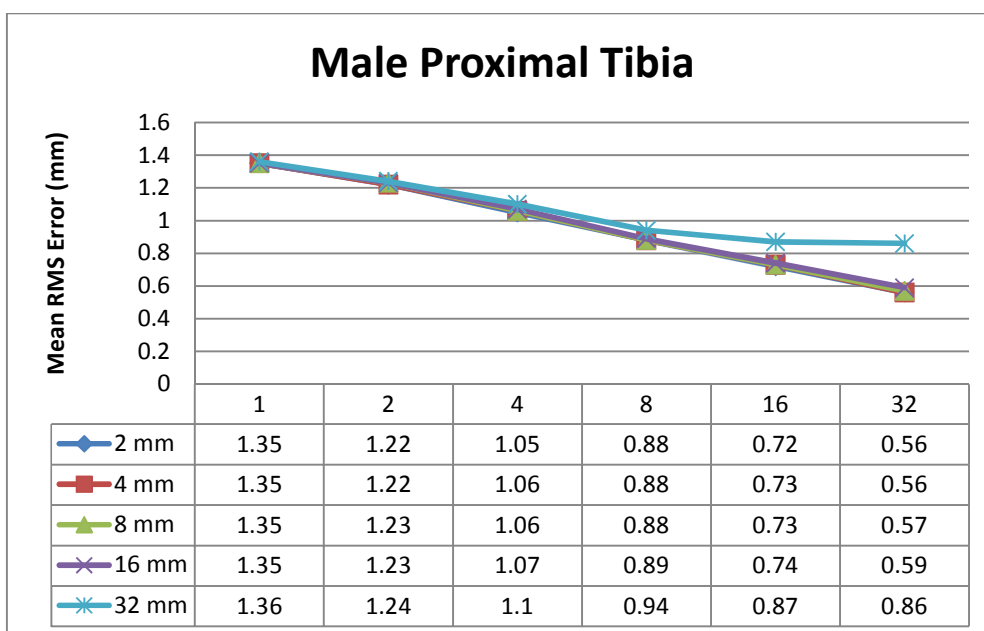


Figure 3.48 Mean RMS errors vs number of principal components for male proximal tibia morphing using the Direction Set method using gender specific jack-knife atlases

3.3.2 Linear Least Squares Morphing

The second optimization method solves directly for the shape descriptors by partial differentiation of the error function E with respect to the shape descriptors (principal component coefficients) to find the minima of the error function [35]. The result of the partial differentiation is a system of linear equations in the shape descriptors. The roots of this system of equations are the optimal shape descriptors that create a model which has the minimum value of the error function E . In the following section depicts the derivation of the systems of linear equations will be derived from the error function.

The error function defined in (3.8) can be expressed in terms of the v_i vertices of V , and points p_i of the point cloud Q as follows:

$$E = \sum_{i=1}^m \|v_i - q_i\|^2 \quad (3.9)$$

Equation (3.9) can also be expressed in terms of the model's shape descriptors as:

$$E = \left\| (V_{avg} + \sum_{k=1}^w a_k U'_k) - Q \right\|^2 \quad (3.10)$$

Where V_{avg} is subset of vertices, from the atlas' mean model vertices, which is corresponding to the vertices set V that contains the closest vertices in the model M (being morphed) to the point cloud Q . U'_k is a reduced version of U_k (the k^{th} eigenbone) that only contains the set of vertices corresponding to the vertices set V .

Combining (3.9) and (3.10), the error function E can be expressed as follows:

$$E = \sum_{i=1}^m \left\| (v_{avg,i} + \sum_{k=1}^W a_k u'_{k,i}) - q_i \right\|^2 \quad (3.11)$$

Where $v_{avg,i}$ is the i^{th} vertex of atlas mean model's vertices subset V_{avg} . Similarly, $u'_{k,i}$ is the i^{th} vertex of the reduced eigenbone (principal component) U'_k .

The shape descriptors α_k that create a bone model which optimally match the point cloud Q (at the minima of the error function E), can then be calculated by partially differentiating the error function E with respect to the shape descriptors α_k and equating the result of differentiation to zero. This will yield a system of homogenous linear equations in the shape descriptors as follows:

The error function E in (3.11) can be further expanded as:

$$E = \sum_{i=1}^m \left[\left(x_{avg,i} + \sum_{k=1}^W a_k x_{u',k,i} - x_{q,i} \right)^2 + \left(y_{avg,i} + \sum_{k=1}^W a_k y_{u',k,i} - y_{q,i} \right)^2 + \left(z_{avg,i} + \sum_{k=1}^W a_k z_{u',k,i} - z_{q,i} \right)^2 \right] \quad (3.12)$$

Where $x_{avg,i}$ is the x-coordinate of the i^{th} vertex of the atlas mean model's vertices subset V_{avg} , $x_{u',k,i}$ is the x-coordinate of the i^{th} vertex of reduced eigenbone U'_k , and $x_{q,i}$ is the x-coordinate of the i^{th} point of Q . Similar arguments apply to the y, and z coordinates. Then calculating the partial derivative of E with respect to each of the shape descriptors (eigenvectors' coefficients) α_k yields

$$\frac{\partial E}{\partial \alpha_k} = 0 \quad \forall k \in [1, W] \quad (3.13)$$

$$\begin{aligned} \frac{\partial E}{\partial \alpha_k} = \sum_{i=1}^m & \left[2 \left(x_{avg,i} + \sum_{l=1}^W a_l x_{u',l,i} - x_{q,i} \right) x_{u',k,i} \right. \\ & + 2 \left(y_{avg,i} + \sum_{l=1}^W a_l y_{u',l,i} - y_{q,i} \right) y_{u',k,i} \\ & \left. + 2 \left(z_{avg,i} + \sum_{l=1}^W a_l z_{u',l,i} - z_{q,i} \right) z_{u',k,i} \right] \\ = 0 & \quad \forall k \in [1, W] \end{aligned} \quad (3.14)$$

Recombining coordinates values into vertices (vectors) , and dividing by 2 yield:

$$\begin{aligned} \frac{\partial E}{\partial \alpha_k} = \sum_{i=1}^m & \left[(v_{avg,i} \cdot u'_{k,i}) + \left(\sum_{l=1}^W a_l u'_{l,i} \right) \cdot u'_{k,i} - q_i \cdot u'_{k,i} \right] \\ = 0 & \quad \forall k \in [1, W] \end{aligned} \quad (3.15)$$

Rearranging yields:

$$\sum_{i=1}^m \left(\sum_{l=1}^W a_l (u'_{l,i} \cdot u'_{k,i}) \right) = \sum_{i=1}^m [(q_i - v_{avg,i}) \cdot u'_{k,i}] \quad \forall k \in [1, W] \quad (3.16)$$

Reformulating (3.16) in a matrix form will result in a linear system of equations in the form of $AX = B$ as follows:

$$\begin{aligned}
& \sum_{i=1}^m \begin{bmatrix} u'_{1,i} \cdot u'_{1,i} & u'_{2,i} \cdot u'_{1,i} & \cdots & \cdots & u'_{W,i} \cdot u'_{1,i} \\ u'_{1,i} \cdot u'_{2,i} & u'_{2,i} \cdot u'_{2,i} & \cdots & \cdots & u'_{W,i} \cdot u'_{2,i} \\ \vdots & \vdots & \ddots & \ddots & \vdots \\ \vdots & \vdots & \ddots & \ddots & \vdots \\ u'_{1,i} \cdot u'_{W,i} & u'_{2,i} \cdot u'_{W,i} & \cdots & \cdots & u'_{W,i} \cdot u'_{W,i} \end{bmatrix} \begin{bmatrix} a_1 \\ a_2 \\ \vdots \\ a_W \end{bmatrix} \\
& = \sum_{i=1}^m \begin{bmatrix} (q_i - v_{avg,i}) \cdot u'_{1,i} \\ (q_i - v_{avg,i}) \cdot u'_{2,i} \\ \vdots \\ (q_i - v_{avg,i}) \cdot u'_{W,i} \end{bmatrix}
\end{aligned} \tag{3.17}$$

This linear system of equations is then solved to calculate the roots of the equations, which are the optimal shape descriptors to create the new 3D model that best fit the point cloud. In this work, singular value decomposition (SVD) [40] was used to solve the linear system of equations.

In this work, the mahalanobis distance used in [35] was omitted because the point clouds used were dense; these dense clouds incurred a great constraining force on the model deformation. Therefore the constraining function of the mahalanobis distance was not needed, but rather was avoided to provide the model deformation with more freedom to generate a new model that best fit the bone' point cloud.

To study the performance of the linear least squares morphing in predicting the bone's morphology given a point cloud representing the bone's shape, the point clouds extracted from the datasets models were used to reconstruct bones models using the gender-specific jack-knife atlases for each model to be reconstructed. To study the effect of the point cloud density on the morphing accuracy, different point cloud densities (as shown in Figure 3.35 through Figure 3.44) were used to reconstruct the bones models.

Another factor included in this morphing accuracy evaluation, was the number of principal components (modes of variations) used in the bone morphology optimization. The closest surface point based RMS error between the reconstructed models, and their reference original models was then calculated as the reconstruction error.

The detailed results for the accuracy study of linear least squares morphing method are presented in the appendix section 9.2.2 . The processing time for the linear least squares method was few seconds using 2-mm point clouds density, using any number of principal components on an Intel Core i7 2.3 GHz processor. The processing time decreases with decreasing the point cloud density. A comparison for the mean RMS reconstruction error for the linear least squares method using different point cloud densities is shown in Figure 3.49 through Figure 3.52 for the female distal femur, male distal femur, female proximal tibia, and male proximal tibia respectively. Examining these figures, it can be shown that that point density has insignificant effect on the model reconstruction accuracy. However, for the 16 mm point cloud density case, the reconstruction error increases by increasing the number of principal components used (approximately in the range of 64 to maximum number of principal components). This is due to the insufficient morphing guidance information available in the low density point clouds (equals to or greater than 16 mm) to guide the local deformations carried out by the least significant (higher order) principal components. For the same reason, point clouds with 32-mm density were not included because of their high reconstruction error.

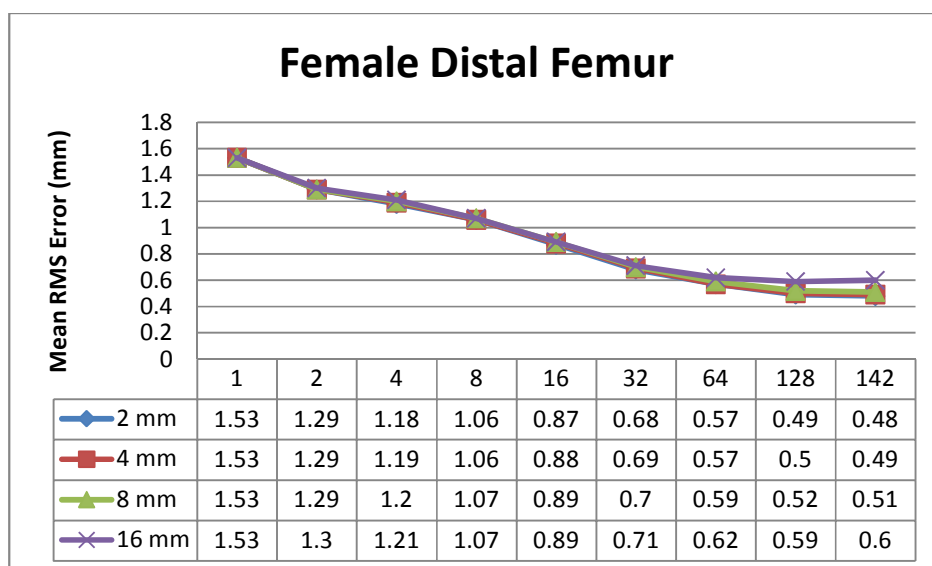


Figure 3.49 Mean RMS errors vs number of principal components for female distal femur morphing using the linear least squares method using gender specific jack-knife atlases

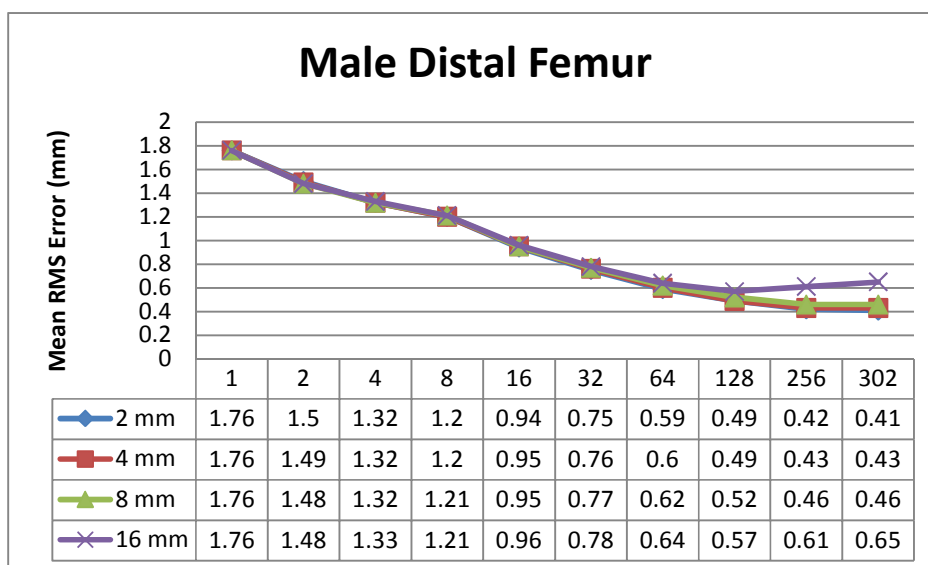


Figure 3.50 Mean RMS errors vs number of principal components for male distal femur morphing using the linear least squares method and gender specific jack-knife atlases

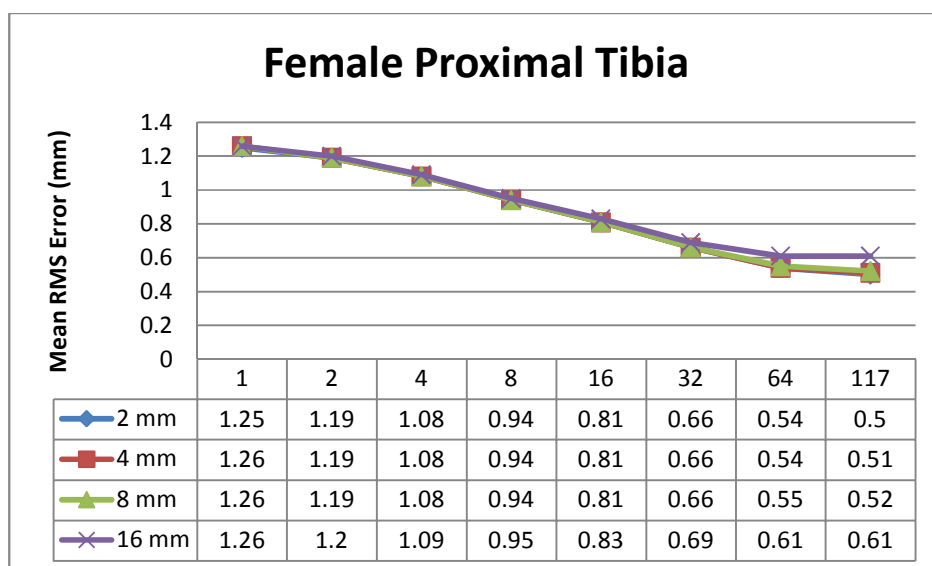


Figure 3.51 Mean RMS errors vs number of principal components for female proximal tibia morphing using linear least squares method and gender specific jack-knife atlases

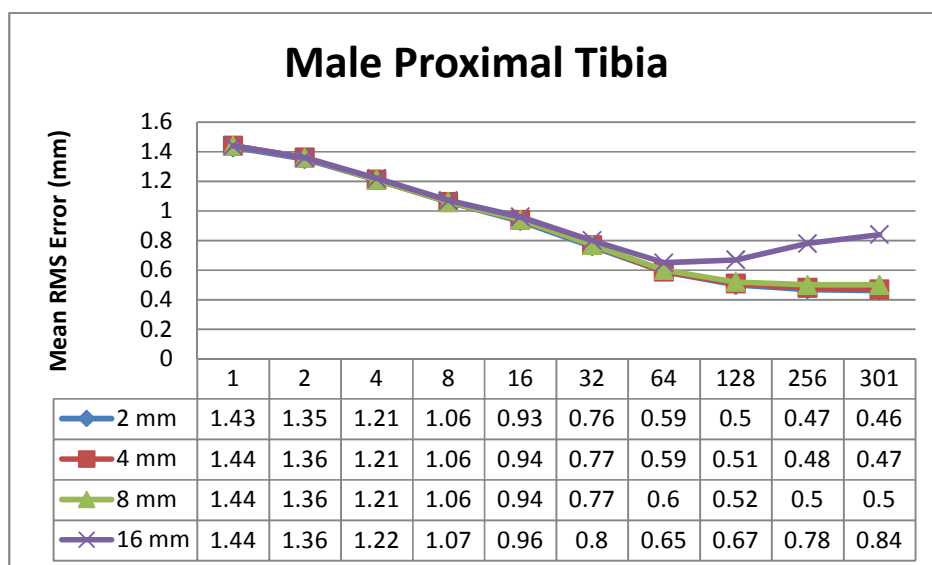


Figure 3.52 Mean RMS errors vs number of principal components for male proximal tibia morphing using linear least squares method using gender specific jack-knife atlases

3.3.3 Hybrid Morphing

The last bone morphing method examined in this work is a combination of the direction-set optimization morphing and the linear least squares morphing methods. The result (the reconstructed model) of the Direction Set morphing is input to the linear least squares morphing as the initial model. The rationale behind the hybrid method is that the Direction Set morphed model will be closer to the bone's point cloud, therefore the selected closest points in the Direction Set morphed model (as the initial model for the linear least squares morphing) will be more accurately selected than the ones that would be selected from the mean model as the initial model (as in the case of applying the linear least squares morphing only). This should increase the reconstruction accuracy.

To study the performance of the hybrid morphing in predicting the bone's morphology given a point cloud representing the bone's shape, the point clouds extracted from the datasets' models were used to reconstruct bones models using the gender-specific jack-knife atlases for each model to be reconstructed. To study the effect of the point cloud density on the morphing accuracy, different point cloud densities (as shown in Figure 3.35 through Figure 3.44) were used to reconstruct the bones models. Another factor included in this morphing accuracy evaluation, was the number of principal components (modes of variations) used in the linear least squares morphing stage. The number of principal components used in the Direction Set morphing stage was selected to be 32. The closest surface point based RMS error between the reconstructed models, and their reference original models was then calculated as the reconstruction error.

The results for the model reconstruction accuracy study of the hybrid morphing method are presented in the appendix section 9.2.3. A comparison for the mean RMS reconstruction errors for the hybrid method using different point cloud densities is shown in Figure 3.53 through Figure 3.56 for the female distal femur, male distal femur, female proximal tibia, and male proximal tibia respectively. Examining these figures, it can be shown that the effect of the point density on the model reconstruction accuracy using the hybrid method is similar to the its effect in the linear least squares morphing. Also, the error charts shows that the hybrid method has lower RMS error than the linear least squares method.

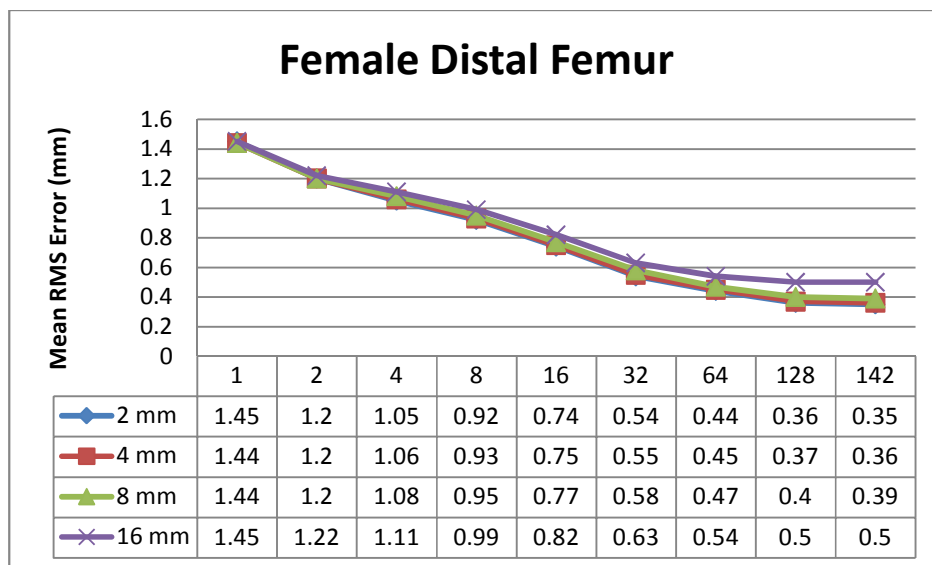


Figure 3.53 Mean RMS errors versus the number of principal components for the female distal femur reconstruction using the hybrid morphing method for the unreduced, 4 mm, 8 mm, and 16 mm reduced models' point clouds using gender-specific jack-knife atlases

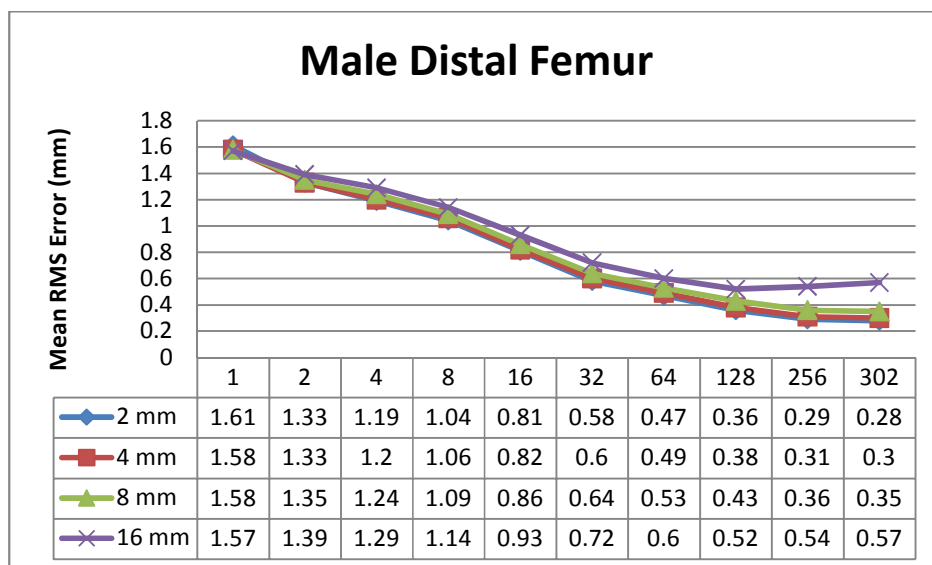


Figure 3.54 Mean RMS errors versus the number of principal components for the male distal femur reconstruction using the hybrid morphing method for the unreduced, 4 mm, 8 mm, and 16 mm reduced models' point clouds using gender-specific jack-knife atlases

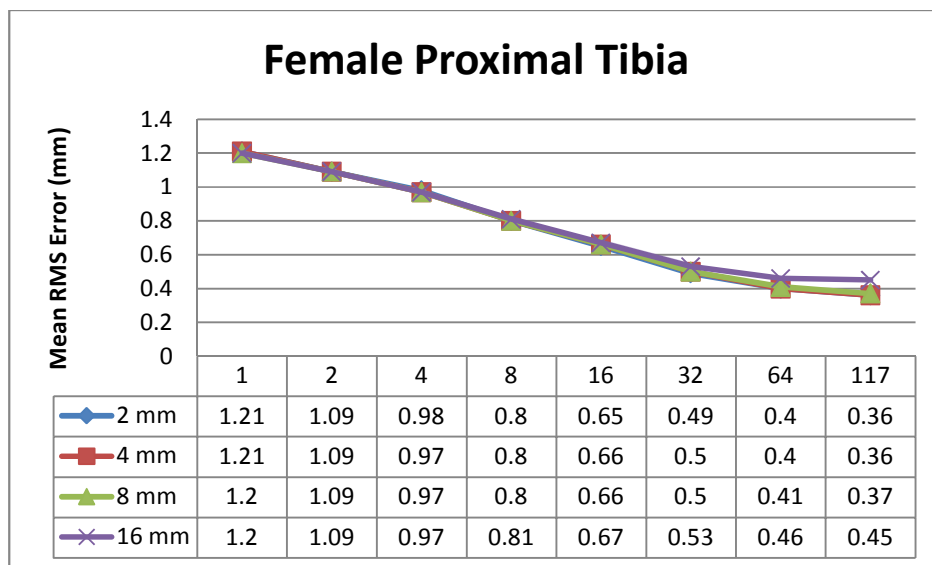


Figure 3.55 Mean RMS errors vs the number of principal components for the female proximal tibia morphing using the hybrid morphing method for the unreduced, 4 mm, 8 mm, and 16 mm reduced models' point clouds using gender-specific jack-knife atlases

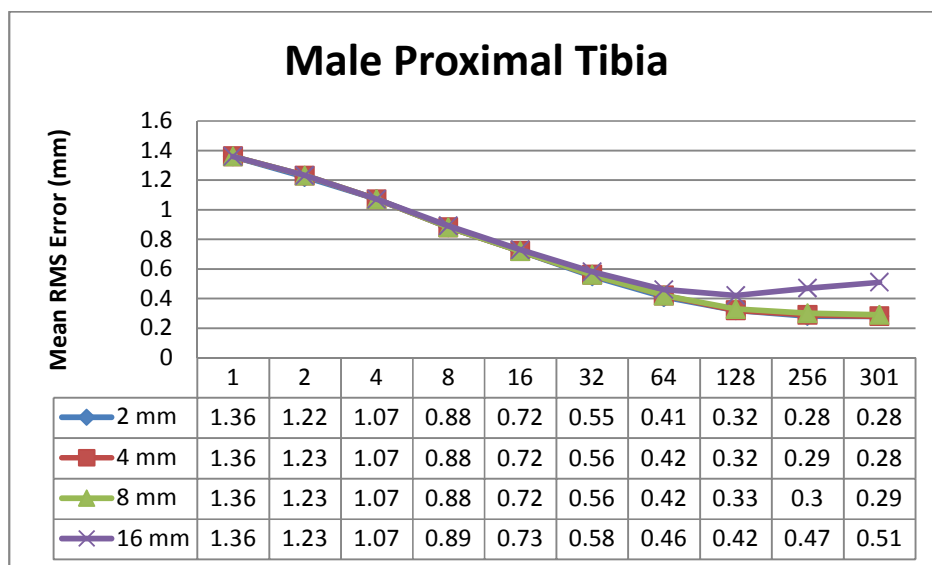


Figure 3.56 Mean RMS errors vs the number of principal components for the male proximal tibia morphing using the hybrid morphing method for the unreduced, 4 mm, 8 mm, and 16 mm reduced models' point clouds using gender-specific jack-knife atlases

Chapter 4 3D Knee Model Reconstruction Using Single-Element Ultrasound Transducer

The first method and system developed in this work for 3D knee model reconstruction using ultrasound RF data is presented in this chapter. This imaging system used a tracked single-element ultrasound transducer to collect a 3D point cloud over the bone's surface, which was then used by the bone morphing module to reconstruct 3D model for the scanned bone. In the following sections, the system setup will be described, followed by the probe calibration method, the ultrasound signal processing method for bone echo detection, and the point cloud reconstruction method.

4.1 System Setup

This imaging system was built using a single-element (A-mode) ultrasound transducer, a pulser/receiver to drive the ultrasound transducer, a data acquisition system, and an optical motion tracking system to track the motion of the ultrasound transducer while being used in the scanning of the bone.

4.1.1 Ultrasound Transducer and Pulser/Receiver

The single element (A-Mode) ultrasound transducer used in this system was immersion type (Olympus NDT) 6 mm in diameter and had a 3.5 MHz center frequency. The ultrasound transducer was driven by a 5072 PR pulser/receiver (Olympus NDT). The pulser/receiver activates the ultrasound transducer by an electric pulse and receives the echo signal from the transducer, amplifies and filters it, and delivers it out through the RF output port. The output of the pulser/receiver is an analog ultrasound RF signal which consists of the echoes generated by the reflections of the transmitted ultrasound pulse at

the different interfaces in the path of the ultrasound beam. Figure 4.1 show the ultrasound transducer, and pulser/receiver used in the developed system. Figure 4.2 shows the impulse response of the ultrasound transducer used, and its frequency spectrum.



Figure 4.1 The A-mode ultrasound transducer (left), and the 5072 pulser/receiver (Olympus NDT) used in the developed single-element ultrasound transducer-based 3D knee model reconstruction system.

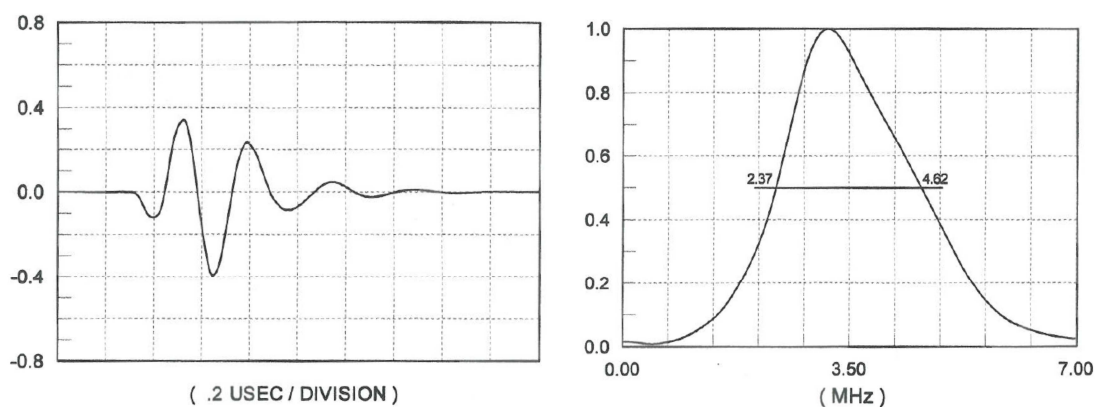


Figure 4.2 The impulse response (left) for the ultrasound transducer used in the system, and its frequency spectrum (right) generated during the transducer test performed by the vendor using a water tank and a rigid reflector (Olympus NDT).

4.1.2 Data Acquisition System

The analog ultrasound RF signal output from the pulser/receiver is fed to a data acquisition system to be digitized and fed in real-time to the imaging software developed for the point cloud reconstruction. The data acquisition system used in this work was the 12-bit Octopus CompuScope (Gage Inc, Lockport, IL), which is an analog to digital converter board that is connected to the computer through the PCI connector. The Octopus data acquisition system has an application programming interface (API) library that allows the control of the data acquisition, and acquiring the data by the imaging software. The sampling frequency used was 20 MHz. Figure 4.3 shows the Octopus data acquisition PCI card used



Figure 4.3 Octopus CompuScope (Gage Inc, Lockport, IL) data acquisition PCI card used in the developed single-element ultrasound transducer-based 3D knee model reconstruction system.

4.1.3 Motion Tracking System

The ultrasound transducer was used to detect the depth of the bone, i.e. the distance between the transducer's face and the bone's surface. In order to convert this one-dimensional bone depth measurement into a 3D point, a motion tracking system was used to track the motion of the ultrasound transducer to register the bone depth measurements into 3D point cloud representing the scanned bone's surface. The motion tracking system used was the OptoTrak3020 (Northern Digital Inc (NDI), Ontario, Canada).

The OptoTrak3020 system is a high accuracy optical motion tracking system (0.1-0.15 mm tracking accuracy [24]) that utilizes the infrared light for motion tracking. This motion tracking system consists of three components:

- **Infrared Camera:** is the main optical unit which contains of infrared receivers which acquire the infrared light emitted by the infrared LEDs in the motion tracking probes. The infrared camera acts as the fixed world coordinate frame of reference of the tracking system.
- **Control Unit:** is the control unit of the tracking system. It is connected to the infrared camera and the computer running the motion tracking software. It receives the detected infrared pulses signals from the camera, triangulates the position of the tracking probe and sends the motion tracking information to the computer.
- **Motion Tracking Probe:** is the probe used for the motion tracking. The tracking probe contains infrared LEDs (at least 3 non collinear, and usually are 4-6 to provide redundancy and higher tracking accuracy) which transmits infrared pulses

that are received by the infrared camera to triangulate the position and orientation of the probe.

The motion tracking system has two coordinate frames of reference. The first coordinate is the fixed world coordinate frame, will be denoted by W , and is defined by (virtually attached to) the optical camera. The second coordinate frame is the tracking probe's local coordinate frame, will be denoted by OP . During its operation, the motion tracking system provides the six position and orientation parameters of the tracking probe's local coordinate frame OP , relative to the fixed world coordinate frame W . These parameters are:

➤ **Rotation Angles (Euler Angles)**

- *Yaw*: is the angle of counterclockwise rotation around the z-axis.
- *Pitch*: is the angle of counterclockwise rotation around the y-axis.
- *Roll*: is the angle of counterclockwise rotation around the x-axis.

➤ **Translation**

- T_x : is the translation along the x-axis.
- T_y : is the translation along the y-axis.
- T_z : is the translation along the z-axis.

The homogenous transformation H_{OP}^W between the probe's local coordinate frame OP and the world coordinate frame W can then be calculated as follows:

Let R_x be the rotation matrix around the x-axis, R_y be the rotation matrix around the y-axis, and R_z be the rotation matrix around the z-axis. These rotation matrices are defined as follows:

$$R_x = \begin{bmatrix} 1 & 0 & 0 \\ 0 & \cos(\text{roll}) & -\sin(\text{roll}) \\ 0 & \sin(\text{roll}) & \cos(\text{roll}) \end{bmatrix} \quad (4.1)$$

$$R_y = \begin{bmatrix} \cos(\text{pitch}) & 0 & \sin(\text{pitch}) \\ 0 & 1 & 0 \\ -\sin(\text{pitch}) & 0 & \cos(\text{pitch}) \end{bmatrix} \quad (4.2)$$

$$R_z = \begin{bmatrix} \cos(\text{yaw}) & -\sin(\text{yaw}) & 0 \\ \sin(\text{yaw}) & \cos(\text{yaw}) & 0 \\ 0 & 0 & 1 \end{bmatrix} \quad (4.3)$$

Then the total rotation matrix denoted by R (which is 3x3 matrix) can be obtained by the multiplication of the individual rotation matrices as follows:

$$R = R_z R_y R_x = \begin{bmatrix} R_{11} & R_{12} & R_{13} \\ R_{21} & R_{22} & R_{23} \\ R_{31} & R_{32} & R_{33} \end{bmatrix} \quad (4.4)$$

The homogenous transformation matrix H_{OP}^W that transforms the local coordinate frame of the tracking probe OP to the world coordinate frame W is then constructed from the rotation matrix and the translation parameters as follows

$$H_{OP}^W = \begin{bmatrix} R_{11} & R_{12} & R_{13} & T_x \\ R_{21} & R_{22} & R_{23} & T_y \\ R_{31} & R_{32} & R_{33} & T_z \\ 0 & 0 & 0 & 1 \end{bmatrix} \quad (4.5)$$

The optical tracking probe was rigidly attached to the ultrasound transducer to track its motion, and acquire the 3D orientation and translation of the ultrasound transducer, while being used in the scanning, in order to transform the measured bone surface points' depths into 3D point cloud representing the bone surface. Figure 4.4 shows the developed imaging system's setup during one of the phantom experiments. Figure 4.5 shows a distal femur phantom, consisting of a saw bone in a water container, while being scanned during one of the system experiments.

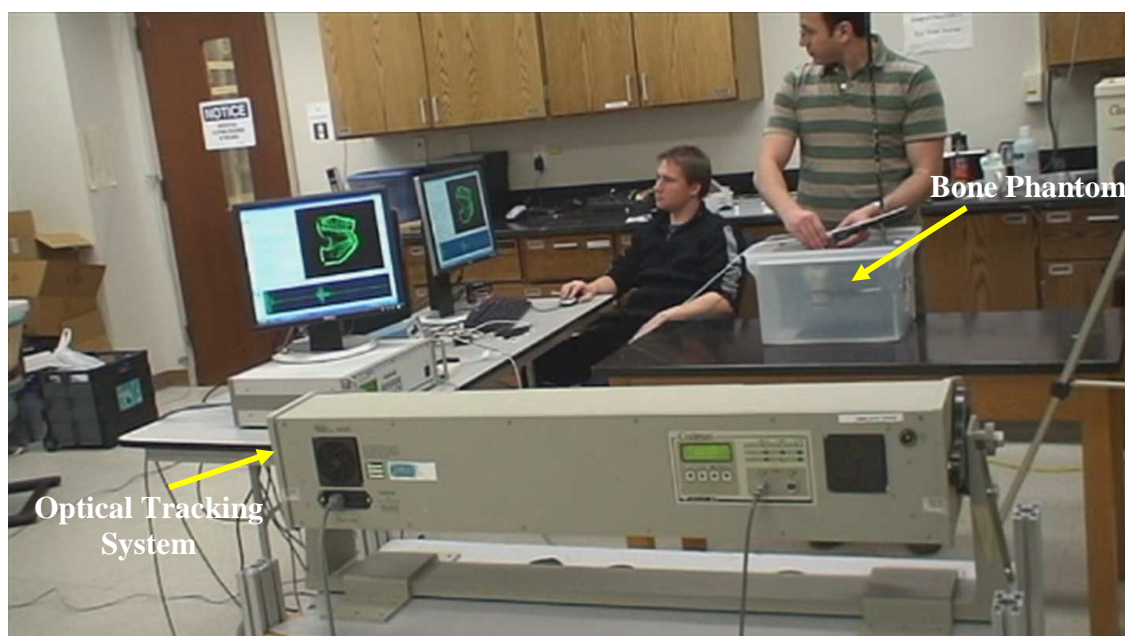


Figure 4.4 The developed single-element ultrasound transducer-based 3D knee model reconstruction system's setup showing the OptoTrak3020 (Northern Digital Inc (NDI), Ontario, Canada) tracking system, the phantom scanning, and the developed imaging software during one of the phantom experiments.

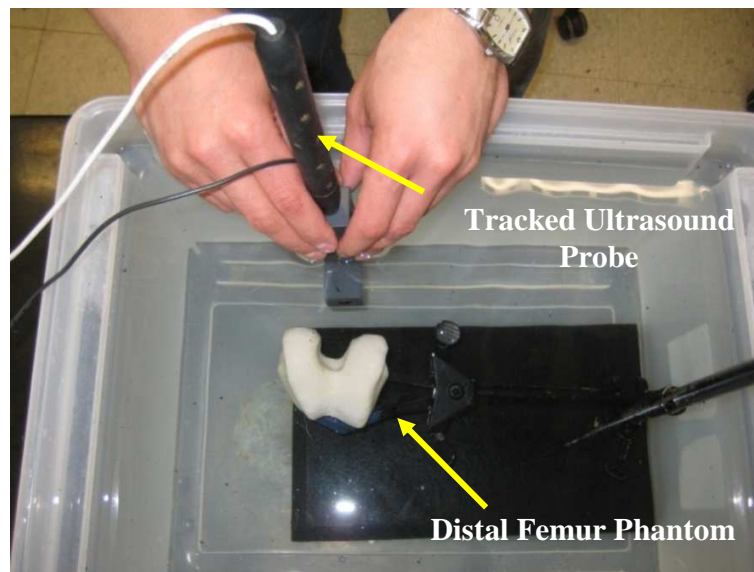


Figure 4.5 A snapshot for a phantom scanning experiment showing the distal femur phantom and the tracked A-mode ultrasound probe during the scanning process.

4.1.4 Imaging Software

The imaging software was developed in Microsoft Visual C++ 2005. QT 4.3 (Nokia, Keilalahdentie, Finland) was used for graphical user interface (GUI), and Open Inventor 7.2 (Visualization Science Group (VSG) Inc, Burlington, MA) was used for 3D visualization. The CompuScope's (the data acquisition system) API was used for interfacing with the data acquisition system to acquire the digitized ultrasound RF signals in real-time. The OptoTrak3020 API was used to acquire ultrasound probe's tracking data in real-time. The imaging software was developed using the multithreading technology in order to allow concurrent ultrasound data, and probe motion tracking data acquisition, processing, and point cloud reconstruction and rendering. Figure 4.6 shows a snapshot for the developed imaging software.

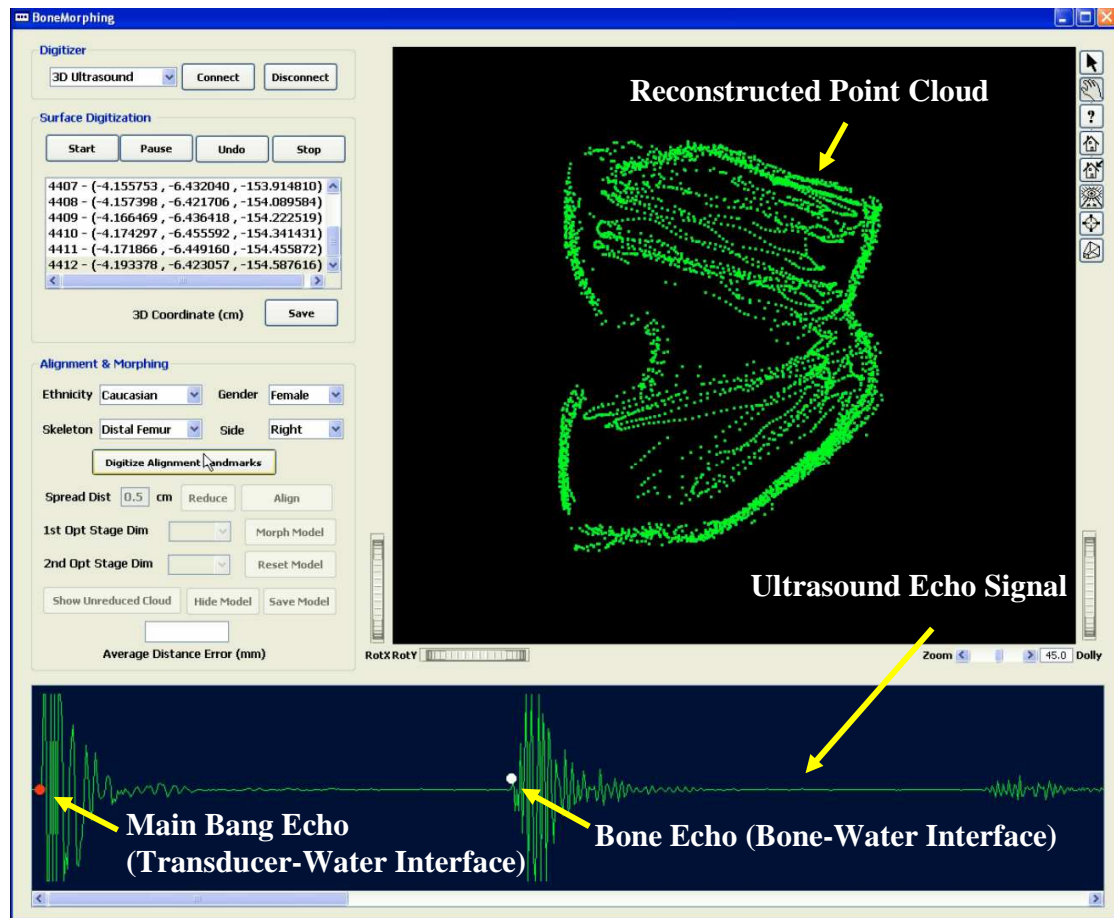


Figure 4.6 A snapshot for the developed imaging software, for 3D knee model reconstruction using single-element ultrasound transducer, during scanning of a phantom.

It shows the reconstructed 3D point cloud for a distal femur phantom and one of the ultrasound A-mode (RF) signals with the initial echo (red dot) reflected by transducer-water interface, and the bone echo (white dot) reflected by the bone-water interface

4.2 Tracked A-Mode Ultrasound Probe Calibration

The probe calibration is a registration process by which the spatial relation between the ultrasound transducer and the motion tracking probe is determined. The calibration process results in a set of calibration parameters, which are characteristic to the tracked A-mode ultrasound probe assembly. These calibration parameters were then

used by the imaging software to transform the acquired depth measurements into 3D points. The calibration parameters are:

- **Center of the Ultrasound Transducer (C^{OP}):** The center point (C), of the ultrasound transducer's face as shown in Figure 4.7, relative to the coordinate frame (OP) of the tracking probe.
- **Ultrasound Transducer's Scan Line Unit Vector (\hat{u}_n^{OP}):** The scan line unit vector (\hat{u}_n) of the ultrasound transducer is the unit vector normal to the ultrasound transducer's face as shown in Figure 4.7. It points towards the direction of the ultrasound beam propagation. This scan line vector is also calculated relative to the local coordinate frame (OP) of the probe assembly's optical tracking probe

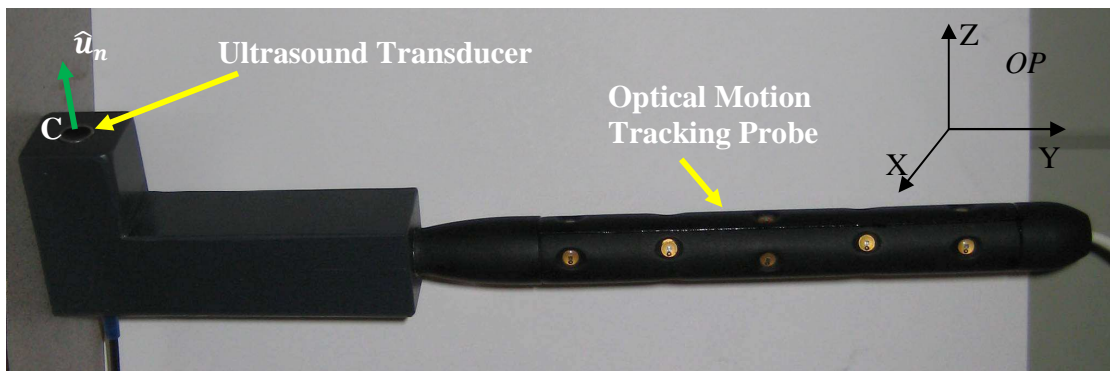


Figure 4.7 The tracked single-element (A-mode) ultrasound probe showing the optical motion tracking probe, the A-mode ultrasound transducer rigidly attached to it, the optical probe's local coordinate frame (OP) and the calibration parameters

In order to calculate the calibration parameters, the ultrasound probe assembly was held fixed, and a set of calibration measurements were collected an additional tracking probe. These collected measurements are:

1. **Transducer's Circumference Points:** The ultrasound transducer's circumference was digitized (a set of points collected from the transducer's circumference) by a tracking probe. A linear least squares circle fitting method was then used to fit a circle to the acquired circumferential points [25]. The center of this circle is the required center point (C^W) of the ultrasound transducer, relative to the tracking system's world coordinate frame (W). The transducer's circumference points were also used to calculate the unit vector (\hat{u}_n^W) normal to the circle plane (which is the transducer's face).
2. **A Point in Transducer's Ultrasound Field:** This point was used to adjust the direction of the calculated ultrasound scan line vector (\hat{u}_n^W), make it point towards direction of the ultrasound propagation.
3. **Optical Probe's Orientation and Position:** The homogeneous transformation (H_{OP}^W) between the tracking probe's coordinate frame (OP) and the world coordinate frame (W). This was used to transform the calculated calibration parameters (transducer center (C^W), and scan line unit vector (\hat{u}_n^W)) from the world coordinate (W) frame to the tracking probe's coordinate frame (OP). This transformation was performed by multiplying the calculated calibration parameters by the inverse of (H_{OP}^W) as follows:

$$C^{OP} = H_{OP}^{W^{-1}} C^w \quad (4.6)$$

$$\hat{u}_n^{OP} = H_{OP}^{W^{-1}} \hat{u}_n^W \quad (4.7)$$

These calibration parameters were then used by the imaging software to transform the calculated bone's surface points' depth measurements (detected using the ultrasound transducer) into 3D point cloud representing the bone's surface.

4.3 Bone Echo Detection and Point Cloud Reconstruction

The bone echo detection process is responsible for real-time detection of the distance between the ultrasound transducer's face, and the bone's surface (this one-dimensional distance will be denoted by bone's surface depth). The probe calibration parameters along with real-time the probe tracking data were used to transform these one-dimensional bone depth measurements into 3D points relative to the tracking system's world coordinate frame. In the following sections, the bone echo detection method will be described, and then followed by a description for the transformation of the bone depth measurements into the 3D point cloud representing the bone's surface.

4.3.1 Bone Echo Detection

The bone echo detection algorithm used in this imaging system (the single-element based system) was designed mainly for the echo signals produced by the phantoms, which consisted of saw bones held fixed in water container. The ultrasound signals generated by these phantoms consist of two main echoes and sometimes other secondary echoes. The two main echoes are:

- **Transducer-Water Interface Echo (Main-Bang Echo):** This echo is produced by the reflection of a portion of the ultrasound pulse's energy at the transducer-water interface due to the difference in the acoustic impedance of the transducer and water [17].
- **Water-Bone Echo (Bone Echo):** This echo is generated by the reflection of the ultrasound beam at the water-saw bone interface. Figure 4.8 shows an ultrasound RF signal, captured during one of the phantom experiments, showing the main bang echo and the bone echo.

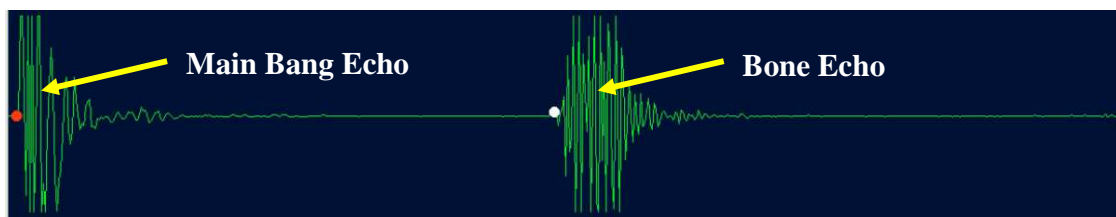


Figure 4.8 An ultrasound RF signal showing the two main echoes, which are the main bang echo (red dot) and the bone echo (white dot).

The secondary echoes that exist in the ultrasound echo signal are:

- **Off-Axis Echoes:** These echoes are generated by reflectors that lie off the axis of the ultrasound transducer (the scan line), which reflects the ultrasound beam travelling in the off-axis direction (side lobes of the ultrasound beam). The off-axis beam is smaller in amplitude and energy content than the main beam. Figure 4.9 shows an ultrasound echo signal that exhibit an off-axis echo.

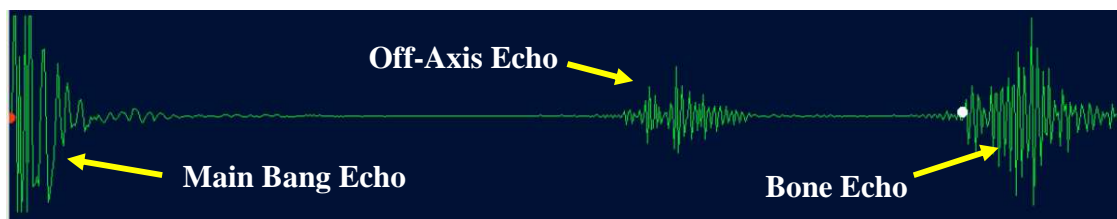


Figure 4.9 An ultrasound echo signal showing the main bang, bone echo, and an off-axis echo.

- **Reverberation Echoes:** These echoes are generated when the ultrasound beam is perpendicular to a reflecting surface with high reflection coefficient (like the case of saw bone in water). This reverberation occurs due to the multiple reflection of the ultrasound beam between the reflector and the ultrasound transducer. This produce secondary reflection echoes which have apparent depths equal to integer multiples of reflector's depth. The reverberation echoes are smaller in amplitude then the main echo due to the energy lost during the distance travelled by the echo. Figure 4.10 shows an echo signal exhibiting reverberation..

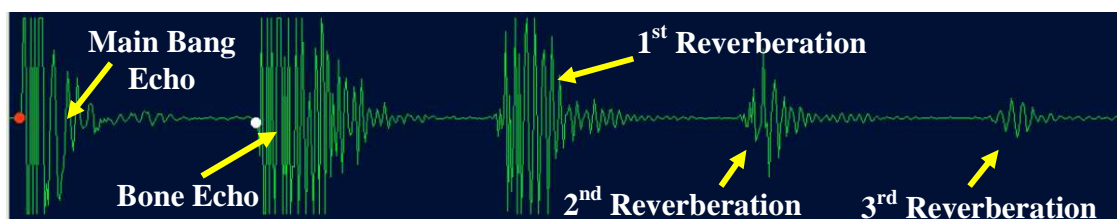


Figure 4.10 An ultrasound echo signal showing the main bang echo, bone echo, and multiple reverberation echoes

The target of the bone echo detection component is to detect distance between the main bang echo) and the bone echo and minimize the effect of the secondary echoes (reverberation and off-axis echoes) on this detection process. The detected distance is equal to double the distance between the transducer's face, and the bone's surface point.

Every ultrasound echo has a temporal pulse length that varies depending on the incident angle of the ultrasound beam on the bone's surface, as well as the distance travelled by the ultrasound pulse. In order to have an accurate measure of the distance between the main bang echo and the bone echo, the pulse's leading point was used to represent the pulse location in the ultrasound signal as shown in Figure 4.8 through Figure 4.10 in which the detected main bang echo leading point is denoted by a red dot, and the detected bone echo leading point is denoted by a white dot.

The main bang echo's leading edge point is defined as the first sample in the ultrasound signal that is above the signal acquisition trigger level, which was set to 20% of the signal maximum (since the signal maximum occurs at the main bang echo). The bone echo is then detected by searching for the first echo following the main bang echo. This is performed by searching for the first sample after the main bang echo which exceeds a predefined threshold. The threshold was determined empirically to be 80% of the signal maximum (the threshold is set to a high value, to avoid the off-axis echoes). The search starts after skipping the complete main bang echo by skipping a number of samples, equals to the average length of the main bang echo (which was empirically determined to be 10 μ s) after the leading edge point of the main bang echo. This search leads to a point in the bone echo's that is not the leading edge point. To reach the leading edge point of the echo, a backward local search starts from the reached point in the bone echo to the leading edge point of the echo. The criteria for stopping this search is finding a point below an empirically determined threshold which has a value of 20% (same as the trigger level in order to detect the same corresponding points in the main bang echo and

bone echo) of the signal maximum value. This final search leads to the bone echo's leading edge point which represents the temporal location of the bone echo in the ultrasound echo signal.

4.3.2 Bone Echoes Registration (Point Cloud Reconstruction)

The detected echo leading edge points are represented as samples indices (denoted as n_{main_bang} for the main bang echo, and n_{bone_echo} for the bone echo). These samples indices are transformed into timestamps (temporal points) on the signal by multiplying the samples indices by the sampling interval, which is equals to the inverse of the sampling frequency (denoted by F_s). The difference between the bone echo timestamp and the main bang echo timestamp is the flight time (denoted by t_{echo}) of the bone echo as follows:

$$t_{echo} = \frac{(n_{bone_echo} - n_{main_bang})}{F_s} \quad (4.8)$$

This flight time is then multiplied by the ultrasound speed in water (denoted by c) to obtain the roundtrip distance travelled by the bone echo (travelling from the transducer to the bone surface, and back again to the transducer). The bone surface point's depth, denoted by d_{echo} and, is equal to half of the calculated roundtrip distance travelled by the bone echo. The bone depth d_{echo} is calculated as follows:

$$d_{echo} = \frac{c * t_{echo}}{2} \quad (4.9)$$

The ultrasound speed c in water is a function of the water temperature and is calculated using the following formula [25]:

$$\begin{aligned}
c = & 1402.38744 + 5.03836171 T - 5.81172916 \\
& \times 10^{-2}T^2 + 3.34638117 \times 10^{-4}T^3 \\
& - 1.48259672 \times 10^{-6}T^4 + 3.16585020 \\
& \times 10^{-9}T^5
\end{aligned} \tag{4.10}$$

Where T is the temperature of the water in Fahrenheit. The detected depth of the bone's surface point is then transformed into a 3D point using probe's calibration parameters and the ultrasound transducer's tracking data represented as the homogeneous transformation (H_{OP}^W) between the tracking probe's coordinate frames (OP), and world coordinate frame (W).

The calibration parameters are first used to transform the detected bone depth into a 3D point, denoted by P_{echo}^{OP} , in the tracking probe's local coordinate frame (OP) as follows:

$$P_{echo}^{OP} = C^{OP} + d_{echo} \hat{u}_n^{OP} \tag{4.11}$$

The bone surface point P_{echo}^{OP} represented in the tracking probe's coordinate frame (OP) is then transformed to the world coordinate (W) using the tracking homogenous transformation H_{OP}^W between the coordinate frames (OP), and (W) as follows:

$$P_{echo}^W = H_{OP}^W P_{echo}^{OP} \tag{4.12}$$

The points P_{echo}^W form the point cloud digitized over the bone's surface using the tracked single-element ultrasound probe.

Chapter 5 3D Knee Model Reconstruction Using Ultrasound RF Data

This chapter describes the second imaging system developed in this work for patient-specific 3D knee model reconstruction using ultrasound RF data. This imaging system was developed as an extension of the tracked A-Mode ultrasound imaging system. This system used the RF data acquired from an ultrasound machine to transcutaneously digitize a 3D point clouds over the surface of the bone. This point cloud is then used to create a patient-specific 3D bone model using the bone morphing. In the following sections, the system components will be described, then followed by the ultrasound RF data processing, and point cloud reconstruction methods used

5.1 Imaging System Setup

The developed system consisted of an ultrasound machine, a motion tracking system, and custom built imaging software for the 3D bone model reconstruction. In the following subsections, each component will be described.

5.1.1 Ultrasound Machine, and Transducer

This imaging system was built using a SonixRP ultrasound machine (Ultrasonix Inc, British Columbia, Canada). The SonixRP machine, shown in Figure 5.1, is a diagnostic ultrasound machine with research capabilities. It allows the access to many imaging parameters, as well as access to the ultrasound raw RF data (post beam forming) through C++ based application programming interface (API) libraries. The API library used in this work is called Porta. The Porta API enables the control of the ultrasound

machine through C++ functions, and the real-time acquisition of the post beam forming RF data. This API was used to develop the 3D bone model reconstruction software to be running in real-time on the ultrasound machine. A linear high frequency transducer with 128 elements (L14-5/38) was used for the scanning to obtain the highest resolution. The transducer's frequency range is 5-14 MHz with center frequency of 7.2 MHz. Its fractional bandwidth is 70% at -6 dB. Its length is 38 mm, with 4 mm elevation height.



Figure 5.1 SonixRP ultrasound machine (Ultrasonix Inc, British Colombia, Canada) used in the second developed patient-specific 3D knee model reconstruction system

5.1.2 Motion Tracking System

In order to reconstruct 3D point cloud from the acquired ultrasound RF data, a motion tracking system was used to track the ultrasound probe's motion while being used in the scanning. The ultrasound probe's motion tracking data were used to register the acquired RF data frames in the 3D coordinate frame of the motion tracking system. The Polaris Spectra Optical motion tracking system (Northern Digital Inc (NDI), Ontario, Canada) was used in this imaging system. The Polaris Spectra is a state-of-art motion tracker that utilizes the infrared light to track the motion of a tracking probe with a number (at least 3, and usually 4 for redundancy) of infrared light emitting diodes (LEDs). This motion tracking system has three components:

- **Infrared Camera:** is the main optical unit which contains the infrared transmitters (which are used for the passive probes), and receivers which receives the infrared light emitted (or reflected in case of passive probes) by the infrared LEDs in the motion tracking probes. It acts as the fixed world coordinate frame of reference for the tracking system.
- **Control Unit:** is the control unit of the tracking system. It is connected to the infrared camera and the computer running the motion tracking software. It receives the detected pulses of infrared light from the camera, process them to triangulate the 3D position and orientation of the tracking probe, then sends the motion tracking data to the computer through a USB port. Figure 5.2 shows the infrared camera and controller of the Polaris Spectra tracking system.

- **Motion Tracking Probe:** is the probe which is used for the motion tracking. The motion tracking probe can be either active or passive probe. The active probe contains infrared LEDs (active probe), or infrared reflectors (passive probe). The active probe contains infrared LEDs (at least 3 non collinear) which transmit infrared pulses that are received by the infrared camera to triangulate the position and orientation of the tracking probe. The passive (wireless) probe contains four reflectors which reflect the infrared pulses transmitted by the infrared camera, and the reflected infrared pulses are then received by the camera to triangulate the probe's position and orientation. Figure 5.3 shows the active and passive probes of the Polaris Spectra motion tracking system. Figure 5.4 shows the tracking volume for the Polaris Spectra tracker.



Figure 5.2 Polaris Spectra optical motion tracking system (Northern Digital Inc (NDI), Ontario, Canada) used in the second developed imaging system; showing the infrared camera, and the control unit



Figure 5.3 Active and passive motion tracking probes for the Polaris Spectra optical motion tracking system (Northern Digital Inc (NDI), Ontario, Canada)

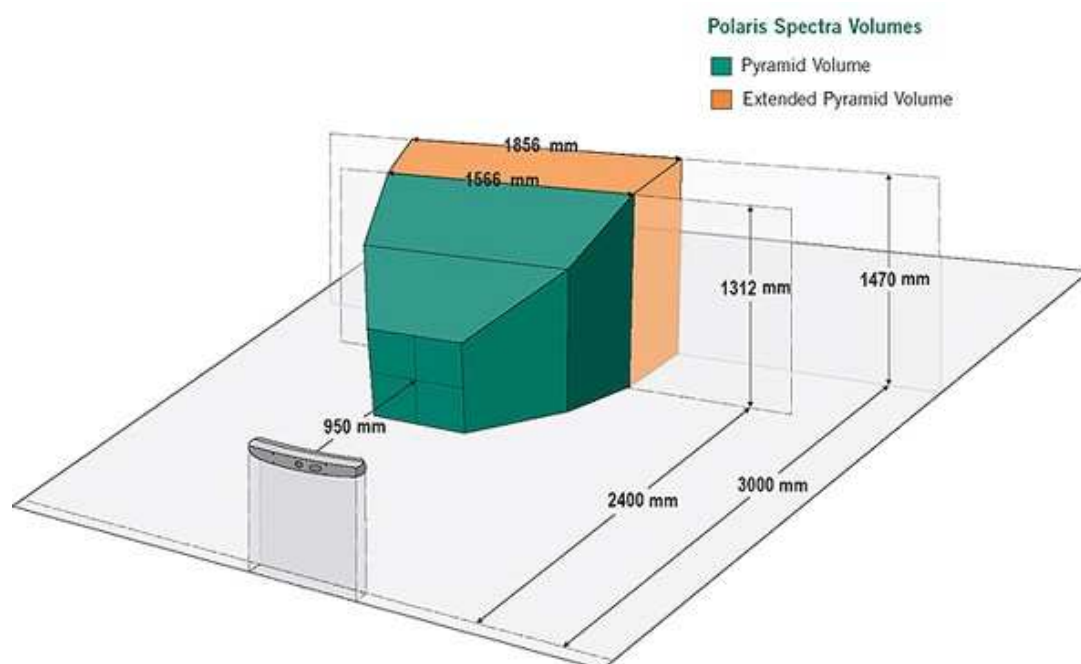


Figure 5.4 Polaris Spectra tracking volume (Northern Digital Inc (NDI), Ontario, Canada)

5.1.3 Imaging Software

The imaging software was developed in C++ using Visual Studio 2005 (Microsoft Inc). QT 4.3 (Nokia, Keilalahdentie, Finland) was used for graphical user interface (GUI), and Open Inventor 7.2 (Visualization Science Group (VSG) Inc, Burlington, MA) was used for 3D visualization. To acquire real-time ultrasound RF data from ultrasound machine, the developed software used the Ultrasonix's Porta API for interfacing with the ultrasound machine's hardware to acquire the digitized ultrasound RF signals in real-time to be processed by the software. The RF data was processed at a rate of 20 frames/second using an Intel dual core 2.4 GHz processor (the SonizRP processor). This processing frame rate was lower than the ultrasound machine's frame rate, which was 25 frames/second. The RF processing module was set to process the latest frame in order to maintain the speed of the contour extraction with the speed of scanning in order to provide the user with real-time extracted bone contours. The sampling frequency used by the ultrasound machine for the RF data was 20 MHz. The ultrasound probe tracking data was acquired in real-time by the developed software using the Polaris Spectra's interfacing API library. The imaging software was developed using the multithreading technology in order to allow concurrent acquisition, and processing of ultrasound RF data, and the probe motion tracking data, and point cloud reconstruction and rendering. Figure 5.5 shows a snapshot of the developed imaging software during scanning of a cadaveric distal femur.

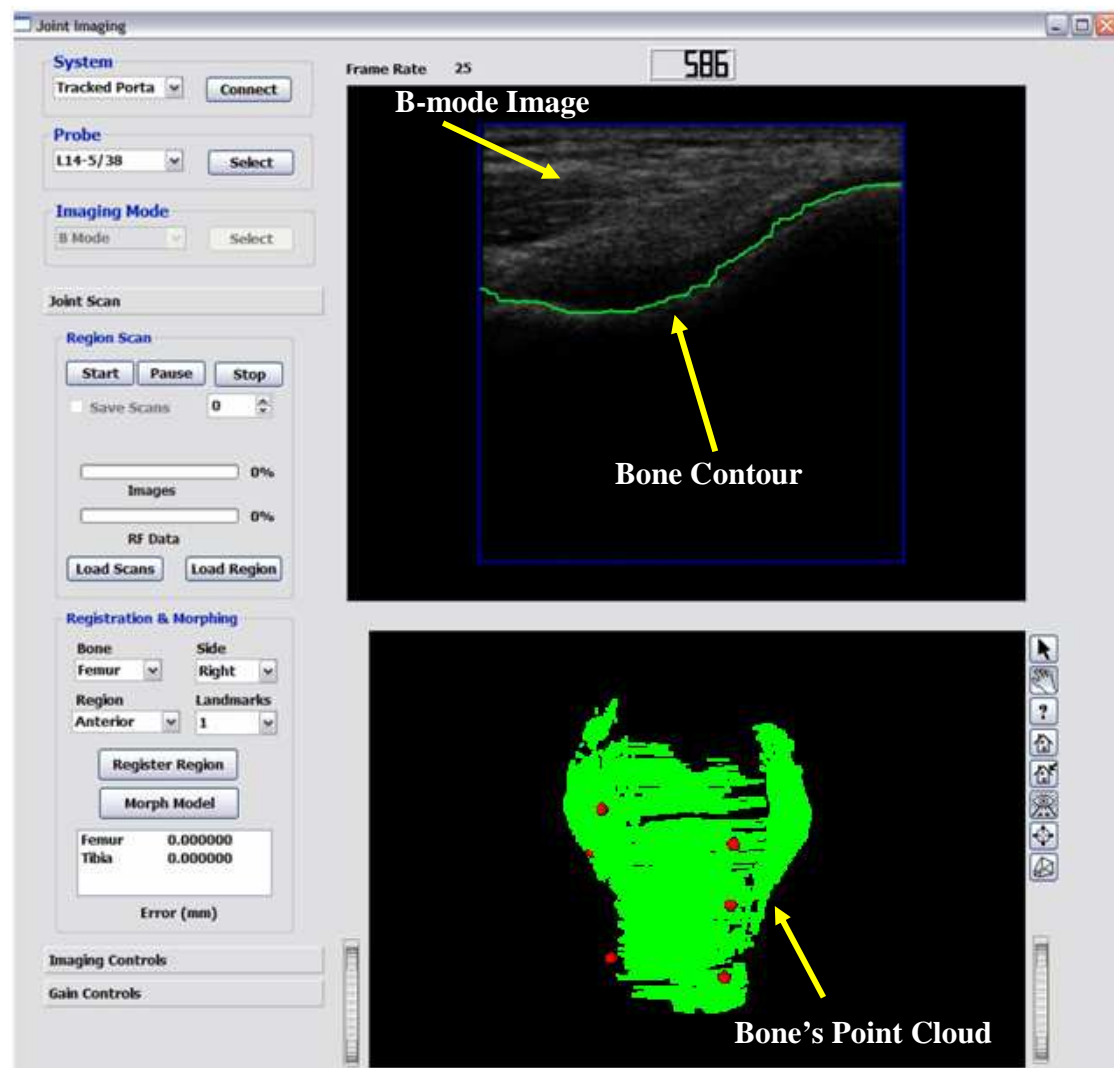


Figure 5.5 A snapshot of the developed imaging software during scanning of a cadaveric distal femur, showing a B-mode ultrasound image, the bone contour extracted from the ultrasound raw RF data, and the reconstructed point cloud while being reconstructed.

5.2 Tracked Linear Ultrasound Probe 3D Calibration

Tracked ultrasound probe 3D calibration is the process by which the tracking probe is registered with the ultrasound probe to obtain the spatial transformation between the coordinate frames of the ultrasound RF data and the tracking probe.

The optical probe has a local coordinate frame of reference virtually attached to it, while the optical camera defines the fixed world coordinate frame. The function of the tracking system is to determine, in real-time, the homogenous transformation H_{OP}^W between the optical probe's local coordinate frame denoted by (OP) and the camera's fixed world coordinate frame of reference (W) . The ultrasound probe has a local coordinate frame virtually attached to it as well. The calibration targets the determination of the spatial transformation between the coordinate frame of the ultrasound RF data, and the coordinate frame of the tracking probe.

In this system, a simple, fast and yet accurate calibration method was used. This method is based on four measured calibration parameters:

- **The origin point of the transducer (P_o^{OP}):** which corresponds to the first sample of the first ultrasound scan line, or alternatively corresponds to the origin of the ultrasound B-mode image. The transducer's origin point is calculated relative to the local coordinate frame (OP) of the tracking probe.
- **The length of the transducer array ($L_{trans}L$):** is provided by the manufacturer specifications.
- **Unit vector along the ultrasound transducer's scan lines (\hat{u}_y^{OP}):** is a unit vector in the direction of the ultrasound beam propagation. This scan line vector is also calculated relative to the local coordinate frame OP of the tracking probe.
- **Unit vector along the ultrasound transducer array (\hat{u}_x^{OP}):** is a unit vector in the direction of the ultrasound transducer array (normal to the scan line). This unit

vector is also calculated relative to the local coordinate frame OP of the tracking probe.

Figure 5.6 shows the calibration parameters illustrated on the tracked ultrasound probe used. In order to obtain these calibration parameters, the following calibration process was performed.

After rigidly attaching the optical probe to the ultrasound probe, the calibration process was performed by holding the probe assembly in a fixed position (throughout the whole calibration process), while a number of points were collected using another tracking probe. The collected points were the two end points of the ultrasound transducers array P_1^W , and P_2^W , and a point P_{plane}^W on the transducer face which is not collinear with the previously collected transducer array end points as shown in Figure 5.6. The homogeneous transformation H_{OP}^W between local coordinate frame OP of the tracking probe (attached to the ultrasound probe), and the world coordinate frame W of the optical camera was also recorded.

The calibration parameters were then calculated using the collected calibration measurements points and transformations as follows:

$$P_o^{OP} = (H_{OP}^W)^{-1} P_1^W \quad (5.1)$$

$$\hat{u}_x^{OP} = (H_{OP}^W)^{-1} \frac{P_2^W - P_1^W}{\|P_2^W - P_1^W\|} \quad (5.2)$$

$$\hat{u}_y^{OP} = (H_{OP}^W)^{-1} \frac{(P_{plane}^W - P_1^W) \times (P_2^W - P_1^W)}{\|(P_{plane}^W - P_1^W) \times (P_2^W - P_1^W)\|} \quad (5.3)$$

These calibration parameters were then used by the imaging software during the system operation, as described in Section 5.4.2.1, to register the detected bone contours from the RF data in the world coordinate frame of the tracking system's to reconstruct the 3D point cloud representing the scanned bone's surface.

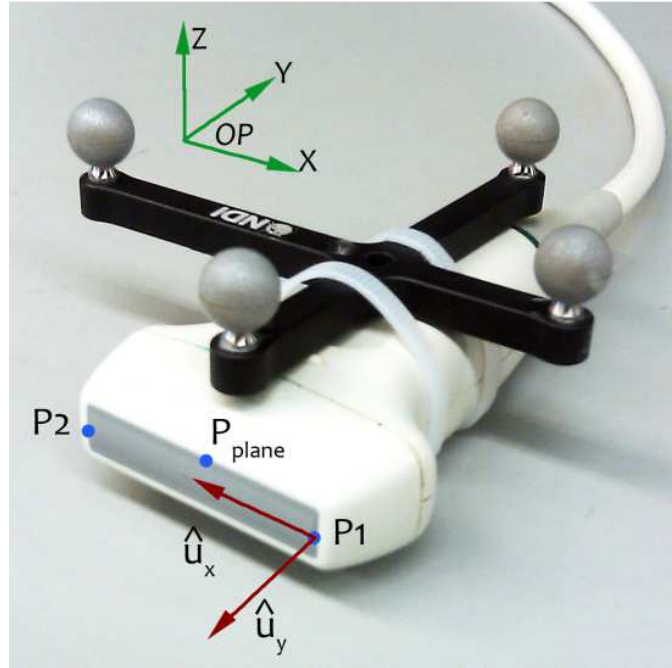


Figure 5.6 The tracked linear ultrasound probe used in the developed system, showing the collected calibration measurements, and the calculated calibration parameters

5.3 Knee Scanning Protocol

The high reflectivity and attenuation of the bone to ultrasound prevents the ultrasound energy from penetrating the bone to image any organ or tissue lying behind it.

This acoustic characteristic of the bone poses a challenge to the use of ultrasound in joint imaging. The knee is one of the main joints of the human body. It is formed of three articulating bones: femur, tibia and patella. These bones articulate together in two sub-joints:

- **Tibio-Femoral Joint:** formed by the articulation of the femur with the tibia at the femoral condyles and tibial condyles.
- **Patello-Femoral Joint:** formed by the articulation of the patella with the femur at the patellar surface of the femur and the articular surface of the patella.

During the flexion-extension motion of the knee, some portions of the articular surfaces of the bones are visible to the ultrasound beam, while others are occluded by the other bones. The two main positions at which most of the knee's articulating bones' surfaces are visible for the ultrasound beam are full extension and deep knee bend (or 90° flexion, if deep knee bend is difficult to achieve by the patient) positions. Figure 5.7 shows a dissected cadaver's knee (one of the two cadaver knees used for experimenting the imaging system) showing the articulating knee bones surfaces visible to ultrasound at 90° flexion. Figure 5.8 shows fluoroscopic images for a volunteer's knee, showing the different articulating surfaces of the knee bones visible to the ultrasound at different flexion angles.

When the knee is in full extension, the posterior parts of the distal femur and proximal tibia are both visible to the ultrasound. While in deep knee bend (or 90° flexion), the anterior surfaces of the distal femur, the trochlear groove, most of the inferior surface of the femoral condyles, the anterior superior surface of the tibia, and the anterior

surface of the tibia are visible to the ultrasound beam. Both the medial and lateral sides of the femur and tibia are visible at all flexion angles of the knee.

Therefore, in order to obtain a point cloud representing the ultrasound-visible knee bones surfaces, the knee should be scanned at different flexion angles. Implanting reference probes into the bones, to track the bones motion during scanning, is would make the imaging system invasive. Attaching references probes to the legs over the skin would greatly deteriorate the accuracy due to the skin-bone motion [27], and [28]. To overcome this problem, partial bones surfaces scans were performed at different flexion angles of the knee. During each partial scan, the knee was held fixed in order to avoid motion artifacts. From these partial scans, 3D partial point clouds were reconstructed which represent the scanned partial bone's surfaces. These partial point clouds were then mutually registered to reconstruct the whole bone's surface point cloud, as described in the following section.

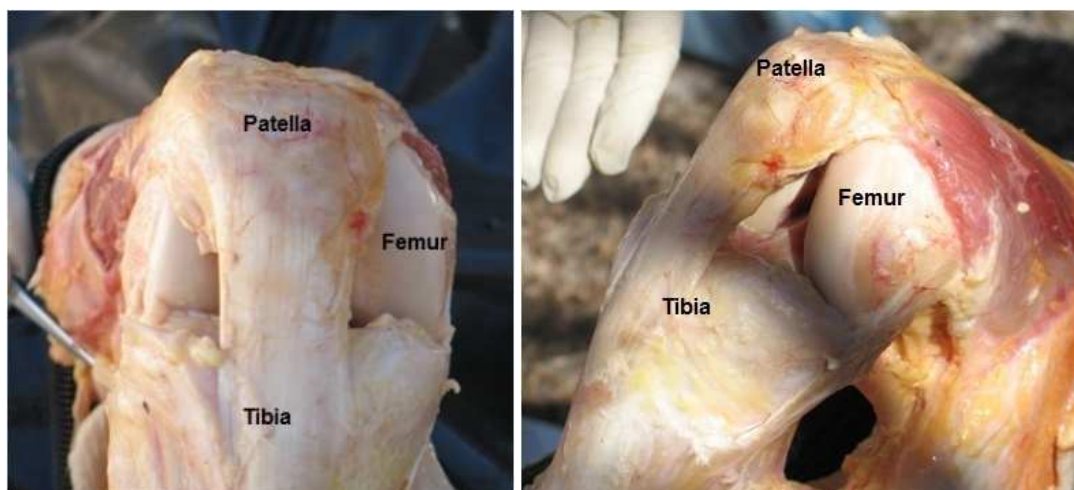


Figure 5.7 Dissected cadaver's knee showing the different ultrasound-visible regions of the patella, distal femur, and proximal tibia at 90 degrees flexion

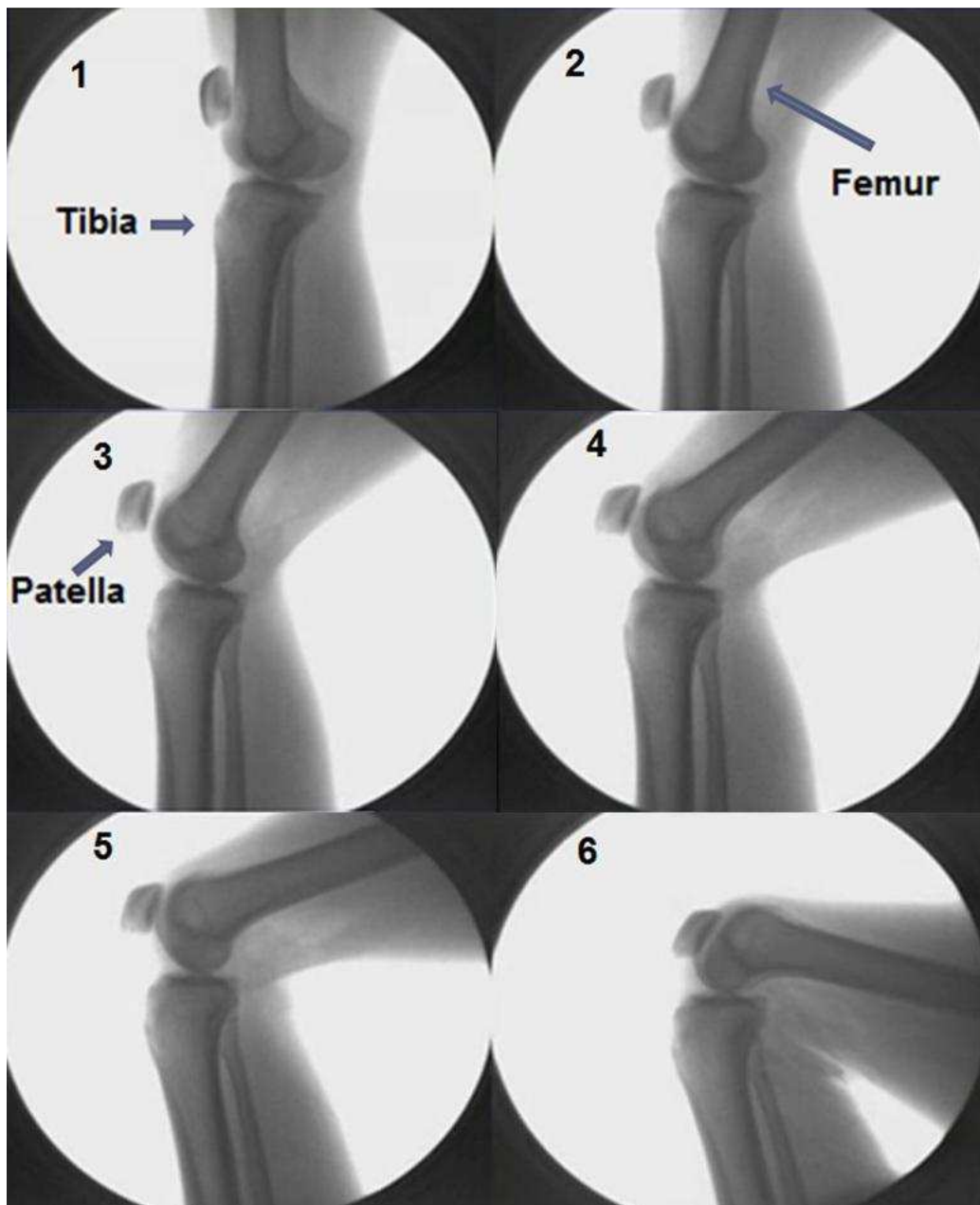


Figure 5.8 Fluoroscopic images of a volunteer's knee [26] at different flexion angles starting from full extension (1) to deep knee bend (6). The images show the different articular bone surfaces of the knee visible to ultrasound at different flexion angles

5.4 Bone Echo Detection and Point Cloud Reconstruction

This part of the system is responsible for transcutaneously localizing a point cloud over the bone's surface using the ultrasound RF data, and the probe's motion tracking data captured by the motion tracking system. In the following sections, the real-time method for the automatic extraction of the bone contours from the RF data will be described followed by description of the registration method of the extracted contours into a 3D point cloud that represents the scanned bone's surface.

5.4.1 Automatic Extraction of Bone Contours from Ultrasound RF Data

The ultrasound RF signal consists of a number of isolated and/or overlapping echoes. These echoes originate from the reflection of different portions of the ultrasound pulse's energy at the different tissue interfaces along the ultrasound beam's path. Of these echoes, is one echo of interest; the bone's echo, which is generated by the reflection of the ultrasound energy at the bone's surface. The process of bone contour extraction from the ultrasound frame is performed by automatically extracting the individual bone echo from each ultrasound RF signal, then combining these individual echoes to form the bone's contour. The extracted bone contours are then filtered to reject non-bone (noise) contours. Figure 5.9 shows a sample ultrasound B-mode image for cadaver's distal femur, showing sample scan lines RF signals as well as the final extracted contour using the developed method. Figure 5.10 shows a flowchart for the bone contour extraction from the ultrasound RF data. In the following sections, each step of the bone contour extraction process is described in details.

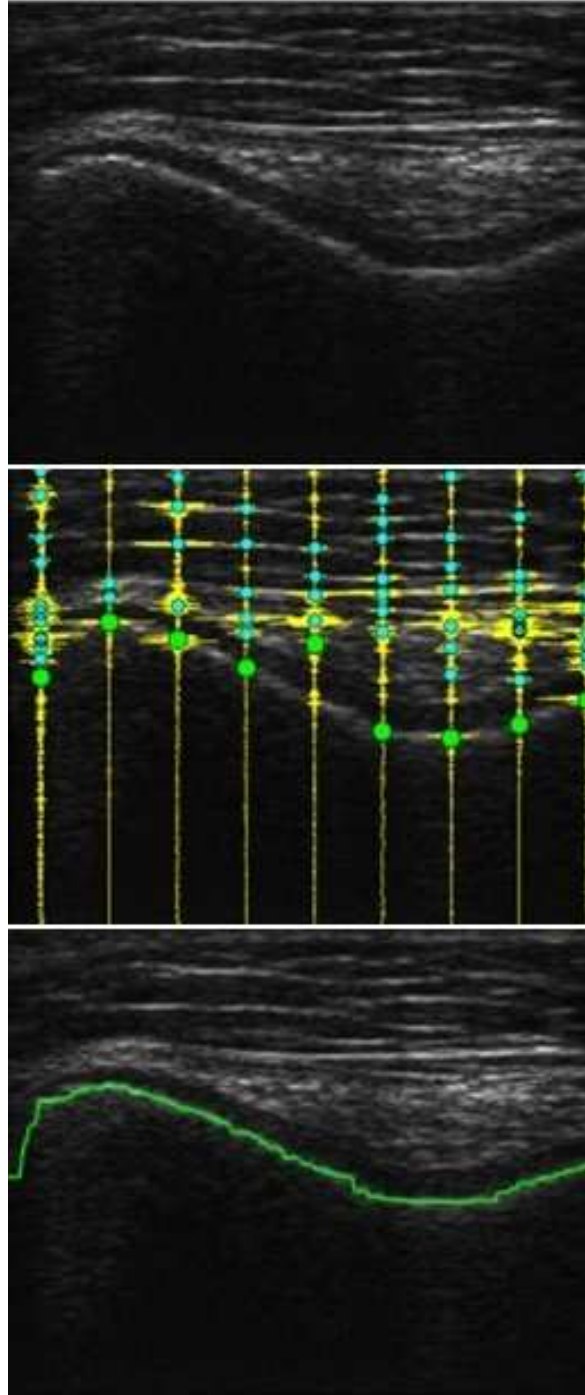


Figure 5.9 An ultrasound B-mode image of a cadaver's distal femoral groove (top), example ultrasound RF signals (middle), and the automatically extracted bone contour overlaid on the reconstructed B-mode image (bottom)

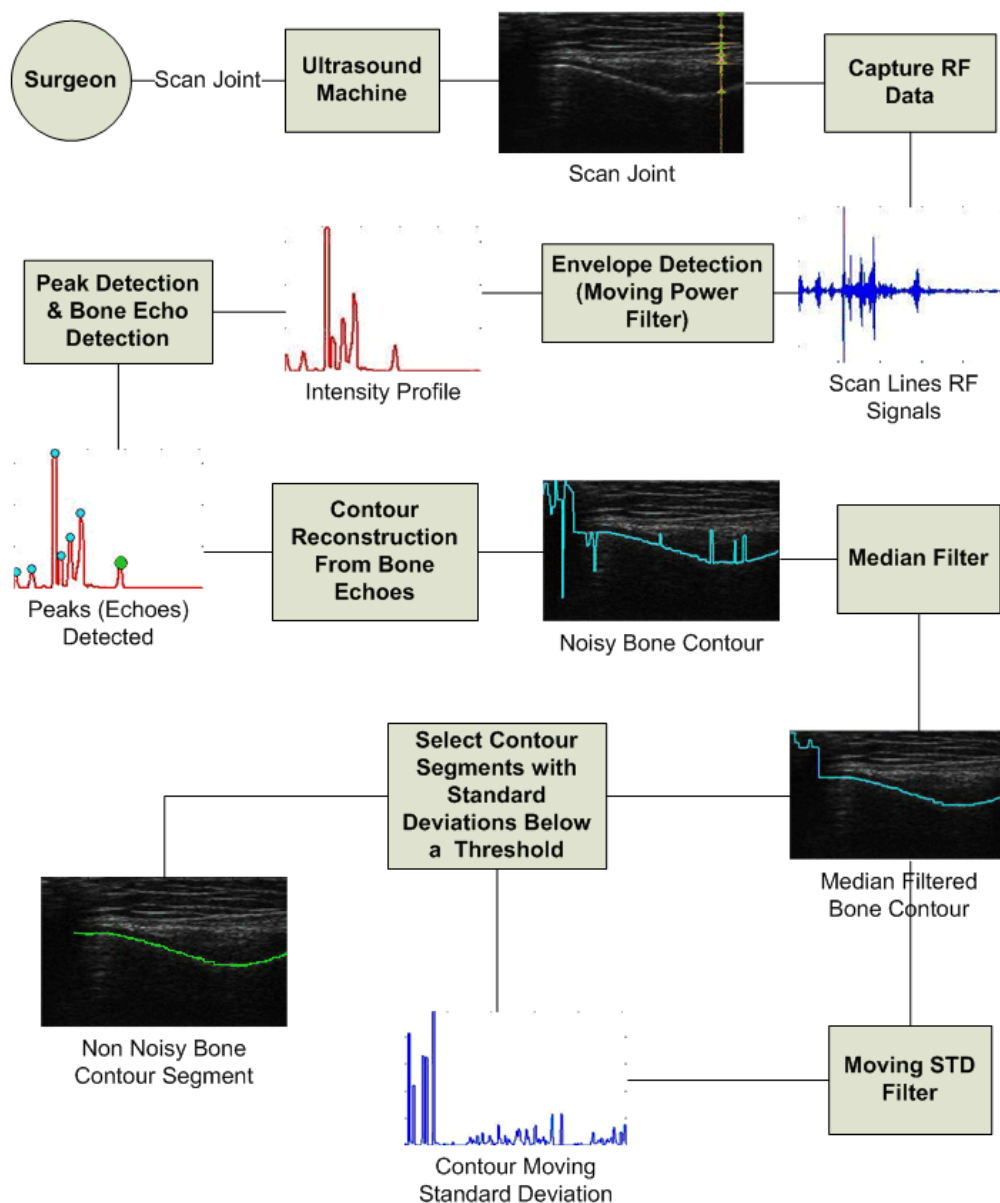


Figure 5.10 Flowchart for the process of automatic bone contour extraction from ultrasound RF data

5.4.1.1 Envelope Detection using Moving Power Filter

The target of this step is to transform the RF ultrasound signal into a smooth envelop which can then be used to extract the individual echoes existing in the RF signal.

A moving power filter, consisting of a moving kernel of length equals to the average length of an individual ultrasound echo, is applied to the RF signal to generate an envelope of the RF signal. At each step of the moving kernel, the power of the RF signal's segment at the kernel position is calculated and its value represents the value of the envelope at that point. The kernel window length of 20 was determined empirically and was used in the performed experiments. Given the discrete-time signal X of length N , the envelope Y using a moving power filter of length L is defined by:

$$Y_k = \sum_{i=k-\frac{L}{2}}^{k+\frac{L}{2}} X_i^2 \quad \forall \quad k \in \left[\frac{L}{2}, N - \frac{L}{2} - 1 \right] \quad (5.4)$$

In this and the following signal processing equations, a one-sided filter of varying length is used for the special cases of the samples before the $\frac{L}{2}$ sample (left-sided filter), and after the $N - \frac{L}{2} - 1$ sample (right-sided filter).

5.4.1.2 Bone Echoes Detection and Contour Reconstruction

The envelope produced by the moving power filter represents an intensity profile for the RF signal, and provides a clear representation for the individual echoes existing in the acquired ultrasound RF signal. This envelope will be denoted as the RF signal's intensity profile. Every echo is represented by a local peak in the RF signal's envelope. These peaks are then extracted automatically to detect the location (sample index) of the individual echoes in the RF signal. Figure 5.11. Shows four ultrasound RF signals (extracted from the ultrasound frame in Figure 5.9), their envelopes, and the extracted bone and non-bone echoes.

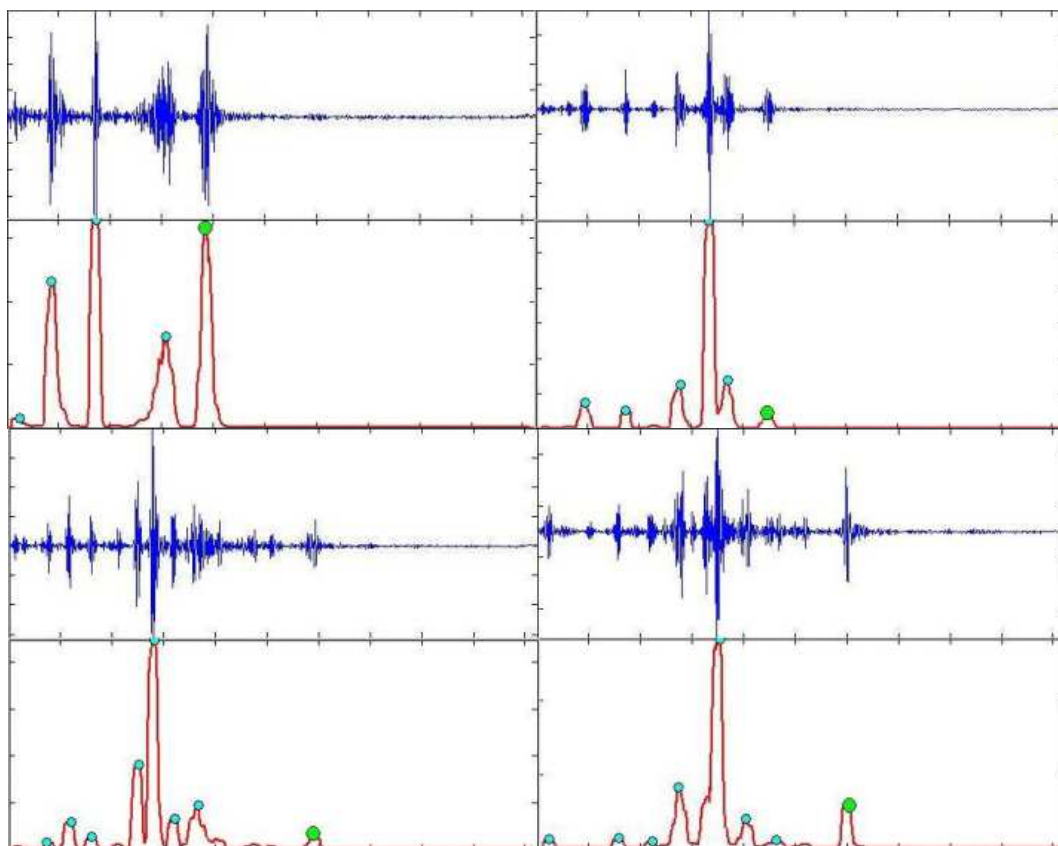


Figure 5.11 Sample RF signals (in blue) from the ultrasound frame in Figure 5.9, and their moving power envelopes (in red). The detected echoes are shown in green for the detected bone-echoes, and in cyan for the other echoes

The soft tissue-bone interface is characterized by high reflection coefficient of 43% [17], which means that 43% of the ultrasound pulse energy reaching the bone's surface is reflected back to the transducer. This high reflectivity gives the bone its characteristic hyper-echoic appearance in the ultrasound image. The bone is also characterized by a high attenuation coefficient (6.9, and 9.94 db/cm/MHz for the trabecular and cortical bone respectively). At the high frequencies (in the range of 7-14 MHz) used in musculoskeletal imaging, the attenuation of the bone becomes very high so that the ultrasound beam ends at the bone's surface [17]. This characteristic makes the

bone echo the last echo in the received ultrasound RF signal. Therefore, the selection of the bone echo from the detected echoes is accomplished by selecting the last echo having normalized intensity value (with respect to the maximum intensity value existing in the intensity profile) above a certain preset threshold. This normalized intensity value at the detected bone echo will be denoted as the bone echo normalized intensity. The threshold used will be denoted as the bone echo normalized intensity threshold, and its value was empirically determined to be 0.05 (or 5%).

The set of bone echoes extracted from the ultrasound RF signals for an acquired frame constitutes the bone's contour existing in that frame. These contours might be noisy and need filtering to remove outlier echoes (falsely detected non-bone echoes). Also some frames do not have any bone contours; therefore, the detected contours for these are noise contours and should be filtered out. Therefore after each contour is extracted from the RF data frame, it is filtered by a number by a number of contour filtering processes which are described in the following section.

5.4.1.3 Bone Contours Filtering

There are two sources of noise in the detected bone's contours; the first noise type is isolated outlier echoes, and the second is outlier contour segments (non-bone contour segments).

➤ Isolated Outlier Echoes

The first noise source is isolated outlier echoes within the bone contour segment where the actual bone echo is not selected, and a non-bone echo is selected instead. This

occurs in two cases; the first case is when the bone echo normalized intensity is smaller than the bone echo normalized intensity threshold. In this case, an echo from the soft tissue layer lying before the bone, in the ultrasound frame, is falsely detected as the bone echo.

The second case is when the normalized intensity of a non-bone echo is greater than the bone echo normalized intensity threshold and lies beyond the bone echo in the RF signal. This leads to falsely detecting noise or scattering echo that appears beyond the bone's echo. With the empirically determined and tested bone echo normalized intensity threshold of 0.05, the noise due to the second case are not frequent; they occur mostly in the case of reverberation, which doesn't occur frequently. However the bone echo detection process is not very sensitive to this threshold, a range of 0.02 to 0.08 was tested and the process was insensitive to variation of the threshold within this range. The noise echoes detected from both types of noise are removed by the different filters applied to the contours and the final reconstructed point cloud.

The filter used for removing bone echo outliers is the median filter, which is very efficient in outlier removal. The filter's kernel half size was empirically determined to be 7 (full kernel length of 15). Given A contour X of length N, the median-filtered contour Y using a median filter of length L is defined by:

$$Y_k = Median \left[X_{k-\frac{L}{2}}, X_{k+\frac{L}{2}} \right] \forall k \in \left[\frac{L}{2}, N - \frac{L}{2} - 1 \right] \quad (5.5)$$

Figure 5.12 shows sample ultrasound frames and the extracted contours from the RF data, before and after the outlier echoes removal using the median filter.

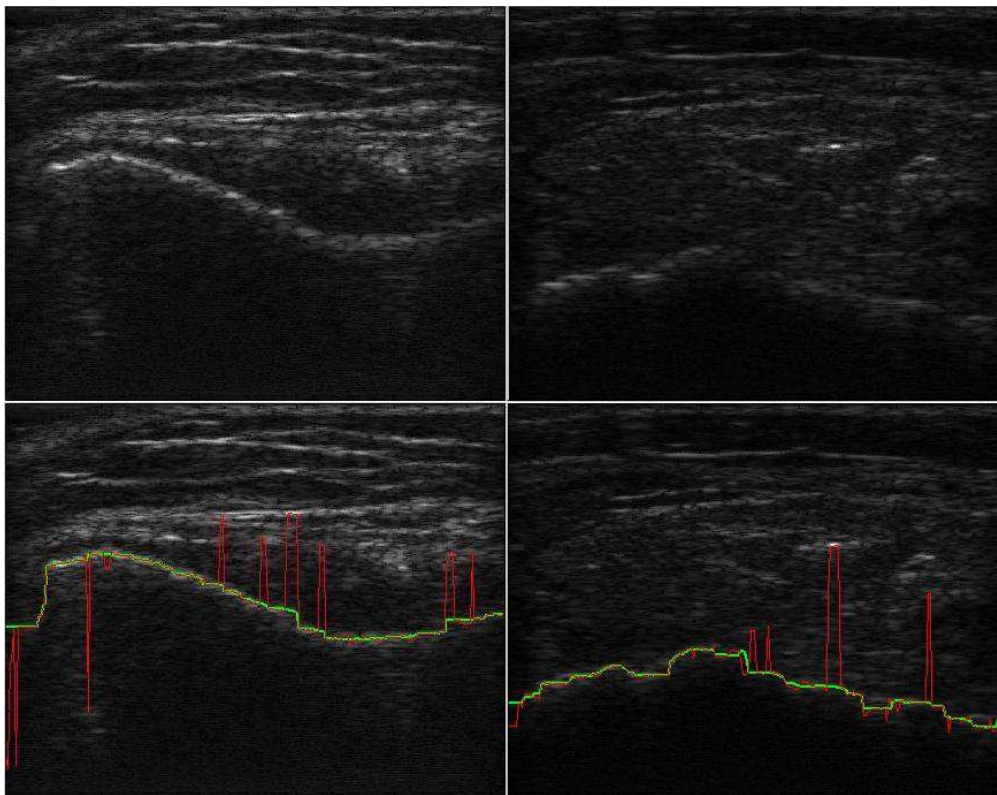


Figure 5.12 Two ultrasound B-mode images (top), and the extracted bone contour from their RF data overlaid on the B-mode images (bottom). The unfiltered contours are shown in red, and the median-filtered contours, to filter the outlier echoes, are shown in yellow

➤ Outlier Contour Segments

The second source of noise in the detected bone contour is falsely detected bone contour for a region where no bone contour exists. This noise occurs when an area containing no bones is scanned, or the probe is not oriented in a perpendicular (or near perpendicular) orientation with respect to the bone's surface, or the bone lies deeper than the preset scanning depth, or the bone lies within the preset scan depth but its echo is highly attenuated by soft tissue lying over the bone (for example the distal femur which has its echo highly attenuated by the posterior knee muscles).

These falsely detected bone contour segments are filtered out using the bone contour continuity criteria. Since the bone surface has regular shape, its 2D contour in the ultrasound frame should exhibit continuity and smoothness. Any non-bone contour segment falsely detected is always non-continuous and exhibits a high degree of irregularity. To filter out the false bone contour segments, a moving standard deviation filter is used to detect contour irregularities, and discontinuity points. The moving window length of 3 was used for the moving standard deviation filter to generate a local standard deviation curve representing the mean deviation in depth between adjacent contour points. Given the contour X of length N , the moving standard deviation Y using a moving standard deviation filter of length L is defined by:

$$Y_k = \sqrt{\frac{1}{L-1} \sum_{i=k-\frac{L}{2}}^{k+\frac{L}{2}} (X_i - \bar{X})^2} \quad \forall \quad k \in \left[\frac{L}{2}, N - \frac{L}{2} - 1 \right] \quad (5.6)$$

The output of this filter is the local standard deviation curve for the contour; it is used as a measure of the regularity and continuity of the contour at every point of the contour. This local standard deviation curve is then used to discriminate between the bone contour segments and the noise contour segments.

Contour segments constructed from echoes that are not generated by reflection from bone's surface have high local standard deviation values due to the irregularity and discontinuity of the contour segments. On the other hand the contour segments formed from echoes generated by ultrasound reflection at the bone's surface are characterized by low values of local standard deviation due to their regularity and continuity.

The input contours to the outlier contour segments filter can be one of the following three cases:

- A full length bone contour which means the entire contour is a true bone contour in the ultrasound frame.
- One or more partial bone contour segments and the rest of the contour are non-bone contour segments.
- The entire contour is noise and is not a bone contour.

The true bone contour segments are detected by the outlier contour segments filter as the contour segments that satisfy two conditions;

- It should satisfy the continuity criteria by having local standard deviation values below a certain empirically determined threshold value of 30 which corresponds to 1.08 mm standard deviation between adjacent contour points.
- It should satisfy a minimum-length criterion to avoid piecewise-smooth noise contour segments from being falsely detected as bone contour segments. The minimum contour segment length threshold was set to 30% of the transducer length.

Figure 5.13 shows sample ultrasound frames with partial bone contour segments, showing the extracted bone contours (in green), and the filtered out noise contour segments (in red). Figure 5.14 shows sample ultrasound frames with no bone contours (the detected contours are entirely noise), and thus were filtered out by the outlier contour segments filter.

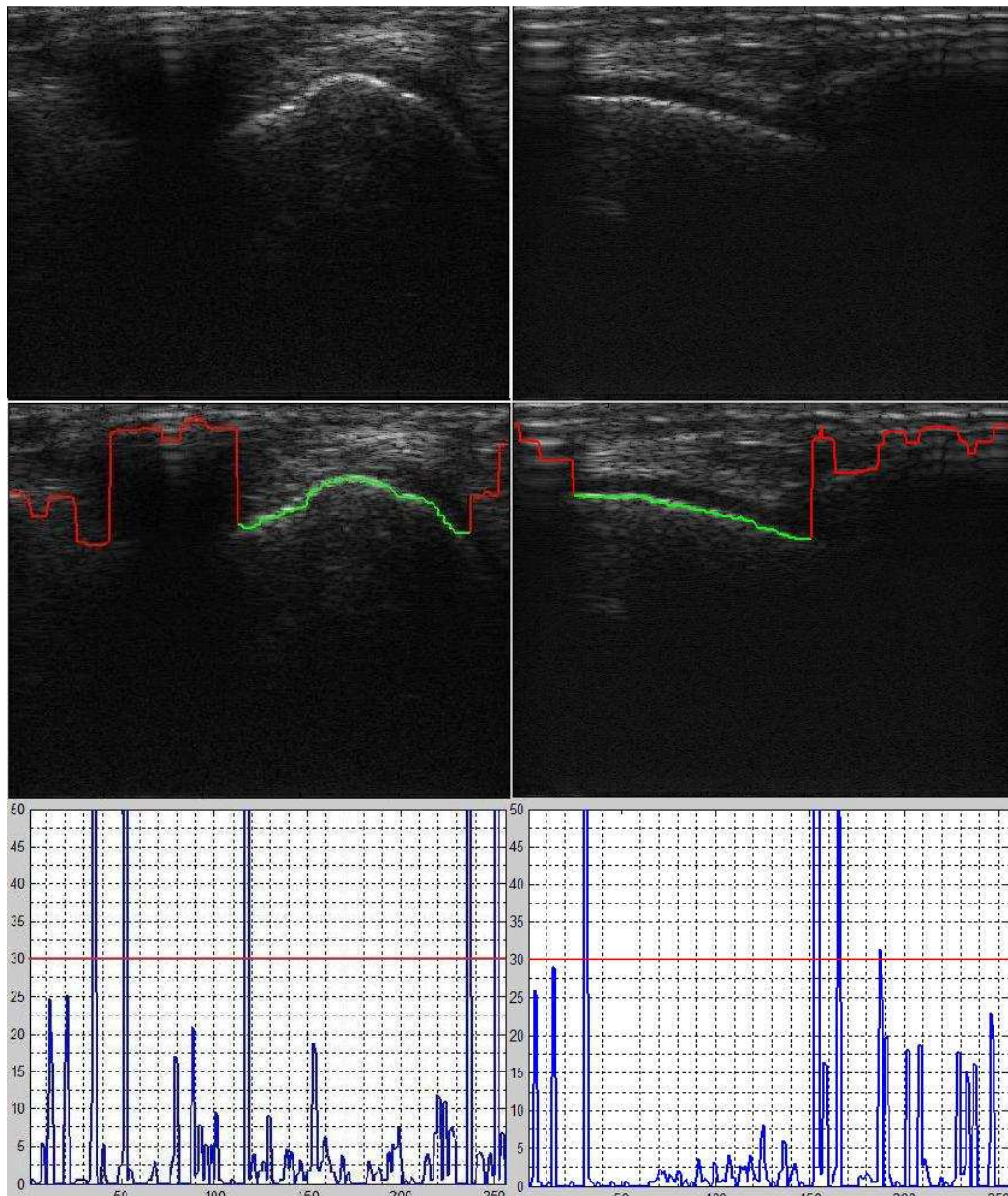


Figure 5.13 Sample ultrasound B-mode images (top) for frames with partial bone contour segments, showing the extracted contour from their RF data overlaid on the B-mode images (middle), and the contour's local standard deviation with the threshold line (bottom). The true bone contour segments are shown in green, while the filtered out noise contour segments are shown in red

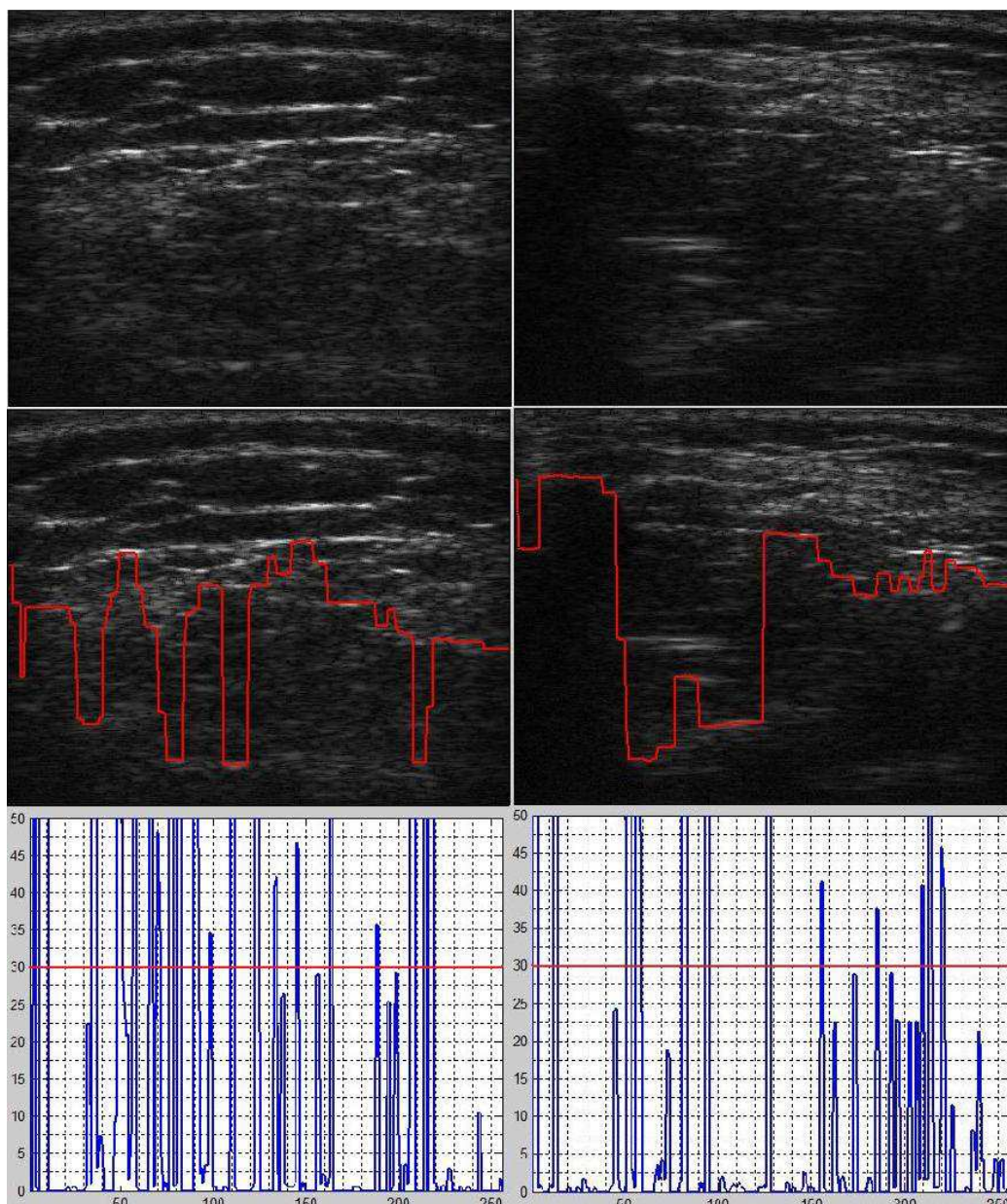


Figure 5.14 Sample ultrasound B-mode images (top) for the case of frames with no bone contour, and the extracted contour from their RF data overlaid on the B-mode images (middle), and the contour's local standard deviation with the threshold line (bottom). The entire extracted contour (red) was detected as noise since no segment in it satisfied the continuity and the minimum-length conditions

5.4.2 Bone Contours Registration

After the extraction from the ultrasound RF data, the bone contours undergoes two registration processes to reconstruct the 3D point cloud representing the scanned bone surface. The first registration step transform the contours from 2D contours, in the ultrasound probe's local coordinate frame (OP), into 3D contours in the world coordinate frame (W) of the motion tracking system as described in section 5.4.2.1. This registration step is performed on all contours extracted from the ultrasound RF data frames of a partial joint scan. The output of this registration is a partial point cloud for the scanned partial bone's surface (scanned at a certain flexion angle; full extension or deep knee bend, or 90° flexion). The second registration process targets integrating the bone's partial point clouds into one point cloud representing the whole scanned bone's surface. Another registration process is performed between the B-mode image and the bone contour extracted from the RF data. This registration step is performed for visualizing the contour overlaid on the B-mode image for real-time visual validation and performance feedback of the contour detection process while the operator is performing the scans. Figure 5.15 shows a flowchart for the contours point cloud, and 3D model reconstruction from the extracted bone contours.

5.4.2.1 Bone Contours 3D Registration

The extracted contours from the RF data are represented as signal's samples indices. Each contour consists of the bone echoes indices in the individual ultrasound RF signals existing in the ultrasound frame containing the contour. To transform this contour

into a 3D contour, every detected bone echo is this contour is transformed into a 3D point as follows:

$$d_{echo} = n_{echo} T_s C_{us} \quad (5.7)$$

$$l_{echo} = L_{trans} \frac{n_{line}}{N_{lines}} \quad (5.8)$$

$$P_{echo}^{OP} = P_o^{OP} + d_{echo} \hat{u}_y^{OP} + l_{echo} \hat{u}_x^{OP} \quad (5.9)$$

$$P_{echo}^W = H_{OP}^W P_{echo}^{OP} \quad (5.10)$$

Where d_{echo} is the depth of the detected bone echo in, n_{echo} is the signal's sample index of the echo. T_s is the RF signal's sampling period, C_{us} is the average speed of ultrasound in soft tissue which is equal to 1540 m/s. l_{echo} is the distance from the origin of the transducer array to the scan line containing the bone echo. n_{line} is the index of the scan line containing the bone echo in the ultrasound frame, and N_{lines} is the total number of scan lines in the ultrasound RF data frame. P_{echo}^{OP} is the detected 3D point on the bone's surface represented relative to the optical probe's coordinate frame. P_o^{OP} , L_{trans} , \hat{u}_x^{OP} , and \hat{u}_y^{OP} are probe's calibration parameters. P_{echo}^W is the detected bone's surface point relative to the fixed world coordinate frame of the optical camera, and H_{OP}^W is the homogeneous transformation between the tracking probe's local coordinate frame (OP) and the world coordinate frame of the tracking system (W). H_{OP}^W is acquired dynamically in real-time from the tracking system, and it contains the position and

orientation of the tracking probe attached to the ultrasound probe during the acquisition of the ultrasound frame.

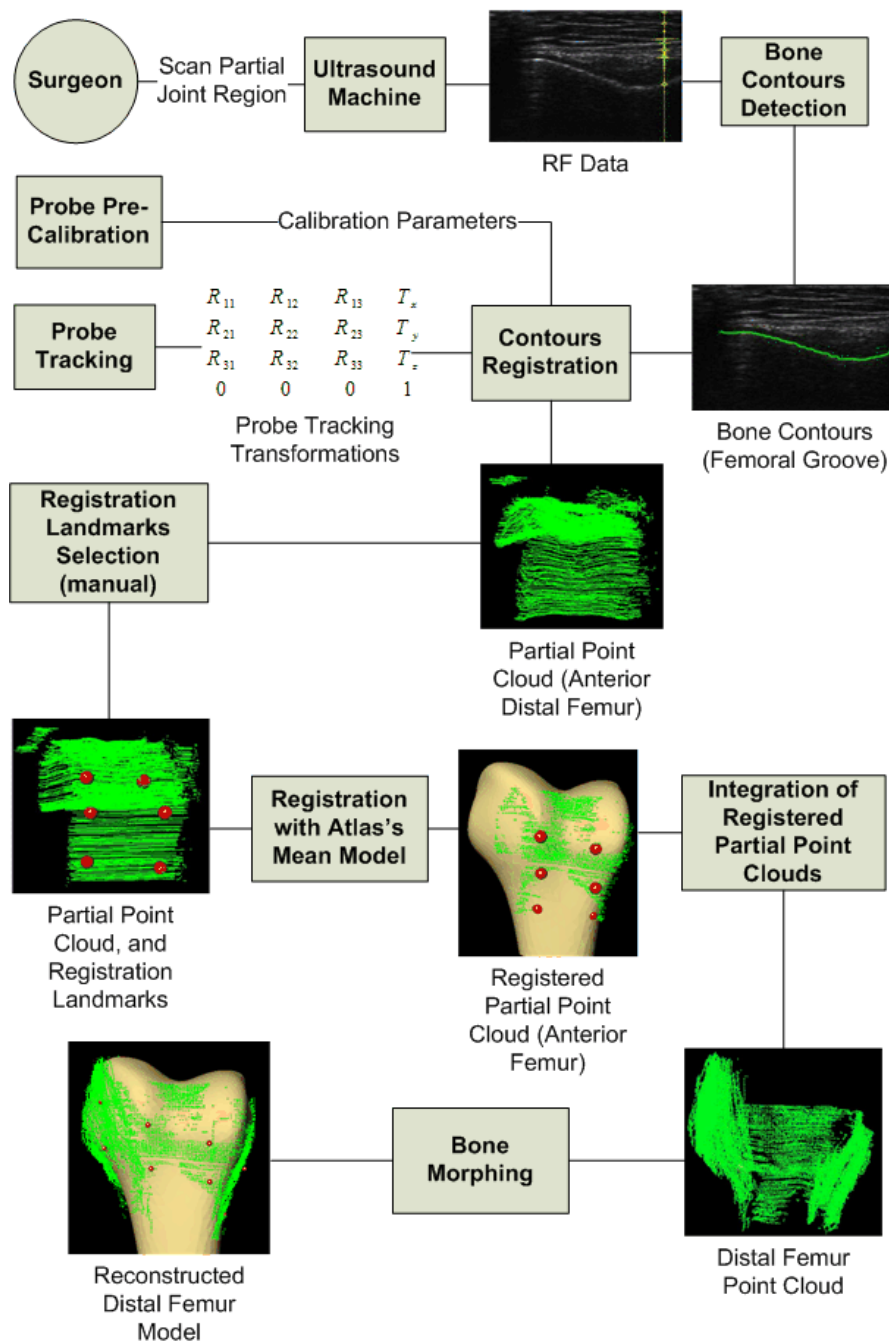


Figure 5.15 Flowchart for the contours registration and bone model reconstruction process.

5.4.2.2 Partial Point Clouds Integration

After the partial bone surface 2D contours are registers in the 3D world coordinate frame, they form a 3D point cloud representing the scanned partial bone surface. This partial point cloud contains some noise points which were not filtered out by the contour filtering processes. Each partial point cloud is then initially aligned to the atlas' mean model using at least three non-collinear pre-specified landmarks which are picked from the partial point cloud by the system's operator. The landmarks do not need to be picked with high accuracy; they merely define the initial alignment between the point cloud and the mean model to avoid any singularity in the registration. Following this initial alignment, an iterative closest point (ICP) registration is performed to accurately align the partial point cloud to the mean model. The noisy points are then removed based on a simple thresholding for the distance between the points of the partial point cloud and their closest vertices in the mean model. The average distance was used as the threshold. The same process is performed for every reconstructed partial point cloud for the scanned bone's surface. Then the aligned partial point cloud are integrated by simply combining them together into one point cloud that represents the whole scanned bone's surface. Figure 5.16 shows an example for the alignment and integration of the partial point clouds reconstructed for one of the cadaver's knee used in the system experiments.

5.4.2.3 Bone Contour to B-Mode Image Registration

In order to visually verify the validity of the extracted bone contours while the joint being scanned, the extracted contours are overlaid on the B-mode images acquired

from the ultrasound machine, and rendered for the operator. The bone contour, represented as samples RF signal's indices, is registered with the ultrasound image as follows:

$$P_{\text{echo}}^I = \begin{bmatrix} l_{\text{echo}} I_x \\ d_{\text{echo}} I_y \end{bmatrix} \quad (5.11)$$

Where I_x , and I_y denotes the image resolution in pixel/cm for the x, and y axes respectively of the B-mode image. P_{echo}^I denotes the 2D coordinates of the contour point relative to the B-mode image.

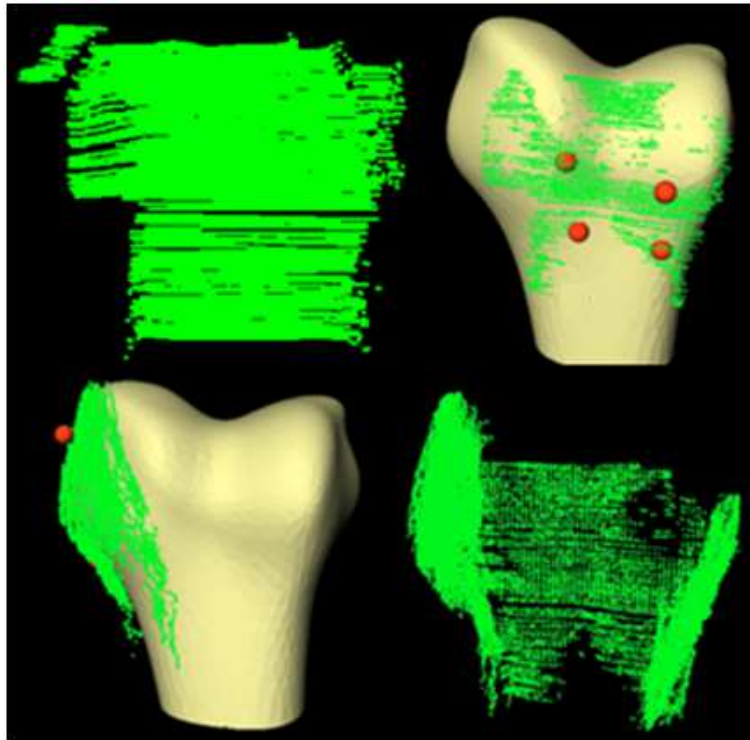


Figure 5.16 An anterior distal femur's partial point cloud (top left), and the partial point cloud aligned to the atlas' mean model (top right). A medial partial point cloud is shown aligned to the mean model (bottom left), and the integrated point cloud after combining the anterior, medial and lateral partial point clouds for the distal femur (bottom right)

Chapter 6 Clinical Study

The results obtained from the cadavers' experiments of the developed system motivated the move to a clinical study for further assessment of the system, and method accuracy and efficiency in 3D model reconstruction of the knee bones. The developed system had to be upgraded to use a newer model of the ultrasound machine, and an electromagnetic motion tracking system which gives more flexibility, efficiency and ease of use than the optical motion tracking system used in the cadaver experiments while maintaining the required accuracy. The following section describes the different system components, the patient scanning setup, and scanning protocol.

6.1 Imaging System Setup

The imaging system developed for the clinical study is very similar to the imaging system described in section 4.1 which was used for the cadaveric experiments. The clinical study system consisted of an ultrasound machine, motion tracking system to track the ultrasound probe's motion. The ultrasound machine, and the motion tracking system were driven by the imaging software developed in this work for ultrasound machine control, ultrasound data acquisition and processing in real time for the reconstruction of the 3D model of the scanned bones. In the following sections, the different components of the clinical system will be described in details.

6.1.1 Ultrasound Machine, and Transducer

The ultrasound machine used for the clinical study was the SonixTOUCH (Ultrasonix Inc, British Colombia, Canada) which is the newer model of the SonixRP

ultrasound machine used in the imaging system described in section 4.1. It provides the same capabilities of the SonixRP machine, from controlling the ultrasound imaging through application programming interface library (API), and access to the ultrasound data (B-mode images, and RF data) through the API library named Porta. Figure 6.1 shows the SonixTOUCH ultrasound machine used in the clinical study.



Figure 6.1 The SonixTOUCH ultrasound machine (Ultrasonix Inc, British Columbia, Canada) used in the clinical study, showing the magnet of the driveBay electromagnetic tracking system (Ascension Inc) fixed to an articulating arm

6.1.2 Motion Tracking System

The motion tracking system used (to track the ultrasound probe's motion during scanning) in the clinical study system was the DriveBay electromagnetic (EM) tracking system (Ascension Inc, Burlington, VT). The DriveBay EM tracking device is integrated in the SonixTOUCH ultrasound machine (connected to its motherboard). The DriveBay electromagnetic tracking system consists of the following components:

1. **Magnet:** is an electric magnet which consists of a coil built on a ferromagnetic core to magnify the magnetic field created by the alternating current in the coil. The magnet provides a magnetic field in the tracking volume in which the tracking sensors (probes) move. The tracking sensors intercept the magnetic field and generate electric signals which are used to triangulate the position and orientation of the motion tracking probe. The magnet defines the fixed world coordinate frame of reference (W) of the tracking system as shown in Figure 6.4.
2. **Control Unit:** is the main component of the tracking system, and it contains the electronics of the tracking system that controls the magnet activation, collects the signal from the tracking sensor, triangulate the position and orientation of the tracking sensors, then send the tracking data to the computer. Figure 6.2 shows the DriveBay control unit and the magnet.
3. **Motion Tracking Sensor (Probe):** is consisting of coils which are used to determine the position and orientation of the sensor using the theoretical knowledge of the magnet's magnetic field. There are several kinds of sensors, depending of their sizes. There are sensors with 90 mm, 130 mm, 180 mm, and 800 mm in size.

Figure 6.3 shows the 800 mm, 180 mm, and 130 mm sensors. Each sensor has its own virtually-attached local coordinate frame of reference as shown in Figure 6.4. Figure 6.5 shows a graph for the position detection noise versus range (distance from the magnet's center) for the four different tracking probes. The tracking noise increase as the size of the tracking probe decreases due to the decreased signal to noise ratio (SNR). The tracking noise increases with the increase of the distance between the tracking sensor (probe) and the magnet. Figure 6.6 shows the tracking volume for the mid-range magnet used in the clinical study system.



Figure 6.2 The DriveBay (Ascension Inc, Burlington, VT) electromagnetic tracking system used in the clinical study, showing the control unit (left), and the magnet (right)



Figure 6.3 The 800 mm (left), 180 mm (middle), and 130 mm (right) electromagnetic motion tracking sensors (Ascension Inc, Burlington, VT)

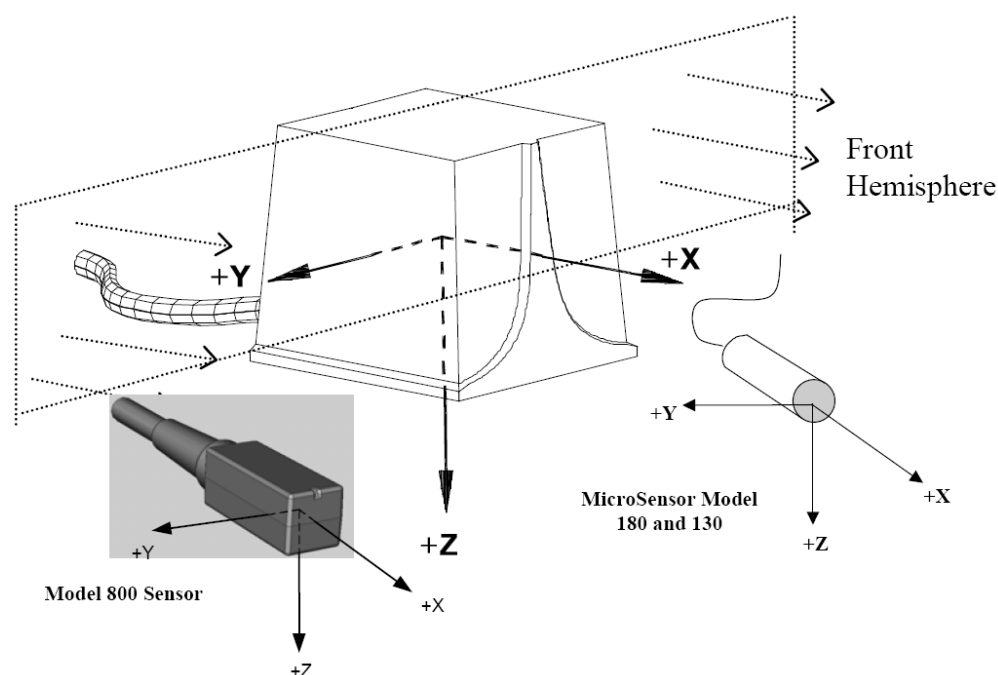


Figure 6.4 Schematics for the magnet, a model for the 800 mm sensor, and micro sensors (the 130 mm, and 180 mm sensors), showing their coordinate frames of reference (Ascension Inc, Burlington, VT)

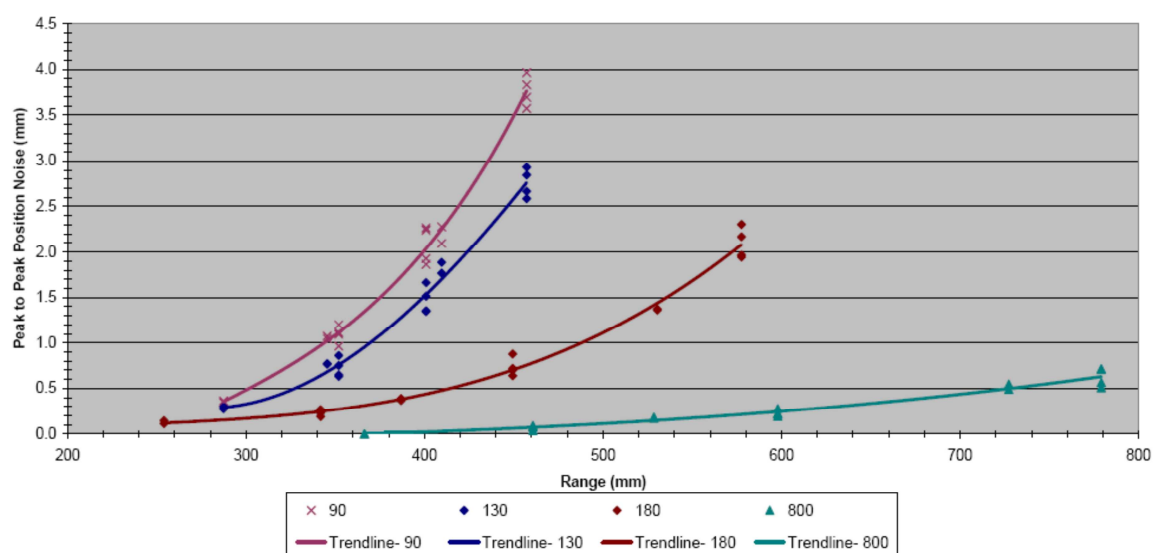


Figure 6.5 Position noise versus range (distance to the magnet's center) comparison for the 90 mm, 130 mm, 180 mm and 800 mm Sensors (Ascension Inc, Burlington, VT)

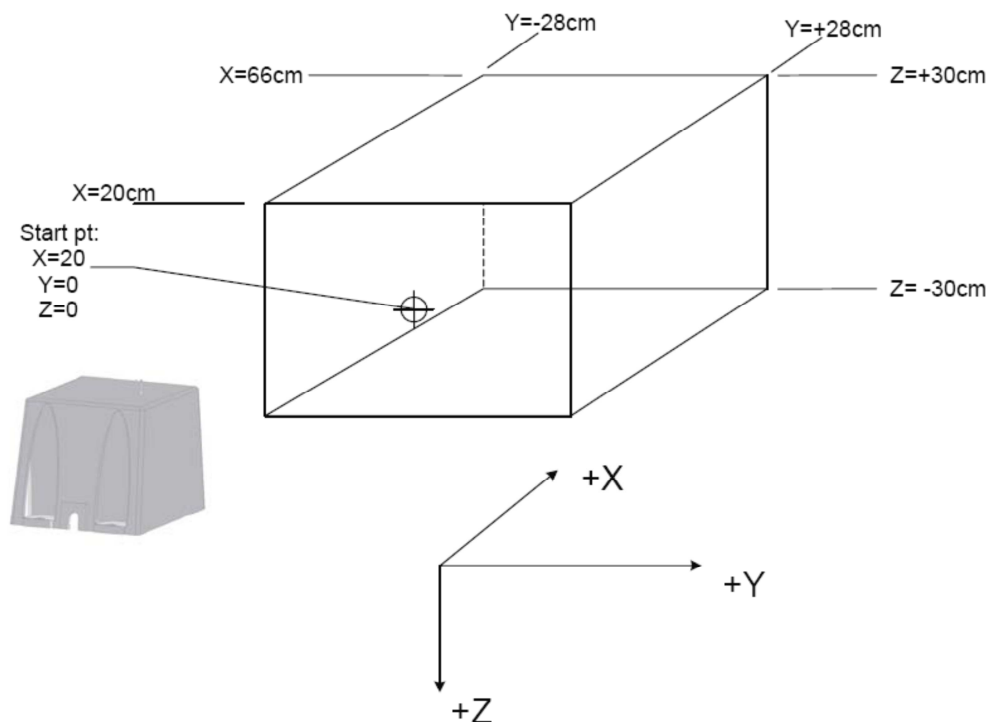


Figure 6.6 Tracking volume for the mid range magnet used in the clinical study system
(Ascension Inc, Burlington, VT)

6.1.3 Imaging Software

The imaging software developed for the SonixRP ultrasound machine-based system was modified to be compatible with the SonixTOUCH ultrasound machine, and to replace the Polaris Spectra optical motion tracking system with the DriveBay electromagnetic motion tracking system. The clinical study imaging software had extra controls than its previous version (used in the cadaveric experiments). It had ultrasound controls for the depth, gain, and time gain compensation (TGC). It also had controls for the automatic bone contour extraction process parameters described in section 5.4.1. These controls were used to empirically determine the optimal values that were used

throughout the clinical study which were identical to the values used for the cadaveric experiments and are shown in Figure 6.7.

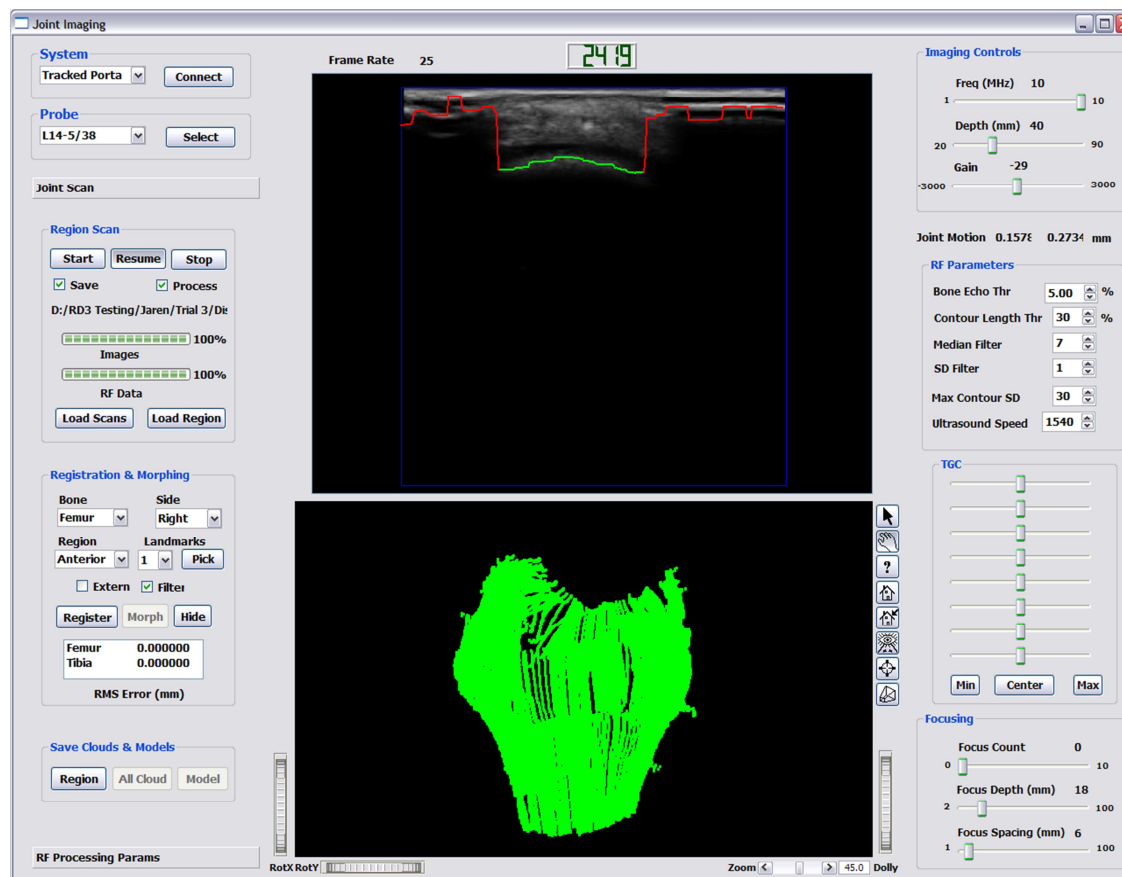


Figure 6.7 Snapshot of the developed imaging software used in the clinical study, showing a reconstructed 3D point cloud for a distal femur, and one of the automatically extracted contours with the bone contour segment (green), and the rejected non-bone contour segments (red).

6.2 Tracked Linear Ultrasound Probe Calibration

The SonixTOUCH ultrasound machine has ultrasound probes which have electromagnetic tracking sensors (model 180) built inside the ultrasound probe. The 3D calibration of the probe was performed by the ultrasound machine manufacturer (Ultrasonix Inc, British Columbia, Canada), and the calibration parameters provided by

the manufacturer were the rotation and translation matrices between the ultrasound image coordinate frame, and the electromagnetic tracking sensor's local coordinate frame. These calibration matrices were used to calculate the developed imaging system-specific calibration parameters described in section 4.2, using unit vectors in the x (to calculate the calibration parameter \hat{u}_x^{OP}), and y (to calculate the calibration parameter \hat{u}_y^{OP}) axis of the ultrasound image reference frame, and the top center point of the ultrasound image (which represents the center point of the ultrasound transducer's face, and was used to calculate the calibration parameter P_o^{OP}).

6.3 Patient's Knee Scanning Setup

The knee joint consists of the femur, tibia, and patella bones articulating at different articular surfaces as described in section 5.3. In order to acquire scans covering the whole surface (or most of it) of the distal femur and proximal tibia, the knee scanning is divided into separate scanning sessions. In each scanning session, the knee is held fixed and a specific region of the distal femur, or proximal tibia bones is scanned. These regions scans are then used to create partial point clouds which are then mutually registered to produce a point cloud representing the whole scanned bone's surface (including all scanned regions).

The patient's knee is scanned in two positions:

1. **Knee Bend:** this position is used to scan the anterior, medial, and lateral regions of the distal femur and proximal tibia. A deep knee bend (130°) is used if the patient can perform the deep knee bend; otherwise a 90° knee bend position is employed. The deep knee bend is preferred because at this position, a larger portion of the

anterior groove of the femur is accessible (un-occluded by other bones) to the ultrasound beam for imaging.

2. **Full Extension:** this position is used to scan the posterior regions of the distal femur, and proximal tibia which are only accessible for scanning at the full extension position of the knee.

A key requirement for the patient scanning setup is to have the patient's knee fixed throughout a region scanning session. To meet this requirement, three leg holders were built to hold the patient's knee fixed during the region scanning sessions. Two of the leg holders are used for scanning of the anterior, medial and lateral regions of the distal femur, and proximal tibia in deep knee bend, and 90° knee bend positions as shown in Figure 6.8. The 90° knee bend leg holder is used when the patient can't have his/her knee at deep knee bend. The third leg holder is used for scanning the posterior regions of the distal femur, and proximal tibia at the full extension position as shown in Figure 6.9



Figure 6.8 Deep, and 90° knee bend leg holders with a volunteer's leg attached to it in the position used for scanning of the anterior, medial, and lateral regions of the distal femur, and proximal tibia bones.



Figure 6.9 Full extension leg holder with a volunteer's leg attached to it in the position for the scanning of the posterior region of distal femur, and proximal tibia bones

6.4 Patient's Knee Scanning Protocol

The patient's knee scan is divided into four scanning regions. Each region is scanned in a scanning session which lasts for approximately 2-3 minutes during which, the knee is fixed to the leg holder to minimize the leg motion artifacts (which would create noise points in the reconstructed point cloud, and decrease the SNR of the point cloud). During the scanning of each region, the developed imaging system creates in real-time the 3D point cloud of the bone's region being scanned. The reconstructed regions point clouds are then mutually registered to generate the whole scanned bone's (distal femur, or proximal tibia) point cloud as described in section 5.4.2.2.

The four scanning regions of the knee are:

1. **Anterior Distal Femur:** The anterior femur region scan is performed while the patient's knee is in deep knee bend or 90 ° knee bend (if the patient can't perform

deep knee bend). The anterior distal femur region scan consists of six sub-regions scans which are:

- i. ***The lateral area of the distal femur (lateral epicondyle):*** which is scanned with the ultrasound transducer in an axial (long-axis) position as shown in Figure 6.10(a)
 - ii. ***The medial area of the distal femur (medial epicondyle):*** which is scanned with the ultrasound transducer in an axial position as shown in Figure 6.10(a)
 - iii. ***The anterior shaft area of the distal femur:*** which is scanned with the ultrasound transducer in an axial position as shown in Figure 6.10(c)
 - iv. ***The inferior area of the medial femoral condyle:*** which is scanned with the ultrasound transducer in an axial position as shown in Figure 6.10(d)
 - v. ***The inferior area of the lateral femoral condyle:*** which is scanned with the ultrasound transducer in an axial position as shown in Figure 6.10(e)
 - vi. ***The trochlear groove of femur:*** which is scanned with the ultrasound transducer in an transverse position (short axis) as shown in Figure 6.10(f)
- 2. Posterior Distal Femur:** The posterior distal femur region scan is performed while the patient's knee in full extension. The posterior distal femur region scan consists of three sub-regions scans which are:
- i. ***Posterior area of the lateral femoral condyle:*** which is scanned with the ultrasound transducer in an axial position as shown in Figure 6.11(a)
 - ii. ***Posterior area of the medial femoral condyle:*** which is scanned with the ultrasound transducer in an axial position as shown in Figure 6.11(b)

- iii. ***Posterior area of the distal femoral shaft:*** which is scanned with the ultrasound transducer in an axial position as shown in Figure 6.11(c)
- 3. **Anterior Proximal Tibia:** The anterior proximal tibia region scan is also performed while the patient's knee is in deep knee bend or 90° knee bend (if the patient can't perform deep knee bend). The anterior proximal tibia region scan consists of two sub-regions scans which are:
 - i. ***Lateral area of the anterior proximal tibia:*** which is scanned with the ultrasound transducer in an axial position as shown in Figure 6.12(a)
 - ii. ***Medial area of the anterior proximal tibia:*** which is scanned with the ultrasound transducer in an axial position as shown in Figure 6.12(b)
- 4. **Posterior Proximal Tibia:** The posterior proximal tibia region scan is performed while the patient's knee in full extension. The posterior proximal tibia region scan consists of four sub-regions scans which are:
 - i. ***Posterior areas of the tibial condyles, and inter-condyler area::*** which are scanned with the ultrasound transducer in an transverse position as shown in Figure 6.13(a)
 - ii. ***Posterior area of the proximal tibial shaft:*** which is scanned with the ultrasound transducer in an axial position as shown in Figure 6.13 (b)



(a)



(b)



(c)



(d)



(e)



(f)

Figure 6.10 Scanning protocol for the anterior distal femur region scan, showing the axial scanning of the lateral (a), medial (b), and anterior (c) areas of the distal femur as well as the medial (d), and lateral (e) condyles. The trochlear groove is scanned transversally (f).

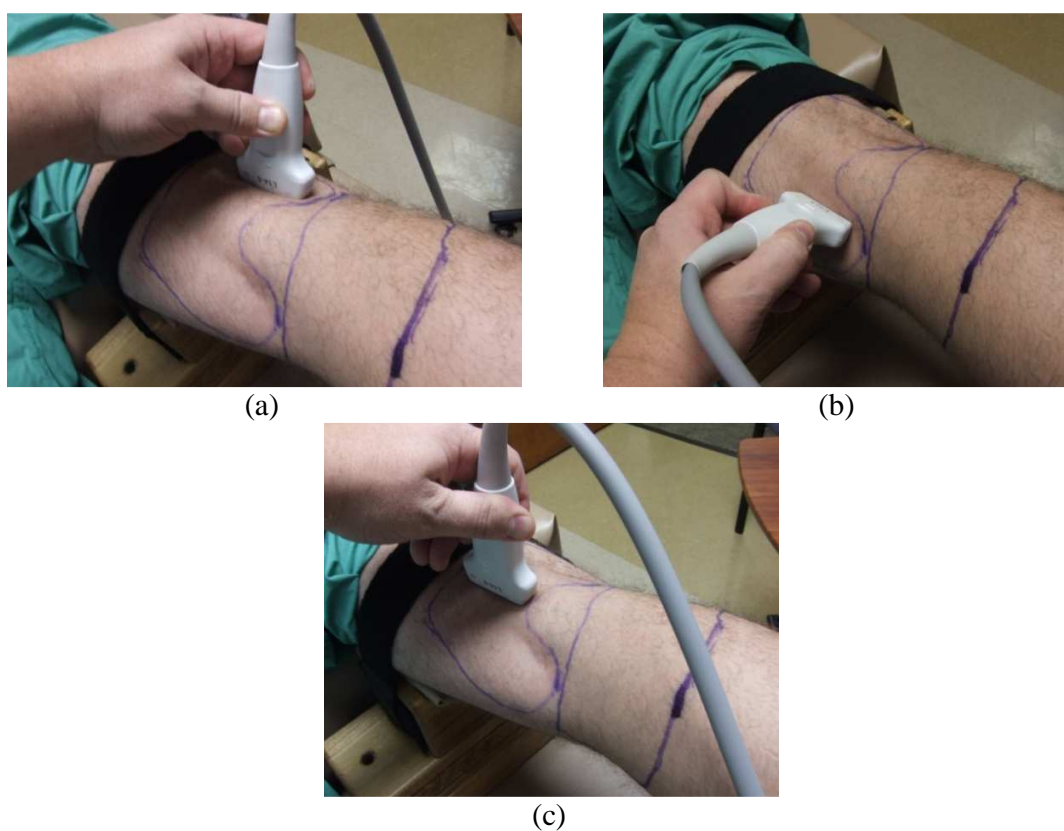


Figure 6.11 Scanning protocol for the posterior distal femur region scan, showing the axial scanning of the lateral condyle (a), medial condyle (b), and posterior distal femoral shaft (c) areas of the distal femur



Figure 6.12 Scanning protocol for the anterior proximal tibia region scan, showing the axial scanning of the lateral (a), and medial areas of the proximal tibia (b)

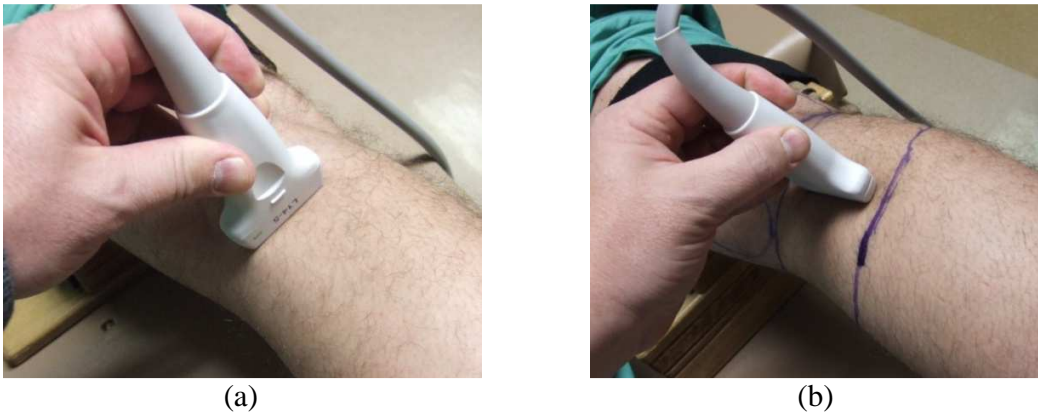


Figure 6.13 Scanning protocol for the posterior proximal tibia region scan, showing the transverse scanning of the posterior areas of the tibial condyles and intercondyler area (a), and the axial scanning of the posterior area of the proximal tibia shaft (b).

Chapter 7 Results

7.1 Single-Element Transducer System‘ Phantoms Experiments Results

The developed imaging system for 3D bone model reconstruction using single element ultrasound transducer was tested on 24 bone phantoms (six female distal femurs, six male distal femurs, six female proximal tibias, and six male proximal tibias). The phantoms were made of plastic bone models, printed from a subset of the atlas models using a fused deposition modeling (FDM) 3D prototyping machine (StratSys Inc, Eden Prairie, MN), The plastic bone models were immersed in a water tank as shown in Figure 4.5 to provide a medium for ultrasound transmission. The water temperature was monitored during the phantoms scanning to change the ultrasound speed setting (which is a function in the water temperature as described in section 4.3.1) in the imaging software according to the water temperature. In the following sections, the point cloud reconstruction results will be presented, then followed by the results of the 3D model reconstruction using the reconstructed point clouds.

7.1.1 Point Cloud Reconstruction

In order to study the accuracy of the reconstructed point clouds in representing the scanned bones surfaces, the point cloud for every phantom was reduced (using octree) to a 1 mm average inter-points cloud density, then registered to its reference 3D bone model (which was used in 3D printing of the phantom’s plastic model) using the ICP method. The ICP registration was performed after an initial landmark-based registration performed using manually-picked three landmarks on the point cloud. The initial registration is necessary to avoid any singularity in the point cloud to 3D model

registration which would cause the entrapment of the registration process in local minima in the registration RMS error function. The distance error between every point in the point cloud and its closest surface point on the reference 3D model was then calculated, and a histogram was generated for these distance errors to examine the accuracy of the reconstructed point cloud. The point clouds used to generate the histograms were the raw acquired point clouds without any filtering performed on them. These raw point clouds were then filtered to remove the noisy points from the point clouds. The filtering was performed by removing a percentage of the point cloud having the highest distance error between the cloud points and the reference model. The percentage used was chosen to be 25%. After each point cloud was filtered, it was registered again to the reference model using the ICP method to perform fine tuning for the registration that might have been affected by the noisy points. The RMS error between the filtered point cloud and the reference model was then calculated.

The reconstructed point clouds and the histograms of the distance error between the reconstructed point clouds and their corresponding reference 3D models are presented in the appendix section 9.3.1. Table 7.1 shows the mean number of points in the acquired point clouds, and the mean RMS error between the 75th percentile filtered point clouds and their reference models for the scanned bone phantoms datasets

Table 7.1 Mean number of points in the acquired point clouds, and the mean RMS error between the 75th percentile filtered point clouds and their reference models.

	Mean Number of Points	Mean RMS Error (mm)
Female Distal Femur	6596	0.83
Male Distal Femur	6523	0.77
Female Proximal Tibia	5210	0.87
Male Proximal Tibia	5980	0.85

7.1.2 3D Bone Model Reconstruction (Bone Morphing)

The reconstructed raw (unfiltered) point clouds were then used to reconstruct 3D models of the scanned bones. The three morphing methods described in section 3.3 were used to reconstruct the 3D models of the scanned bones. Before the bone morphing was performed, the raw point clouds were reduced in density using octree to different point cloud densities, and then the reduced point clouds were registered with their gender-specific jack-knife atlases mean models. The mean distance errors between each point cloud and its corresponding jack-knife atlas' mean model was calculated, and used to filter the point cloud by removing the points with distance, between it and its closest surface point on the mean model, greater than a certain threshold. The threshold was set equal to the average mean distance error between the point cloud and its corresponding jack-knife atlas' mean model. The point cloud reduction, registration, and filtering processes were performed using different point cloud densities (1 to 19 mm, with 2 mm increment) to study the effect of the point cloud density on the 3D model reconstruction

accuracy with the point cloud registration, and filtering factors included. The RMS errors between the reconstructed 3D models and the reference models were calculated. The following sections present the results using the three morphing methods (Direction Set, linear least squares, and the hybrid method).

7.1.2.1 Direction Set Morphing

The Direction Set morphing method was applied to the reconstructed point clouds (with different point cloud densities). The number of principal components used was chosen to be 32, which yield the highest reconstruction accuracy with reasonable processing time. This was concluded from the Direction Set morphing method performance analysis in described in section 3.3.1. The first 32 principal components carried 94.97%, 94.58%, 93.95%, and 92.5% for the female distal femur, male distal femur, female proximal tibia, and male proximal tibia atlases.

Appendix section 9.3.2.1 presents the RMS error for the 3D model reconstruction (for the reconstructed phantoms' point clouds with different point cloud densities) using the Direction Set method using the first 32 principal components. Examining the RMS error graphs, it can be concluded that the point cloud filtering, and registration as well as the 3D model reconstruction are affected by the point cloud density. However, this effect is not large, as the change in the mean RMS error is approximately 0.2-0.4 mm between the 1 mm, and the 19 mm point cloud densities for the four bones datasets. The reconstruction error graphs show that the 1 mm point clouds (the highest density point cloud) exhibits the lowest mean RMS error for 3D model reconstruction using the Direction Set optimization method.

7.1.2.2 Linear Least Squares Morphing

The linear least squares morphing method was applied to the reconstructed point clouds (with different point cloud densities). The number of principal components used was chosen to be 64 which carried 98.22%, 97.38%, 97.61%, and 95.77% for the female distal femur, male distal femur, female proximal tibia, and male proximal tibia atlases respectively. The number of principal components was chosen to be 64 (and not higher) because this represents approximately 97% of the morphology variations in each bone's atlas. The remaining 3% of the morphology variations are responsible for the local features in the bones morphology, and therefore these modes of variations are very sensitive to noise in the point cloud, and can lead to an increase in the 3D model reconstruction (bone morphing) error.

Appendix section 9.3.2.2 presents the RMS errors for the 3D model reconstruction (for the reconstructed phantoms point clouds with different point cloud densities) using the linear least squares morphing method using the first 64 principal components. Examining the RMS error graphs, it can be shown that the effect of the point cloud density on the model reconstruction is higher using the linear least squares method than the Direction Set method. This can lead to the conclusion that the linear least squares method is more sensitive to the point cloud density than the Direction Set method. However the RMS error does not increase monotonically with decreasing the point cloud density.

7.1.2.3 Hybrid Morphing

The hybrid morphing method was applied to the reconstructed point clouds (with different point cloud densities). The reconstructed models using the Direction Set morphing method using the first 32 principal components were used as the initial models for the linear least squares morphing method. The number of principal components used, for the linear least squares morphing stage of the hybrid morphing was set to 64 principal components. Appendix section 9.3.2.3 presents the RMS errors for the 3D model reconstruction (for the reconstructed phantoms point clouds with different point cloud densities) using the hybrid morphing method (using the first 32 principal components for the Direction Set morphing stage, and the first 64 principal components for the linear least squares stage) for the female distal femur, male distal femur, female proximal tibia, and male proximal tibia phantoms. The mean RMS error was the lowest for the 1 mm point cloud density.

Table 7.2 shows the mean RMS and average distance error for the 3D model reconstruction using the three morphing methods for the scanned bone phantoms. The three morphing methods showed very similar performance and reconstruction accuracy.

A mean distance error color map was generated for the RMS distance error between the reconstructed 3D models (using the Direction Set, and linear least squares methods) and their corresponding reference models for each of the bones datasets. Figure 7.1, and Figure 7.2 show the mean RMS error color maps for the distal femur, and proximal tibia models respectively.

Table 7.2 Mean reconstruction RMS errors (in mm) for the three morphing methods using the point clouds with 1 mm density.

	Direction Set		Linear Least		Hybrid	
	Method		Squares		Method	
	Avg	RMS	Avg	RMS	Avg	RMS
Female Distal Femur	0.8	1.02	0.81	1.03	0.82	1.04
Male Distal Femur	0.98	1.22	0.99	1.24	0.98	1.23
Female Proximal Tibia	0.96	1.18	0.91	1.12	1.04	1.3
Male Proximal Tibia	1.19	1.45	1.34	1.6	1.2	1.46
Average	0.983	1.218	1.013	1.248	1.01	1.258

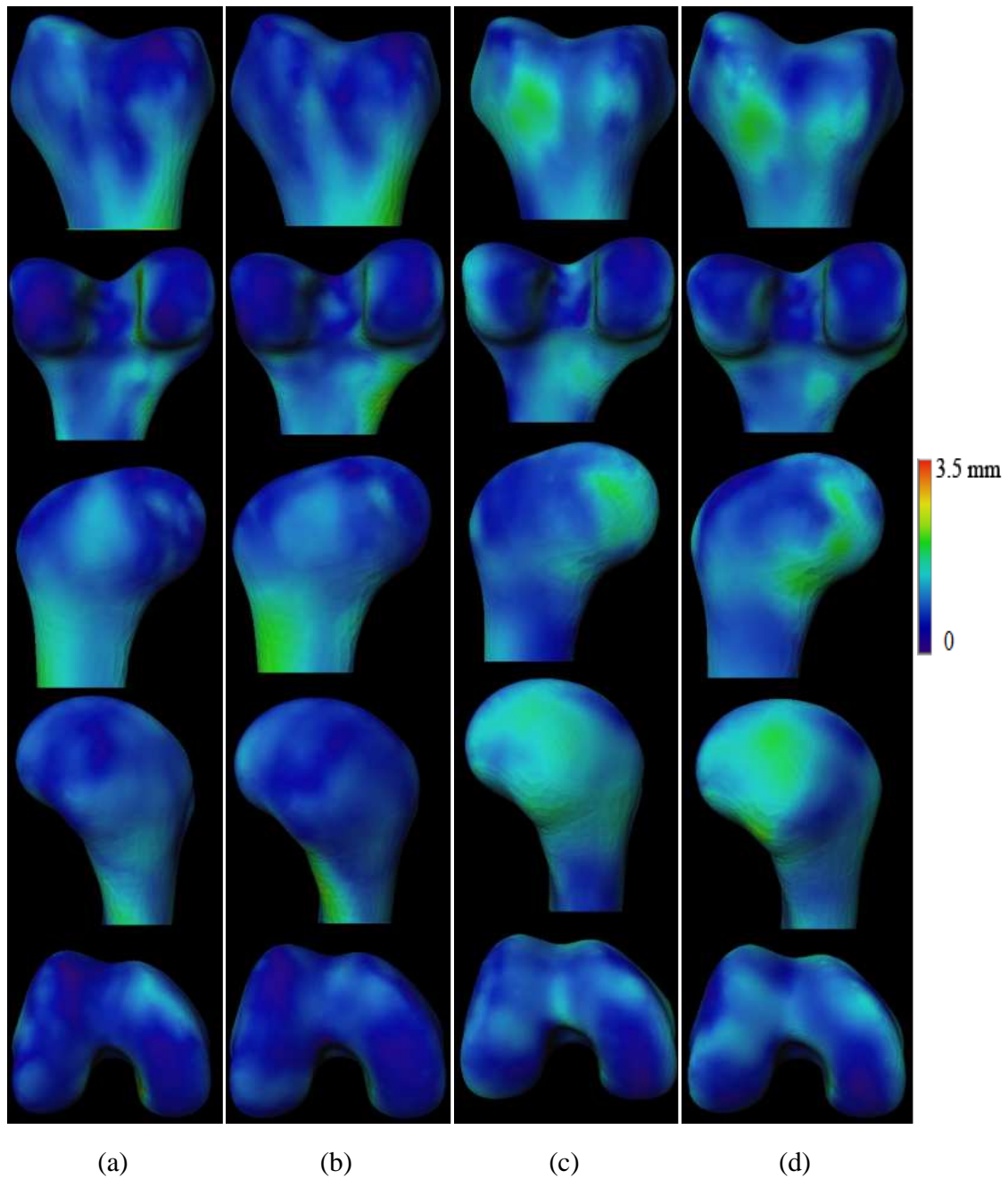


Figure 7.1 Mean RMS distance error color maps for the female distal femurs reconstructed using the Direction Set method with maximum error of 2.49 mm (a), the linear least squares method with maximum error of 2.46 mm (b), and for the male distal femurs reconstructed using the Direction Set method with maximum error of 2.38 mm (c), and the linear least squares method with maximum error of 2.35(d).

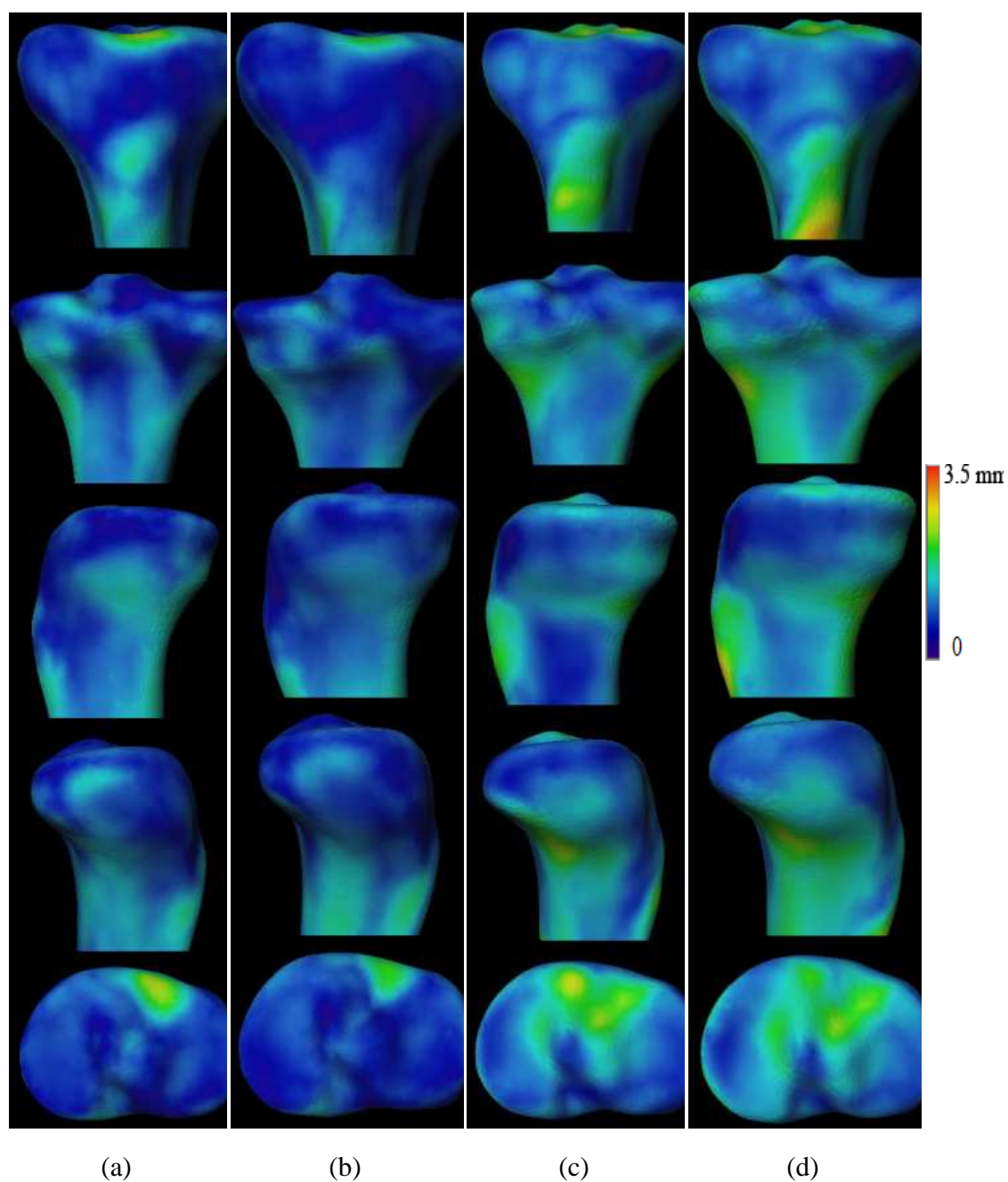


Figure 7.2 Mean RMS distance error color maps for the female proximal tibias reconstructed using the Direction Set method with maximum error of 2.7 mm (a), the linear least squares method with maximum error of 2.1 mm (b), and for the male proximal tibias reconstructed using the Direction Set method with maximum error of 2.89 mm (c), and the linear least squares method with maximum error of 3.2 (d).

7.2 Ultrasound RF Data System Cadavers' Experiments Results

The first ultrasound RF data based imaging system developed in this work (built using the SonixRP ultrasound machine) was experimented on two cadaveric distal femurs, and a proximal tibia. Each bone (distal femur, and proximal tibia) was scanned individually in order to increase the signal to noise ratio of the reconstructed point cloud, and simplify the point cloud filtering process. Figure 7.3 shows a picture for one of the cadaveric experiments, showing developed imaging system running on the SonixRP ultrasound machine.

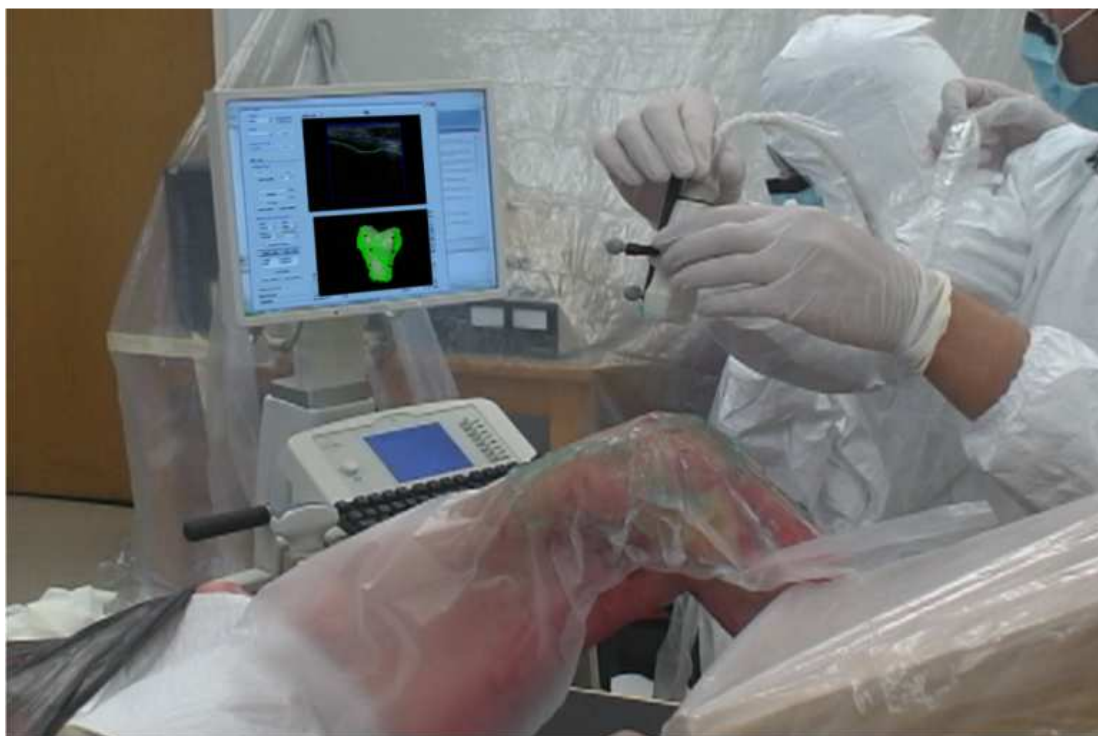


Figure 7.3 A picture for the one of the cadaveric experiments showing the developed imaging system running on the SonixRP ultrasound machine

Each bone's scan contained approximately 1200 ultrasound frames which were automatically processed in real-time to extract the bones' contours as described in section 5.4.1. A large number of RF data frames was acquired for each bone's scan to test the developed method for real-time automatic bone contour detection from the RF data. The high density of the point cloud reconstructed from these contours is not necessary for accurate 3D model reconstruction as shown in the bone morphing analysis described in section 3.3. The developed contour extraction process showed high reliability; approximately 95% of the acquired frames were processed correctly to extract the bone contours. Figure 7.4 shows sample B-mode images, and the extracted bone contours using their RF data.

The extracted bone contours were then mutually registered, by the developed imaging software, using the ultrasound probe's motion tracking data and the probe's calibration parameters as described in section 5.4.2, to reconstruct partial 3D point clouds for the scanned regions (anterior, posterior, medial, and lateral). Due to the line of sight constrain of the optical tracking system used in the ultrasound probe's motion tracking, it was not possible to scan the full anterior part of the bones as one region (in a scan session in which the leg is held fixed). Therefore the anterior region of the distal femur was scanned in three partial (region) scans; which were anterior, medial, and lateral regions with the knee in a flexion angle of approximately 120 degrees. The anterior scans of the tibia were divided into two regions; medial-anterior, and lateral-anterior with the knee in a flexion angle of approximately 120 degrees. The posterior scans of the distal femur and proximal tibia were also acquired as separate region scans with the knee in full extension.

The partial point clouds were then mutually registered into one point cloud representing the whole scanned bone surface as described in section 5.4.2.2.

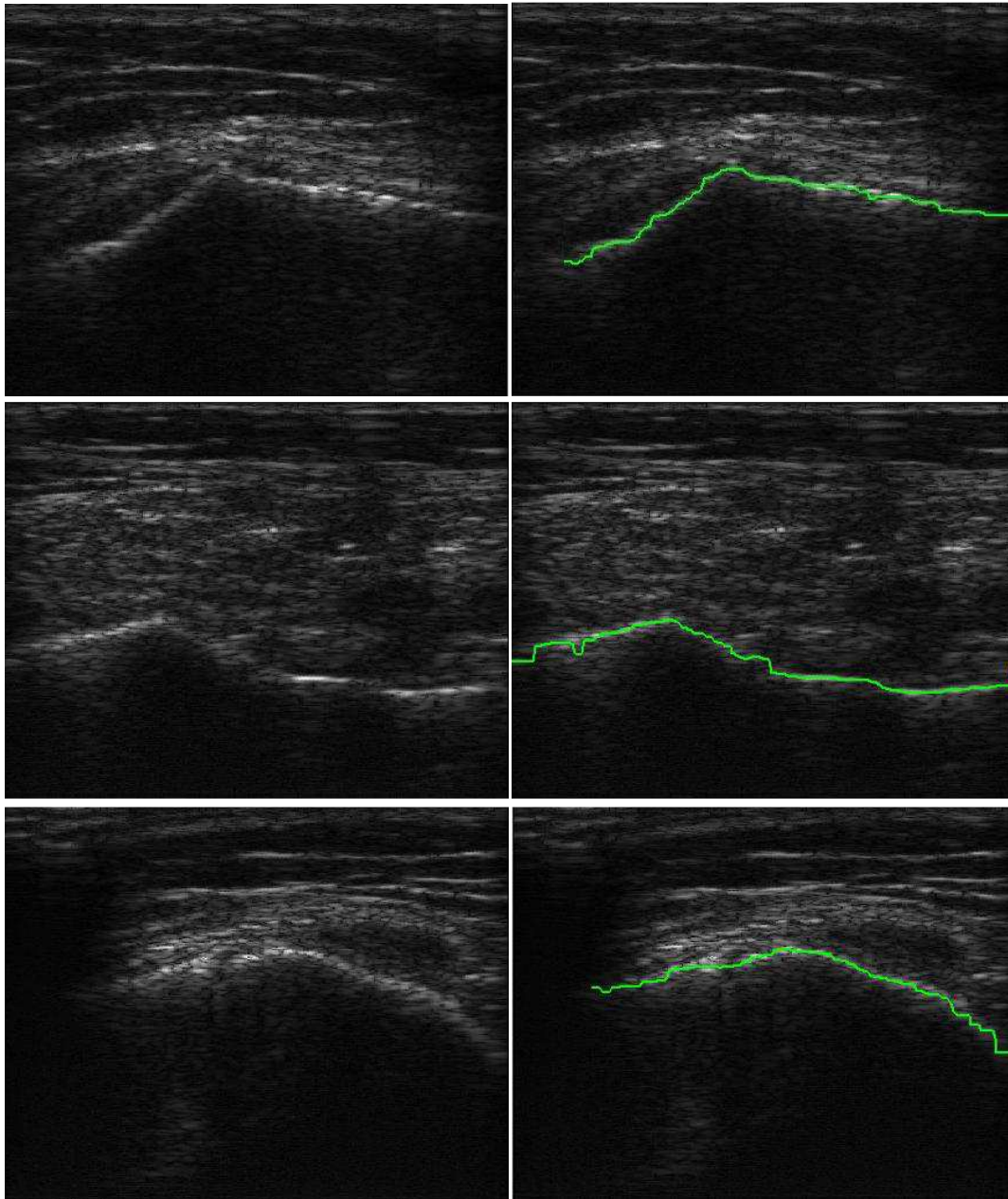


Figure 7.4 Ultrasound B-mode image (left), reconstructed by applying Hilbert transform to the ultrasound RF data, for a different regions of a cadaveric knee, and the extracted bone contour from the RF data overlaid on the B-mode image (right)

The reconstructed bones' point clouds were then used to reconstruct 3D models of the scanned bones. The three morphing methods described in section 3.3 were used to reconstruct the 3D models for each reconstructed point cloud to compare the accuracy of morphing methods. In order to study the combined effect of the point cloud density on the point cloud to atlas' mean model registration and bone morphing, the point clouds were reduced to different point cloud densities, then registered to the atlas' mean model, and used in the reconstruction of the bones' 3D models.

Computed tomography (CT) scanning of the cadavers' knees was performed, and the CT scans were manually segmented to create the golden reference 3D bone models of the cadavers' distal femurs and proximal tibia which were used to assess the accuracy of the 3D point clouds, and models reconstructed using the ultrasound RF data. The RMS errors between the reconstructed point clouds and the reference CT segmented 3D bone models were then calculated. The point clouds to reference CT models RMS errors were 1.32 mm, 1.3 mm, and 1.69 for the first cadaver's distal femur, first cadaver's proximal tibia, and second cadaver's distal femur respectively.

The RMS errors between the reconstructed 3D bones models and the reference CT models were then calculated for the three morphing methods, and the different point cloud densities used. In order to study the error distribution over the bone's surface, distance error color maps were generated for reconstructed 3D model with the highest accuracy (among the models reconstructed using different point cloud densities, and morphing methods) for each scanned cadaveric bone. Table 7.3 shows the average, RMS, and maximum distance errors for the highest accuracy reconstructed models for each

scanned cadaveric bone. Appendix section 9.4 shows the reconstructed 3D point clouds, and models for the scanned cadaveric distal femurs, and proximal tibia. It shows also the color maps for the distance error between the reconstructed 3D models, and the reference CT models.

Table 7.3 3D model reconstruction errors (in mm) between the reconstructed models using the developed ultrasound RF data system, and the CT-segmented models for the scanned cadavers' bones.

	Avg. Error	RMS Error
Distal Femur1	1.01	1.26
Distal Femur2	0.93	1.19
Proximal Tibia	0.99	1.22
Average	0.976	1.223

7.3 Ultrasound RF Data Imaging System's Clinical Study Results

The developed 3D knee model reconstruction system (running on the SonixTOUCH ultrasound machine) was experimented on four volunteers. The system was tested on the right knees of two volunteers, and the both right and left knees of two volunteers, with a total of six knees. The patient scanning setup, described in section 6.2, was used for holding the volunteers' knees fixed while being scanned. Each volunteer's knee was scanned using the scanning protocol described in section 6.4.

The ultrasound RF data of each region's scan was processed in real-time, by the imaging software running on the ultrasound machine, to generate the bone contours, and the bone's surface point cloud. The bone contours were overlaid on the B-mode images of the scans in real time to provide feedback for the system's operator about the quality of the bone contours extracted. This feedback was used to notify the scanner if he/she needs to change the tilt angle of the ultrasound probe to get clearer scans of the bone contours. The real-time reconstructed point cloud provided the system operator with feedback for the quality of the bone cloud as well as the areas uncovered by the scanning, so he/she can scan these areas. Figure 7.5 through Figure 7.8 shows pictures taken during the scanning of the anterior distal femur, anterior proximal tibia, posterior distal femur, and posterior proximal tibia regions of one of the volunteers' knee, respectively.

The reconstructed point clouds were then reduced to a 4-mm density point clouds which were used, by the imaging software, to reconstruct 3D models for the scanned bones using the described morphing methods. The Direction Set method showed slightly higher reconstruction accuracy than the linear least squares method, and the hybrid

method. This is due to the tendency of the linear least squares method to over-fit the reconstructed 3D model to the point cloud, which makes it more sensitive to the noise in the point cloud. This over-fitting results in a small drop in accuracy (around 0.2 mm). Therefore the Direction Set method was used for the 3D model reconstruction of the distal femurs, and proximal tibias of the scanned volunteers' knees.

In order to assess the accuracy of the 3D bone model reconstructed using the developed imaging system, the volunteers' knees were scanned using the Magnetic Resonance Imaging (MRI), and manually segmented to create golden reference 3D models of the scanned knees bones (distal femurs, and proximal tibias). Sagittal 3D VIBE fat saturation MRI scanning with 0.6 mm slice thickness, and 0.6 mm pixel size (voxel size of 0.6 mm).was used to scan the volunteers knees.

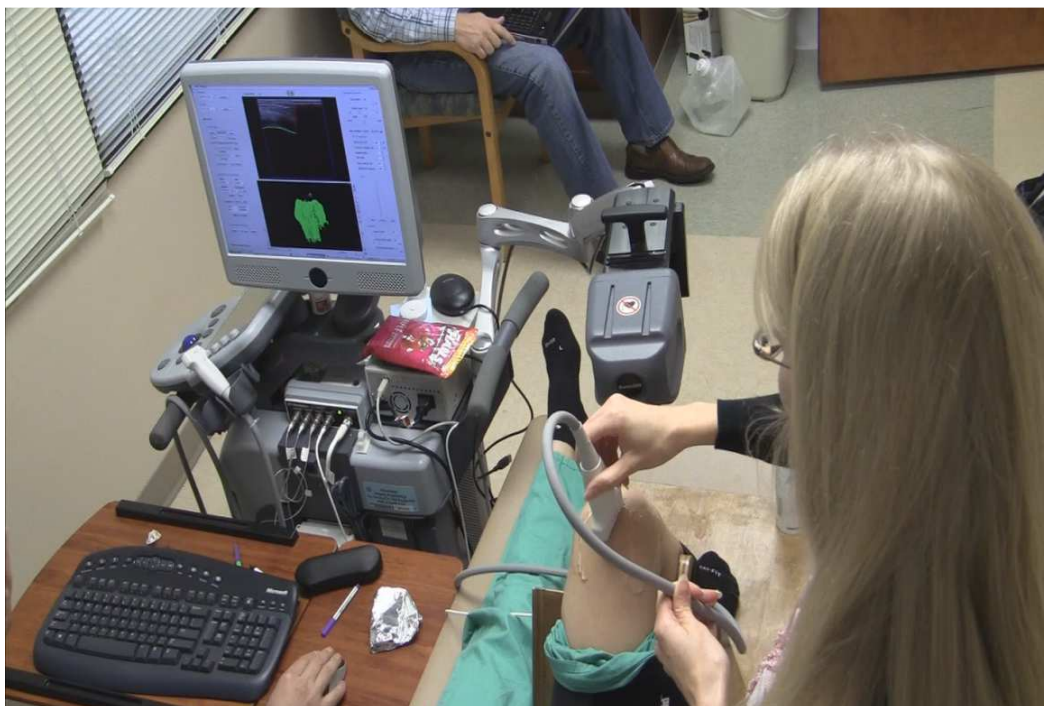


Figure 7.5 A snapshot from scanning the anterior distal femur of a volunteer's knee



Figure 7.6 A snapshot from scanning the anterior proximal tibia of a volunteer's knee



Figure 7.7 A snapshot from scanning of the posterior distal femur of a volunteer's knee



Figure 7.8 A snapshot from scanning of posterior proximal tibia of a volunteer's knee.

In order to study the repeatability of the developed imaging system, each volunteer's knee was scanned three times (three trials) to generate three independent point clouds for each scanned bone. These three point clouds were then used to reconstruct three independent 3D models for the bone. Appendix section 9.5 shows the reconstructed point clouds, models, and the distance errors color maps for the three scanning, and reconstruction trials for the six volunteers' knees scanned in the clinical study. Table 7.4 lists the average (Avg.) and root mean square (RMS) errors for the three trials for each scanned volunteer's knee. It also lists the body mass index (BMI) for each volunteer. Table 7.5 lists the mean (μ), standard deviation (σ), and relative standard deviation for the distance errors for the three trials of each bone model reconstruction.

Table 7.4 3D model reconstruction average (Avg.), and root mean square (RMS) errors (in mm) for the 3 trials for the distal femur and proximal tibia 3D model reconstruction for the 6 volunteers' knees (Vol. 1 to Vol. 4 refers to the four volunteers). The Body Mass Index (BMI) for the volunteers is shown in the last column.

	Bone	Trail 1		Trail 2		Trial 3		BMI
		Avg	RMS	Avg	RMS	Avg	RMS	
Vol. 1 Knee 1 (Right)	<i>Distal Femur</i>	0.64	0.84	0.74	0.94	0.8	1.04	19
	<i>Proximal Tibia</i>	0.6	0.78	0.62	0.79	0.75	0.96	
Vol. 2 Knee 2 (Right)	<i>Distal Femur</i>	0.72	0.94	0.85	1.09	0.78	1	22
	<i>Proximal Tibia</i>	0.98	1.2	0.71	0.91	0.73	0.95	
Vol. 3 Knee 3 (Right)	<i>Distal Femur</i>	0.93	1.18	0.83	1.05	0.81	1.01	25
	<i>Proximal Tibia</i>	0.8	1.05	0.69	0.88	0.68	0.89	
Vol. 3 Knee 4 (Left)	<i>Distal Femur</i>	0.89	1.14	0.92	1.17	0.95	1.2	
	<i>Proximal Tibia</i>	0.68	0.87	0.75	0.94	0.66	0.86	
Vol. 4 Knee5 (Right)	<i>Distal Femur</i>	0.96	1.19	1.01	1.28	1.04	1.3	35
	<i>Proximal Tibia</i>	1.08	1.3	1.13	1.42	1.2	1.49	
Vol. 4 Knee 6 (Left)	<i>Distal Femur</i>	1	1.27	0.92	1.17	0.97	1.21	
	<i>Proximal Tibia</i>	1.27	1.61	1.23	1.54	1.43	1.75	

Table 7.5 Mean (μ), standard deviation (σ) for the average (Avg.), and root mean square (RMS) errors (in mm), and their relative standard deviation (σ/μ) for the three trials for the three trials for the distal femur and proximal tibia 3D model reconstruction for the 6 volunteers' knees. The BMI for the volunteers is shown in the last column.

Bone		μ		σ		σ/μ (%)		BMI
		Avg	RMS	Avg	RMS	Avg	RMS	
Vol. 1 Knee 1 (Right)	<i>Distal Femur</i>	0.727	0.94	0.066	0.082	9.08	8.69	19
	<i>Proximal Tibia</i>	0.657	0.843	0.067	0.083	10.13	9.79	
Vol. 2 Knee 2 (Right)	<i>Distal Femur</i>	0.783	1.01	0.053	0.062	6.78	6.10	22
	<i>Proximal Tibia</i>	0.807	1.02	0.123	0.128	15.23	12.58	
Vol. 3 Knee 3 (Right)	<i>Distal Femur</i>	0.857	1.08	0.053	0.073	6.13	6.72	25
	<i>Proximal Tibia</i>	0.723	0.94	0.054	0.078	7.52	8.29	
Vol. 3 Knee 4 (Left)	<i>Distal Femur</i>	0.92	1.17	0.025	0.025	2.66	2.09	
	<i>Proximal Tibia</i>	0.697	0.89	0.039	0.036	5.54	3.99	
Vol. 4 Knee5 (Right)	<i>Distal Femur</i>	1.02	1.257	0.033	0.048	3.29	3.81	35
	<i>Proximal Tibia</i>	1.137	1.403	0.049	0.079	4.33	5.59	
Vol. 4 Knee 6 (Left)	<i>Distal Femur</i>	0.963	1.217	0.033	0.041	3.43	3.38	
	<i>Proximal Tibia</i>	1.31	1.633	0.086	0.087	6.6	5.35	
Average		0.882	1.117	0.057	0.069	6.73	6.37	

The 3D model reconstruction for the three trials for six volunteers' knees had an mean average error of 0.88 mm, and RMS error of 1.12 mm. The average relative standard deviation of the results of the three scanning, and model reconstruction trials performed on each volunteer's knee was shown to be 6.73 % for the average error, and 6.37% for the RMS error. This means that average change in the reconstruction error change between different trails for the same knee is 6.37% for the average error, and 6.73% for the RMS error. This results shows that the output of the system is repeatable with an average change of 6.5% in the reconstruction error, which can be translated into 93.5 % repeatability.

The results obtained also showed that the 3D model reconstruction error increases with the increase in the BMI, this is due to two factors which are:

1. The increased depth of the bone under the skin's surface results in an increase in error introduced in the calculated bone depth (the roundtrip distance travelled by the ultrasound pulse from the skin surface to the bone surface). This error is due to the approximation used in the ultrasound speed estimation, which is assumed to have an average value of 1540 m/s in soft tissue. This is the ultrasound speed used in the developed system. The actual ultrasound speed depends on the tissue type encountered by the ultrasound pulse in its roundtrip. Therefore as this trip increases, the error in estimated trip distance increases due to the inexact ultrasound speed estimation. Table 7.6 lists the ultrasound speed for the water and different soft tissues in the knee.

2. In most of the cases of high BMI subjects the amount of adipose tissue in the knee is larger than those of the low BMI subjects. As shown in Table 7.6, the ultrasound speed in fat tissue is 1459 m/s which is 5.3% lower than the average ultrasound speed in soft tissue used which is 1540 m/s. This difference between the actual and the estimated and used ultrasound speed introduce an error in the calculated depth of the bone, which propagates to the point cloud accuracy, and finally to the 3D model reconstruction accuracy. This error can be eliminated or reduced by using a different estimate of ultrasound speed for higher BMI patients. This new estimate should be adjusted according to the ratio between the fat and muscle content of the scanned knee regions.

Table 7.6 Ultrasound speed for the water and different soft tissue types in the knee [17].

Ultrasound Speed (m/s)	
Average Soft Tissue	1540
Bone	4080
Muscle	1580
Fat	1459
Blood	1575
Water (20° C)	1480

Chapter 8 Future Work

8.1 System Enhancement, Accuracy Improvement, and Inclusion of other Joints

The developed method and system for 3D knee model reconstruction from ultrasound RF data showed high accuracy (0.88 mm average reconstruction error without the need of bone-implanted motion tracking reference probes), and high-speed real-time performance (20 frames/second). The developed system showed also high repeatability with an average change of 6% between different independent 3D model reconstruction trials for the same knee. The developed system has some limitation that can be overcome in future work. These limitations are; the need for fixing the knee during each region scanning session, and the increase in the model reconstruction accuracy with the increase of the subject's BMI due to the used inexact average ultrasound speed in soft tissue. Future enhancement and extension of the developed system can include:

- **Using tissue-specific ultrasound speed:** The estimate of the bone's depth from the ultrasound RF data is a function of the ultrasound speed in the soft tissue interrogated by the ultrasound pulse in its roundtrip from the transducer's surface, to the bone surface, and back to the transducer again. The developed system uses a constant average speed of ultrasound in the soft tissue of 1540 m/s. A more accurate estimate of the bone's depth can be calculated by using tissue-specific ultrasound speed at different segments of the pulse's trip. One approach of doing that could be using an anatomical model of the soft tissue types and thickness of the tissues in the way of the ultrasound pulse (muscles, tendons, cartilage, adipose, and other connective tissues) in the joint. Using this anatomical model along with the position

and orientation of the ultrasound pulse's scan line, obtained from the motion tracking probe attached to the ultrasound probe, the distance travelled by the ultrasound pulse can be divided into segments depending on the tissue type travelled during each of the trip segments. In each of these segments, there will be an estimated tissue type (obtained from the anatomical model of the joint) with its associated speed of ultrasound. Therefore, the distance travelled in each segment of the pulse's trip will be calculated independently using the speed of ultrasound in this segment. The bone depth will equal to the sum of the distance travelled by the ultrasound pulse (in one-way trip) through the different segments composed of the different tissue types, estimated by the anatomical model, interrogated by the ultrasound pulse.

- **Reduction of the sensitivity of the system to knee motion:** The developed system requires the knee to be held fixed (using the leg holders) during every region scanning session as described in section 6.3. This requirement was implemented in the scanning protocol to eliminate the need for invasive bone-implanted motion tracking reference probes. In order to eliminate this requirement, the sensitivity of the system to the motion artifact (noise), produced in the reconstructed point cloud by the motion of the joint during the region scanning sessions, should be reduced. This can be partially achieved by using motion-tracking reference probes firmly attached to the patient's leg (in the case of the knee) on the bone being scanned (distal femur, or proximal tibia). This reference probe will provide tracking data for the bone's motion occurring during the region scanning session, and can be used to

correct the noise added to the point cloud due to this motion. This can be achieved by recording the ultrasound probe's motion tracking data relative to this reference probe. However, since the reference probe is only attached to the subjects' skin (outer surface of the joint), it will be affected by the skin motion artifact, and hence will reduce the accuracy of the reconstructed point cloud, and consequently reduce the accuracy of the reconstructed bone model. Therefore, the elimination of the joint fixation constraint might be at the expense of reduced accuracy.

- **Inclusion of other joints:** The developed method for bone contour extraction, and point cloud, and 3D model reconstruction is not specific to the knee joint, and can be applied with no change to other joints of the body, such as the shoulder and hip. The partial point cloud integration method is also applicable to other bones, and joints. However, every joint has its own unique anatomy, and a different scanning protocol, and setup (joint holder) has to be developed for each joint type.

8.2 3D Knee Injection Guidance

One of the innovative technologies that can be built based on the developed 3D knee model reconstruction technology is 3D knee injection guidance system. This 3D knee injection guidance system uses the 3D models of the knee bones reconstructed using the ultrasound-based 3D bone model reconstruction technology developed in this work. 3D model of the injection needle is rendered along with the 3D models of the knee bones. The motion of the injection needle is tracked using a micro electromagnetic tracking sensor attached to the needle. The 3D model of the needle moves on the screen as the real needle moves inside or outside of the knee joint. Since the reconstructed 3D bone models are registered with the patient's knee bones, the motion of the 3D needle model, relative to the 3D models of the bones, represents the motion of the real needle relative to the patient's knee bones. Current injection guidance technologies are 2-D based which uses either ultrasound-based guidance or fluoroscopy to show the needle inside the joint being injected. The latest ultrasound-based injection guidance technologies utilize the electromagnetic tracking system to track the motion of the needle, and overlay its projection on the 2D ultrasound image whether it is in the ultrasound image plane or out of the image plane as shown in Figure 8.1. These guidance systems still lack the 3D view of the organ or joint being injected which is provided by the novel 3D injection guidance system. Figure 8.2 shows a schematic comparison between the current 2D ultrasound-based injection guidance, and the 3D injection guidance system. Figure 8.3 shows a flowchart for the proposed 3D joint injection guidance system.

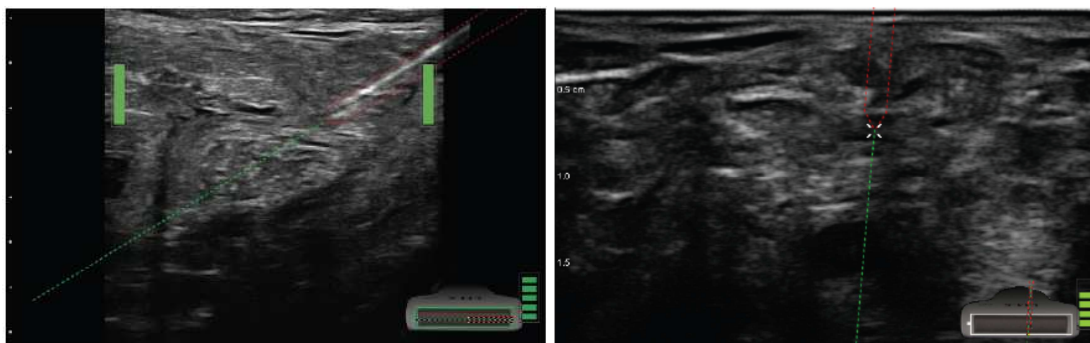


Figure 8.1 Example for the latest ultrasound-based needle guidance systems (Ultrasonix Inc) using the electromagnetic tracking system (Ascension Inc) to track the needle's motion and project it on the ultrasound image. It shows the two cases when the needle is in the image plane (left), and when the needle is out of the image plane, i.e. the needle is not in the ultrasound image (right)

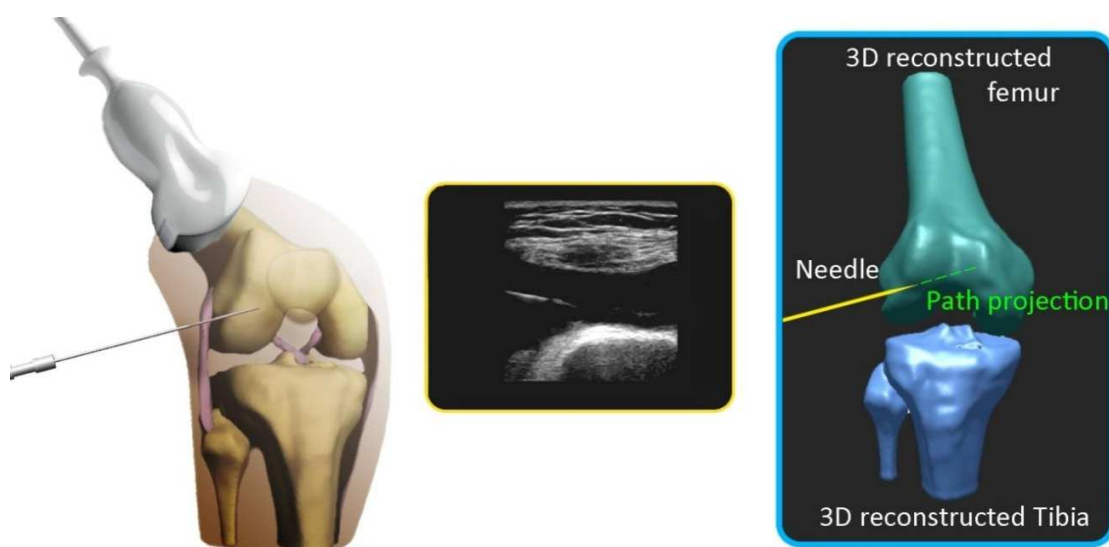


Figure 8.2 A schematic comparison between the traditional 2D and the 3D ultrasound-based injection guidance, showing a schematic of a patient's knee while being injected (left), the 2D ultrasound-based injection guidance (center), and the 3D injection guidance with the visualized 3D joint bone models and real-time tracked needle (right).

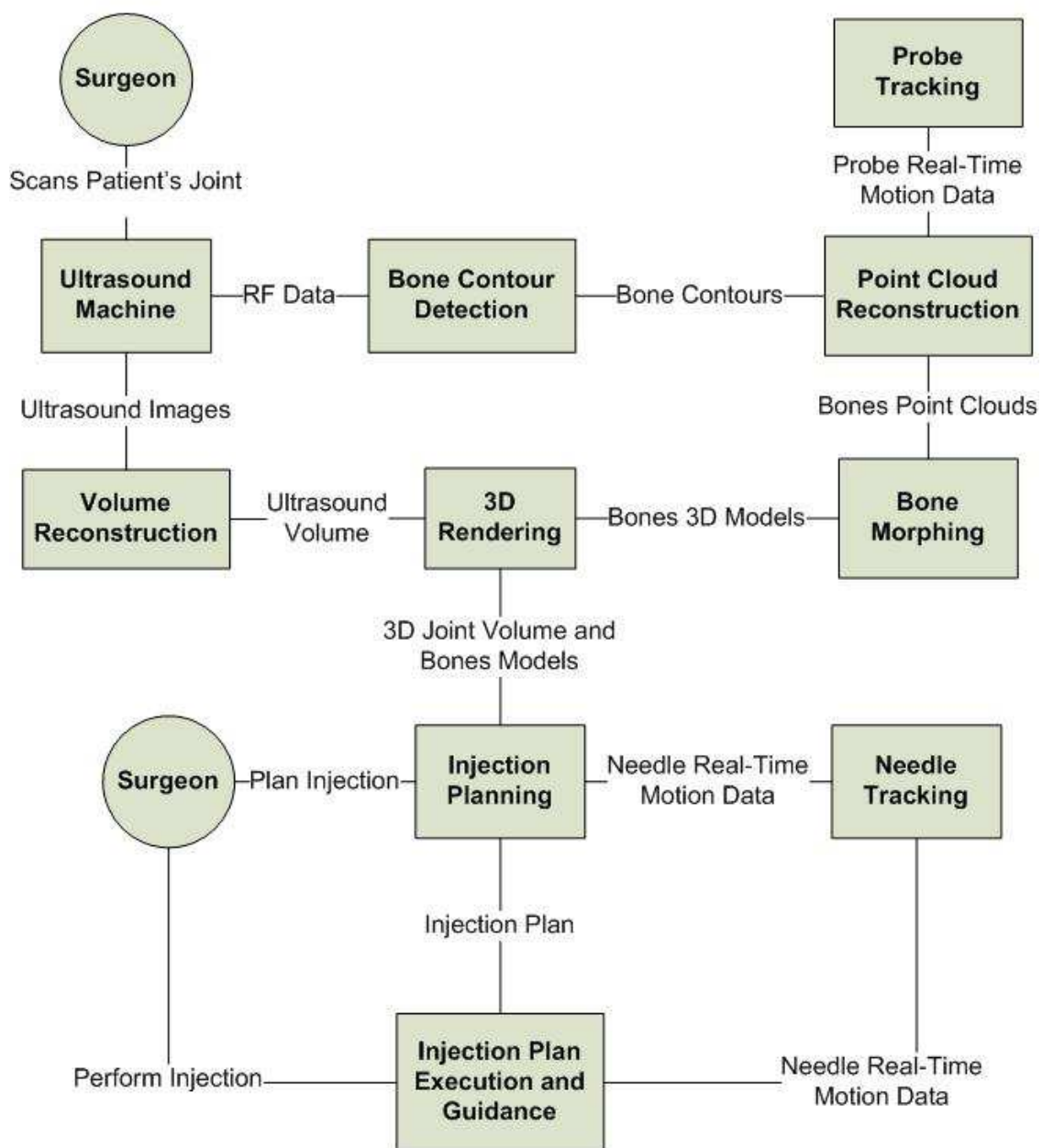


Figure 8.3 Flowchart for the proposed 3D joint injection guidance system, showing the process flow starting from the scanning of the joint, then automatic real-time 3D bones models reconstruction, then volume reconstruction (for soft tissue visualization), then injection planning, and finally injection execution and needle guidance.

This innovative technology will enable the orthopedic surgeon to plan the trajectory for the injection before performing the injection process, which will yield a potential decrease in the number of missed injections. This will result in elimination of the injection cost and the pain associated with missed injections. This technology will also provide the surgeon with more insight in the patient's knee, and enable him/her to visualize the knee in 3D views, and to visualize it from different viewing angles, which are expected to provide more user-friendly imaging modality for the joint which will enable more efficient and accurate injections. This technology can also be extended to include other joints, such as the shoulder, and hip.

In this work, a prototype for the 3D knee injection system was developed, using Microsoft Visual C++ 2005 for development, QT 4.3 for graphical user interface, and Open Inventor 7.2 for 3D visualization. The system was implemented on the SonixTOUCH (Ultrasonix Inc) ultrasound machine, and using the DriveBay electromagnetic tracking system (Ascension Inc) for the needle tracking. This prototype was developed as an extension to the 3D knee model reconstruction system used in the clinical study. The 3D injection prototype used the model 90 electromagnetic tracking sensor (0.9 mm diameter) to track a special hollow needle that house the electromagnetic sensor inside it. A simulation for the injection was performed (no actual injection was performed, just positioning of the needle over the skin was performed) for a volunteering surgeon after reconstructing the 3D models of his knee bones (distal femur, and proximal tibia) using the developed imaging system. Figure 8.4 shows a picture for the developed 3D injection guidance prototype while being experimented in injection planning



Figure 8.4 A picture taken for the developed 3D injection guidance prototype while experimenting it in injection planning (no injection was performed) for a volunteering surgeon, showing the reconstructed 3D models of the knee bones (distal femur, and proximal tibia), and the 3D model of the needle, while being tracked, showing its position and orientation relative to the knee bones.

8.3 Knee Kinematics Tracking Using A-Mode Ultrasound

Kinematics tracking is the process of tracking the relative motion of between joints bones while doing an activity involving the joint being studied (such as knee, shoulder, and hip). This motion consists of rotation and translation of the joint bones relative to each others. Joint motion analysis is used in diagnosis of joint pathology, as well as studying the normal joint function. Currently, fluoroscopy is the most accurate method for joint kinematics tracking [42]-[45].

Fluoroscopy-based kinematics tracking is performed by imaging the patient with fluoroscopy while doing an activity involving the joint under study. Then the patient's joint is scanned using computed tomography (CT) or magnetic resonance imaging (MRI). The CT or MRI scans are then segmented to create 3D models of the joint bones. The 3D models of the bones are registered to each of the fluoroscopy images using 3D/2D registration to estimate the 3D motion of the joint bones from the consecutive 2D fluoroscopy images [46],[47]. Figure 8.5 shows a flowchart for the fluoroscopy-based kinematics tracking method.

A potential novel technology that can be developed, using the developed ultrasound-based 3D knee model reconstruction system, is a high-accuracy knee kinematics tracking system using A-mode ultrasound. This novel kinematics tracking technology can replace the fluoroscopy-based kinematics tracking to avoid the harmful X-ray radiation the the patient and physician are exposed to during the fluoroscopy. This new technology can also replace the markers-based knee kinematics tracking to avoid its low accuracy due to the skin-bone motion artifact which introduced high bone tracking errors.

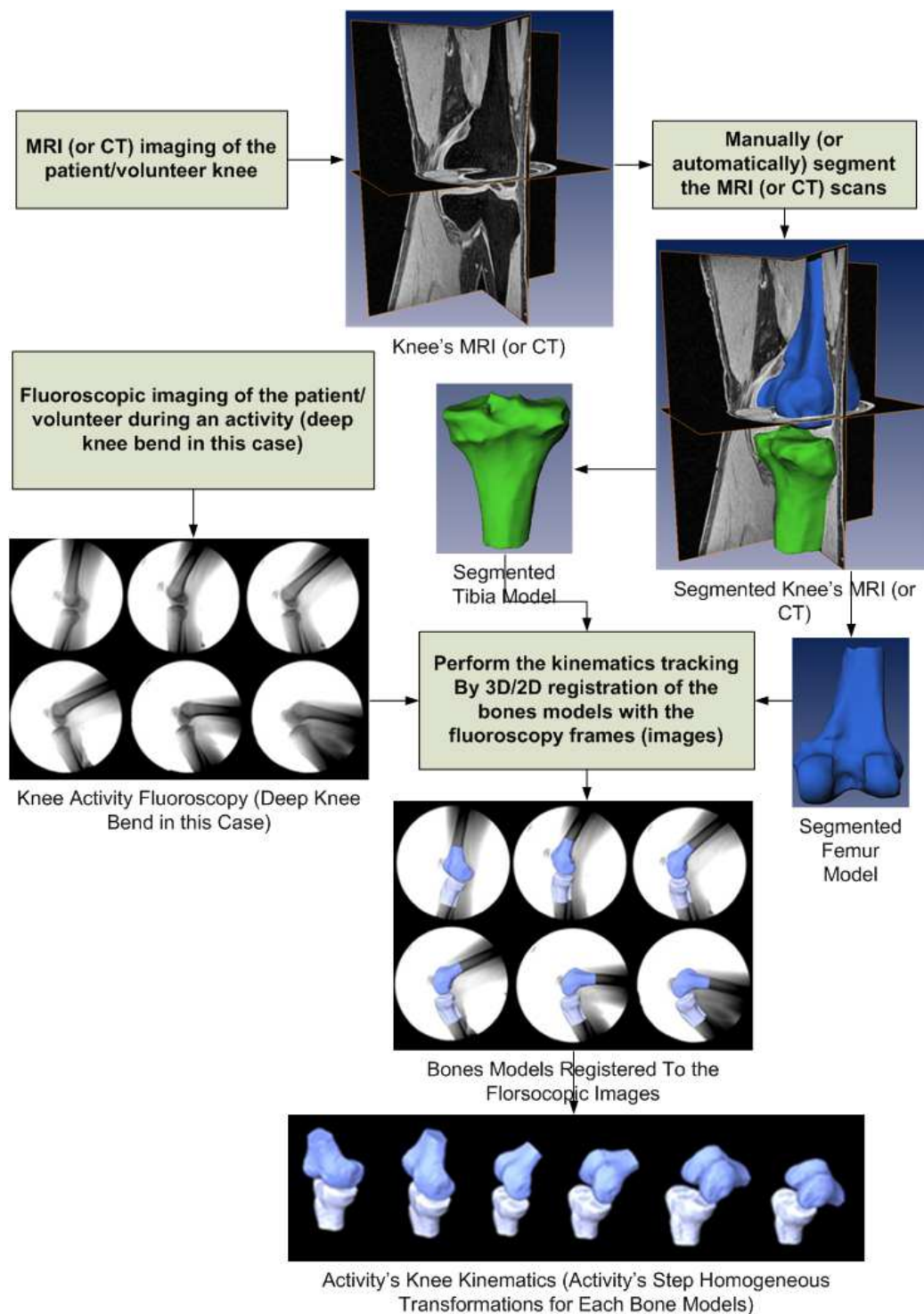


Figure 8.5 Flowchart for fluoroscopy-based kinematics tracking of the knee. Fluoroscopy images copied from the work in [26], and modified for illustration in the flowchart.

The new kinematics tracking system shall be built using a number of single-element ultrasound transducers attached to a knee-wearable brace as shown in Figure 8.6. This brace shall have an optical or electromagnetic tracking system's probe attached to it in order to track the global motion of the brace. The ultrasound transducers will be responsible for transcutaneously detecting 3D points over the bone's surface. This 3D point detection will be performed by automatic extraction, and 3D registration of the bone's echoes from the ultrasound RF signals received by the single-element transducers. The bone echo detection will be performed using the automatic bone echo detection method developed in this work and described in section 5.4.1. The bone echo point (represented as 1D depth measurement between the bone's surface and the ultrasound transducer's face) will be registered into a 3D bone surface point in the reference coordinate frame of the motion tracking probe attached to the brace. Figure 8.6 shows a schematic for the proposed A-mode ultrasound-based knee kinematics tracking system

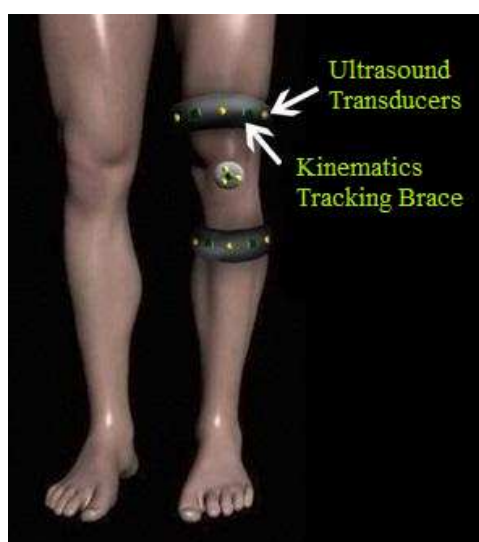


Figure 8.6 Schematic for the ultrasound-based knee kinematics tracking system, showing the femoral, and tibial braces that host the single-element ultrasound transducers.

The bone surface point detection process will be performed for each single-element ultrasound transducer in the brace at a tracking frame rate (determined by the whole system speed), and thus collecting a number of bone surface points equals to the number of ultrasound transducers in the brace for each tracking frame. This set of points collected for each bone identifies the new position and orientation of the bone at time instance (t_n) while the patient is doing the activity involving the knee. This set of bone surface points is then registered to the reconstructed 3D bone model representing the patient's bone position at time instance (t_{n-1}) using the iterative closest point algorithm (ICP) to predict the relative transformation between the position and orientation of the patient's bone at time instances (t_{n-1}), and (t_n). This relative transformation will then be applied to the 3D bone model (currently at the position of time instance (t_{n-1})) to register it with the patient's bone at time (t_n). Then this process of detecting a set of bone surface points at time (t_{n+1}), and is registered to the 3D bone model at the position and orientation at time (t_n) using the ICP method to predict the new patient's bone position and orientation at time (t_{n+1}). Each iteration of this process is called a tracking step. The tracking process starts at time (t_0) when the 3D models of the knee bones are reconstructed and registered to the patient's knee position and orientation using the system developed in this work. Therefore the tracking system has an initial condition of 3D models registered to the patient's knee bones before performing the activity. Then the tracking system estimates the incremental (residual) position and orientation of the patient's knee bones at each tracking step. The tracking steps shall be executed at a frame rate fast enough to sample the motion of the knee bones (depending on the activity performed).

In this work, a simulation framework was developed, using Microsoft visual C++2005 for development, QT 4.3 for graphical user interface, and Open Inventor 7.2 for 3D visualization, to determine the feasibility of the concept and to determine the best configuration (number of transducers and their spatial distribution) of the ultrasound transducers that can achieve a high-accuracy tracking.

The simulation framework uses real kinematics data obtained for patients during an activity such as gait, deep knee bend, stair climbing. These kinematics data were obtained using fluoroscopy [26] as shown in the flowchart in Figure 8.5. 3D models of the proximal tibia and distal femur were segmented from CT or MRI scans of the patient's knee. The 3D models of the distal femur and proximal tibia, along with the kinematics data obtained using fluoroscopy, were then used to perform the ultrasound-based kinematics tracking simulation.

The ultrasound-based kinematics tracking simulation consists of the following steps:

1. The 3D patient-specific models of the distal femur and proximal tibia (segmented from CT or MRI scans) are first positioned in their initial positions acquired by the fluoroscopy-based kinematics tracking data. These 3D models will be simulating the real bones motion (in the actual proposed system), and will be denoted by motion-simulating bone models.
2. A number of points on the motion-simulating 3D bones models are selected by the user of the simulation. These selected points will simulate the bone surface points detected using the single-element ultrasound transducers at the selected locations. These points will be denoted by simulated bone's surface points.

3. The kinematics tracking data are then applied to the motion-simulating bone models in incremental steps to simulate the volunteer's bones motion (as acquired using from the fluoroscopy-based kinematics tracking data).
4. At each motion simulation step, the new coordinates of the simulated bone's surface points are calculated using the fluoroscopy-based kinematics tracking data. So these points simulate the points detected on the surface of the actual patients bones, using the single-element ultrasound transducers attached to the patient's knee, at each tracking step for the patient's knee motion. These new simulated bone's surface points carries the information of the new position and orientation of the motion-simulating 3D bones models after applying one step of the fluoroscopy-based kinematics tracking data. In the actual proposed system, these points shall be detected using the single-element ultrasound transducers attached to the patient's knee. These detected points shall carry the information of the new orientation and position of the patient's bone at each tracking step.
5. The new position and orientation of the motion-simulating bone models are then estimated by registering, using the iterative closest point method (ICP), the new calculated simulated bone's surface points to another set of 3D patient specific bone models (distal femur, and proximal tibia 3D bone models) which are identical to the motion-simulating bone models but have independent orientation and position than the motion-simulating bone models. These set of bone models will be denoted by the bones tracking models. They are the models that will be tracking the motion of the patients' knee bones in the proposed system. These tracking bone models shall be

reconstructed using the ultrasound-based 3D bone model reconstruction system developed in this work. The tracking bone models shall be registered (at every tracking step or frame) to the moving patient's knee bones by the ultrasound-based kinematics tracking system. In the simulation framework, the bone tracking models track the motion-simulating bone models using the simulated bone's surface points calculated at each tracking step using the fluoroscopy-based kinematics data. While in the actual proposed kinematics system, the bone tracking models shall track the motion of the patient's bones using the bone surface points acquired using the single-element ultrasound transducers attached to the patient's knee. The estimated orientation and position data for the motion-simulating bone models (or the patient's bones in proposed system) are then used to update the position and orientation of the bones tracking models.

6. At every tracking step (or simulation step), the tracking error (or registration error) between the bone tracking models, and the motion simulating models is calculated (as the root mean square (RMS) between them) and plotted in a tracking error chart.

Therefore the tracking simulation step consists of applying the kinematics data to the motion-simulating bone models, then calculating the new coordinates of the set of simulated bone's surface points, then register the bone tracking models to these simulated bone's surface points using the ICP method to estimate the new orientation and position of the motion-simulating bone models, then apply these new position and orientation to the bone tracking models. Then calculate the registration RMS error between the bones tracking models, and the motion simulating bone models. Figure 8.7 shows a flowchart

for the kinematics tracking simulation with snapshots of the kinematics tracking simulation for a knee, using 22 simulated single-element ultrasound transducers (or simulated bone's surface points), shown as green spheres, were used for the distal femur, and 19 for the proximal tibia. The motion simulating models are in beige, and the motion tracking models are in red and blue. The tracking steps error graph is shown in the flowchart with an average tracking error was 0.54 mm for the proximal tibia, and 0.01 mm for the distal femur.

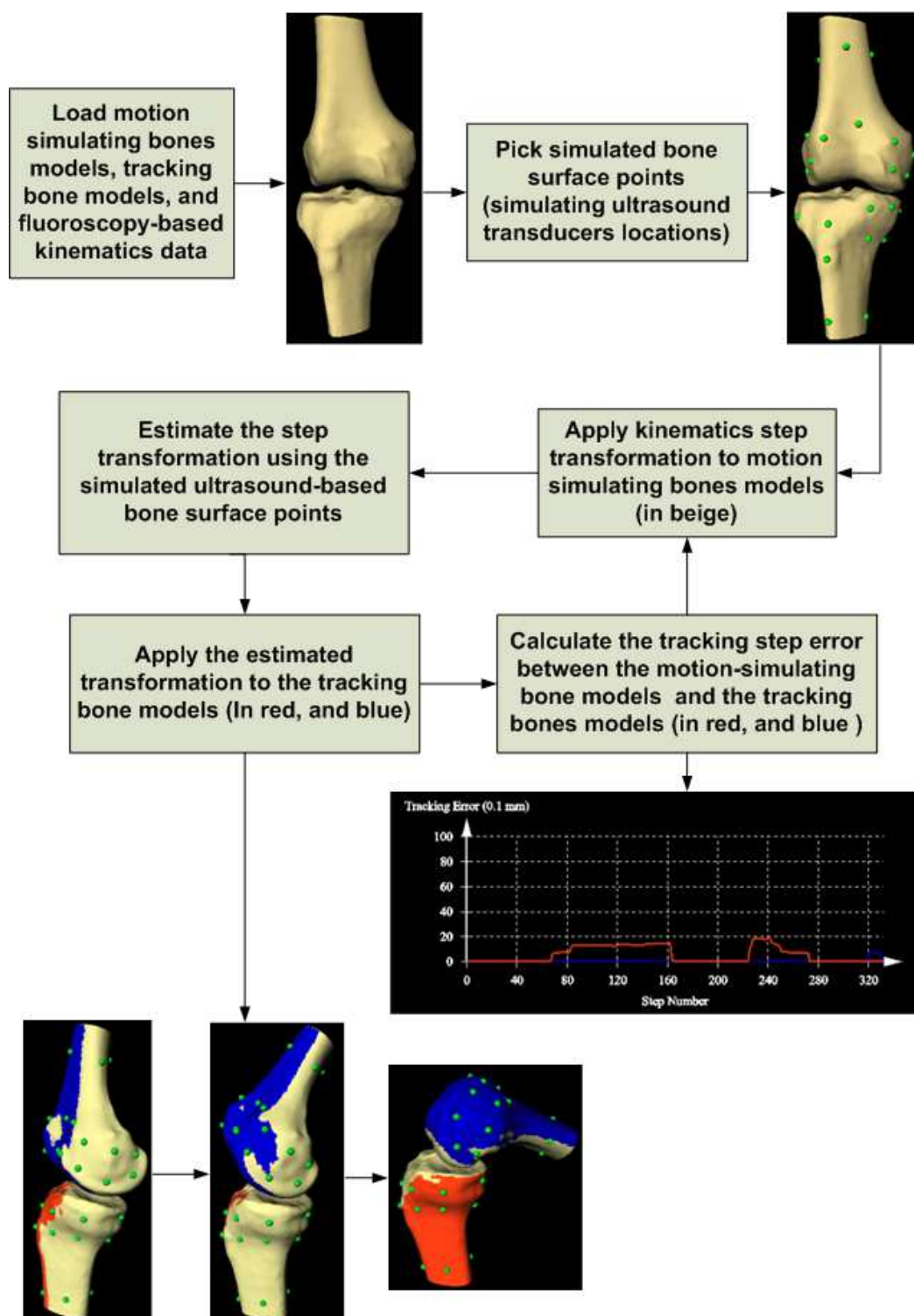


Figure 8.7 A flowchart for the A-mode ultrasound based kinematics tracking simulation

8.4 Cartilage Model Reconstruction

A potential extension for the developed ultrasound-based 3D knee bone model reconstruction system is the reconstruction of patient specific 3D model of the knee cartilage. The cartilage thickness is very essential indicator in several knee pathologies, and most important the osteoarthritis. Monitoring the cartilage thickness for osteoarthritis patients is a very important procedure for orthopedic physicians. Currently the cartilage thickness examination is performed using MRI, which is expensive. The ultrasound can be used as an alternative tool create a 3D model of the cartilage which can provide the orthopedic physician with 3D map of the cartilage thickness similar to the one that can be obtained from MRI but with much less cost.

In this work, the feasibility of automatic extraction of the cartilage contours from ultrasound RF data frames, to reconstruct 3D point cloud representing the cartilage's outer surface (the bone's point cloud and 3D model represents the cartilage's inner surface), was studied. The ultrasound RF data for the 3rd trial of the clinical study's 1st volunteer distal femur scan was used to automatically extract the cartilage echoes, and mutually register the extracted cartilage echoes in the 3D reference coordinate frame of the tracking system to reconstruct a 3D point cloud representing the outer surface of the scanned cartilage. The reconstructed cartilage's outer surface 3D point cloud was then merged with the bone's 3D point cloud at the cartilage areas (which also represents the inner surface of the cartilage at the bone-cartilage interface areas).

The difference in the acoustic impedance between the cartilage and the soft tissue lying above it gives defines the outer surface of the cartilage in the ultrasound RF data

frames or B-mode images. Similarly, the difference in acoustic impedance between the cartilage and the bone lying under it defines the cartilage's inner boundary (and also the bone's surface boundary) in the ultrasound RF data frames B-mode images. The cartilage tissue is hypogenic (doesn't generate ultrasound echoes), but its two surrounding edges (one at the bone-cartilage interface, and the other is at the muscle-cartilage interface) generate detectable echoes which the cartilage's delineate its boundary.

The cartilage echo detection method is an extension of the bone echo detection method described in section 5.4.1. The cartilage echo is detected as the falling edge point of the echo preceding the bone echo (which was detected during the bone echo detection process). Figure 8.8 shows 4 sample RF signals showing the detected bone, and cartilage echoes. Figure 8.9 shows two example ultrasound frames for femoral condyle scans showing the extracted bone and cartilage contours from the ultrasound RF data overlaid on the B-mode images. The detected cartilage echoes was then transformed into 3D point cloud using the same process of transforming the bone echoes into 3D point cloud as described in section 5.4.2.1. Figure 8.10 shows the reconstructed cartilage 3D point cloud for the distal femur of the 3rd trial for the 1st volunteer's scans of the clinical trial. The limitation to the cartilage surface reconstruction is the limited areas of the cartilage accessible to the ultrasound scanning.

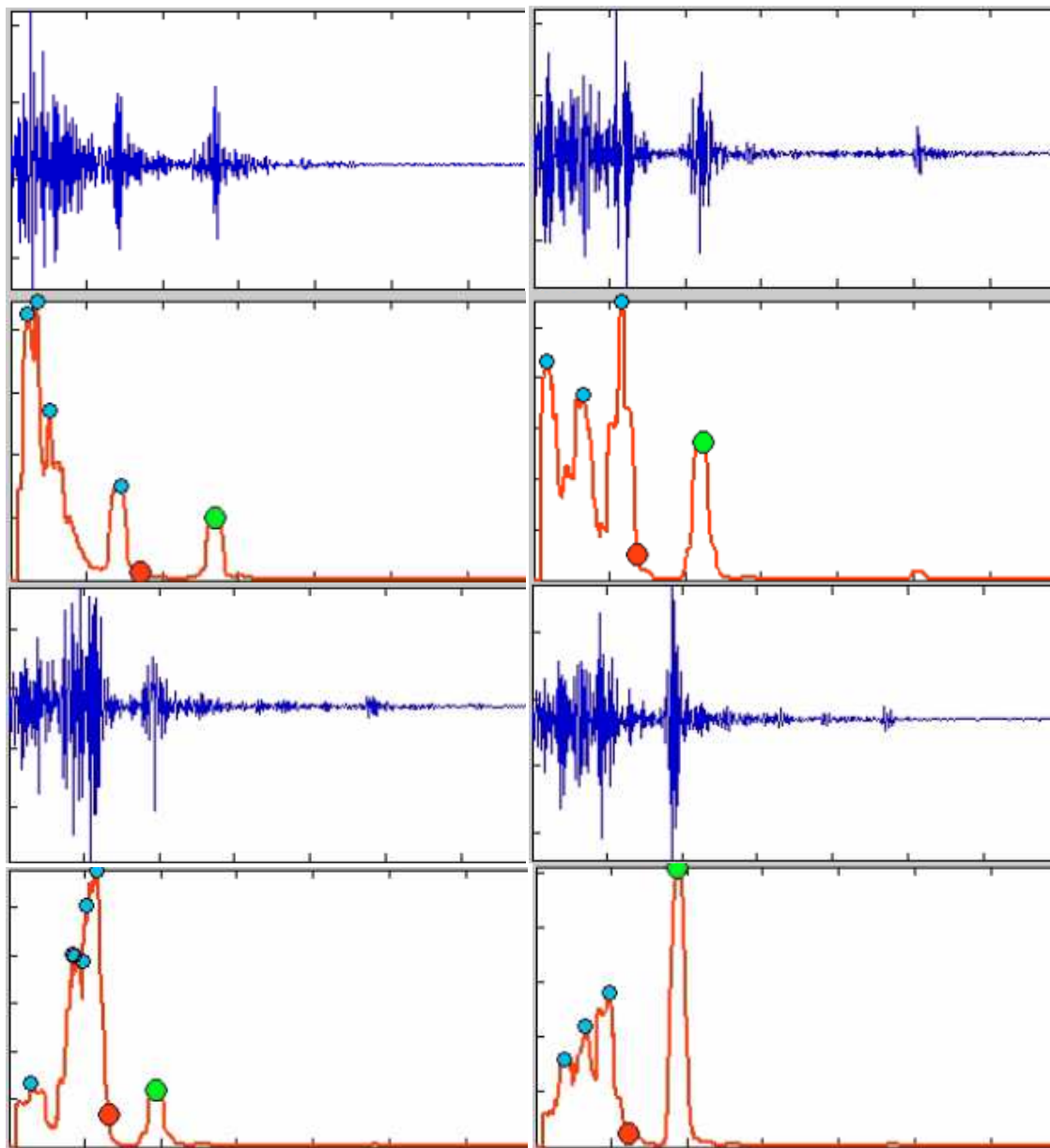


Figure 8.8 Sample raw ultrasound RF signals (in blue), and their processed versions (in red) below them, showing the detected bone echoes (green dots), and cartilage echoes (red dots), and the other detected non-bone non-cartilage echoes (cyan dots)

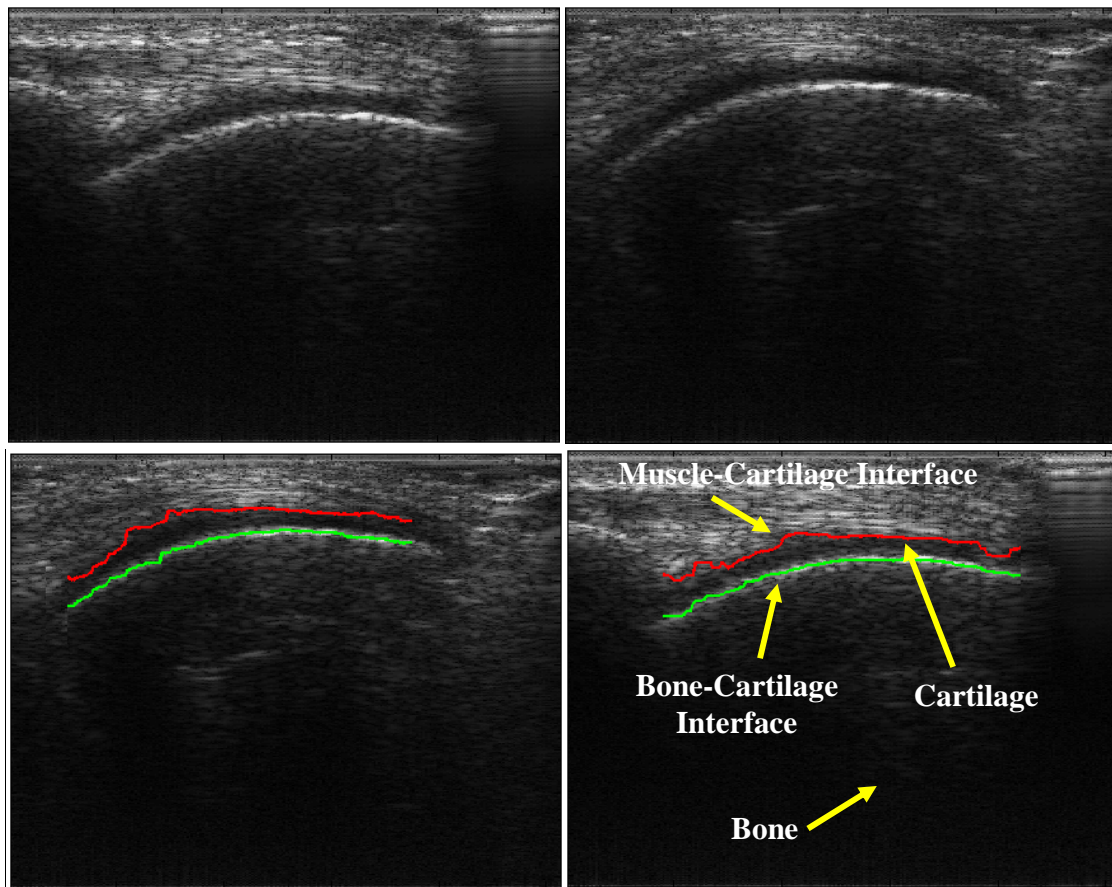


Figure 8.9 Two examples for bone (in green) and cartilage (red) contours extracted using the ultrasound RF data overlaid on their B-mode images, for two frames of one of the clinical study volunteers' femoral condyle scans. The cartilage is the hypo echoic region lying between the bone and cartilage contours.

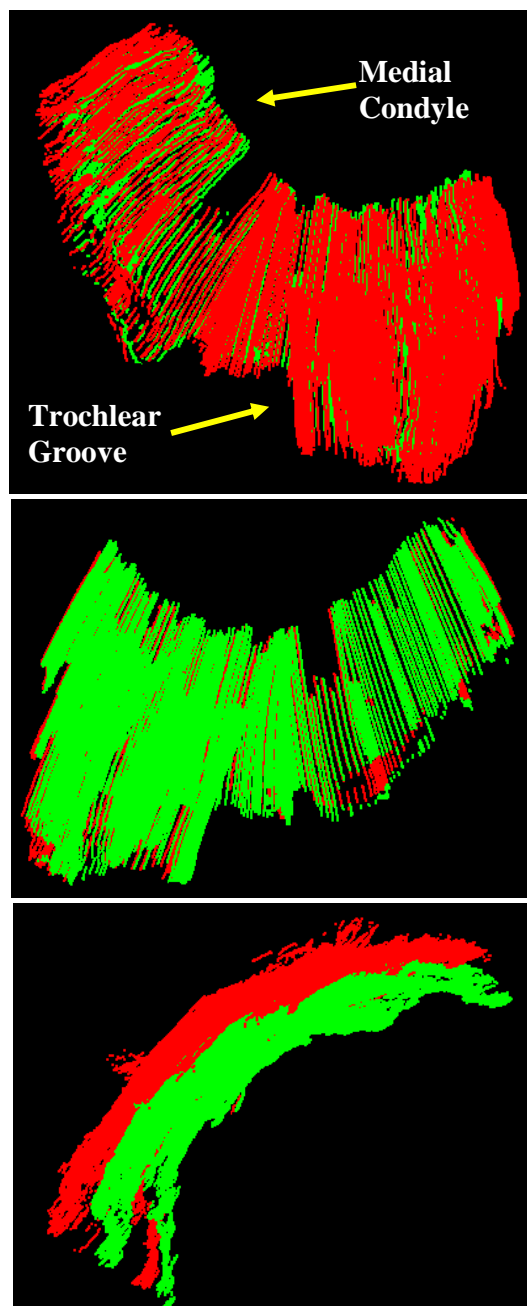


Figure 8.10 The reconstructed 3D cartilage point cloud, showing the outer (red), and inner (green) cartilage surfaces of the distal femur of the 3rd trial for the 1st volunteer's knee of the clinical study. The cartilage's inner surface point cloud is itself the bone's surface point cloud. Three views of the point cloud are shown; superior view(top), inferior view(middle), and side view(bottom)

Chapter 9 Appendix

The first section of the appendix (9.1) includes RMS errors graphs for the knee bones atlas analysis performed on the gender-specific, non gender-specific, jack-knife, and non jack-knife combinations of the atlases. Section 9.2 includes RMS errors graphs for the bone morphing methods analysis for the Direction Set, linear least squares, and the hybrid methods. Section 9.3 includes RMS errors graphs for the results for the phantoms experiments of the developed A-mode ultrasound based 3D bone patient-specific model reconstruction system. All RMS error graphs are plotted versus the number of principal components used. Sections 9.4, and 9.5 includes the cadaveric experiments and clinical study results respectively.

9.1 Knee Bones Atlas Analysis

9.1.1 Female Distal Femur

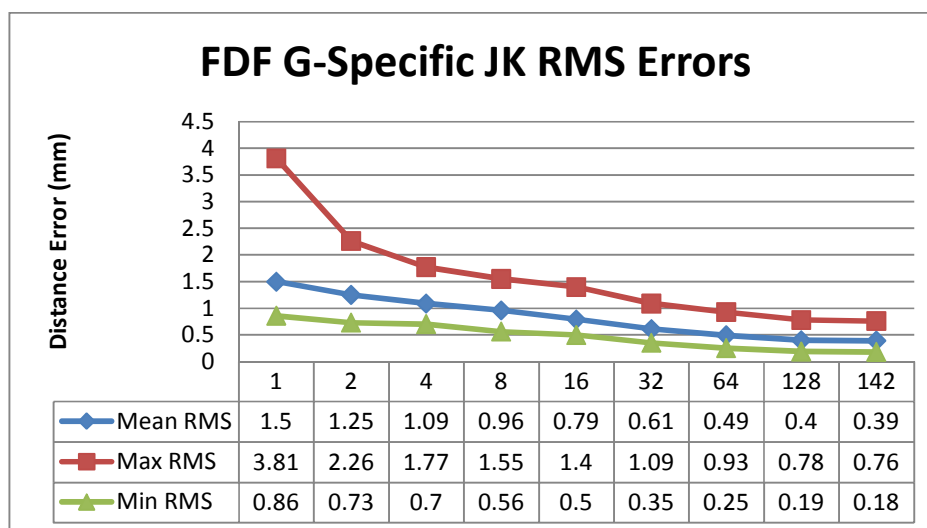


Figure 9.1 Mean, maximum, and minimum RMS errors for the models projection-reconstruction using gender-specific, jack-knife atlas for the female distal femur

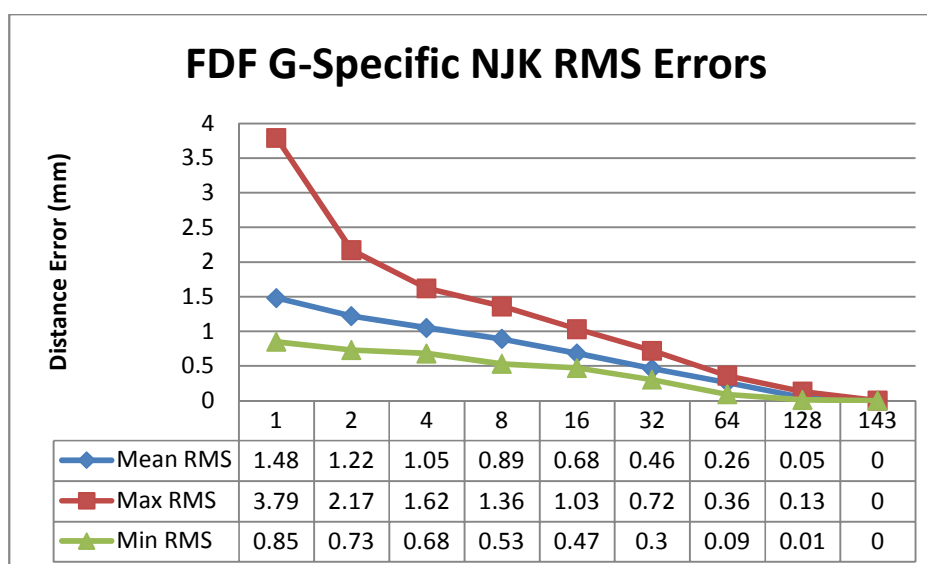


Figure 9.2 Mean, maximum, and minimum RMS errors for the model projection-reconstruction using gender-specific, non jack-knife atlas for the female distal femur

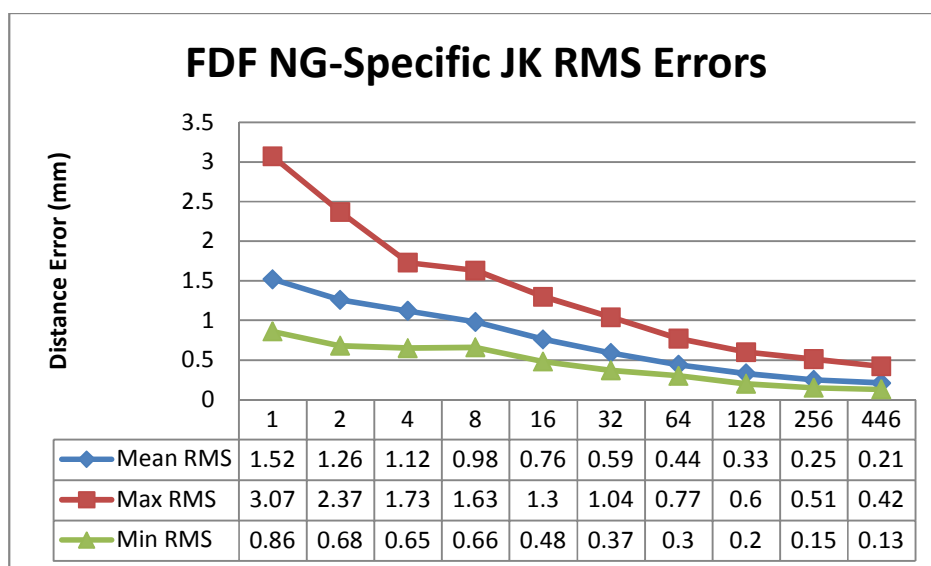


Figure 9.3 Mean, maximum, and minimum RMS errors for the models projection-reconstruction using non gender-specific, jack-knife atlas for the female distal femur

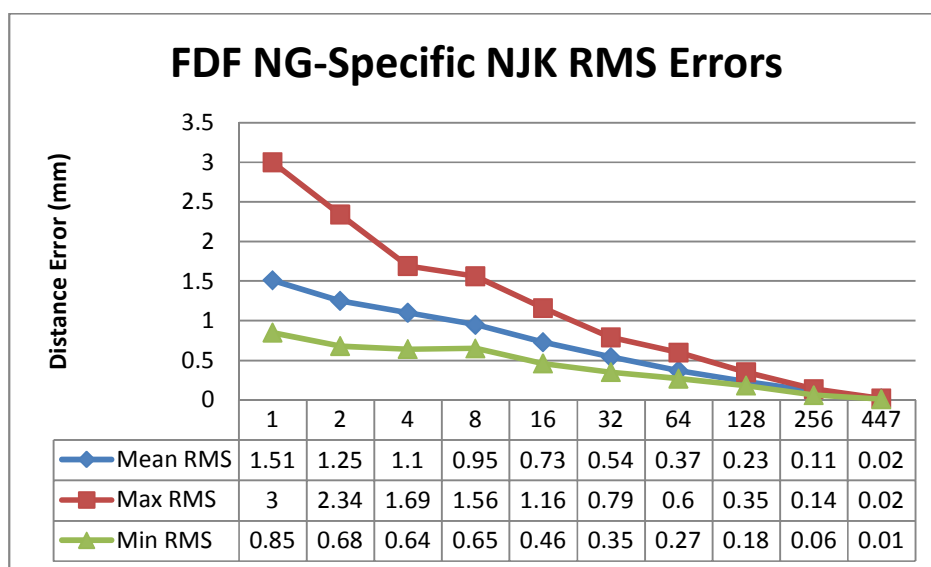


Figure 9.4 Mean, maximum, and minimum RMS errors for the projection-reconstruction using non gender-specific, non jack-knife atlas for the female distal femur

9.1.2 Male Distal Femur

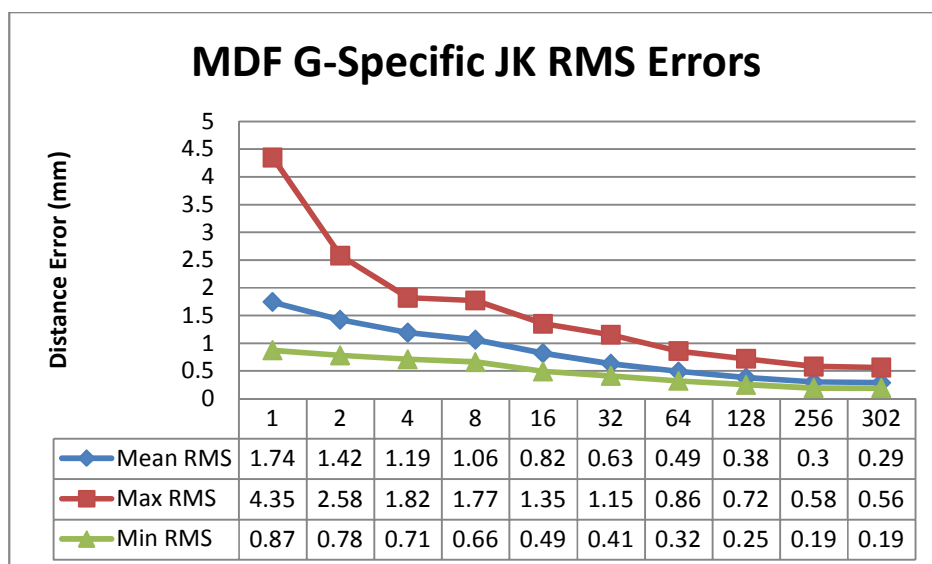


Figure 9.5 Mean, maximum, and minimum RMS errors for the models projection-reconstruction using gender-specific, jack-knife atlas for the male distal femur

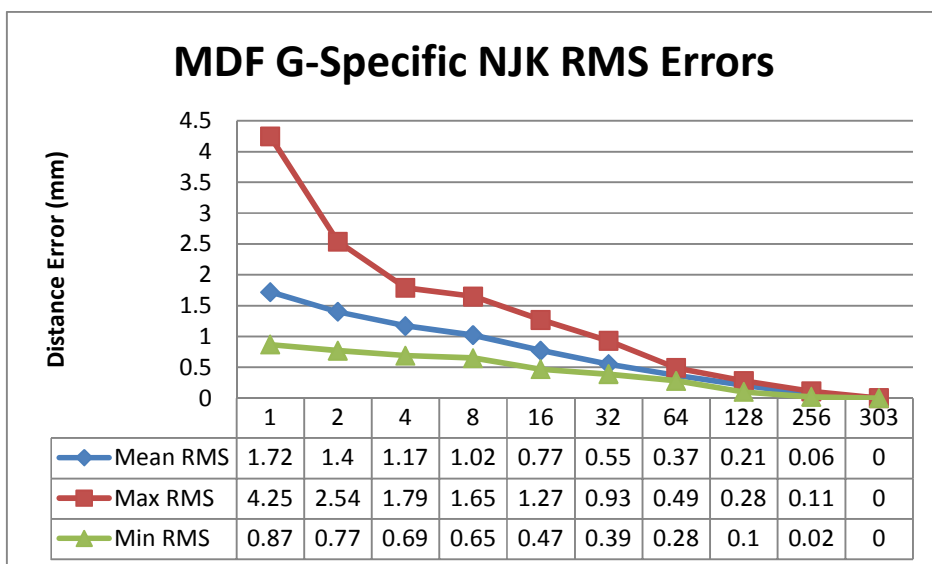


Figure 9.6 Mean, maximum, and minimum RMS errors for the models projection-reconstruction using gender-specific, non jack-knife atlas for the male distal femur

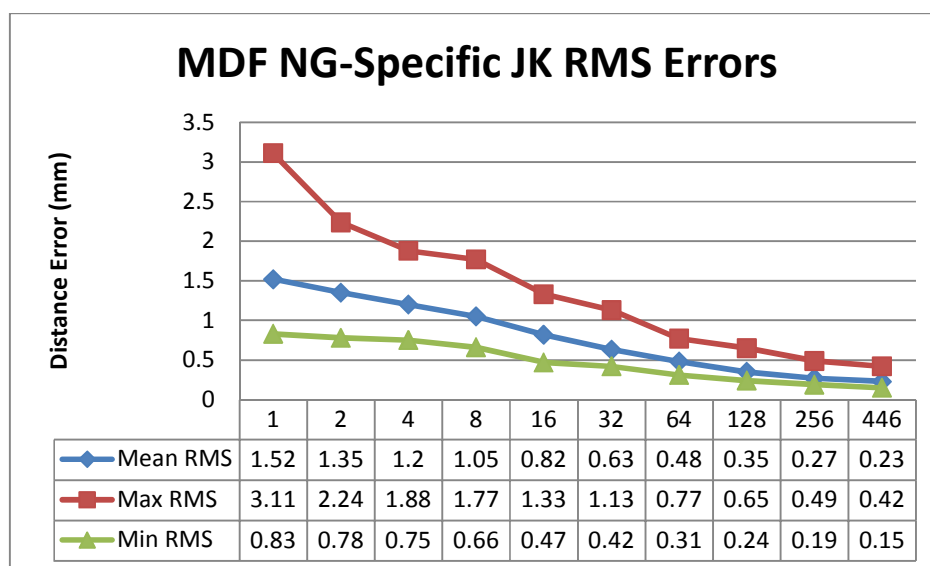


Figure 9.7 Mean, maximum, and minimum RMS errors for the models projection-reconstruction using non gender-specific, jack-knife atlas for the male distal femur

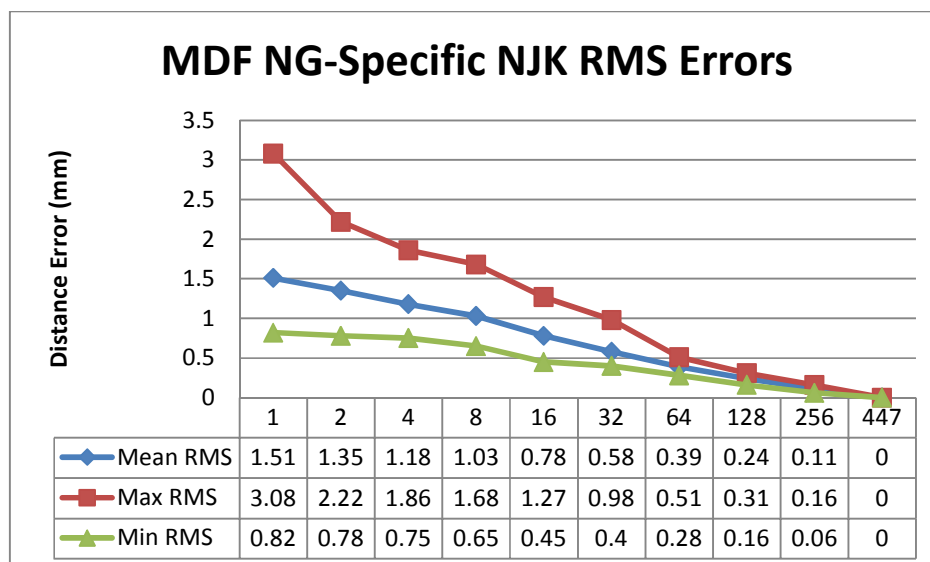


Figure 9.8 Mean, maximum, and minimum RMS errors for the models projection-reconstruction using non gender-specific, non jack-knife atlas for the male distal femur

9.1.3 Female Proximal Tibia

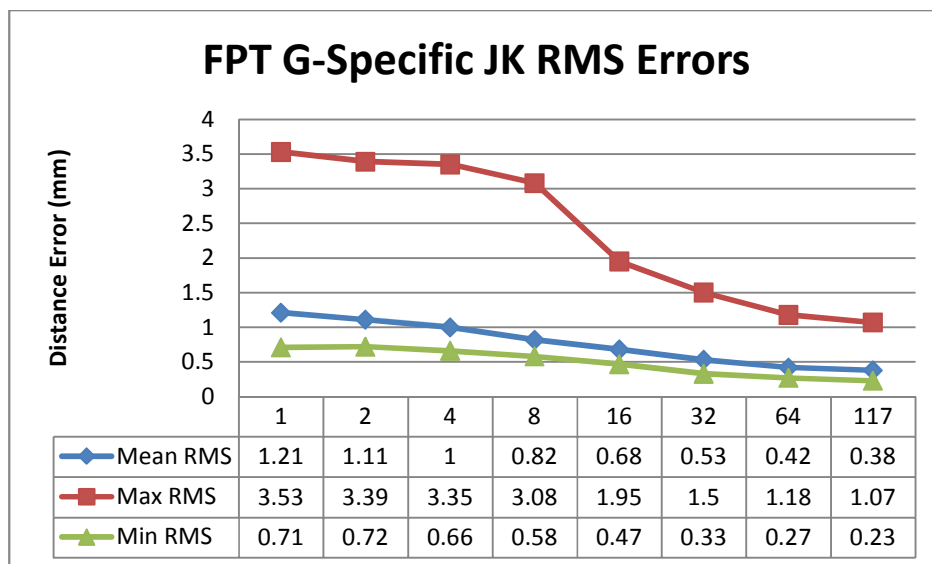


Figure 9.9 Mean, maximum, and minimum RMS errors for the models projection-reconstruction using gender-specific, jack-knife atlas for the female proximal tibia

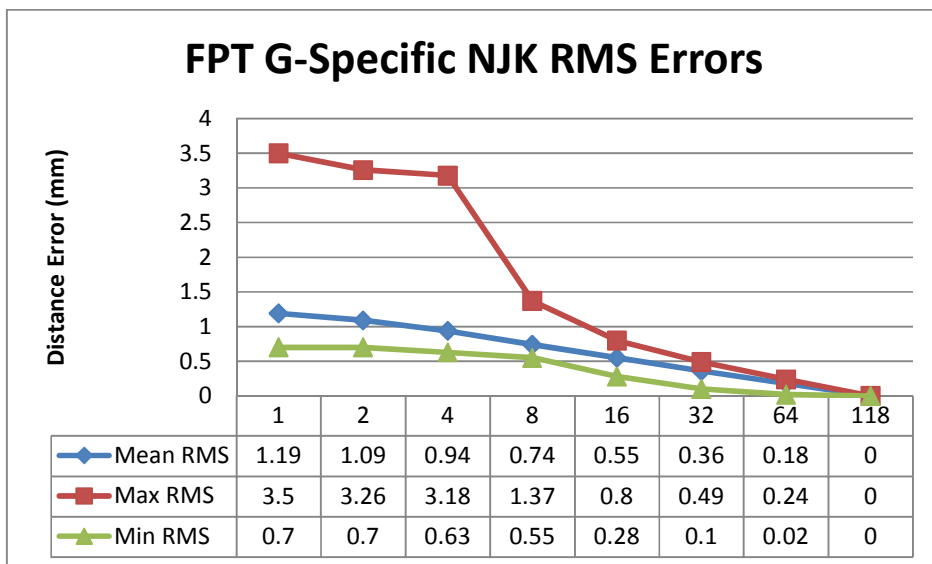


Figure 9.10 Mean, maximum, and minimum RMS errors for the models projection-reconstruction using gender-specific, non jack-knife atlas for the female proximal tibia

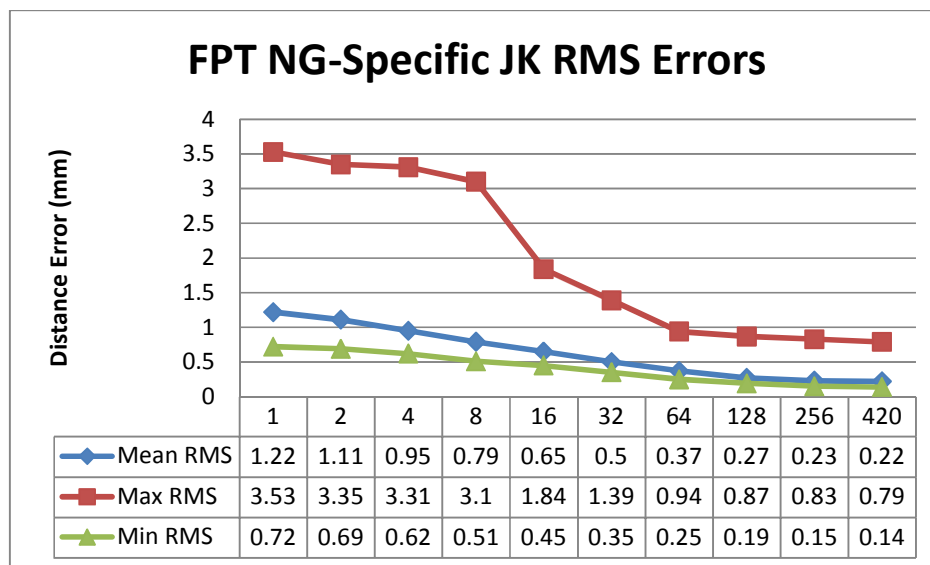


Figure 9.11 Mean, maximum, and minimum RMS errors for the models projection-reconstruction using non gender-specific, jack-knife atlas for the female proximal tibia

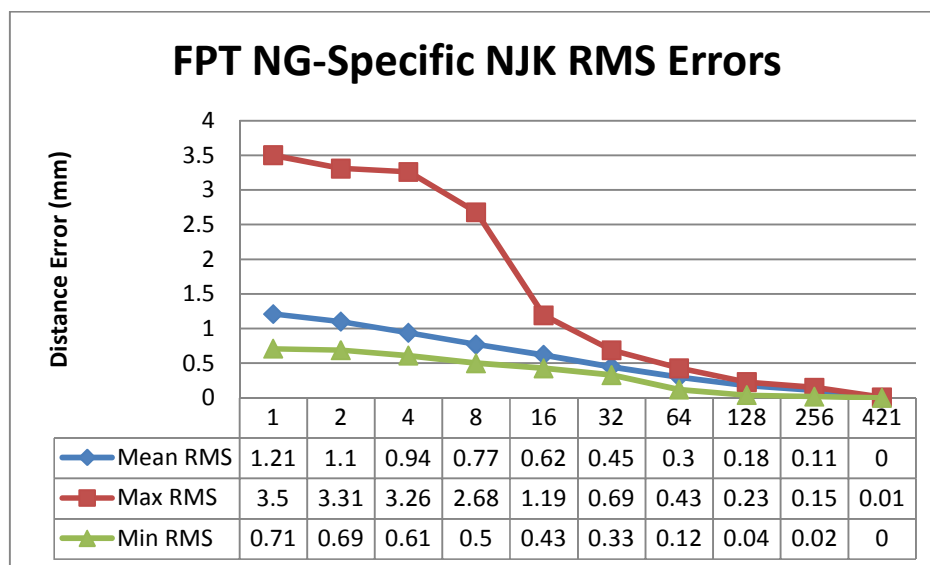


Figure 9.12 Mean, maximum, and minimum errors for the models projection-reconstruction using non gender-specific, non jack-knife atlas for the female proximal tibia

9.1.4 Male Proximal Tibia

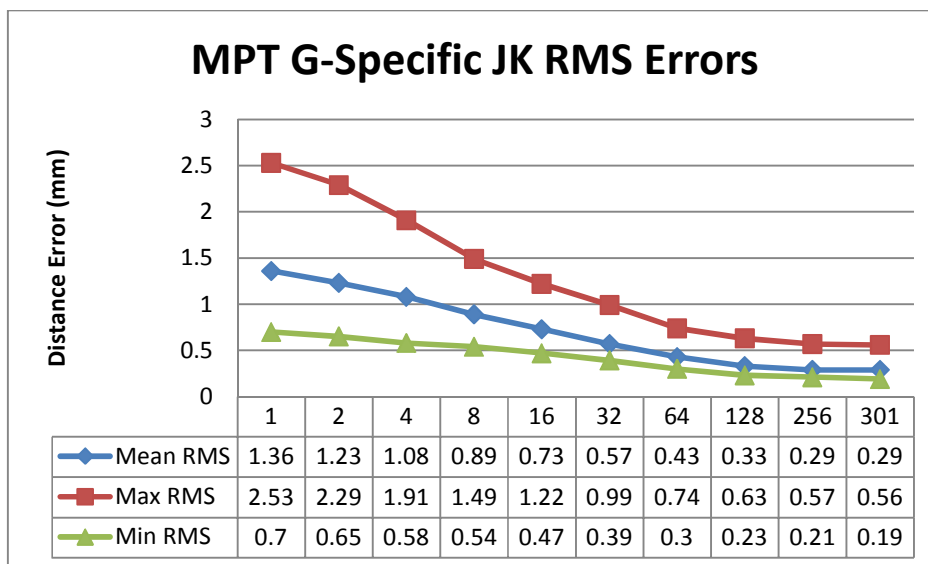


Figure 9.13 Mean, maximum, and minimum RMS errors for the models projection-reconstruction using gender-specific, jack-knife atlas for the male proximal tibia

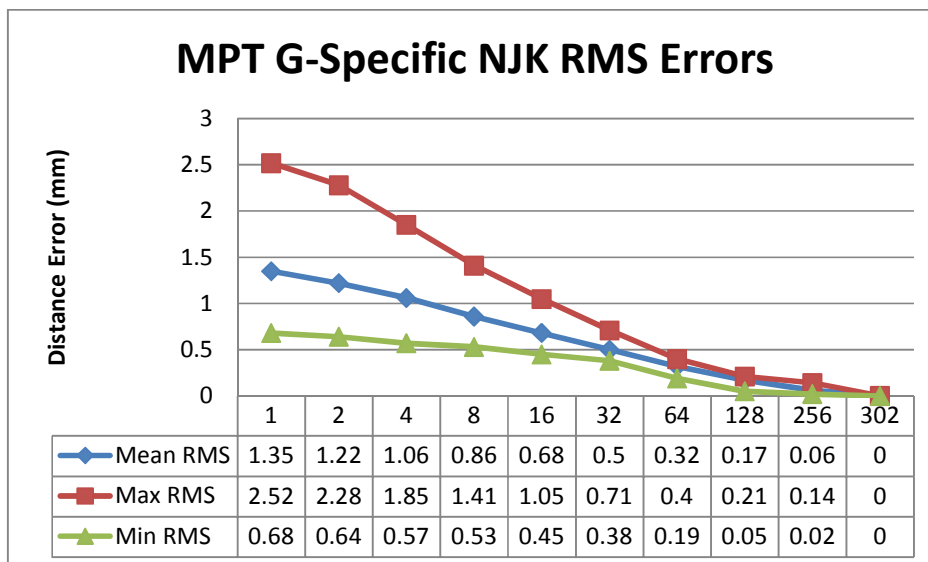


Figure 9.14 Mean, maximum, and minimum RMS errors for the models projection-reconstruction using gender-specific, non jack-knife atlas for the male proximal tibia

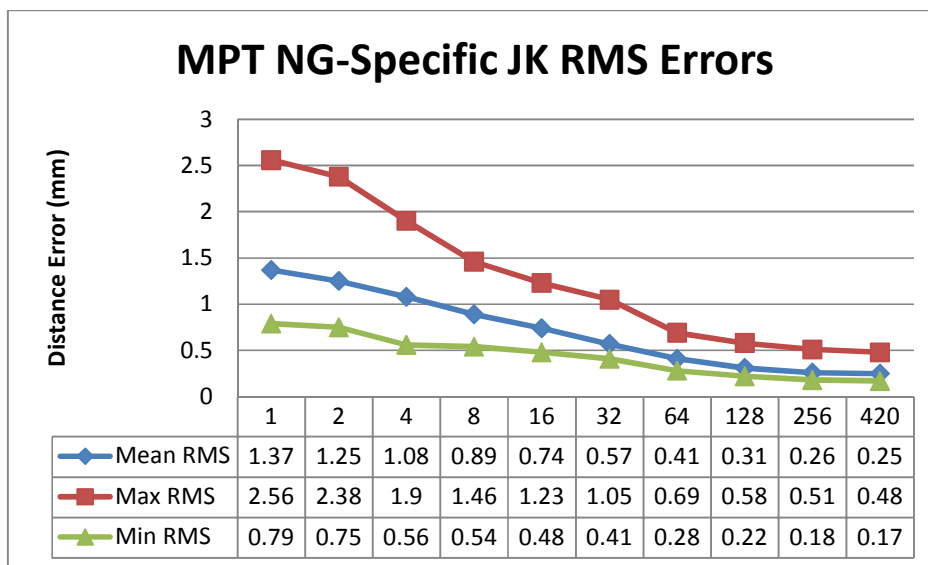


Figure 9.15 Mean, maximum, and minimum RMS errors for the models projection-reconstruction using non gender-specific, jack-knife atlas for the male proximal tibia

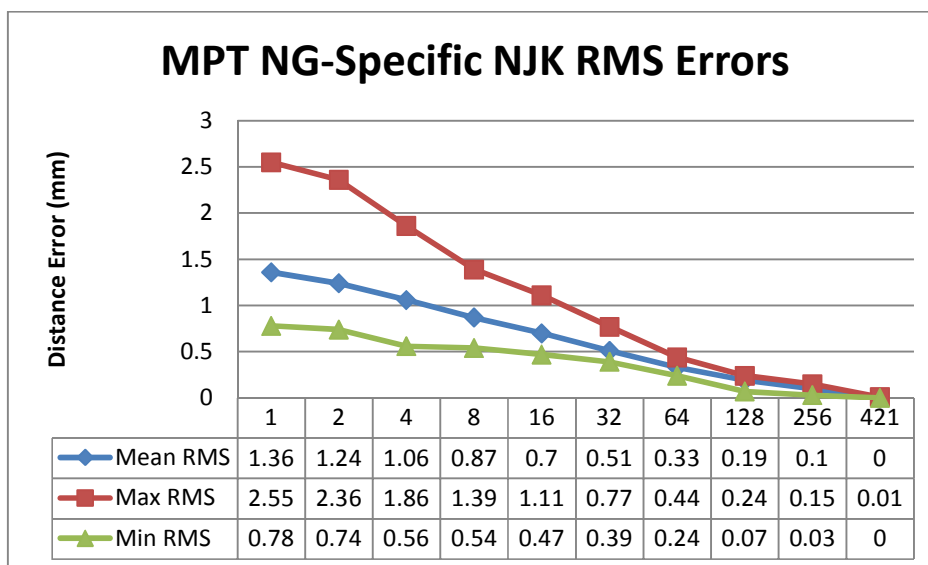


Figure 9.16 Mean, maximum, and minimum RMS errors for the models projection-reconstruction using non gender-specific, non jack-knife atlas for the male proximal tibia

9.2 Bone Morphing Analysis

9.2.1 Direction Set Method

9.2.1.1 Using unreduced point clouds

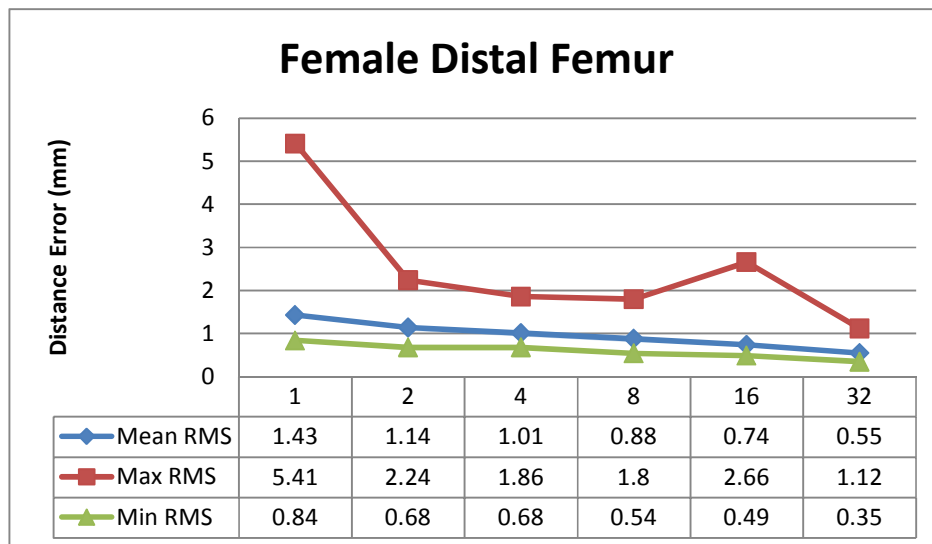


Figure 9.17 Mean, maximum, and minimum RMS errors for the female distal femur morphing using the Direction Set method for the unreduced models' point clouds

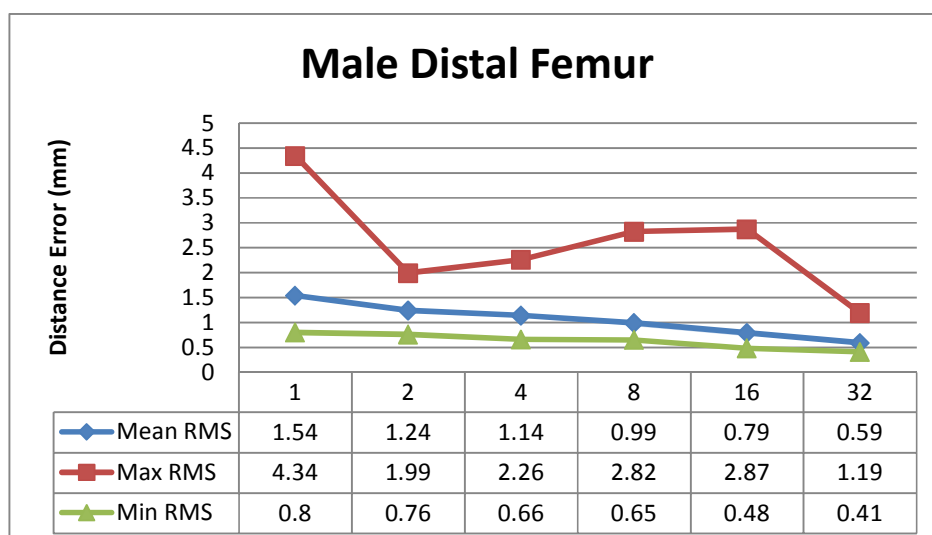


Figure 9.18 Mean, maximum, and minimum RMS errors for the male distal femur morphing using the Direction Set method for the unreduced models' point clouds

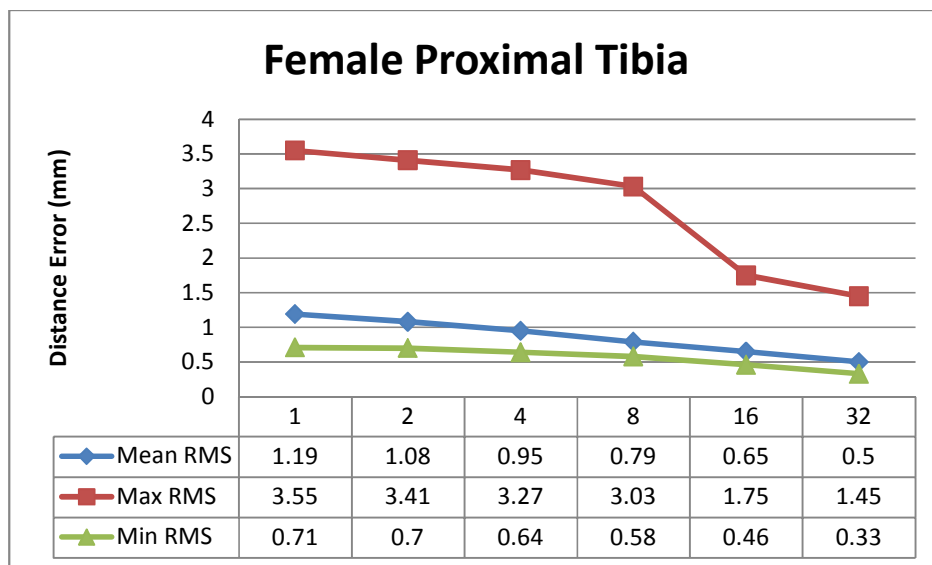


Figure 9.19 Mean, maximum, and minimum RMS errors for the female proximal tibia morphing using the Direction Set method for the unreduced models' point clouds

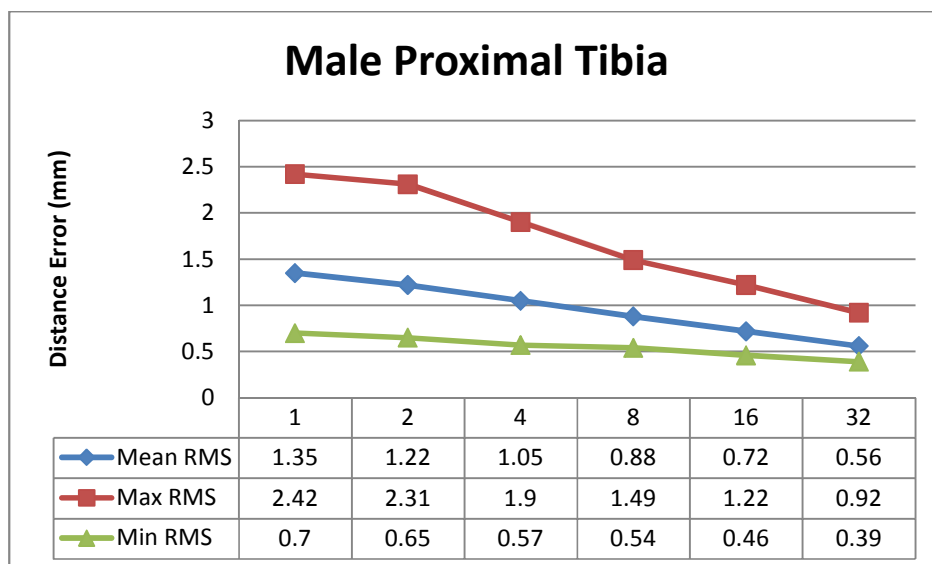


Figure 9.20 Mean, maximum, and minimum RMS errors for the male proximal tibia morphing using the Direction Set method for the unreduced models' point clouds

9.2.1.2 Using 4 mm reduced point clouds

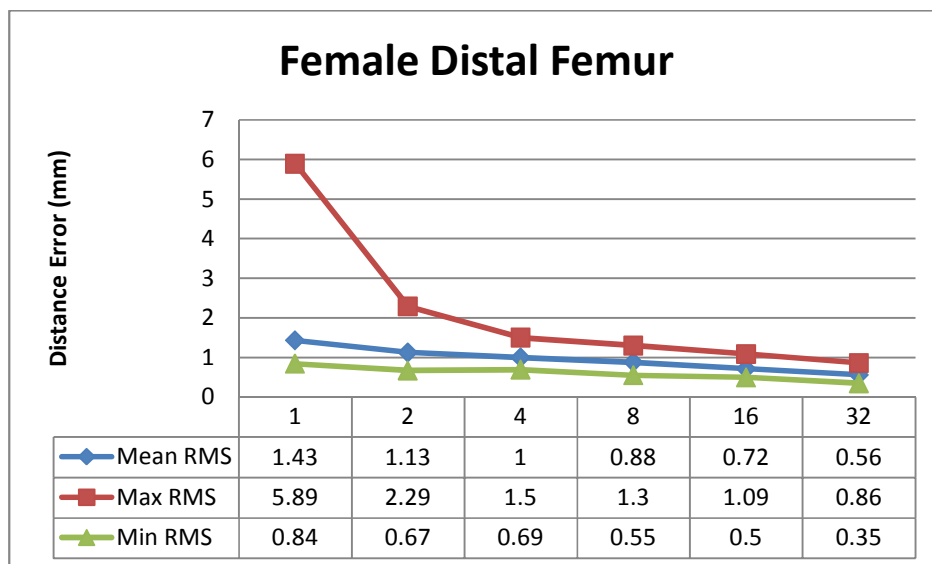


Figure 9.21 Mean, maximum, and minimum RMS errors for the female distal femur morphing using the Direction Set method for the 4 mm reduced models' point clouds

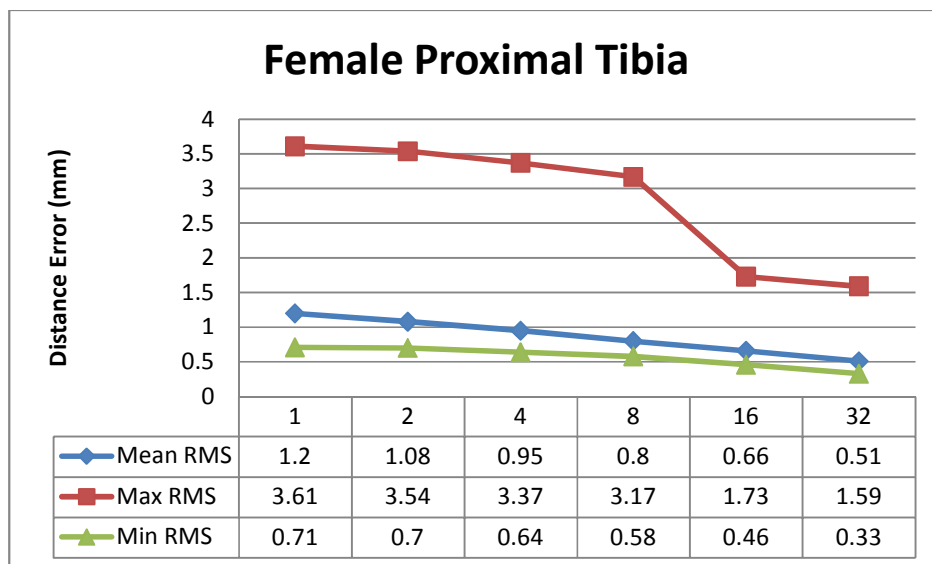


Figure 9.22 Mean, maximum, and minimum RMS errors for the female proximal tibia morphing using the Direction Set method for the 4 mm reduced models' point clouds

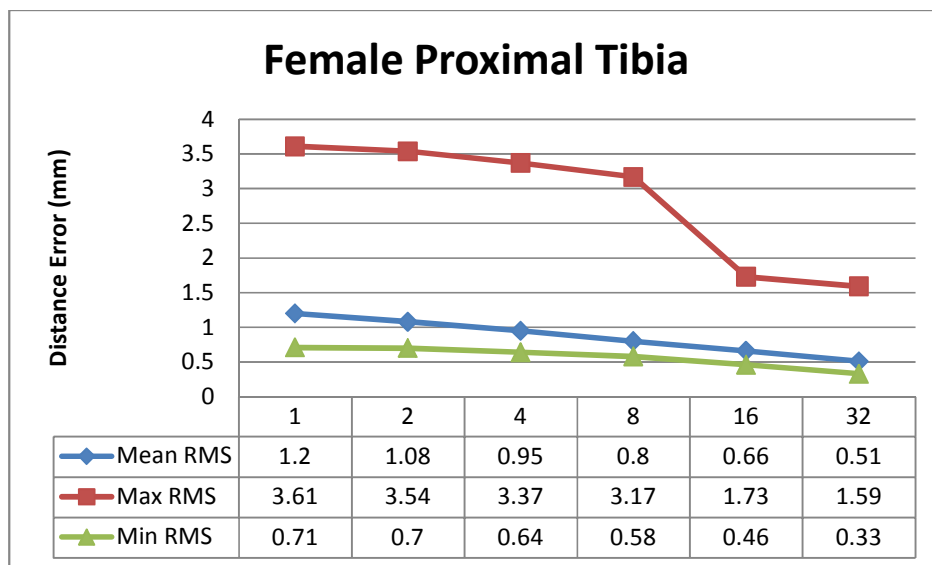


Figure 9.23 Mean, maximum, and minimum RMS errors for the female proximal tibia morphing using the Direction Set method for the 4 mm reduced models' point clouds

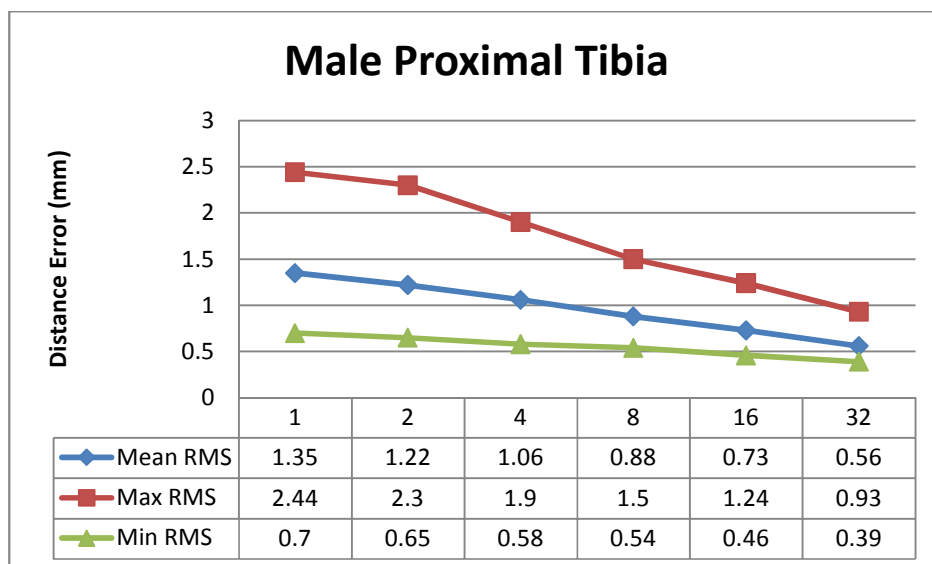


Figure 9.24 Mean, maximum, and minimum RMS errors for the male proximal tibia morphing using the Direction Set method for the 4 mm reduced models' point clouds

9.2.1.3 Using 8 mm reduced point clouds

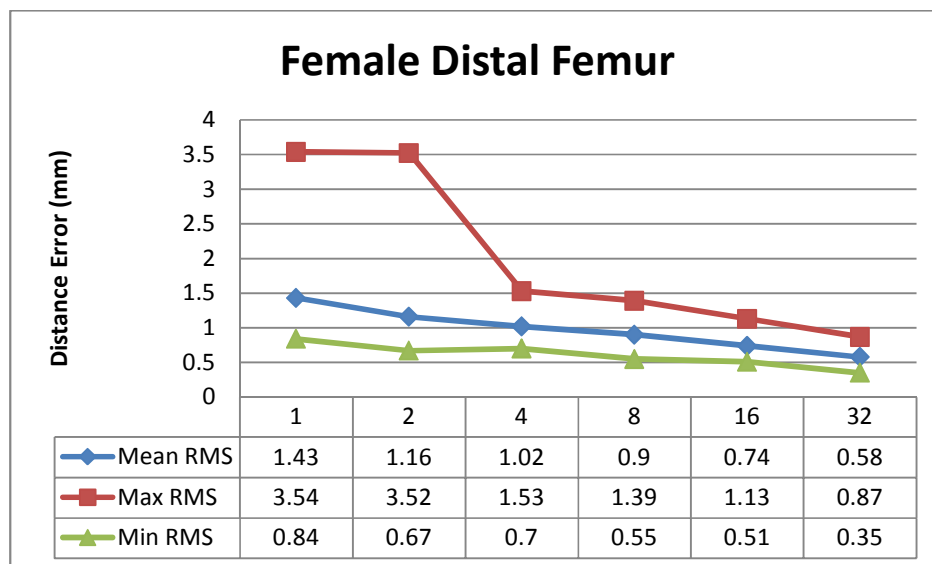


Figure 9.25 Mean, maximum, and minimum RMS errors for the female distal femur morphing using the Direction Set method for the 8 mm reduced models' point clouds

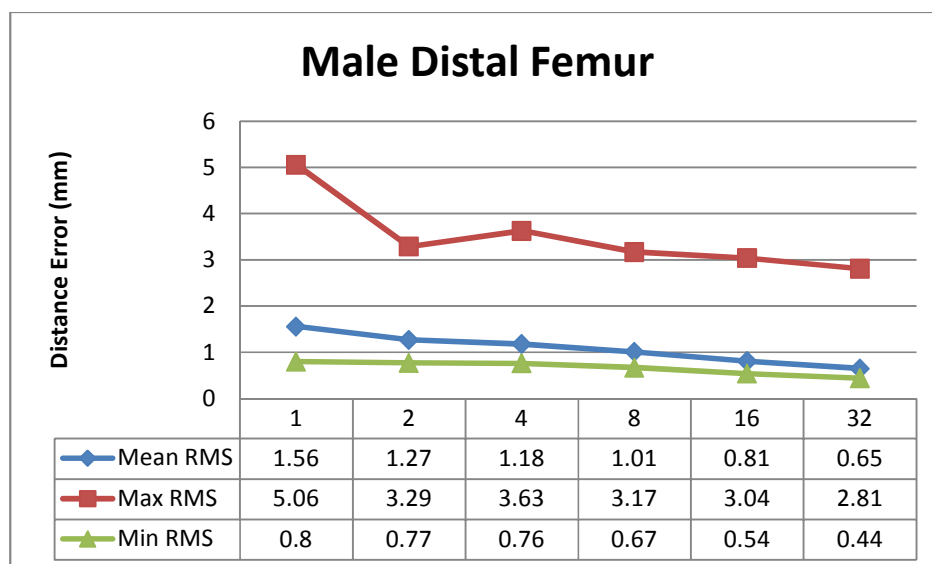


Figure 9.26 an, maximum, and minimum RMS errors for the male distal femur morphing using the Direction Set method for the 8 mm reduced models' point clouds

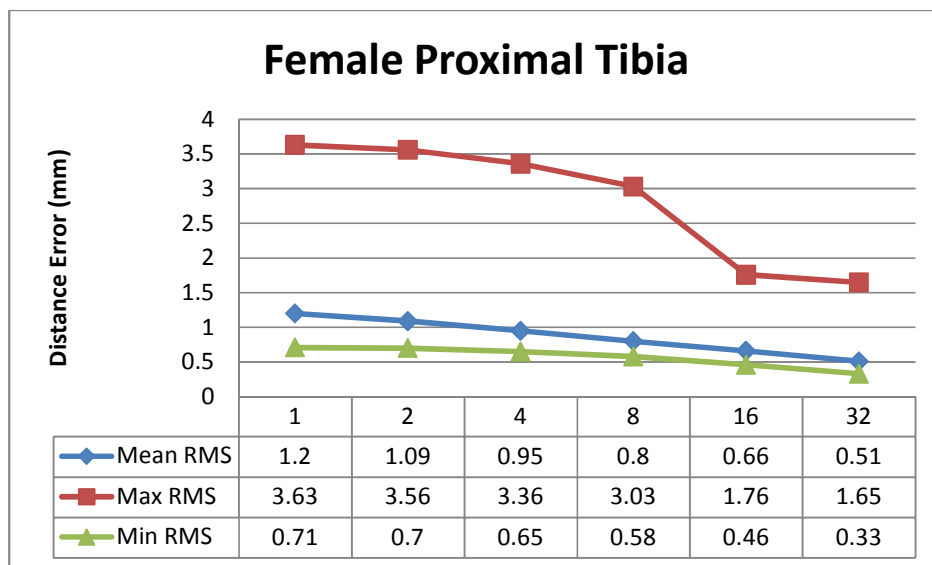


Figure 9.27 Mean, maximum, and minimum RMS errors for the female proximal tibia morphing using the Direction Set method for the 8 mm reduced models' point clouds

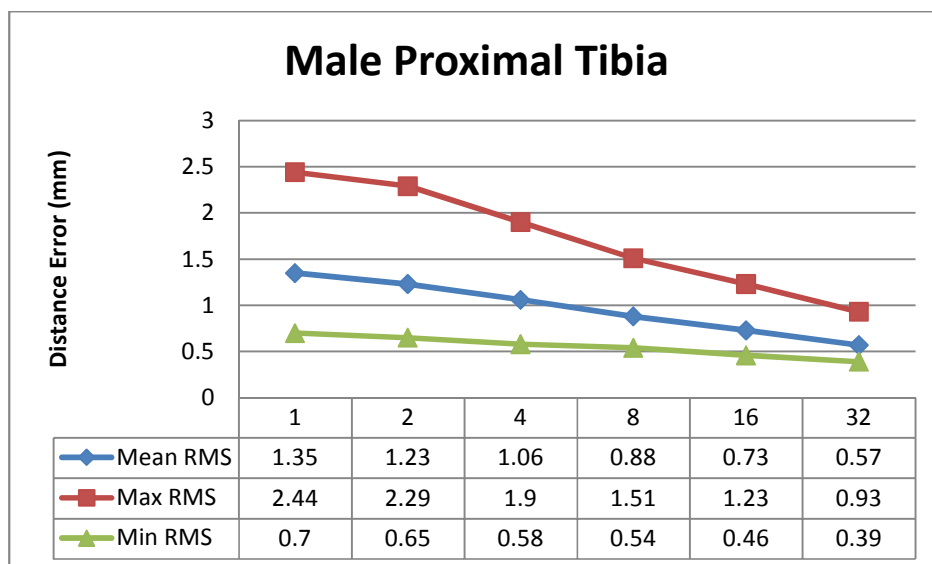


Figure 9.28 Mean, maximum, and minimum RMS errors for the male proximal tibia morphing using the Direction Set method for the 8 mm reduced models' point clouds

9.2.1.4 Using 16 mm reduced point clouds

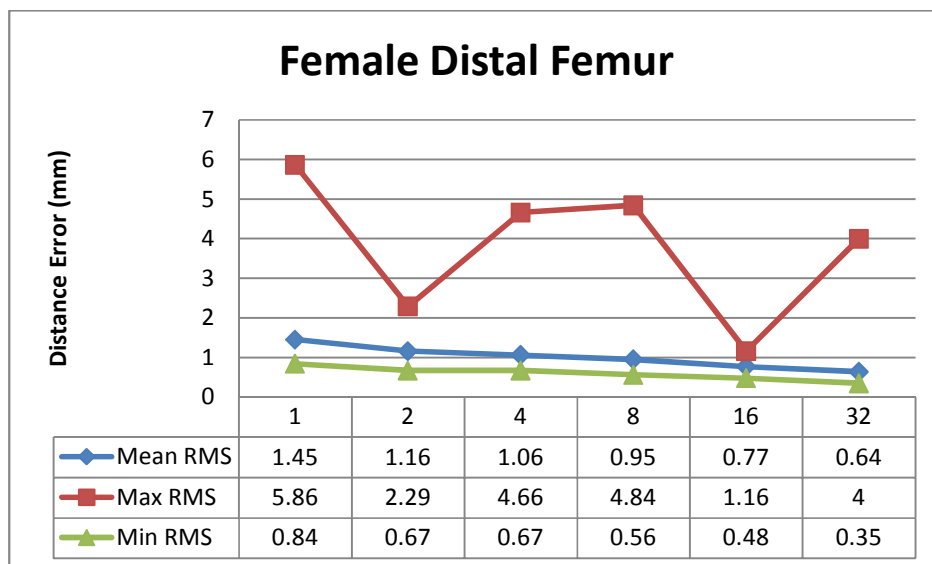


Figure 9.29 Mean, maximum, and minimum RMS errors for the female distal femur morphing using the Direction Set method for the 16 mm reduced models' point clouds

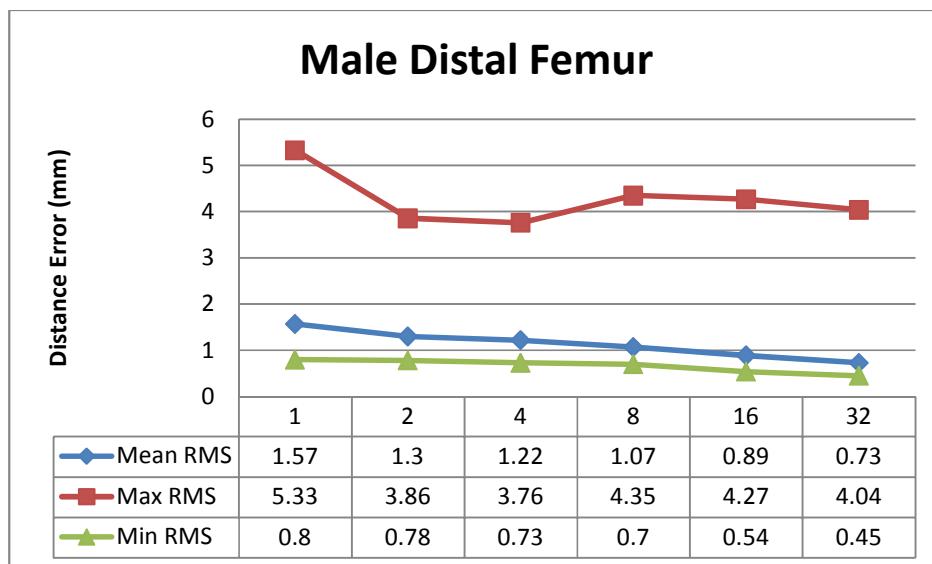


Figure 9.30 Mean, maximum, and minimum RMS errors for the male distal femur morphing using the Direction Set method for the 16 mm reduced models' point clouds

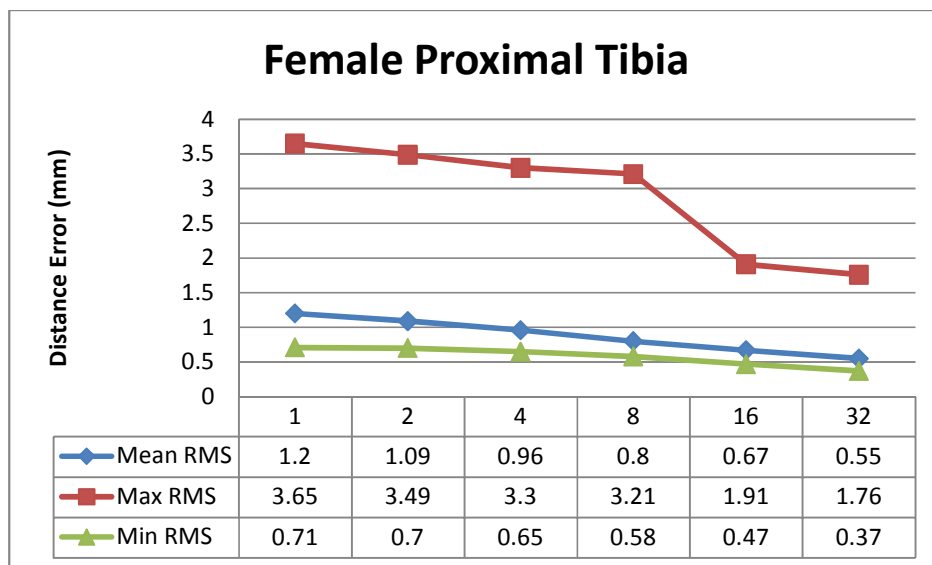


Figure 9.31 Mean, maximum, and minimum RMS errors for the female proximal tibia morphing using the Direction Set optimization method for the 16 mm reduced models' point clouds

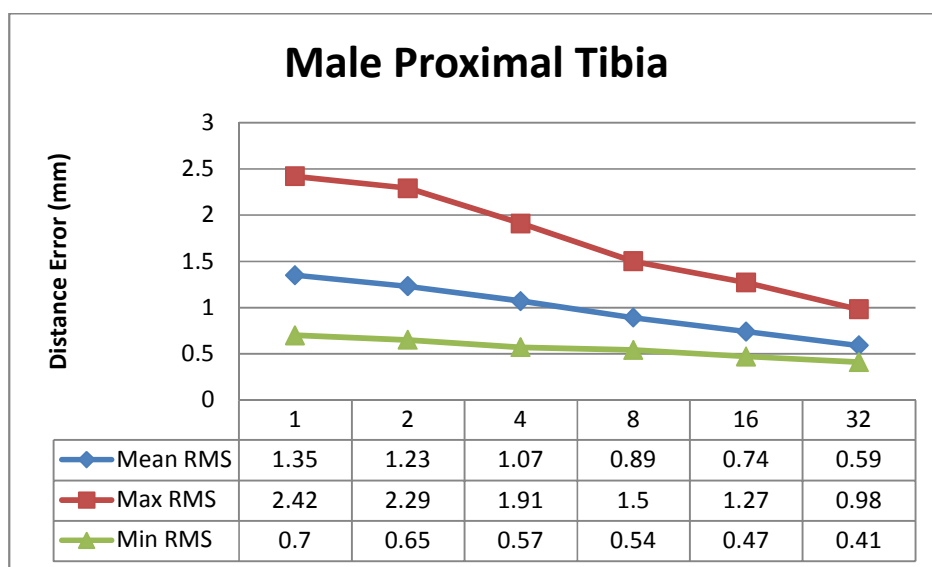


Figure 9.32 Mean, maximum, and minimum RMS errors for the male proximal tibia morphing using the Direction Set method for the 16 mm reduced models' point clouds

9.2.1.5 Using 32 mm point clouds

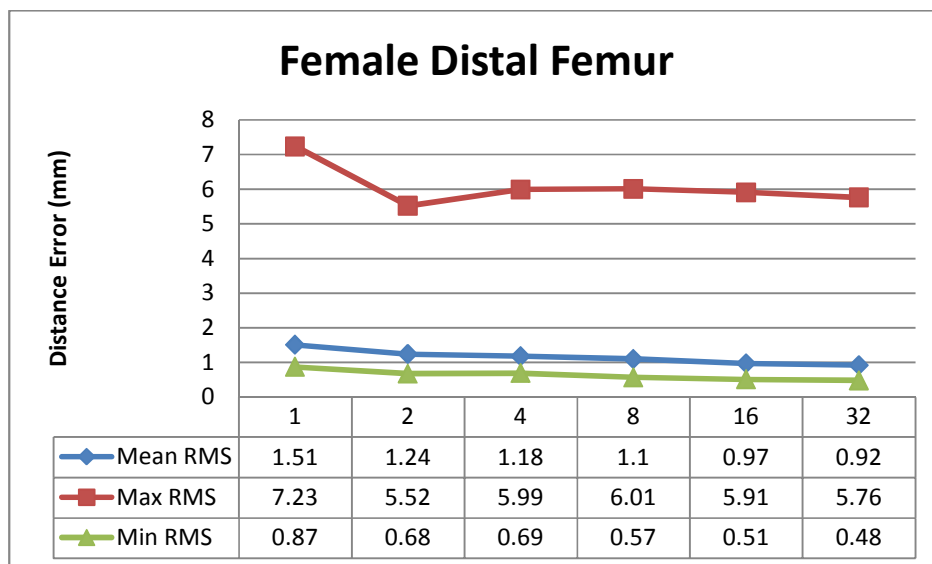


Figure 9.33 Mean, maximum, and minimum RMS errors for the female distal femur using the Direction Set method for the 32 mm reduced models' point clouds

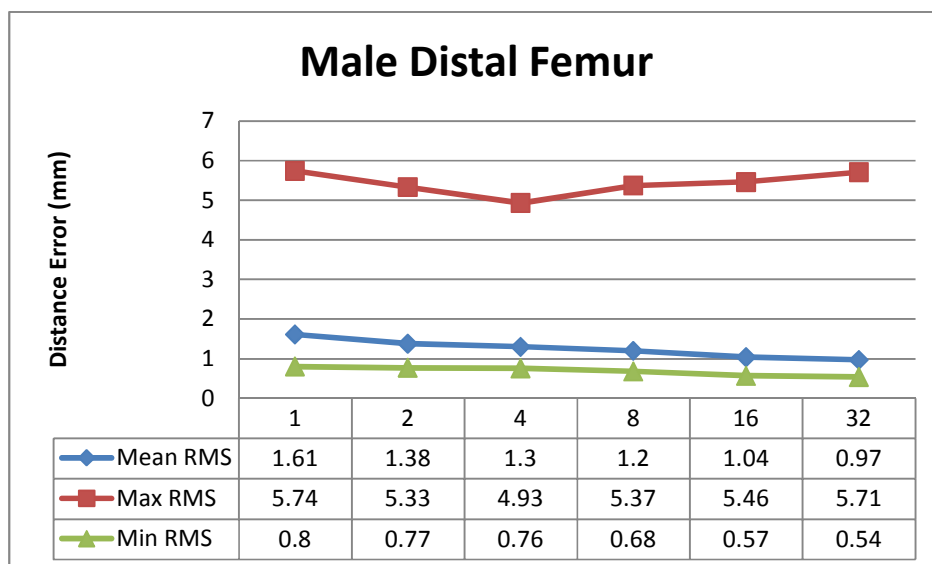


Figure 9.34 Mean, maximum, and minimum RMS errors for the male distal femur using the Direction Set method for the 32 mm reduced models' point clouds

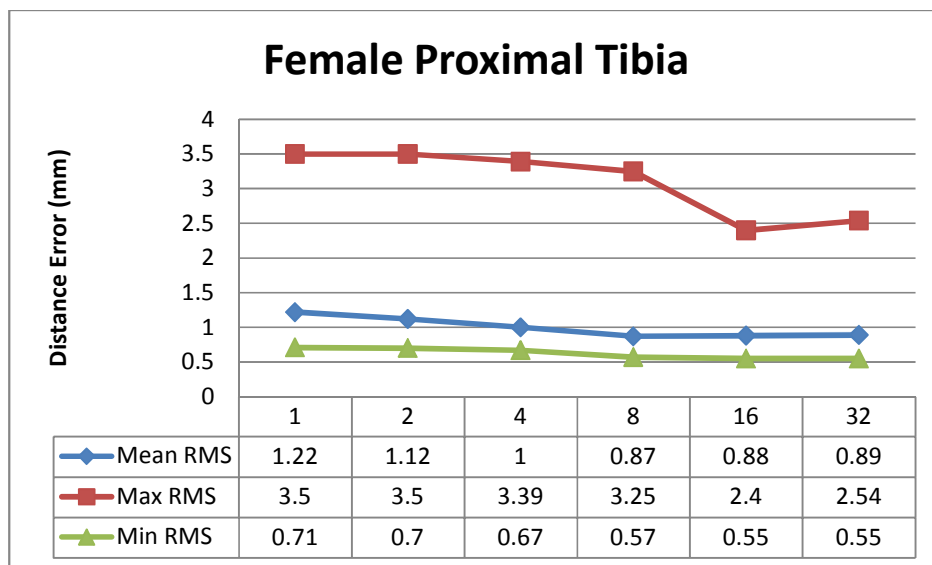


Figure 9.35 Mean, maximum, and minimum RMS errors for the female proximal tibia using the Direction Set method for the 32 mm reduced models' point clouds

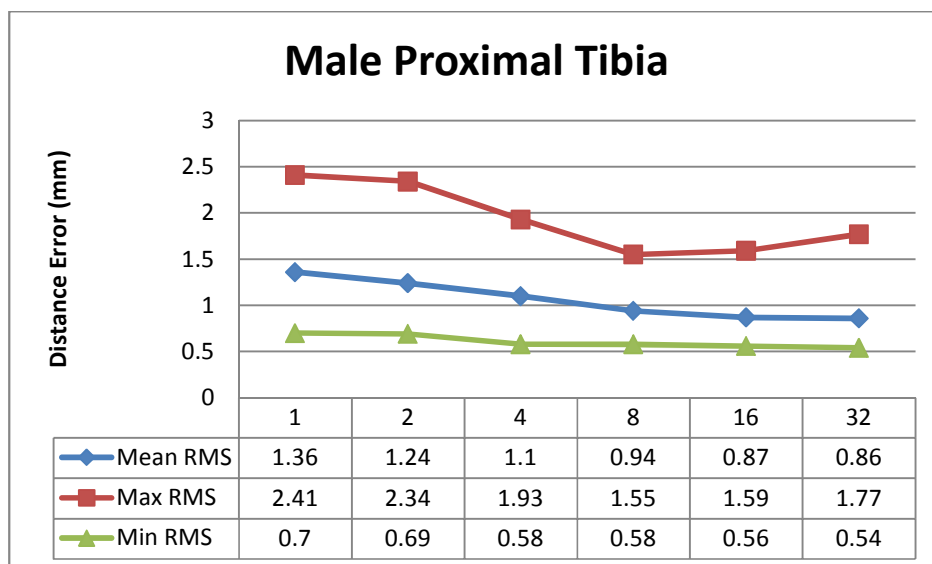


Figure 9.36 Mean, maximum, and minimum RMS errors for the male proximal tibia using the Direction Set method for the 32 mm reduced models' point clouds

9.2.2 Linear Least Squares Method

9.2.2.1 Using unreduced point clouds

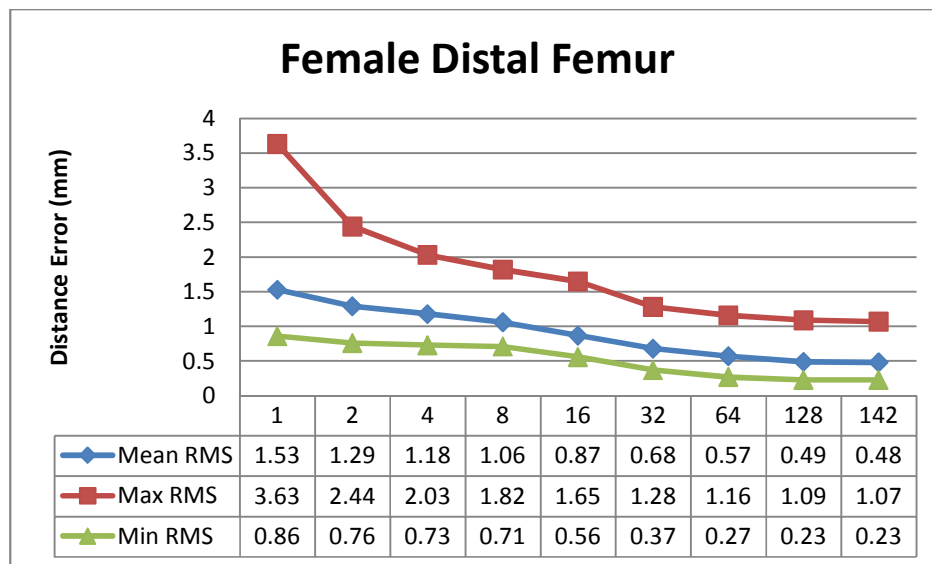


Figure 9.37 Mean, maximum, and minimum RMS errors for the female distal femur using the linear least squares method for the unreduced models' point clouds

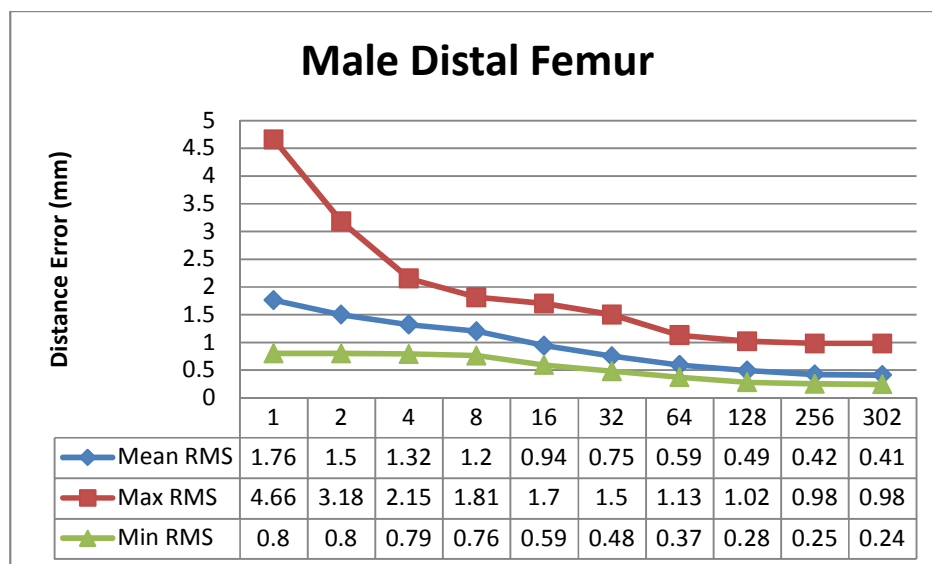


Figure 9.38 Mean, maximum, and minimum RMS errors for the male distal femur using the linear least squares method for the unreduced models' point clouds

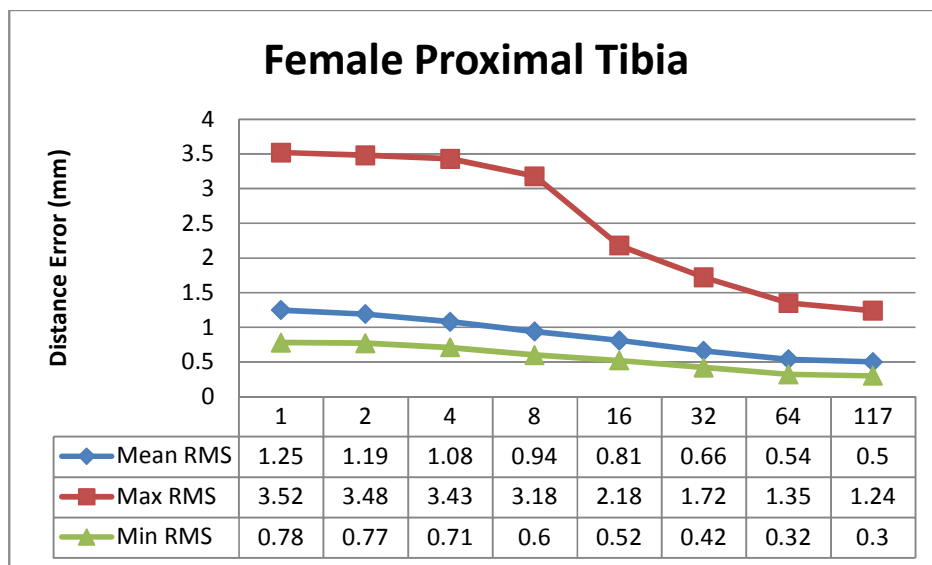


Figure 9.39 Mean, maximum, and minimum RMS errors for the female proximal tibia using the linear least squares method for the unreduced models' point clouds

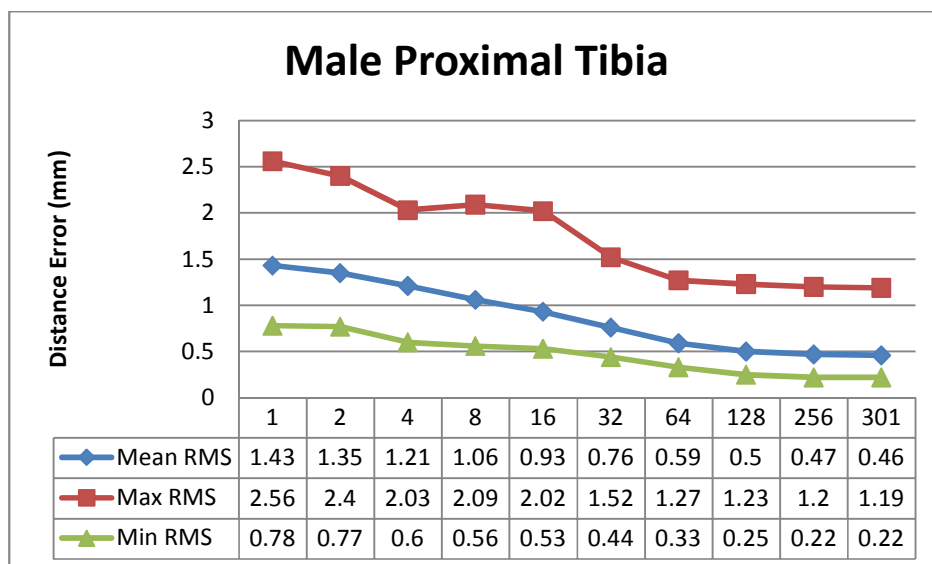


Figure 9.40 Mean, maximum, and minimum RMS errors for the male proximal tibia using the linear least squares method for the unreduced models' point clouds

9.2.2.1 Using 4 mm point clouds

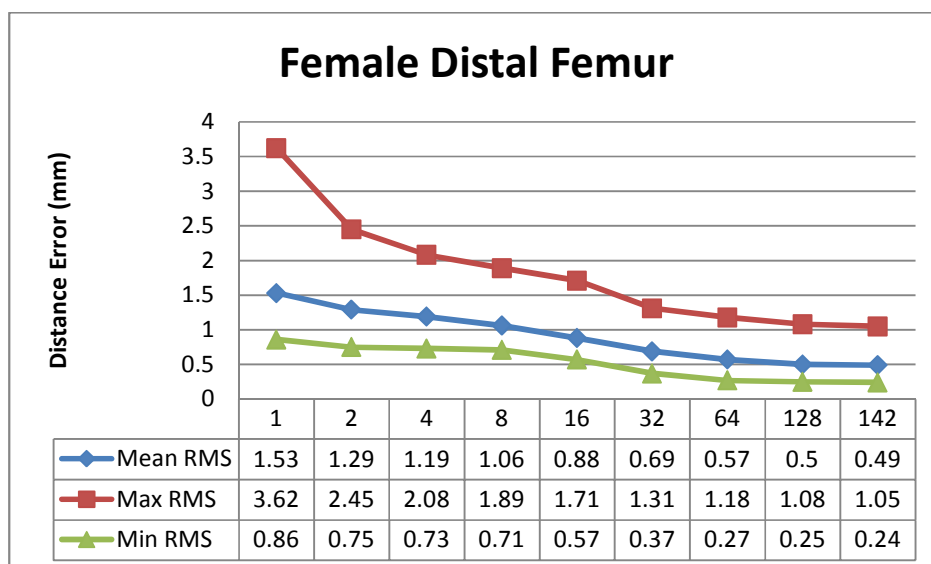


Figure 9.41 Mean, maximum, and minimum RMS errors for the female proximal tibia using the linear least squares method for the 4 mm reduced models' point clouds

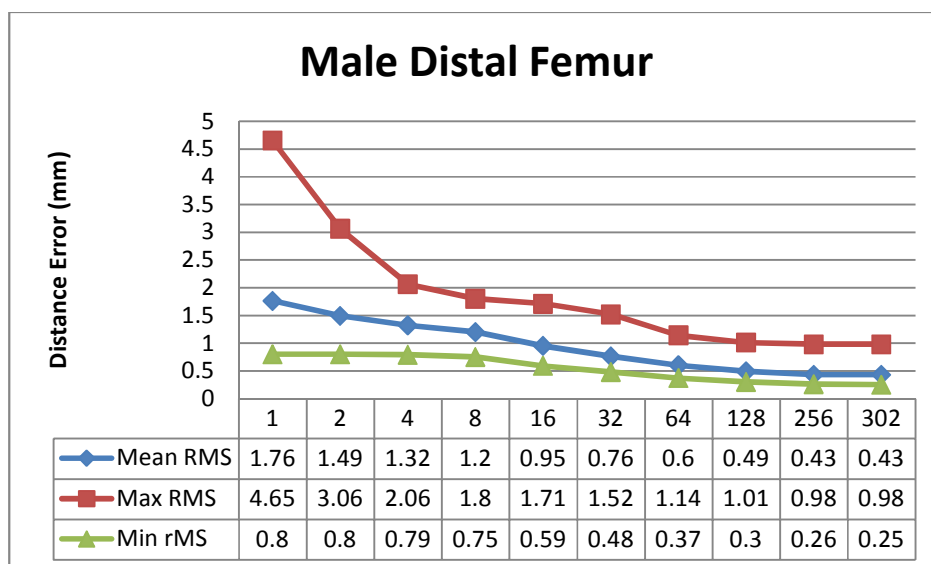


Figure 9.42 Mean, maximum, and minimum RMS errors for the female proximal tibia using the linear least squares method for the 4 mm reduced models' point clouds using

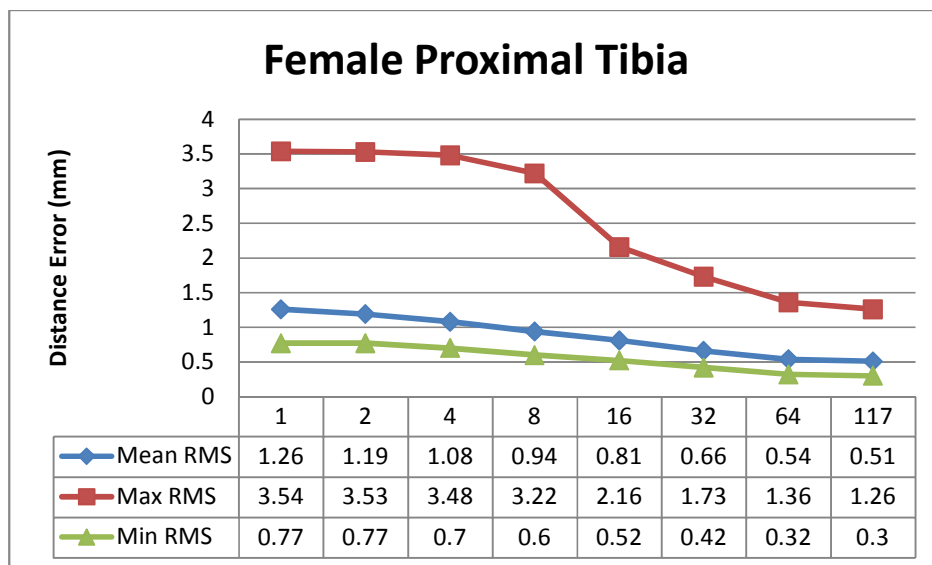


Figure 9.43 Mean, maximum, and minimum RMS errors for the female proximal tibia using the linear least squares method for the 4 mm reduced models' point clouds

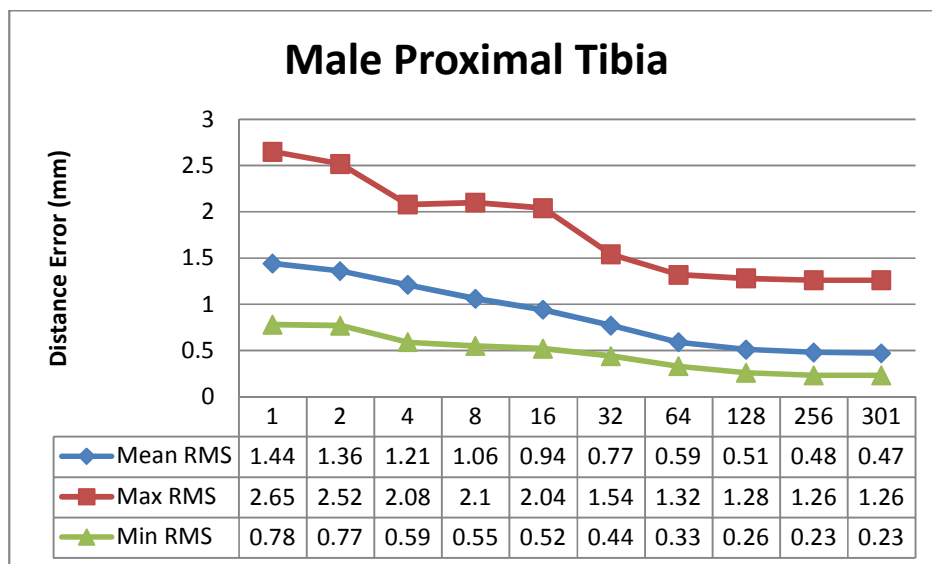


Figure 9.44 Mean, maximum, and minimum RMS errors for the male proximal tibia using the linear least squares method for the 4 mm reduced models' point clouds

9.2.2.2 Using 8 mm point clouds

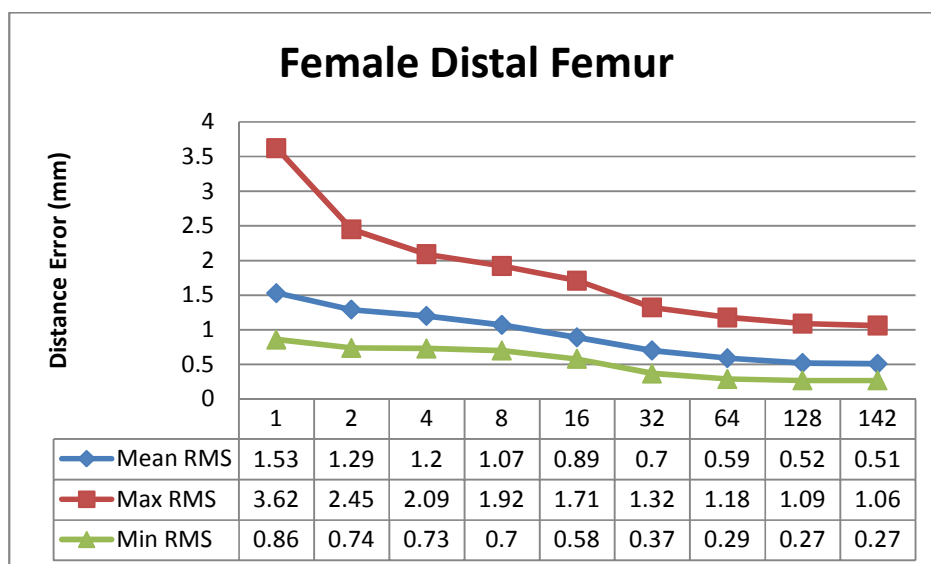


Figure 9.45 Mean, maximum, and minimum RMS errors for the female distal femur using the linear least squares method for the 8 mm reduced models' point clouds

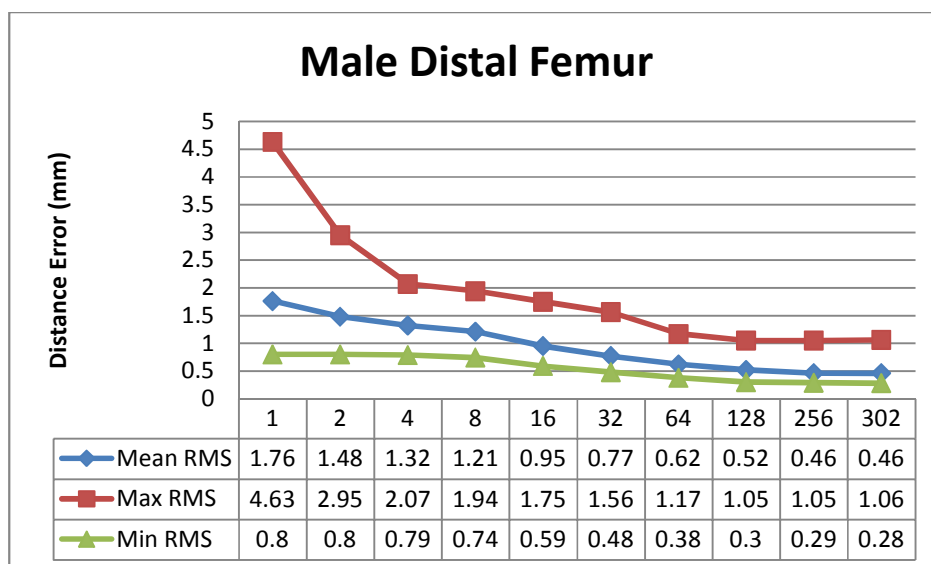


Figure 9.46 Mean, maximum, and minimum RMS errors for the female distal femur using the linear least squares method for the 8 mm reduced models' point clouds

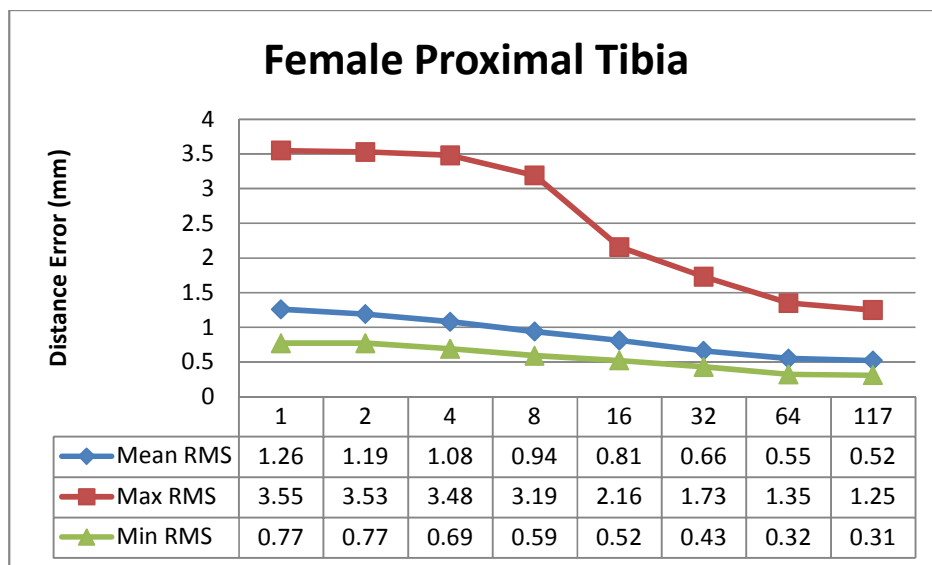


Figure 9.47 Mean, maximum, and minimum RMS errors for the female proximal tibia using the linear least squares method for the 8 mm reduced models' point

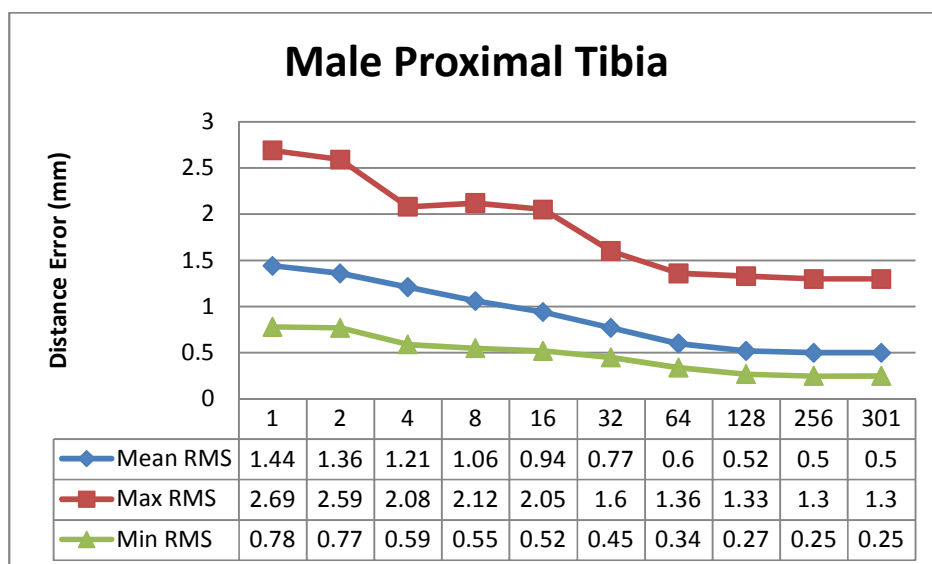


Figure 9.48 Mean, maximum, and minimum RMS errors for the male proximal tibia using the linear least squares method for the 8 mm reduced models' point clouds

9.2.2.3 Using 16 mm point clouds

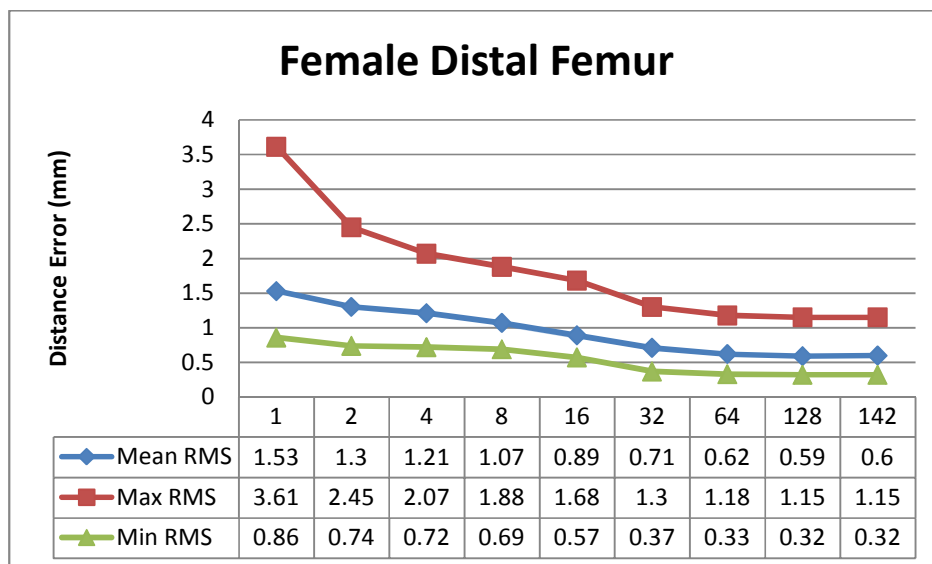


Figure 9.49 Mean, maximum, and minimum RMS errors for the female distal femur using the linear least squares method for the 16 mm reduced models' point clouds

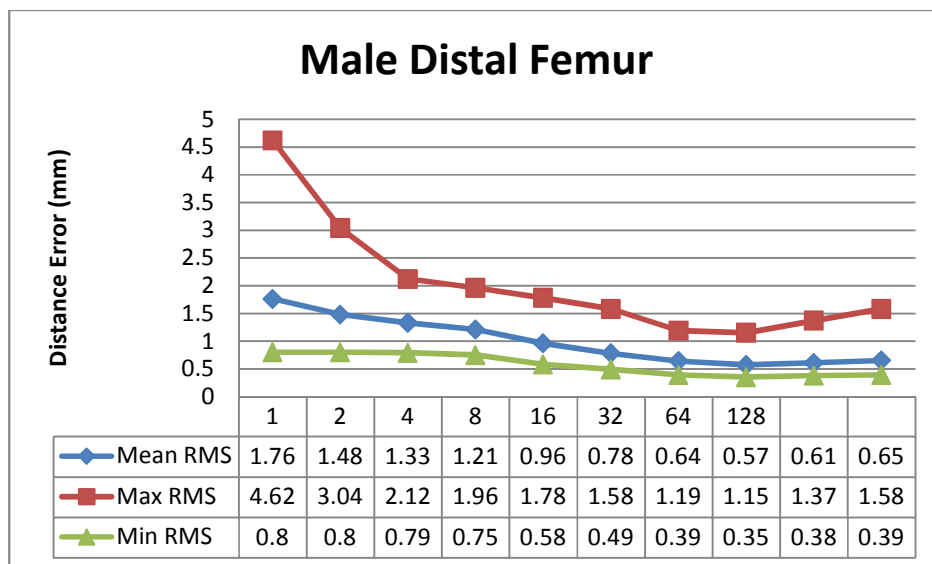


Figure 9.50 Mean, maximum, and minimum RMS errors for the male distal femur using the linear least squares method for the 16 mm reduced models' point clouds

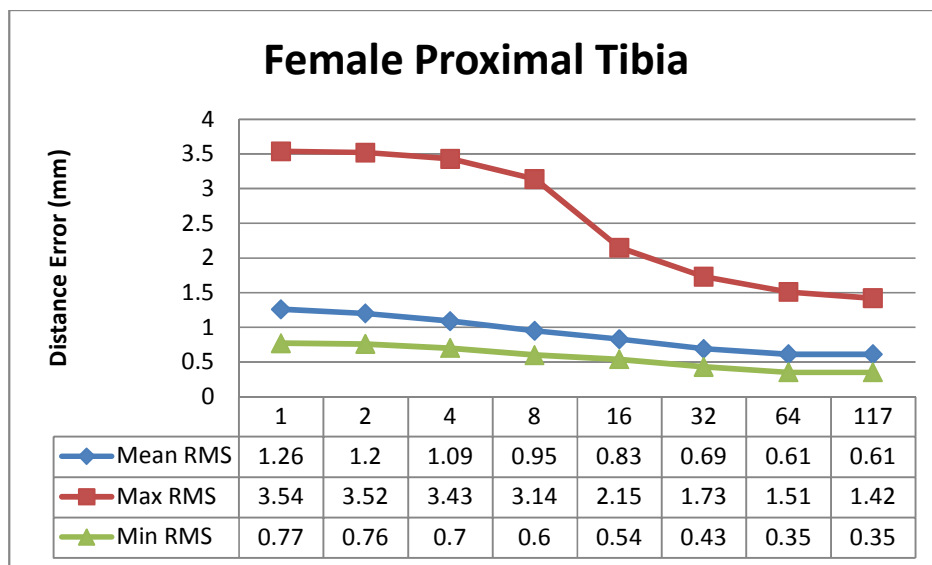


Figure 9.51 Mean, maximum, and minimum RMS errors for the female proximal tibia using the linear least squares method for the 16 mm reduced models' point clouds

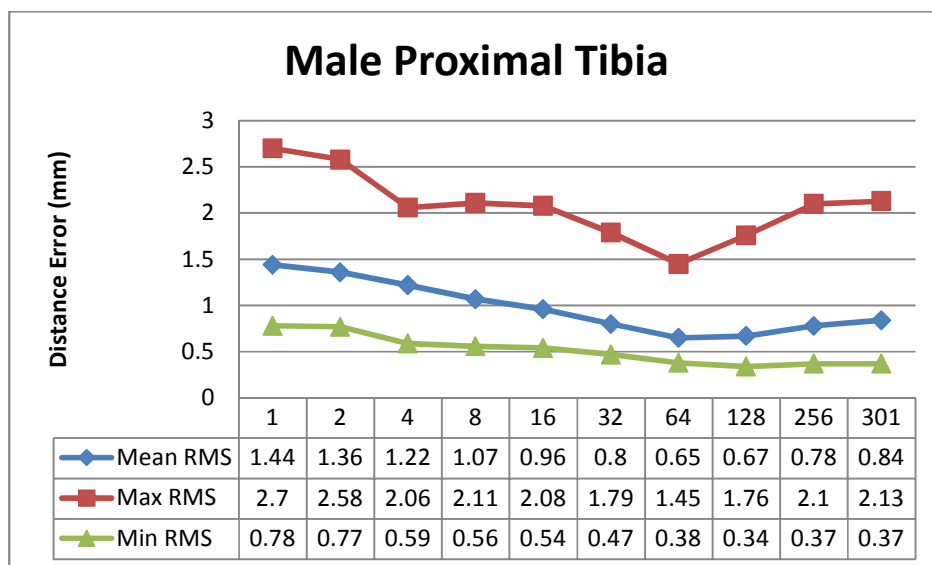


Figure 9.52 Mean, maximum, and minimum RMS errors for the male proximal tibia using the linear least squares method for the 16 mm reduced models' point clouds Hybrid Morphing

9.2.3 Hybrid Method

9.2.3.1 Using unreduced point clouds

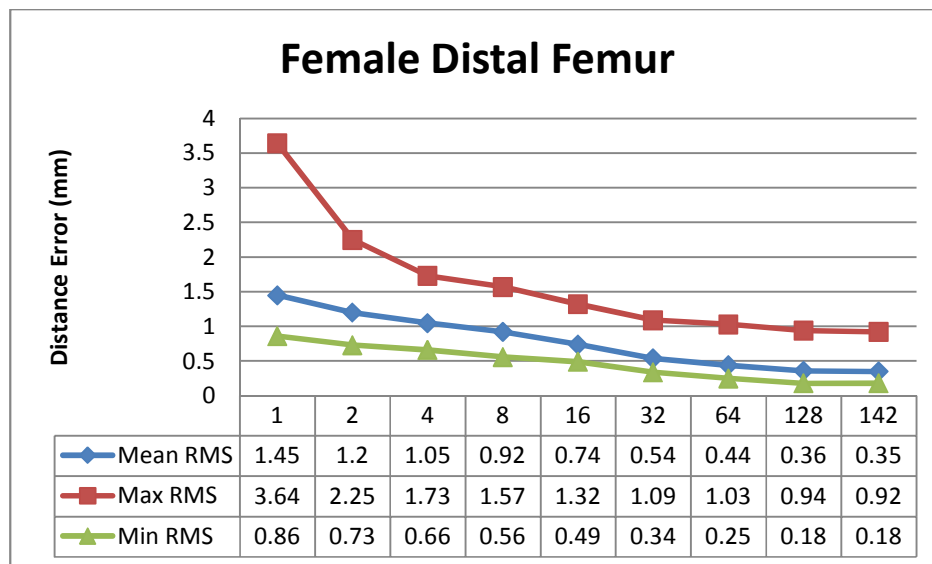


Figure 9.53 Mean, maximum, and minimum RMS errors for the female distal femur using the hybrid method for the unreduced models' point clouds

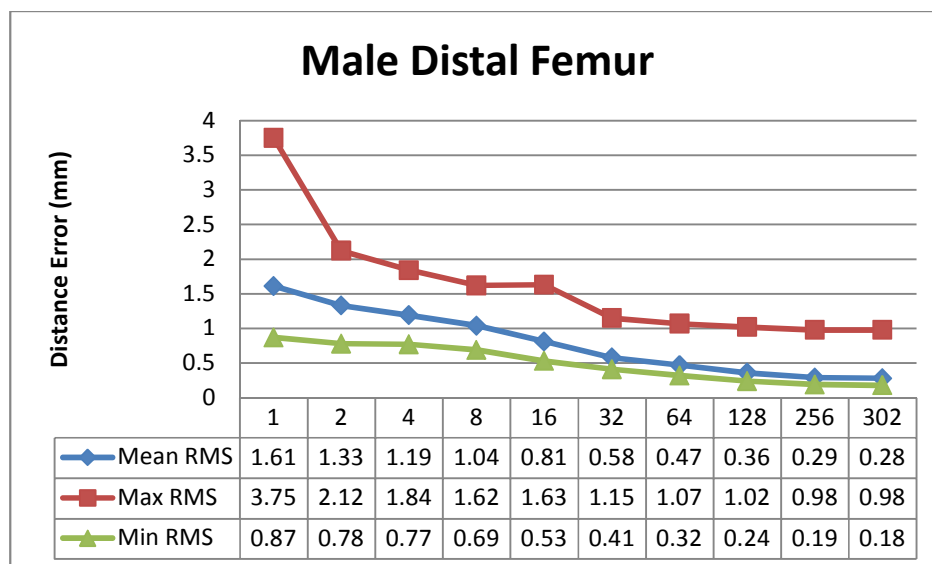


Figure 9.54 Mean, maximum, and minimum RMS errors for the male distal femur using the hybrid method for the unreduced models' point clouds

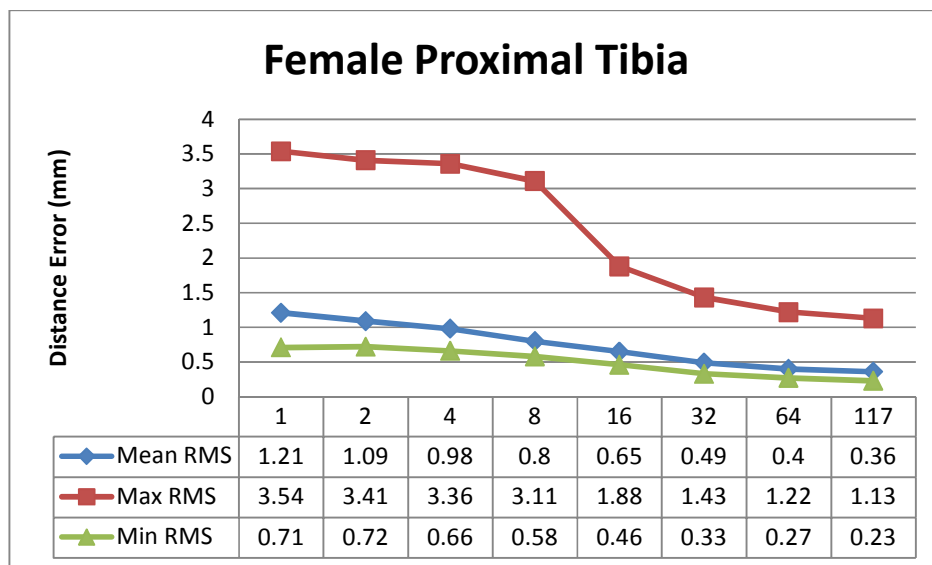


Figure 9.55 Mean, maximum, and minimum RMS errors for the female proximal tibia using the hybrid method for the unreduced models' point clouds

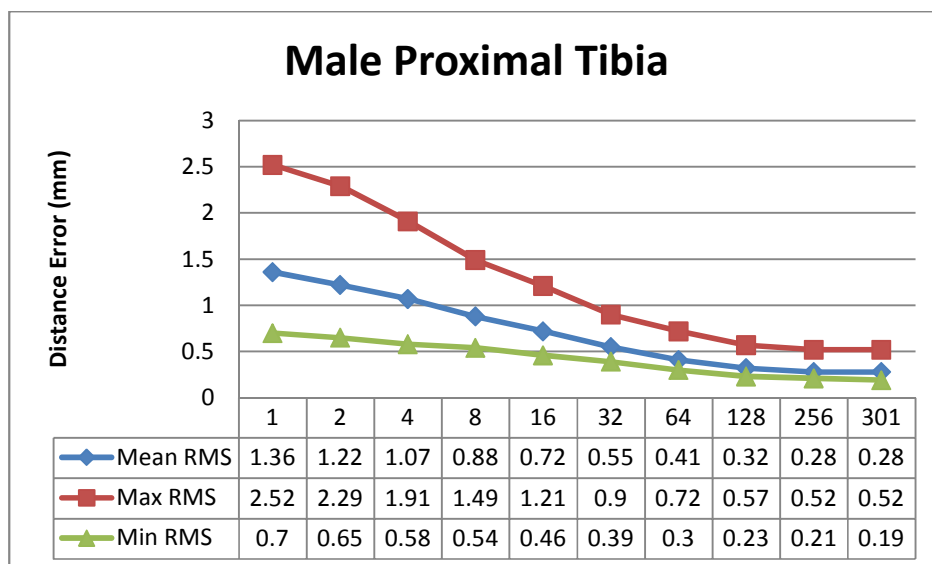


Figure 9.56 Mean, maximum, and minimum RMS errors for the male proximal tibia using the hybrid method for the unreduced models' point clouds

9.2.3.2 Using 4 mm point clouds

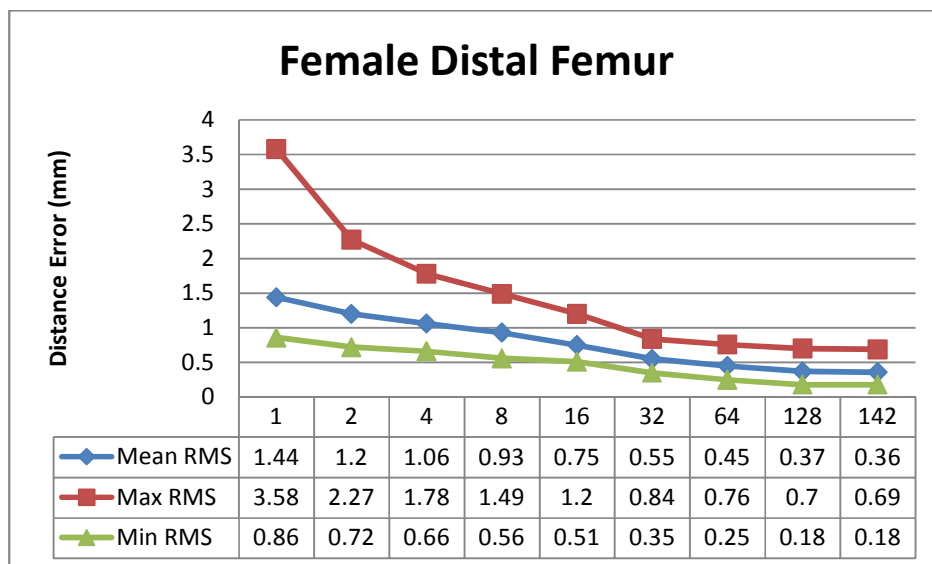


Figure 9.57 Mean, maximum, and minimum RMS errors for the female distal femur using the hybrid method for the 4 mm reduced models' point clouds

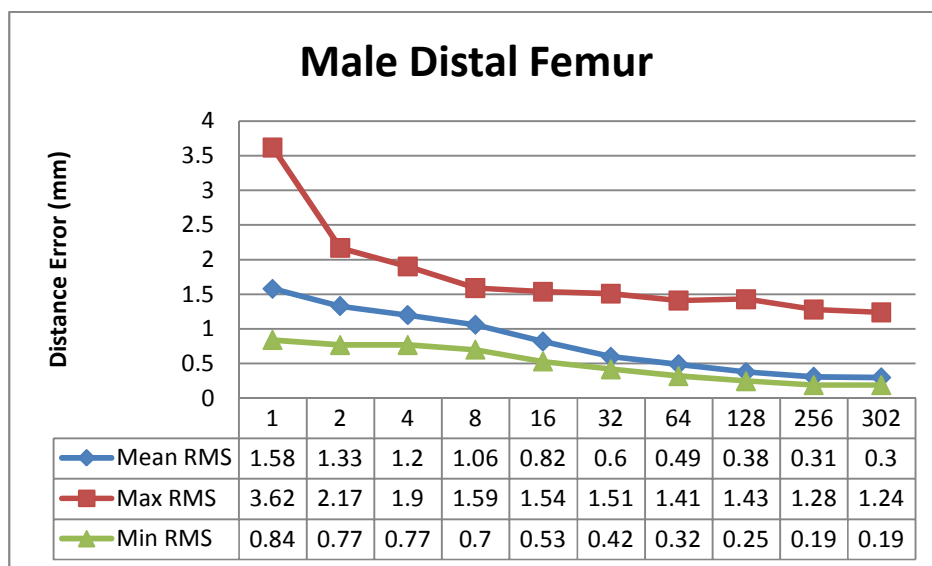


Figure 9.58 Mean, maximum, and minimum RMS errors for the male distal femur using the hybrid method for the 4 mm reduced models' point clouds

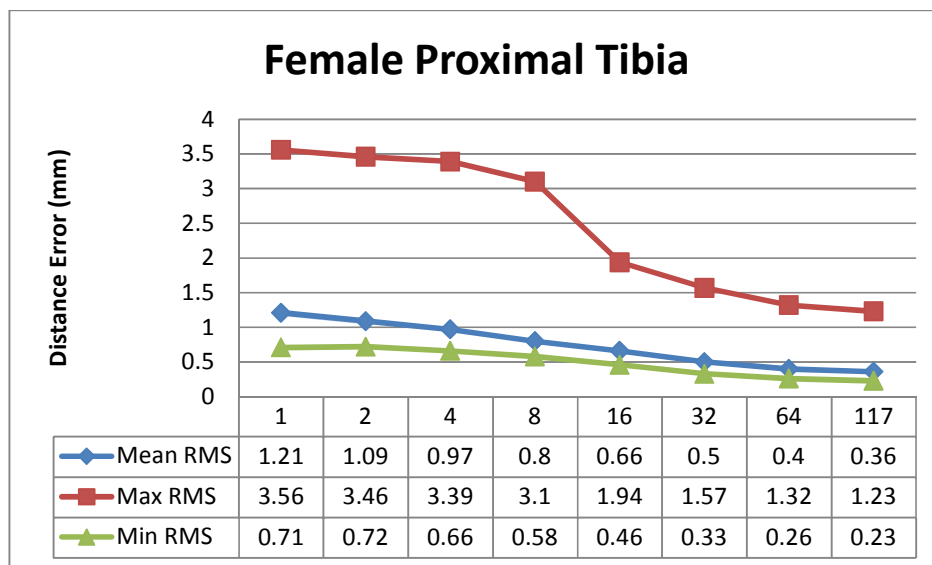


Figure 9.59 Mean, maximum, and minimum RMS errors for the female proximal tibia using the hybrid method for the 4 mm reduced models' point clouds

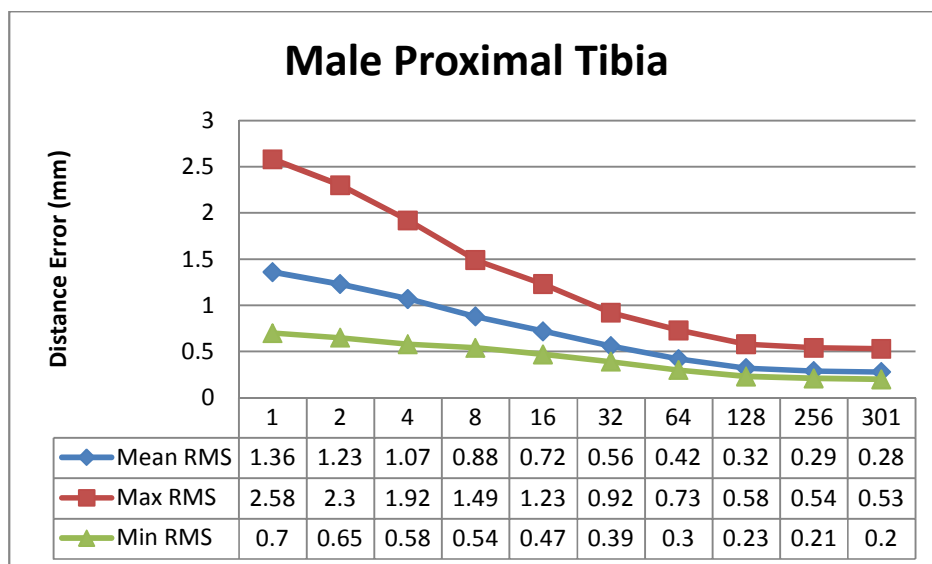


Figure 9.60 Mean, maximum, and minimum RMS errors for the male proximal tibia using the hybrid morphing method for the 4 mm reduced models' point clouds

9.2.3.3 Using 8 mm point clouds

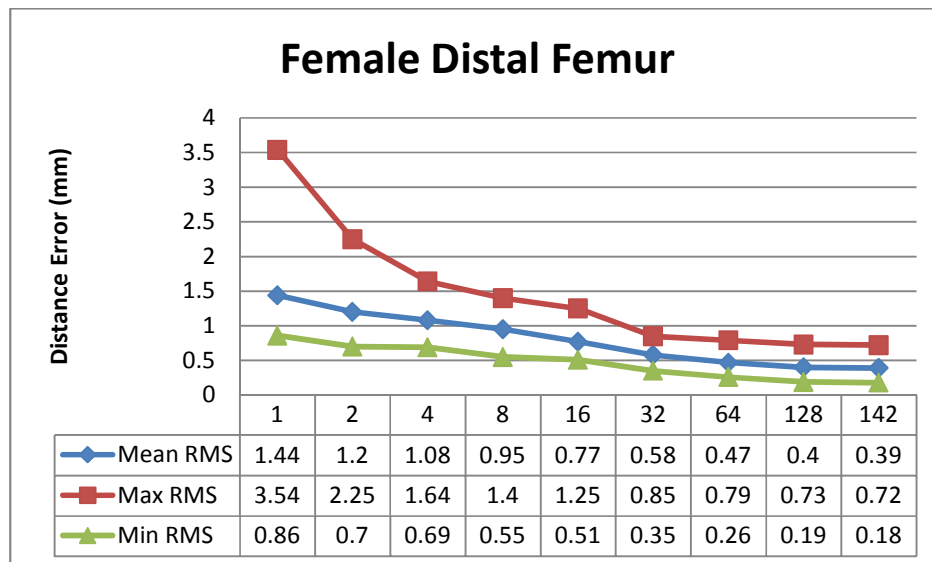


Figure 9.61 Mean, maximum, and minimum RMS errors for the female distal femur using the hybrid method for the 8 mm reduced models' point clouds

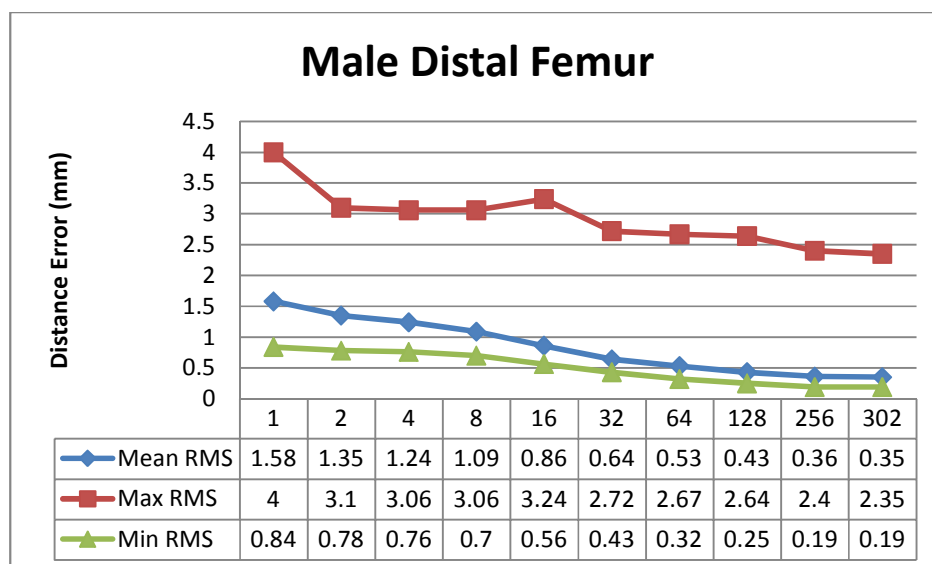


Figure 9.62 Mean, maximum, and minimum RMS errors for the male distal femur using the hybrid method for the 8 mm reduced models' point clouds

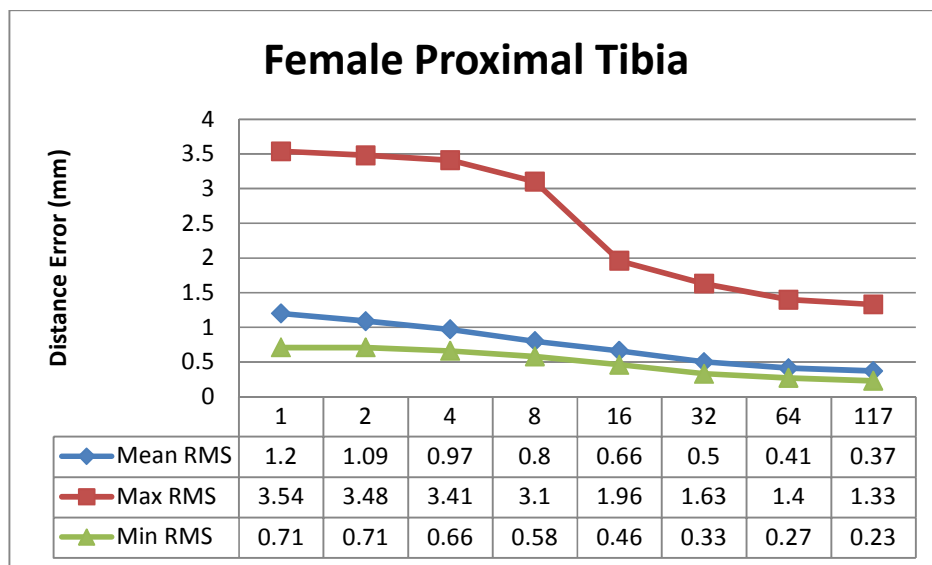


Figure 9.63 Mean, maximum, and minimum RMS errors for the female proximal tibia using the hybrid method for the 8 mm reduced models' point clouds

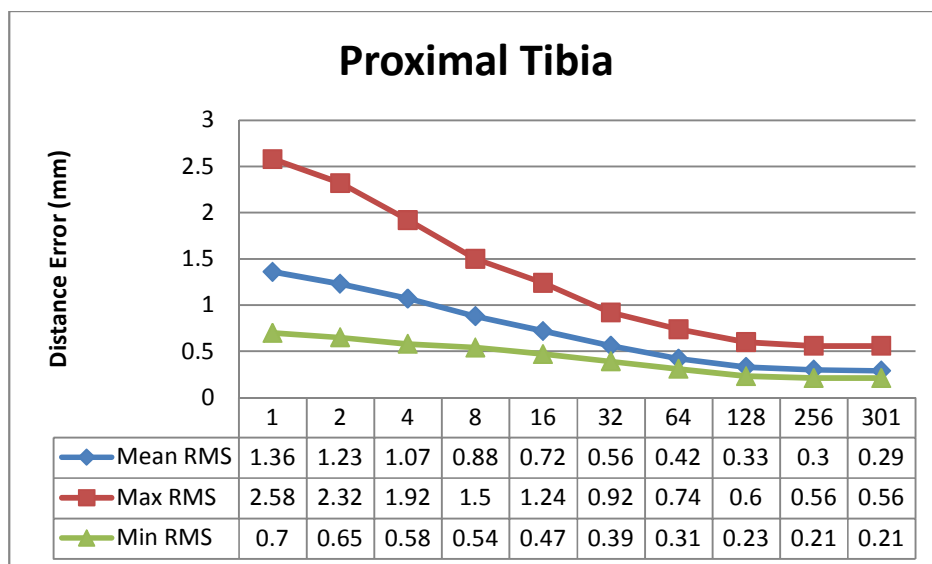


Figure 9.64 Mean, maximum, and minimum RMS errors for the male proximal tibia using the hybrid method for the 8 mm reduced models' point clouds

9.2.3.4 Using 16 mm point clouds

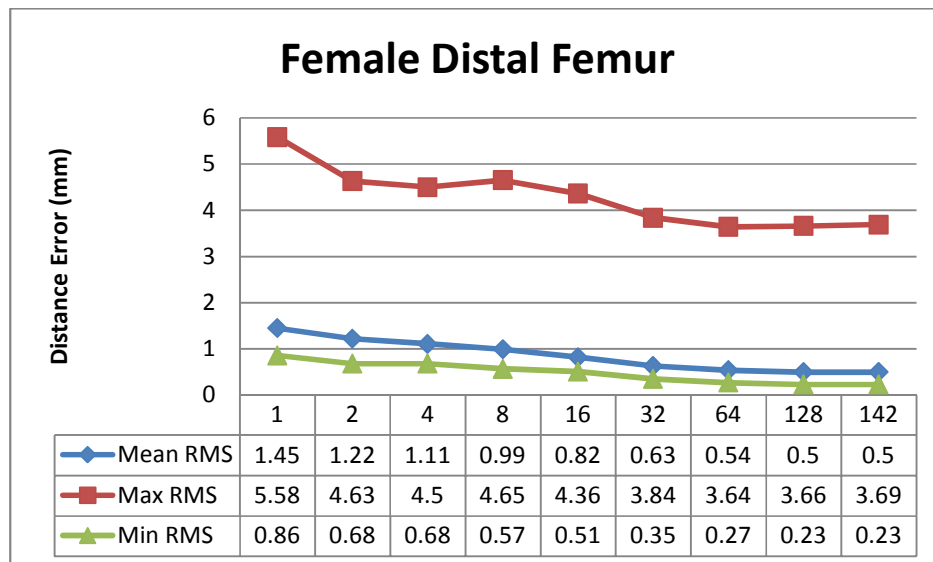


Figure 9.65 Mean, maximum, and minimum RMS errors for the female distal femur using the hybrid method for the 16 mm reduced models' point clouds

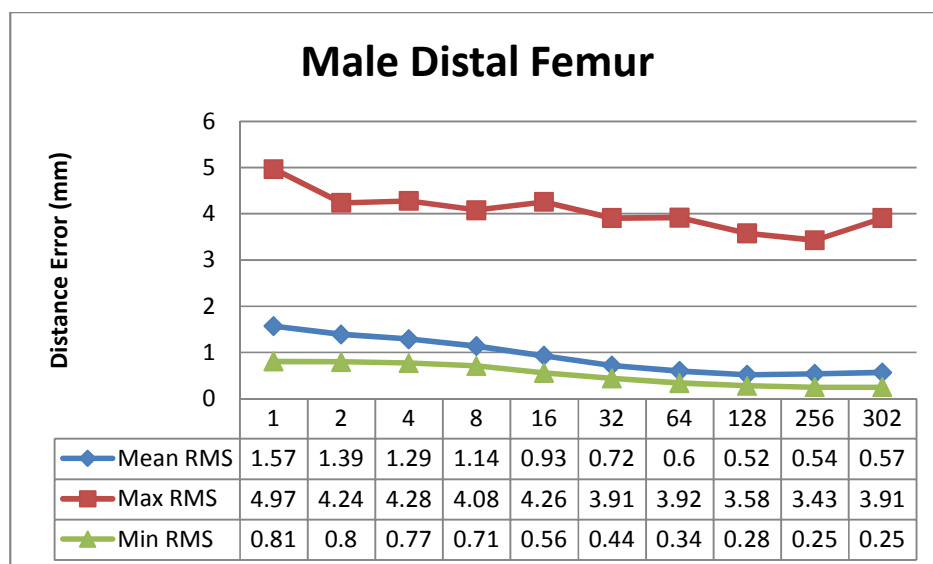


Figure 9.66 Mean, maximum, and minimum RMS errors for the male distal femur using the hybrid method for the 16 mm reduced models' point clouds

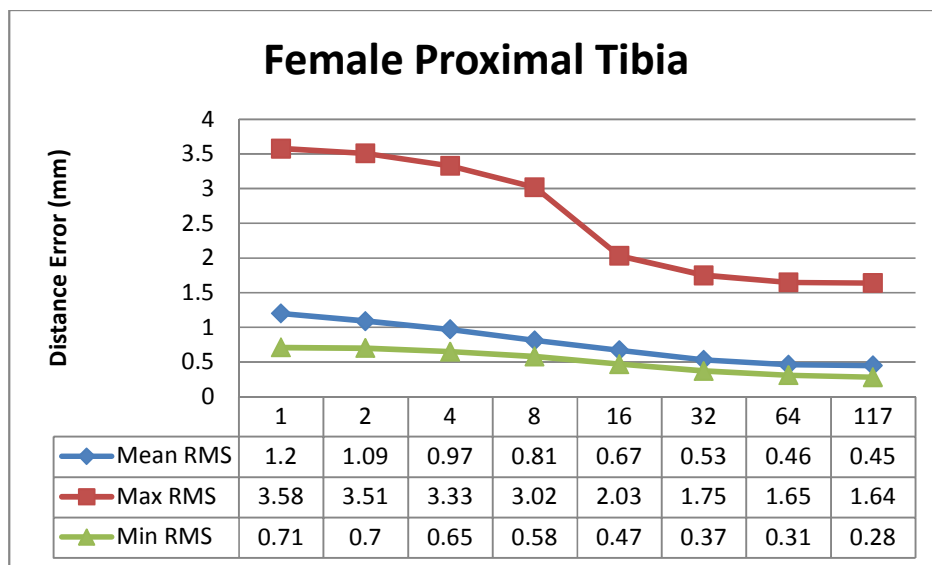


Figure 9.67 Mean, maximum, and minimum RMS errors for the female proximal tibia using the hybrid method for the 16 mm reduced models' point clouds

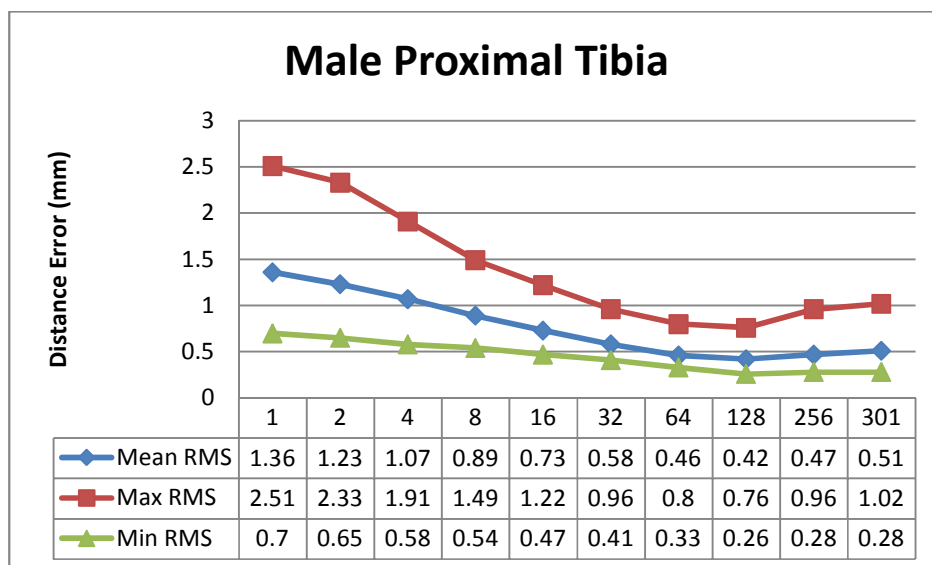


Figure 9.68 Mean, maximum, and minimum RMS errors for the male proximal tibia using the hybrid method for the 16 mm reduced models' point clouds

9.3 Single-Element Ultrasound Transducer-Based Systems' Phantom Results

9.3.1 Reconstructed Point Clouds Results

9.3.1.1 Female Distal Femur

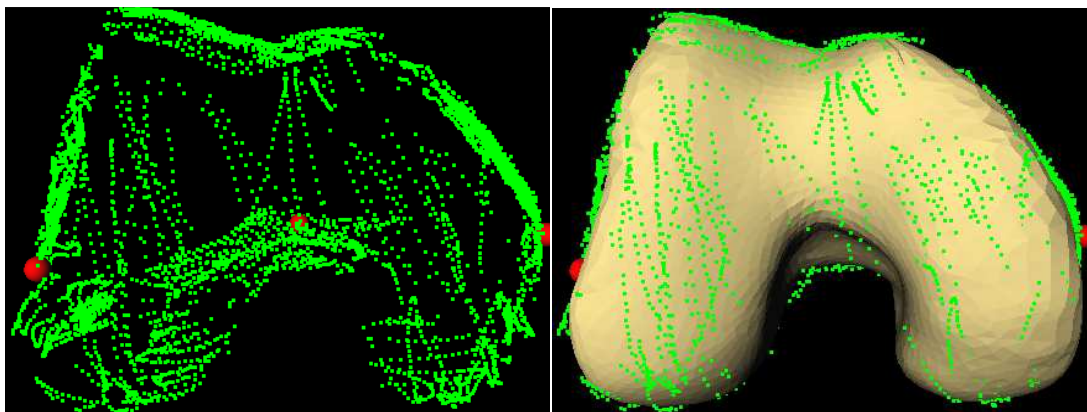


Figure 9.69 Point cloud for the ID_27_01 female distal femur phantom (left), and the point cloud overlaid on its reference model (right), with 6721 points and RMS error of 0.8 mm between the 75th percentile filtered point cloud and the reference model

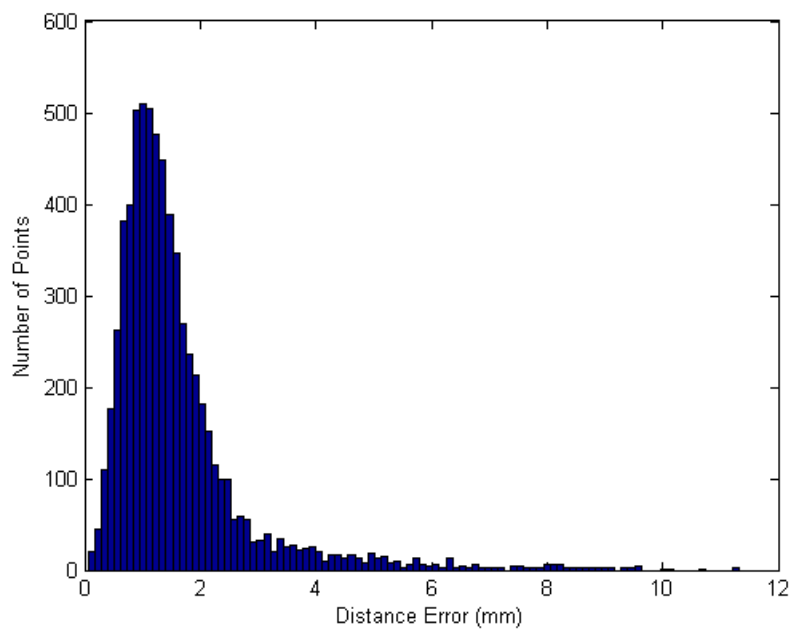


Figure 9.70 Histogram of the error between the point cloud and its reference model for the ID_27_01 female distal femur phantom with median error of 1.29 mm

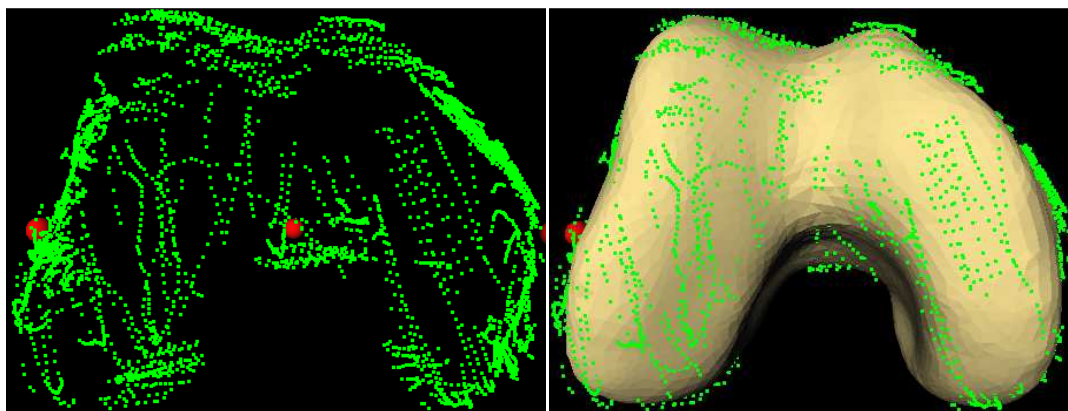


Figure 9.71 Point cloud for the ID_33_03 female distal femur phantom using (left), and the point cloud overlaid on its reference model (right), with 5322 points and RMS of 0.73 mm error between the 75th percentile filtered point cloud and the reference model

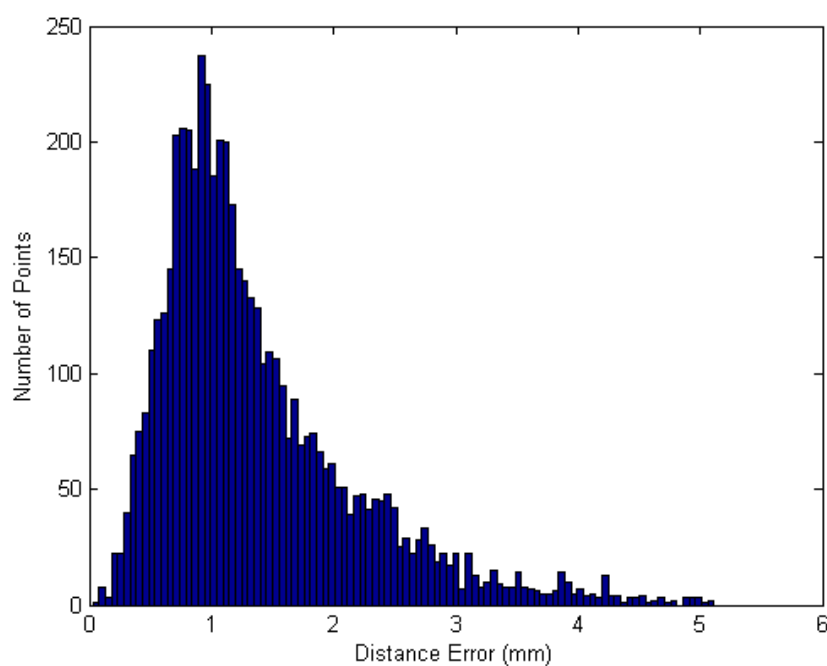


Figure 9.72 Histogram of the error between the point cloud and its reference model for the ID_33_03 female distal femur phantom with median error of 1.14 mm

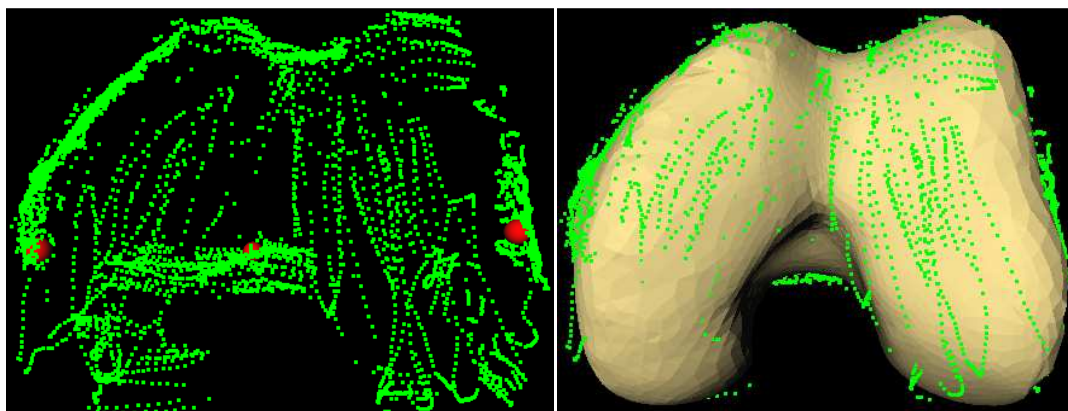


Figure 9.73 Point cloud for the ID_37_23 female distal femur phantom (left), and the point cloud overlaid on its reference model (right) with 6624 points and RMS of 0.83 mm error between the 75th percentile filtered point cloud and the reference model

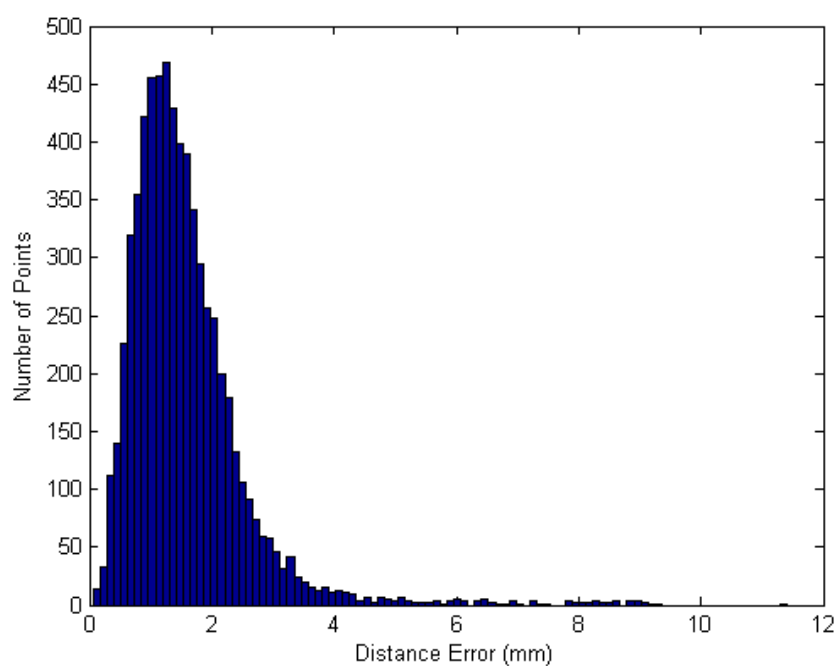


Figure 9.74 Histogram of the error between the point cloud and its reference model for the ID_37_23 female distal femur phantom with median error of 1.4 mm

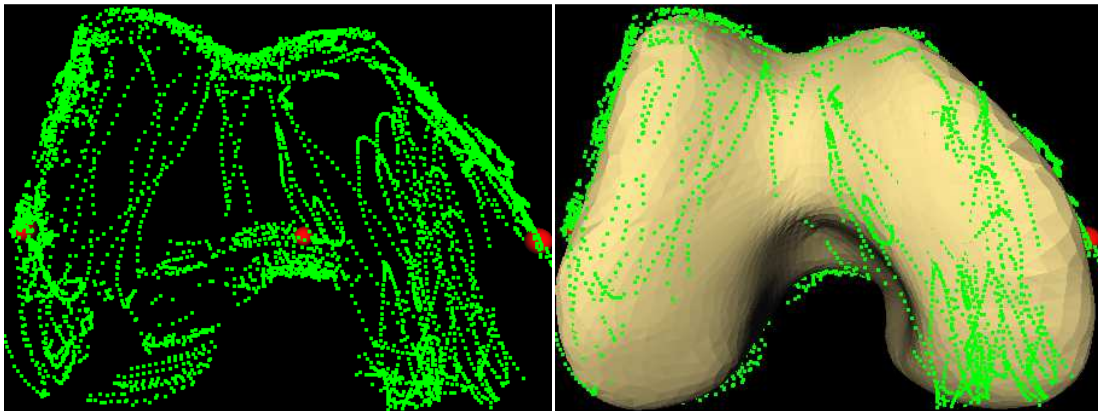


Figure 9.75 Point cloud for the ID_39_01 female distal femur phantom using (left), and the point cloud overlaid on its reference model (right) with 6837 points and RMS error of 1 mm between the 75th percentile filtered point cloud and the reference model

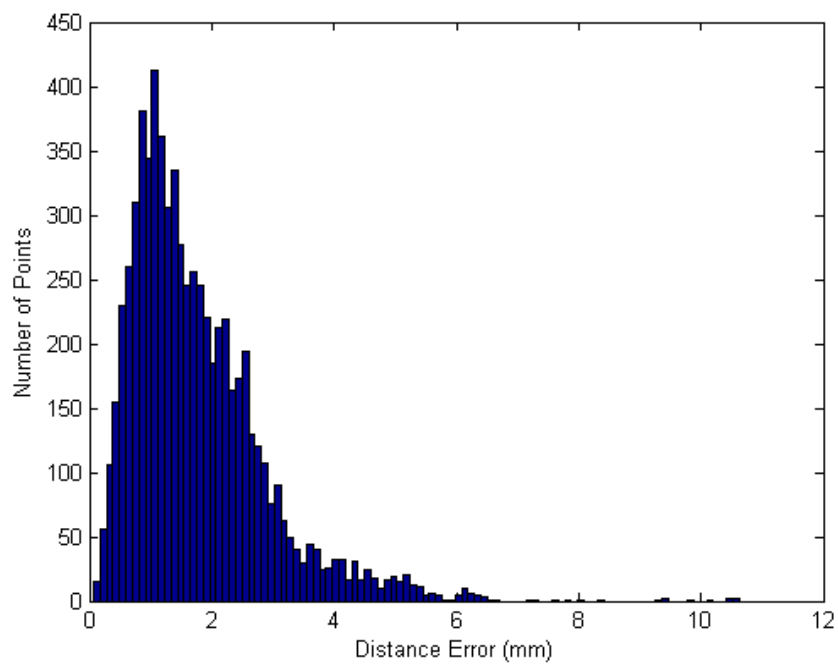


Figure 9.76 Histogram of the error between the point cloud and its reference model for the ID_39_01 female distal femur phantom with median error of 1.5 mm

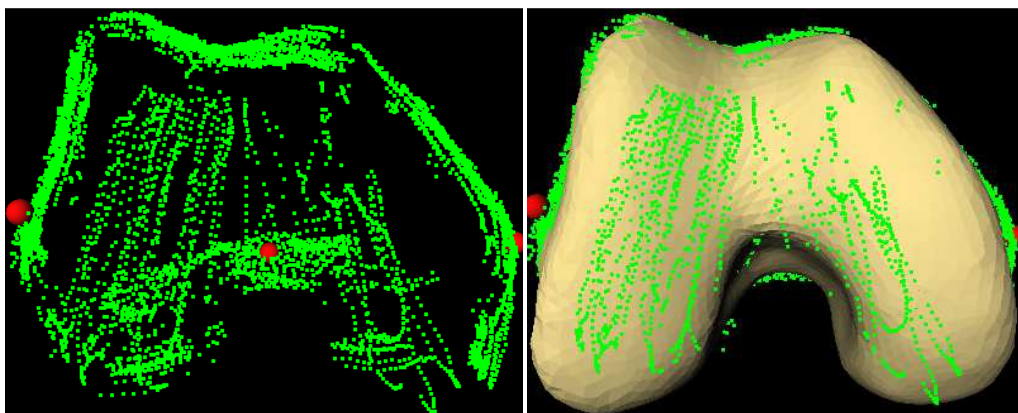


Figure 9.77 Point cloud for the ID_11_90 female distal femur phantom (left), and the point cloud overlaid on its reference model (right) with 7022 points and RMS error of 0.89 mm between the 75th percentile filtered point cloud and the reference model

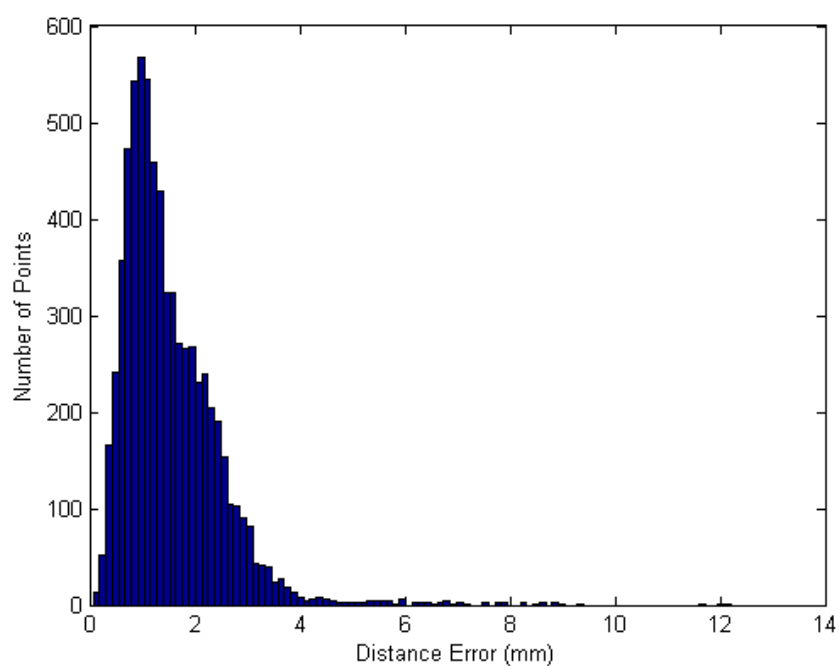


Figure 9.78 Histogram of the error between the point cloud and its reference model for the ID_11_90 female distal femur phantom with median error of 1.31 mm

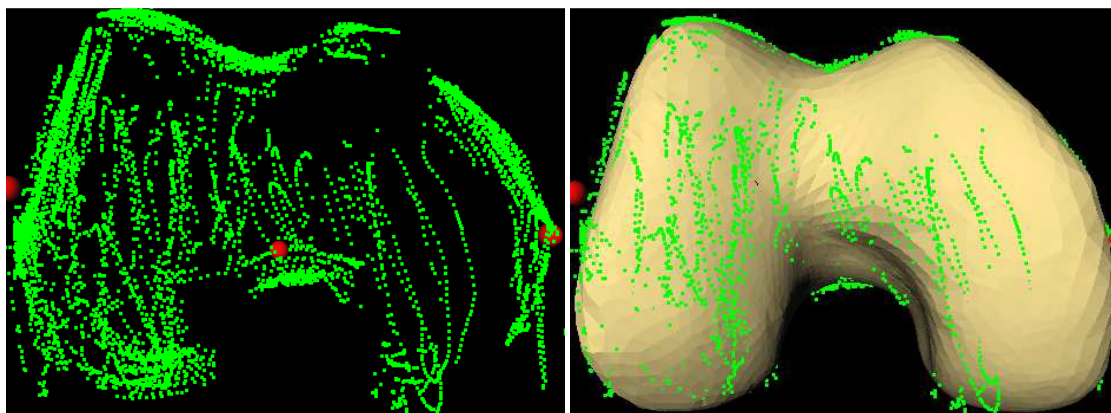


Figure 9.79 Point cloud for the ID_12_02 female distal femur phantom (left), and the point cloud overlaid on its reference model (right) with 7051 points and RMS error of 0.7 mm between the 75th percentile filtered point cloud and the reference model

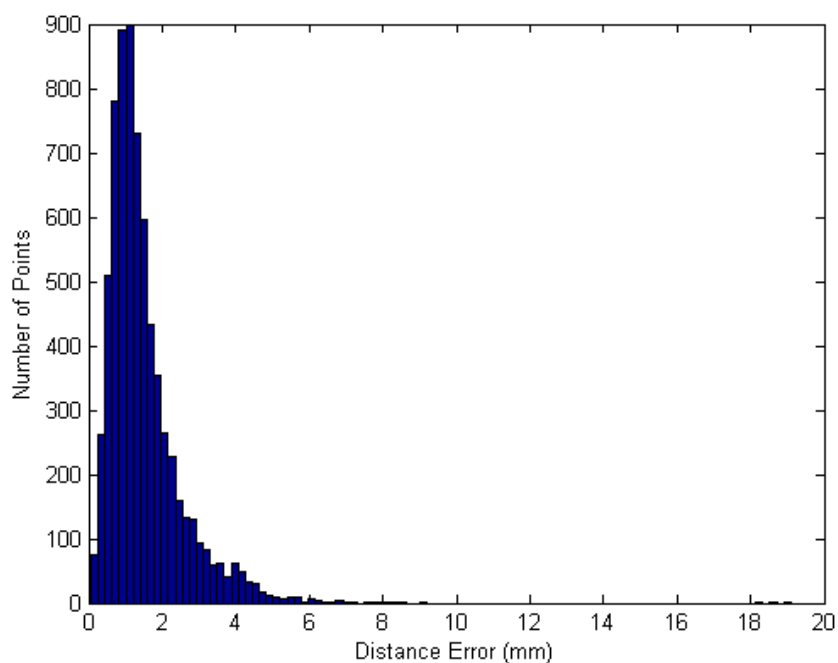


Figure 9.80 Histogram of the error between the point cloud and its reference model for the ID_12_02 female distal femur phantom with median error of 1.23 mm

9.3.1.2 Male Distal Femur

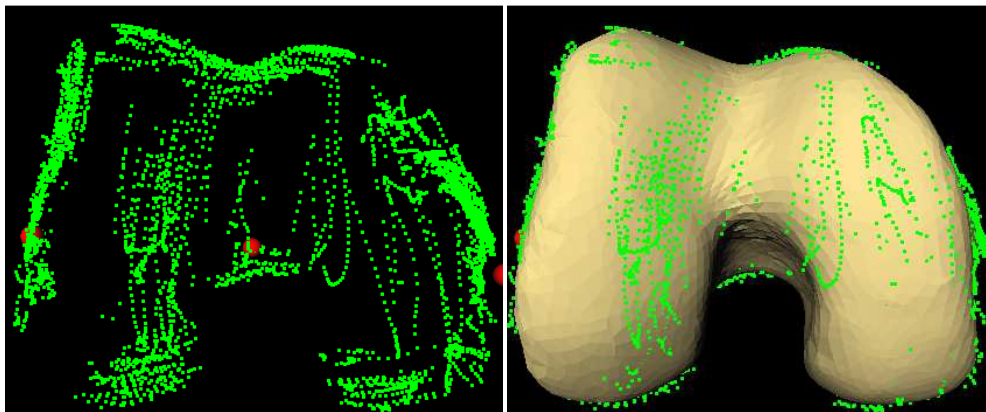


Figure 9.81 Point cloud for the ID_1_03 male distal femur phantom (left), and the point cloud overlaid on its reference model (right), with 5034 points and RMS error of 0.75 mm between the 75th percentile filtered point cloud and the reference model

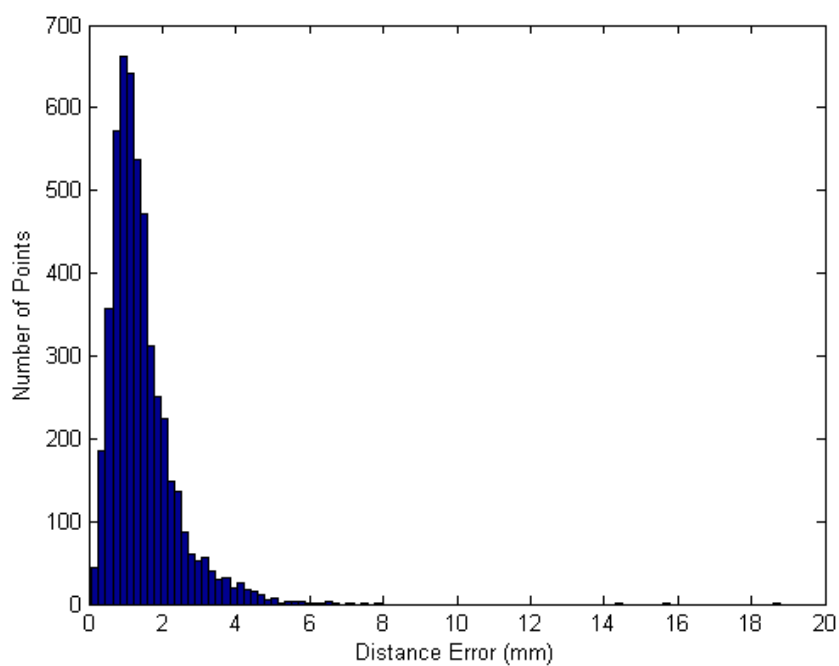


Figure 9.82 Histogram of the error between the point cloud and its reference model for the ID_1_03 male distal femur phantom with median error of 1.2 mm

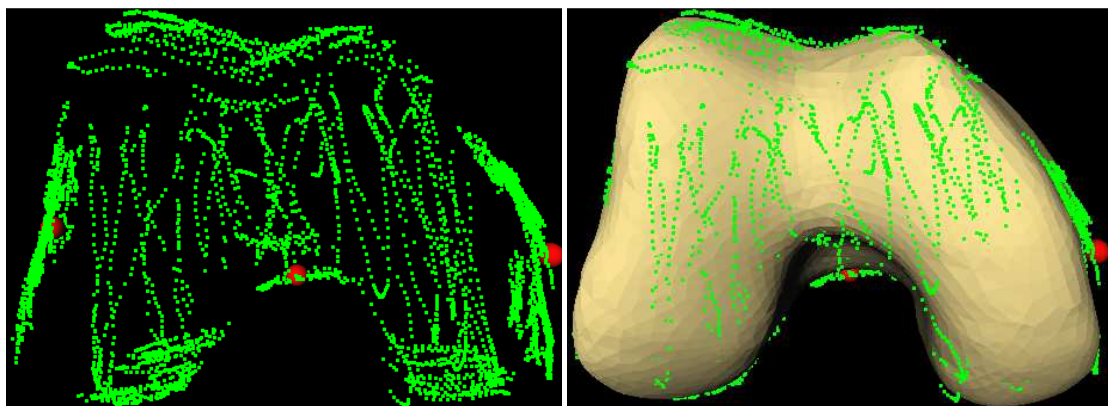


Figure 9.83 Point cloud for the ID_31_00 male distal femur phantom (left), and the point cloud overlaid on its reference model (right), with 5713 points and RMS error of 0.75 mm between the 75th percentile filtered point cloud and the reference model

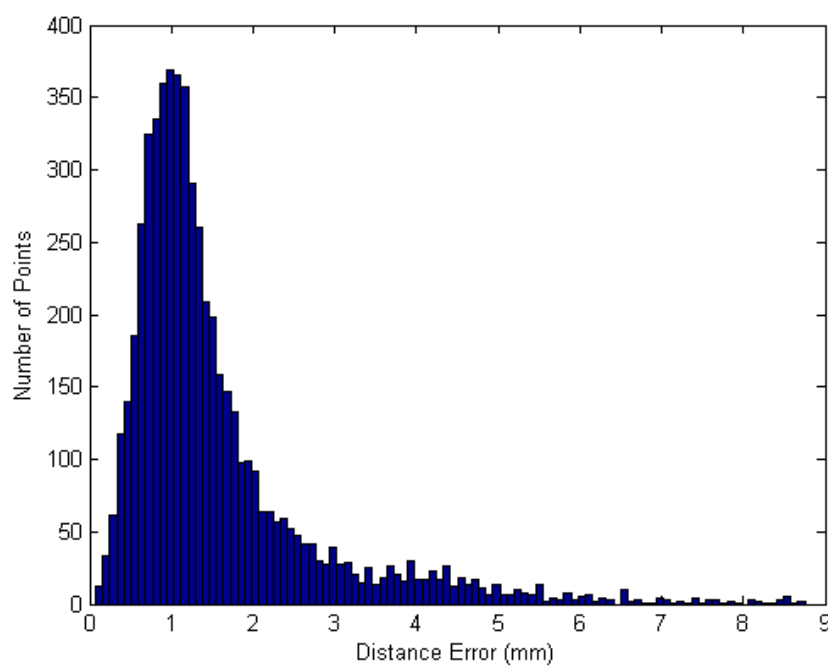


Figure 9.84 Histogram of the error between the point cloud and its reference model for the ID_31_00 male distal femur phantom with median error of 1.19 mm

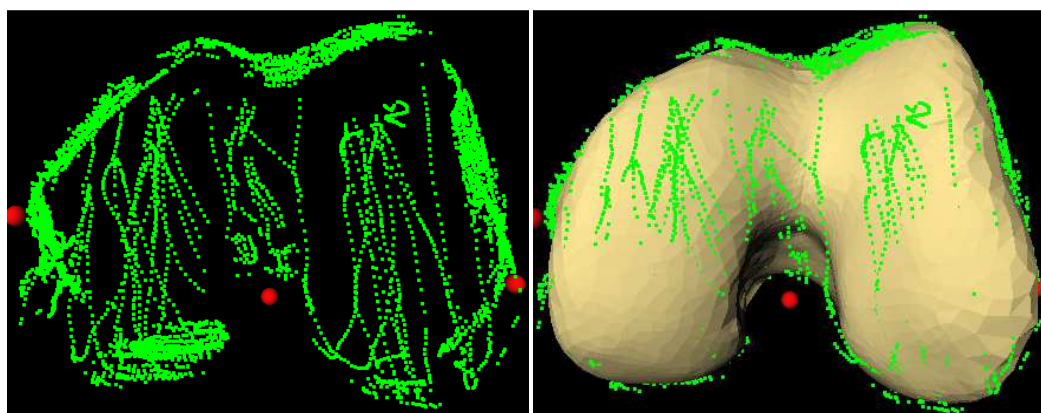


Figure 9.85 Point cloud for the ID_1_87 male distal femur phantom (left), and the point cloud overlaid on its reference model (right), with 6471 point and RMS error of 0.93 mm between the 75th percentile filtered point cloud and the reference model

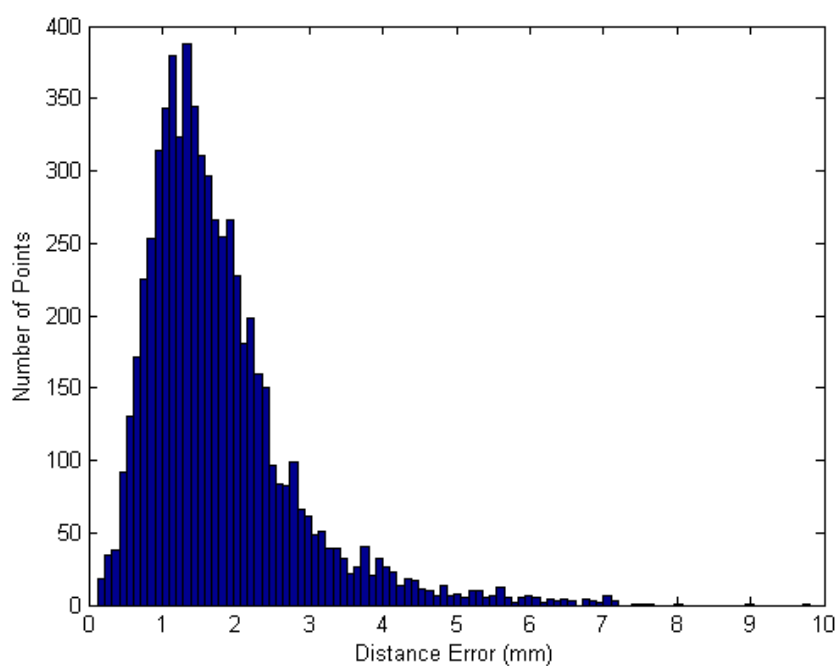


Figure 9.86 Histogram of the error between the point cloud and its reference model for the ID_1_87 male distal femur phantom with median error of 1.54 mm

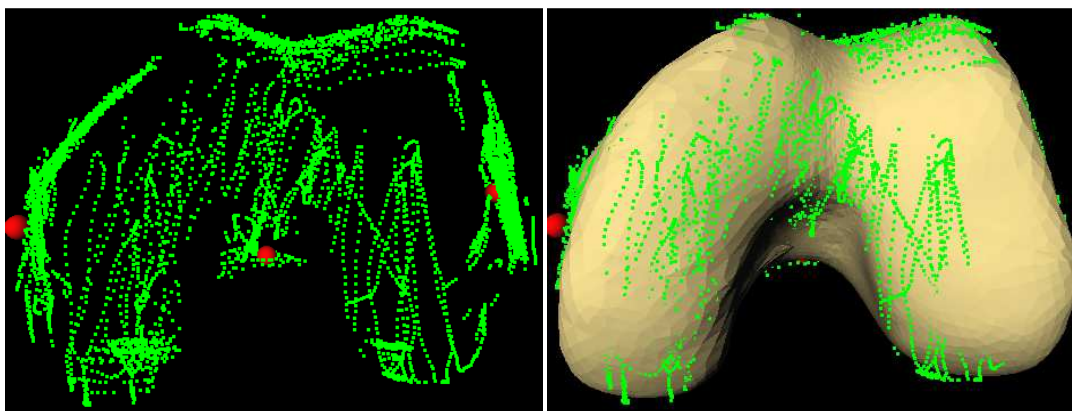


Figure 9.87 Point cloud for the ID_4_97 male distal femur phantom (left), and the point cloud overlaid on its reference model (right), with 7154 points and RMS of 0.86 mm error between the 75th percentile filtered point cloud and the reference model

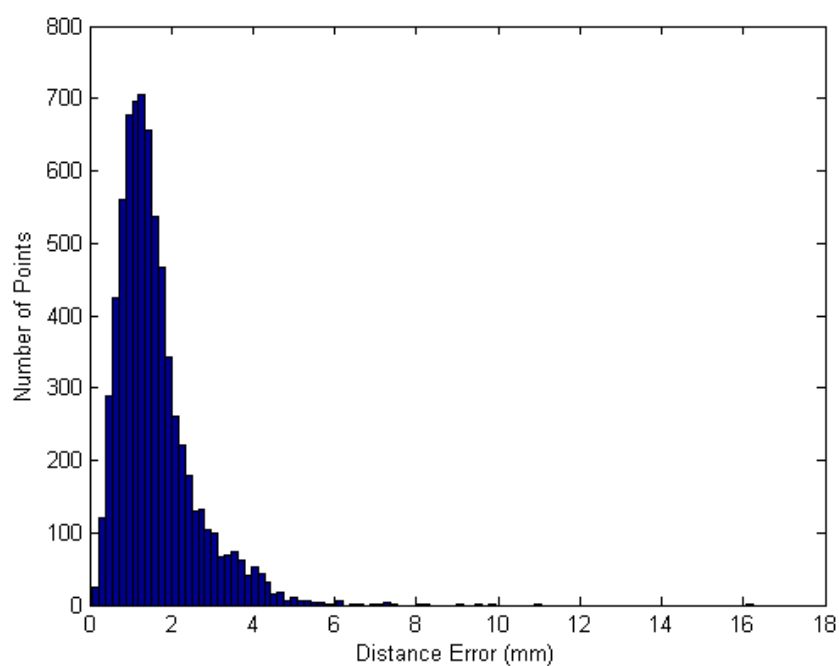


Figure 9.88 Histogram of the error between the point cloud and its reference model for the ID_4_97 male distal femur phantom with median error of 1.38 mm

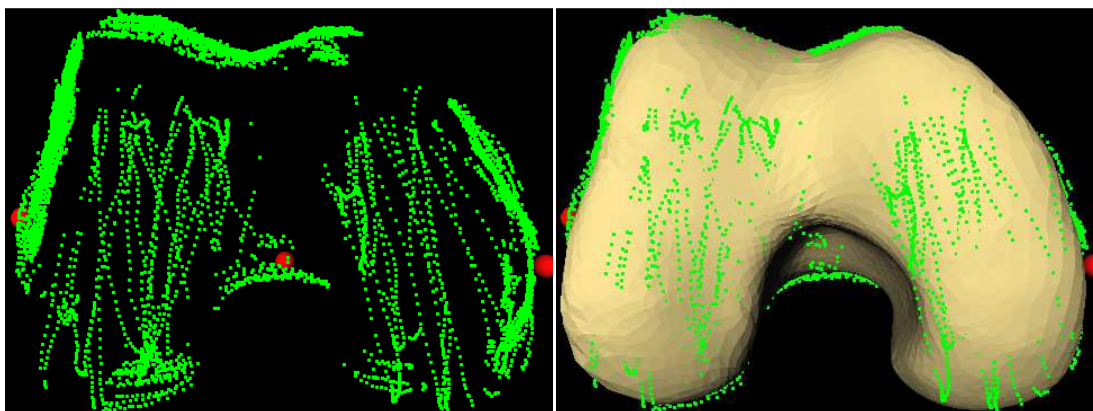


Figure 9.89 Point cloud for the ID_11_97 male distal femur phantom (left), and the point cloud overlaid on its reference model (right), with 8183 points and RMS error of 0.63 mm between the 75th percentile filtered point cloud and the reference model

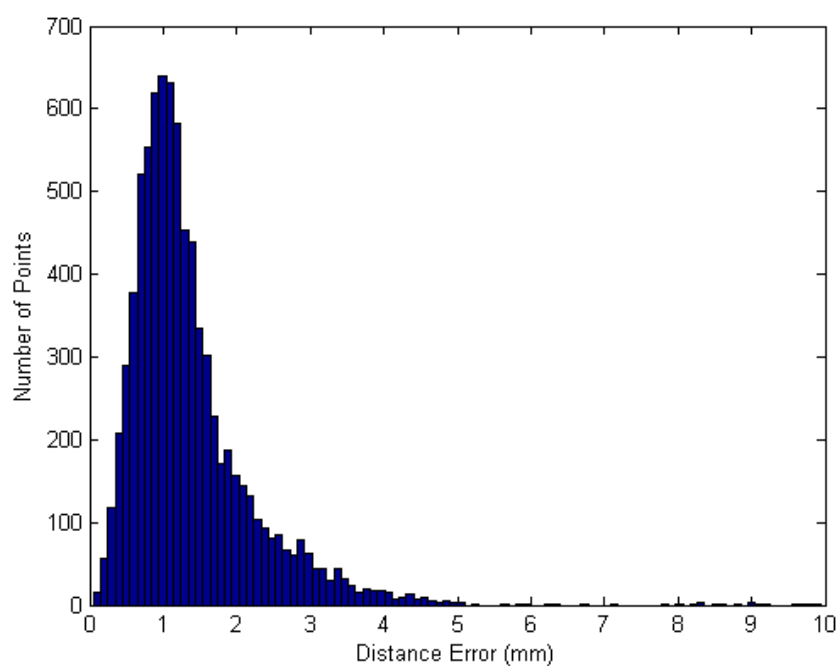


Figure 9.90 Histogram of the error between the point cloud and its reference model for the ID_11_97 male distal femur phantom with median error of 1.15 mm

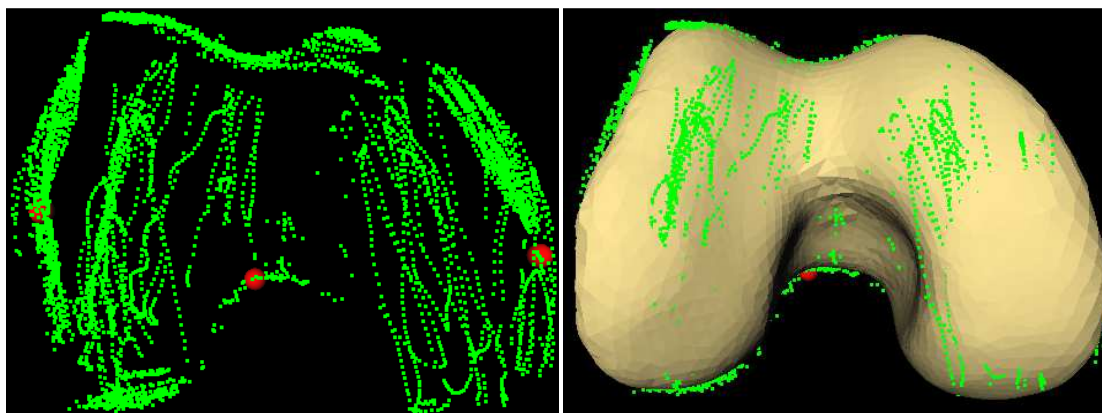


Figure 9.91 Point cloud for the ID_14_90 male distal femur phantom (left), and the point cloud overlaid on its reference model (right), with 6583 points and RMS error of 0.72 mm between the 75th percentile filtered point cloud and the reference model

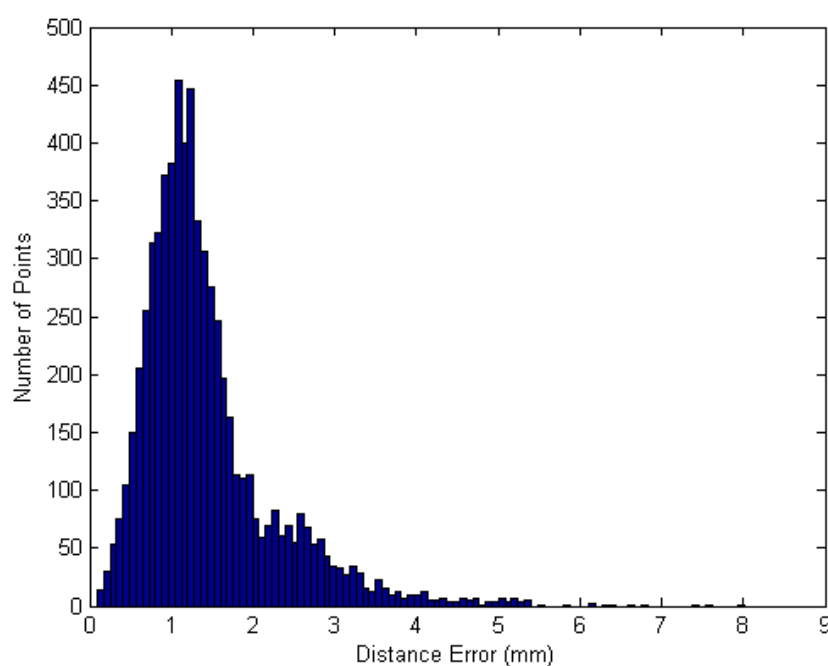


Figure 9.92 Histogram of the error between the point cloud and its reference model for the ID_14_90 male distal femur phantom with median error of 1.23 mm

9.3.1.3 Female Proximal Tibia

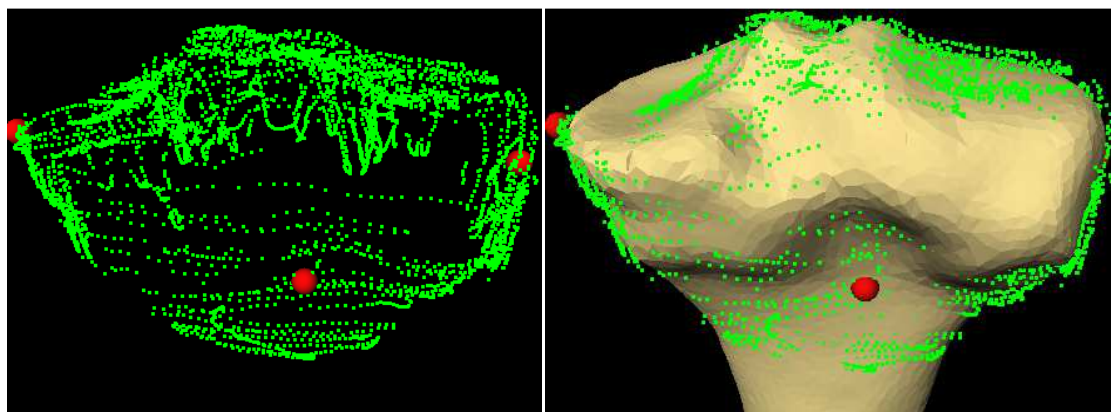


Figure 9.93 Point cloud for the ID_39_01 female proximal tibia phantom (left), and the point cloud overlaid on its reference model (right), with 5767 points and RMS error of 0.85 mm between the 75th percentile filtered point cloud and the reference model

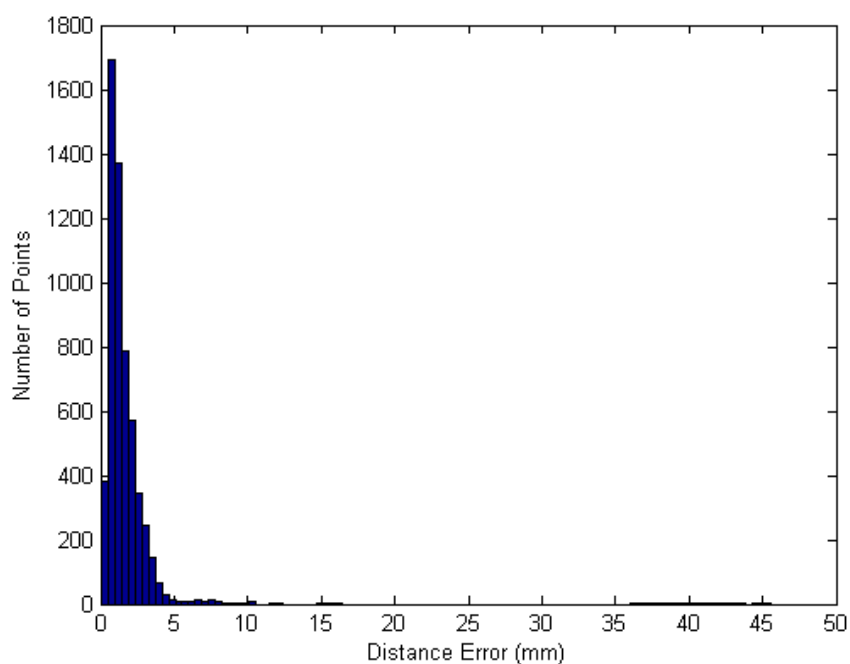


Figure 9.94 Histogram of the error between the point cloud and its reference model for the ID_39_01 female proximal tibia phantom with median error of 1.2 mm

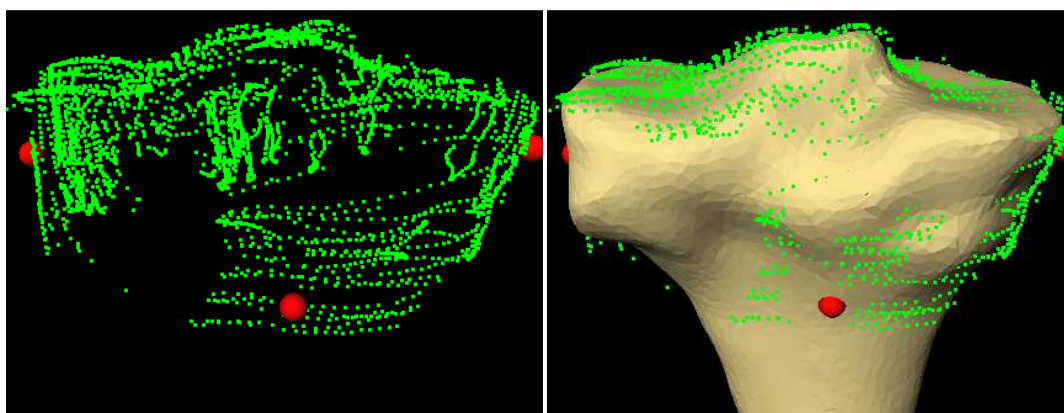


Figure 9.95 Point cloud for the ID_37_02 female proximal tibia phantom (left), and the point cloud overlaid on its reference model (right), with 4159 points and RMS error of 0.97 mm between the 75th percentile filtered point cloud and the reference model

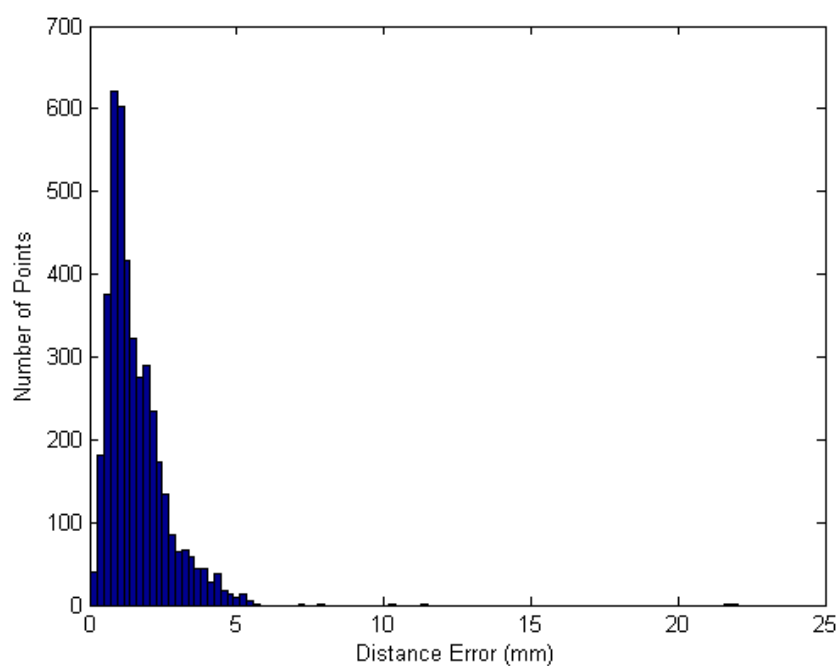


Figure 9.96 Histogram of the error between the point cloud and its reference model for the ID_37_02 female proximal tibia phantom with median error of 1.29 mm

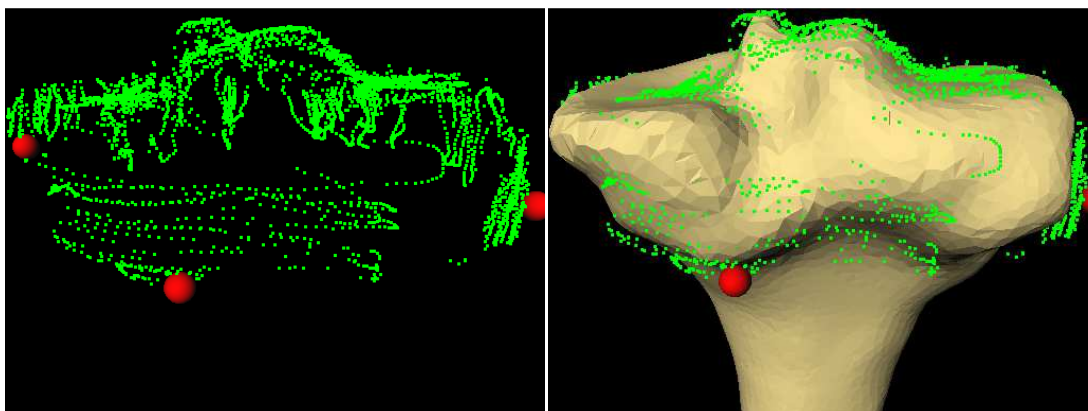


Figure 9.97 Point cloud for the ID_27_01 female proximal tibia phantom (left), and the point cloud overlaid on its corresponding model (right), with 5039 points and RMS error of 0.98 mm between the 75th percentile filtered point cloud and the reference model

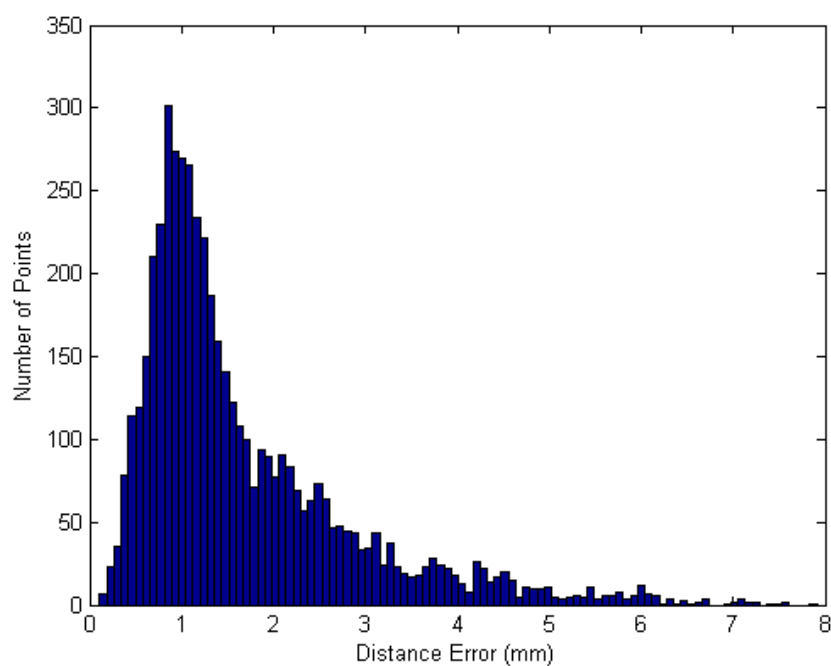


Figure 9.98 Histogram of the error between the point cloud and its reference model for the ID_27_01 female proximal tibia phantom with median error of 1.27 mm

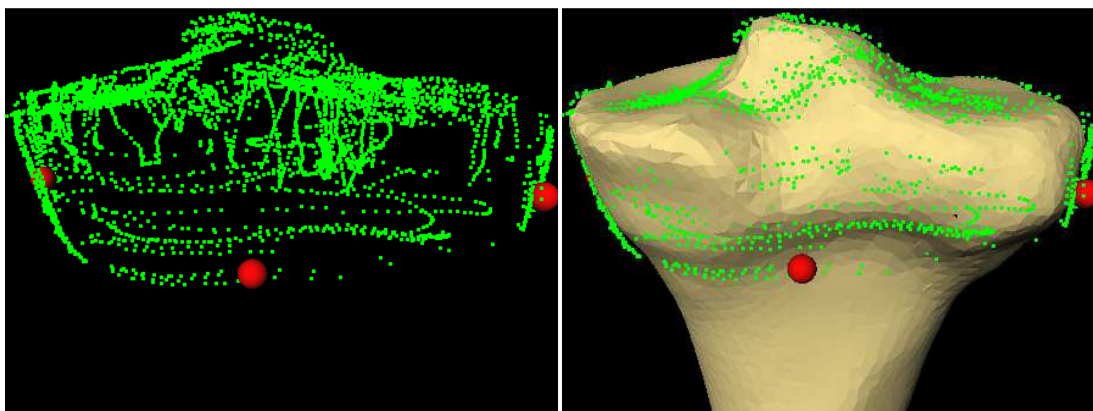


Figure 9.99 Point cloud for the ID_12_02 female proximal tibia phantom (left), and the point cloud overlaid on its reference model (right), with 5248 points and RMS error of 0.6 mm between the 75th percentile filtered point cloud and the reference model

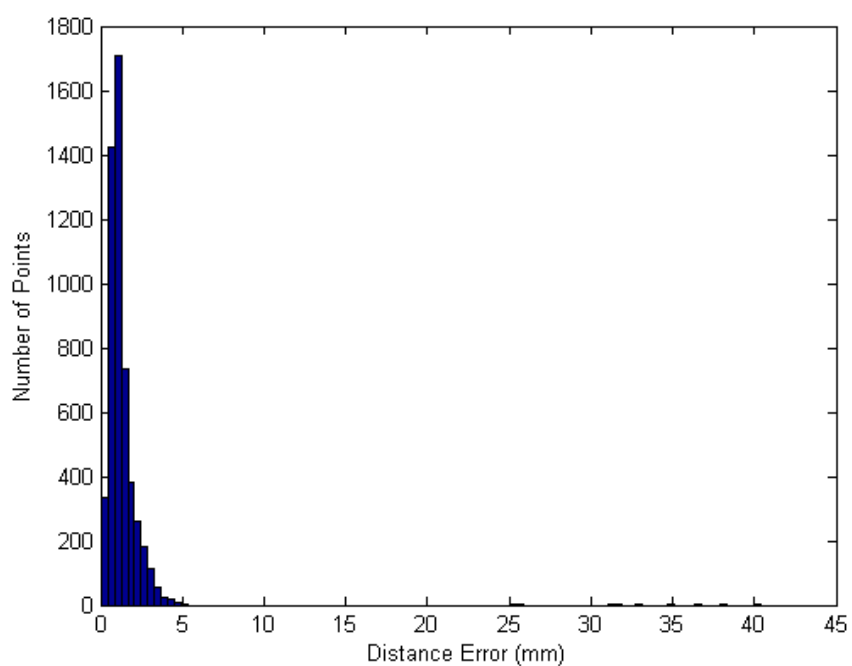


Figure 9.100 Histogram of the error between the point cloud and its reference model for the ID_12_02 female proximal tibia phantom with median error of 1.05 mm

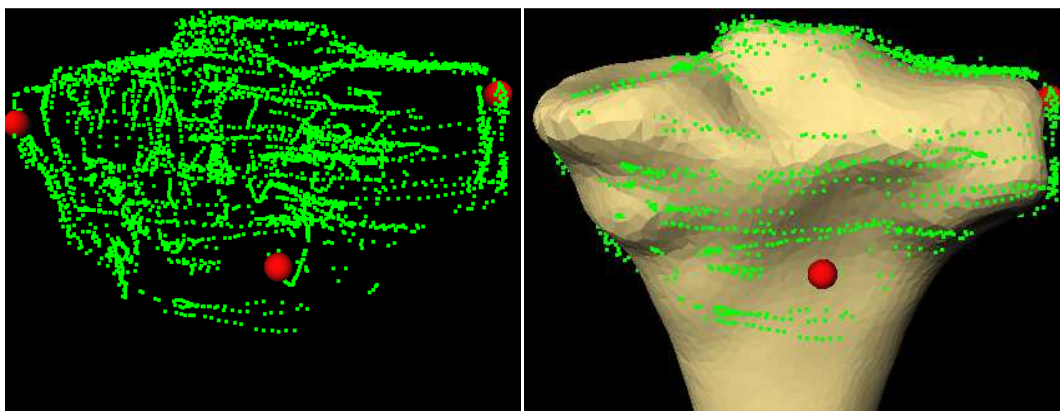


Figure 9.101 Point cloud for the ID_11_90 female proximal tibia phantom (left), and the point cloud overlaid on its reference model (right), with 4887 points and RMS error of 0.94 mm between the 75th percentile filtered point cloud and the reference model

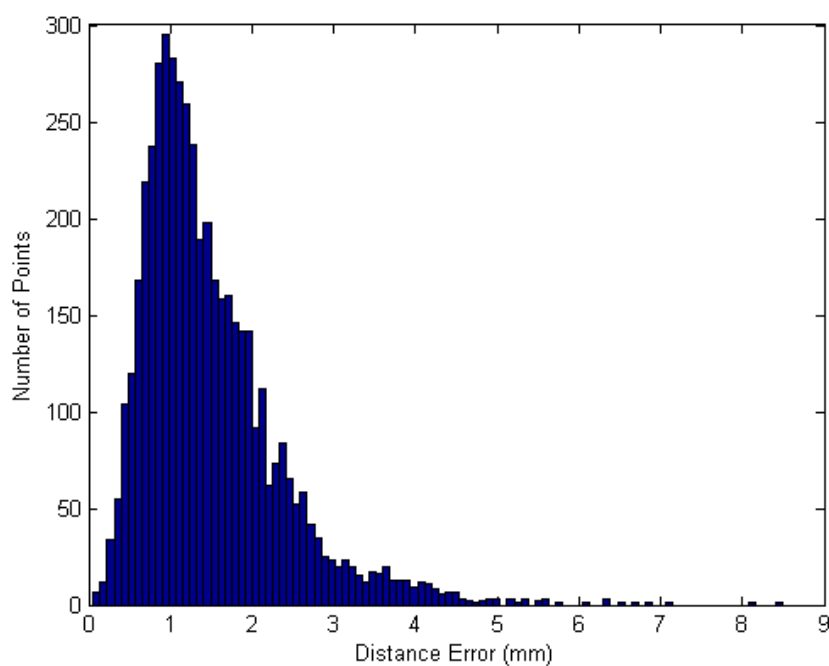


Figure 9.102 Histogram of the error between the point cloud and its reference model for the ID_11_90 female proximal tibia phantom with median error of 1.28 mm

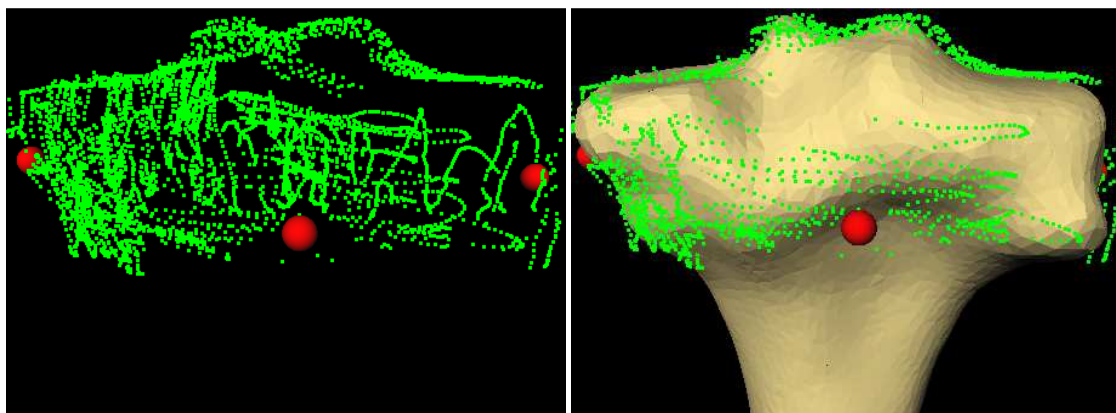


Figure 9.103 Point cloud for the ID_33_03 female proximal tibia phantom (left), and the point cloud overlaid on its reference model (right), with 6163 points and RMS error of 0.85 mm between the 75th percentile filtered point cloud and the reference model

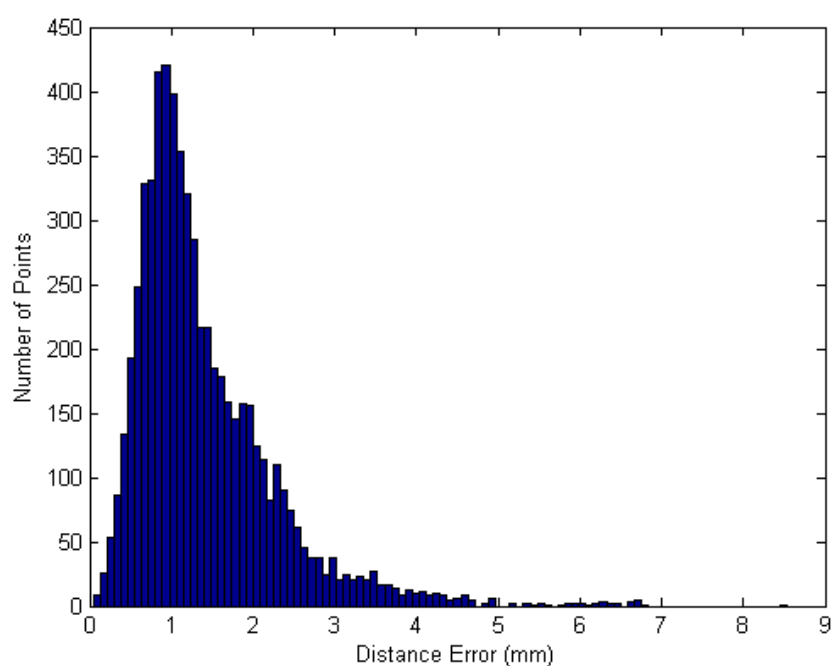


Figure 9.104 Histogram of the error between the point cloud and its reference model for the ID_33_03 female proximal tibia phantom with median error of 1.17 mm

9.3.1.4 Male Proximal Tibia

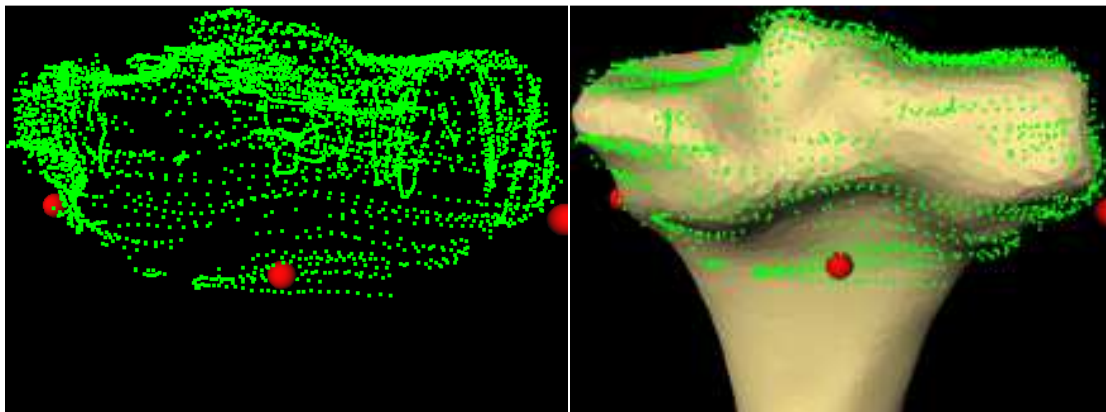


Figure 9.105 Point cloud for the ID_1_03 male proximal tibia phantom (left), and the point cloud overlaid on its of 0.94 mm model (right), with 5711 points and RMS error of 0.85 mm between the 75th percentile filtered point cloud and the reference model

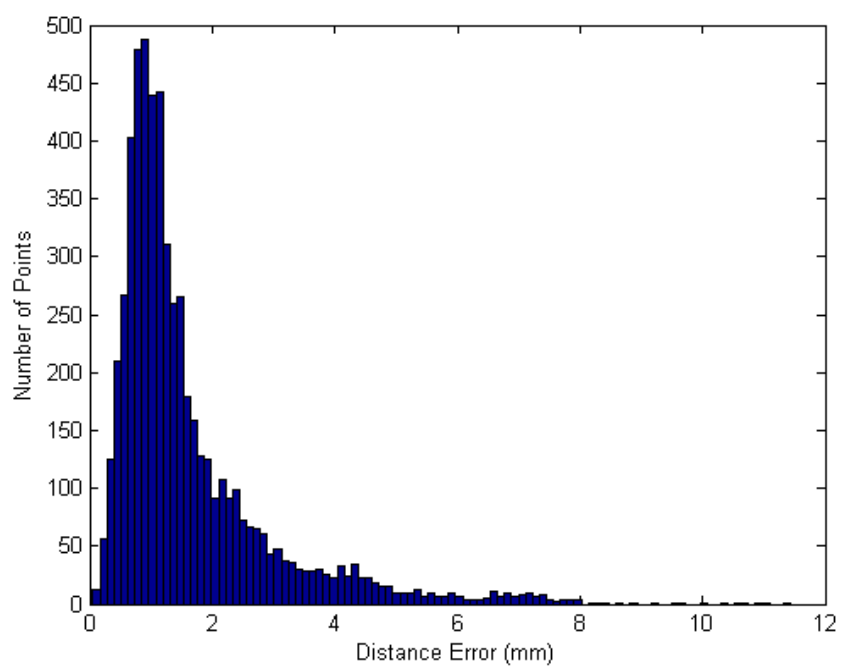


Figure 9.106 Histogram of the error between the point cloud and its reference model for the ID_1_03 male proximal tibia phantom with median error of 1.18 mm

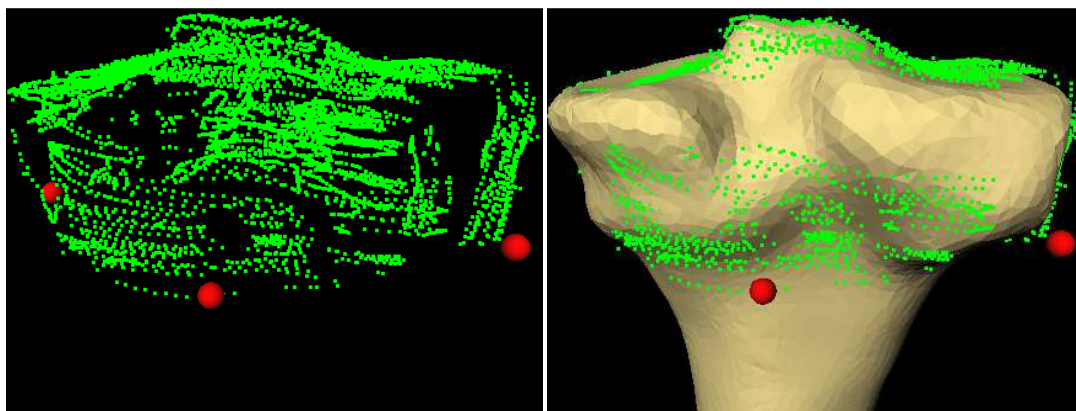


Figure 9.107 Point cloud for the ID_14_90 male proximal tibia phantom (left), and the point cloud overlaid on its reference model (right), with 7222 points and RMS error of 0.86 mm between the 75th percentile filtered point cloud and the reference model

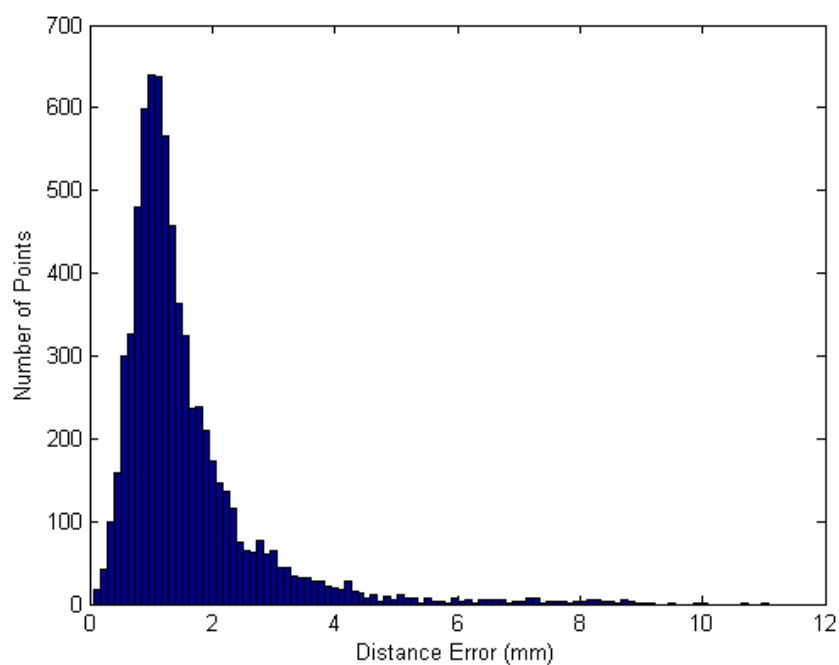


Figure 9.108 Histogram of the error between the point cloud and its reference model for the ID_14_90 male proximal tibia phantom with median error of 1.24 mm

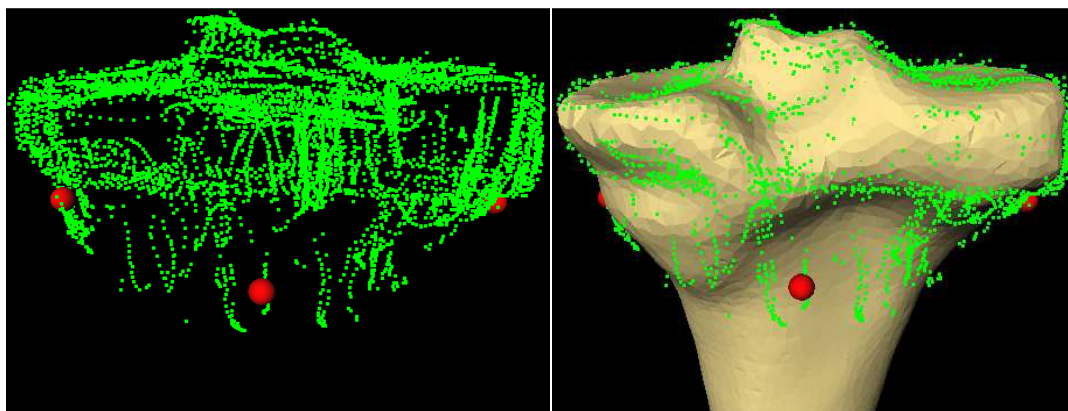


Figure 9.109 Point cloud for the ID_31_00 male proximal tibia phantom (left), and the point cloud overlaid on its reference model (right), with 8155 points and RMS error of 0.77 mm between the 75th percentile filtered point cloud and the reference model

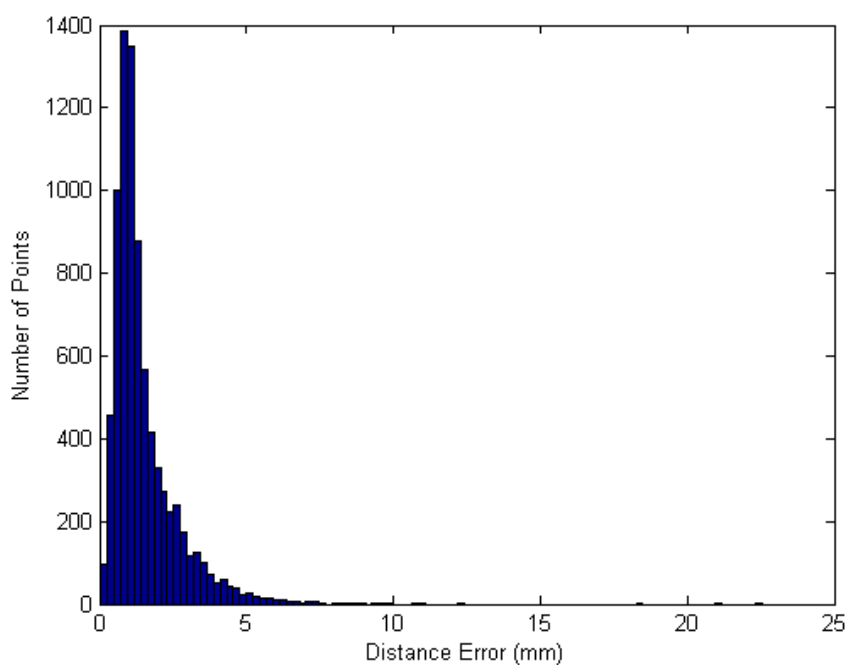


Figure 9.110 Histogram of the error between the point cloud and its reference model for the ID_31_00 male proximal tibia phantom with median error of 1.13 mm

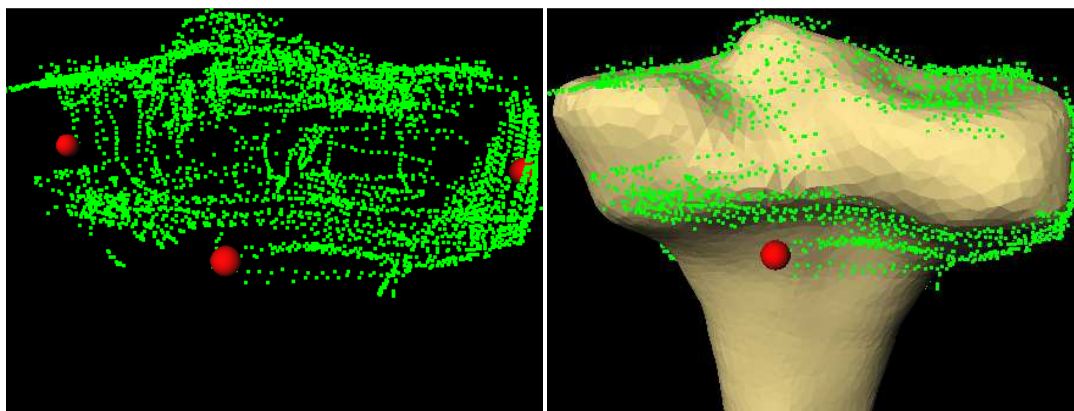


Figure 9.111 Point cloud for the ID_11_97 male proximal tibia phantom (left), and the point cloud overlaid on its reference model (right), with 5481 points and RMS error of 1 mm between the 75th percentile filtered point cloud and the reference model

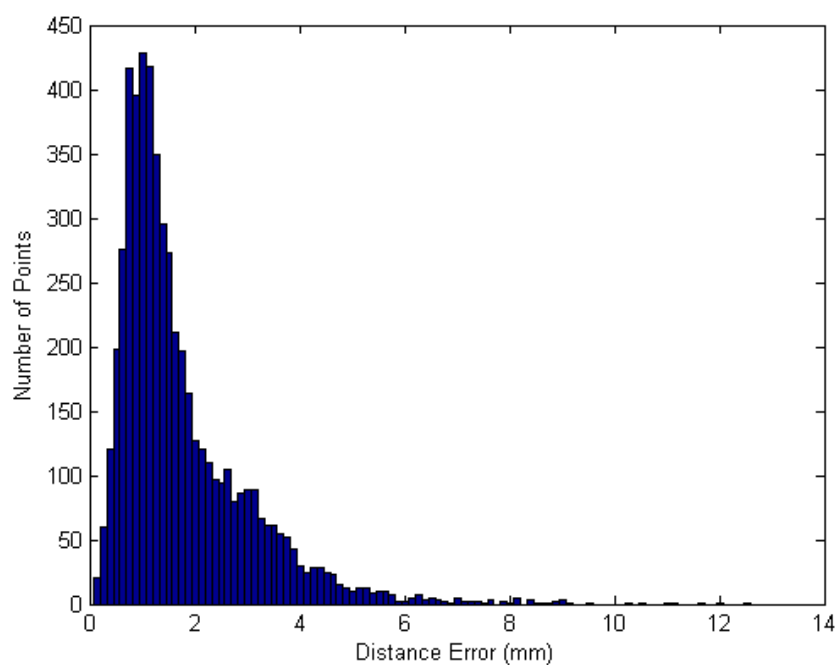


Figure 9.112 Histogram of the error between the point cloud and its reference model for the ID_11_97 male proximal tibia phantom with median error of 1.35 mm

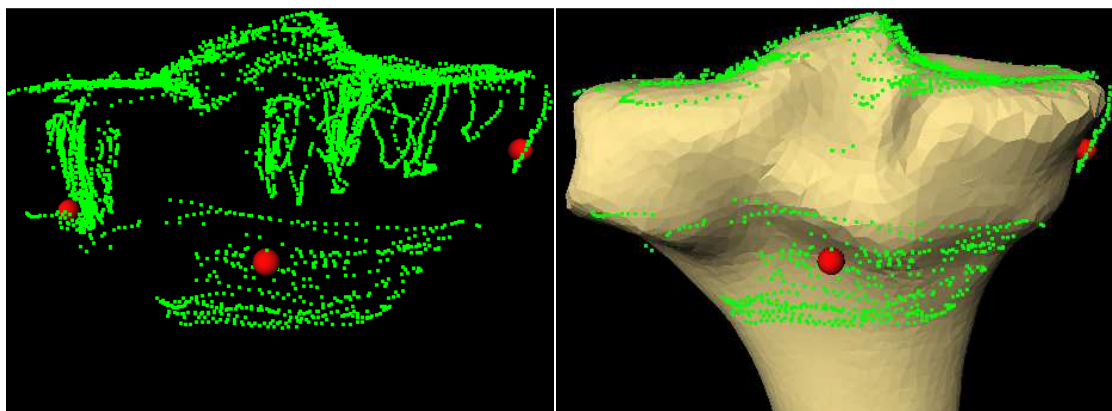


Figure 9.113 Point cloud for the ID_1_87 male proximal tibia phantom (left), and the point cloud overlaid on its reference model (right), with 4968 points and RMS error of 0.82 mm between the 75th percentile filtered point cloud and the reference

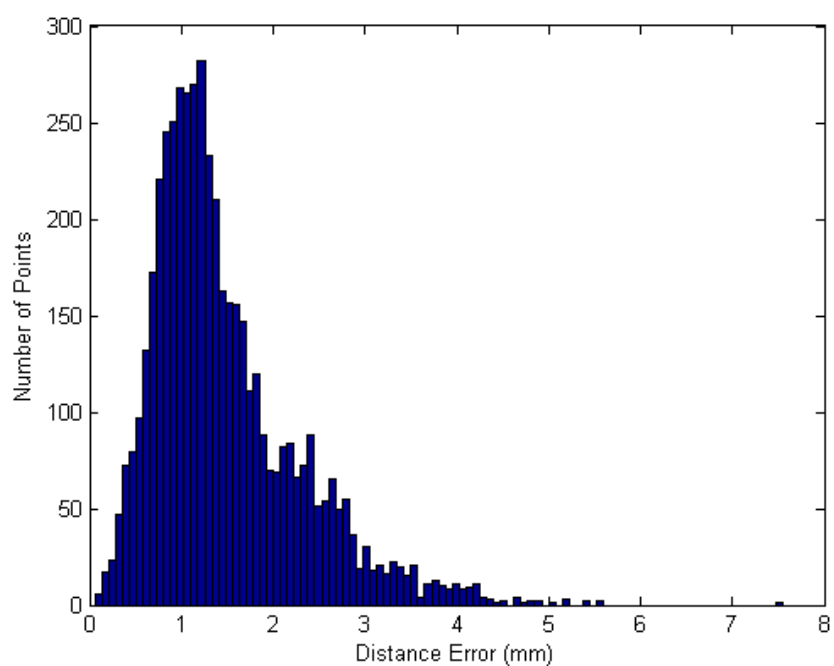


Figure 9.114 Histogram of the error between the point cloud and its reference model for the ID_1_87 male proximal tibia phantom with median error of 1.27 mm

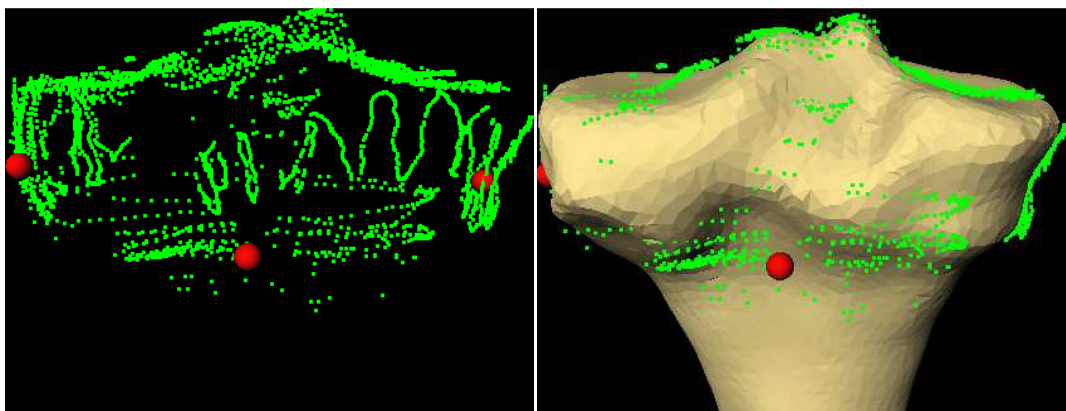


Figure 9.115 Point cloud for the ID_4_97 male proximal tibia phantom (left), and the point cloud overlaid on its reference model (right), with 4346 points and RMS error of 0.8 mm between the 75th percentile filtered point cloud and the reference model

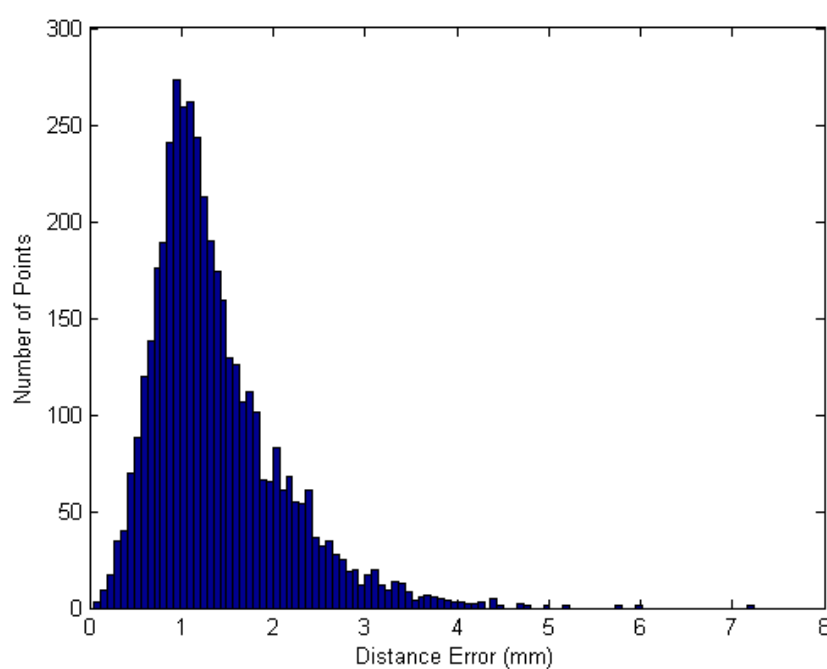


Figure 9.116 Histogram of the error between the point cloud and its reference model for the ID_4_97 male proximal tibia phantom with median error of 1.21 mm

9.3.2 3D Model Reconstruction Results

9.3.2.1 Direction Set Morphing Method (32 Principal Components)

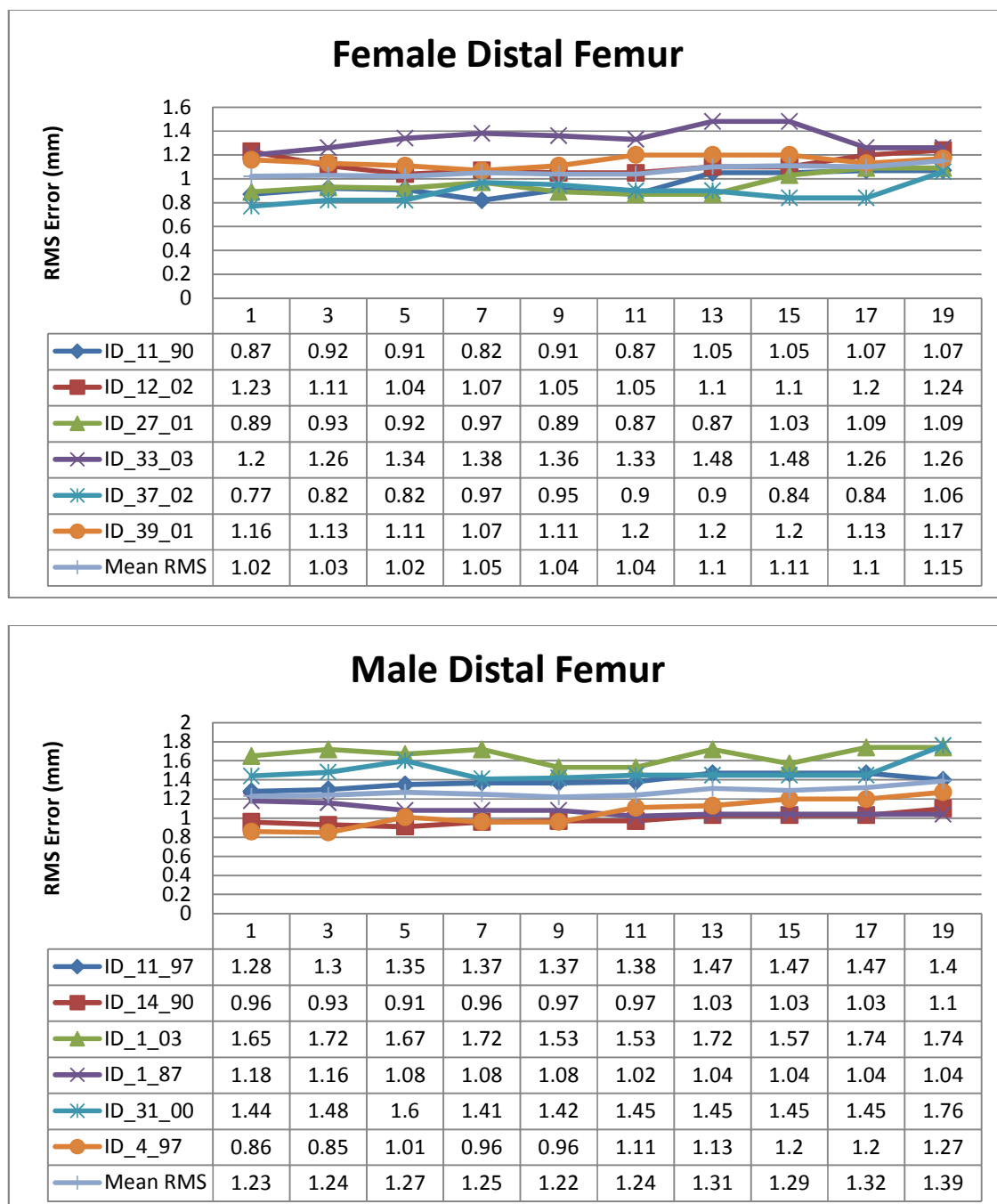


Figure 9.117 Reconstruction RMS errors vs. point cloud density (in mm) for the female (top), and male (bottom) distal femur phantoms using the linear least squares method

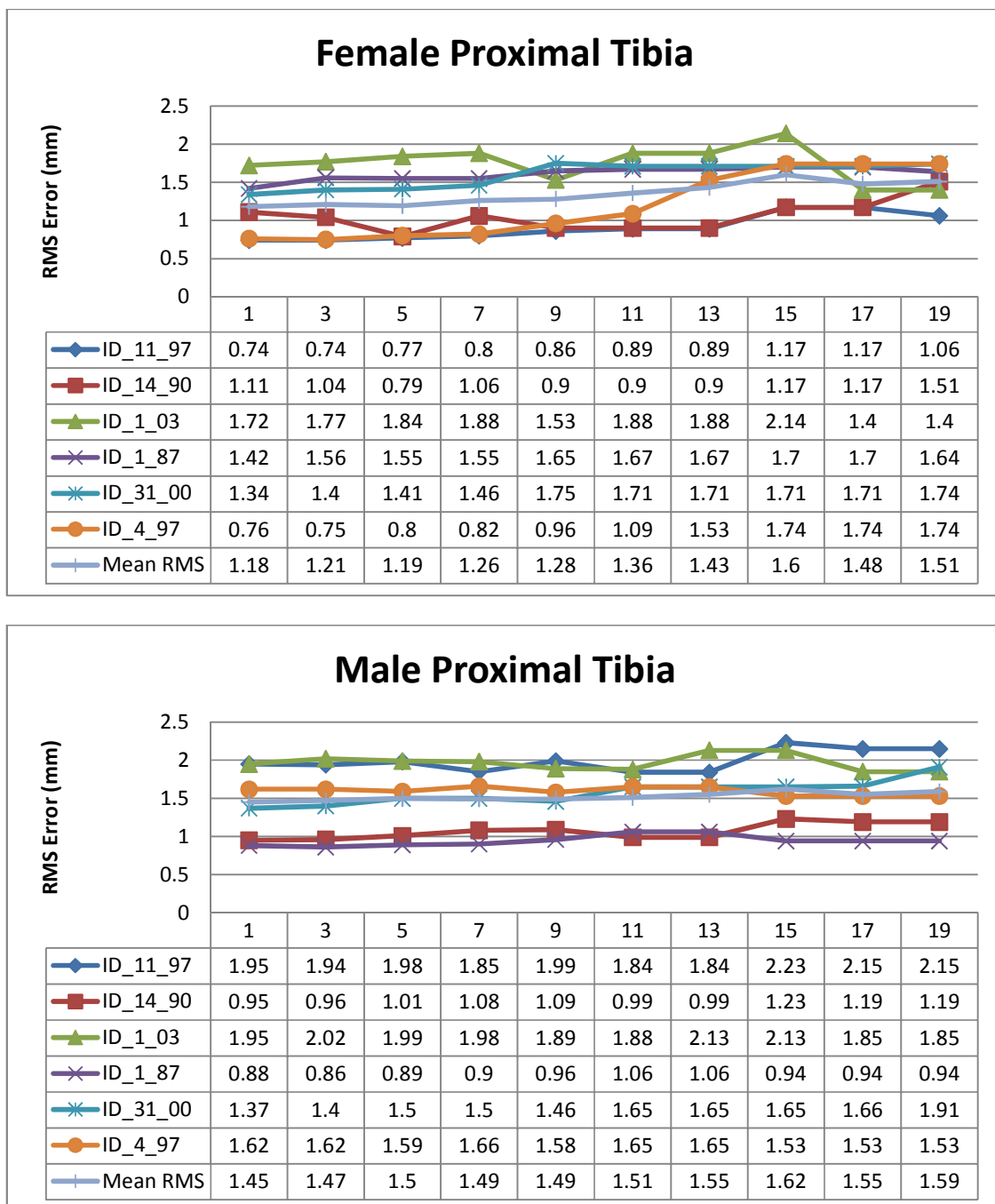


Figure 9.118 Reconstruction RMS errors vs. point cloud density (in mm) for the female (top), and male (bottom) proximal tibia phantoms using the linear least squares method

9.3.2.2 Linear Least Squares Method (64 Principal Components)

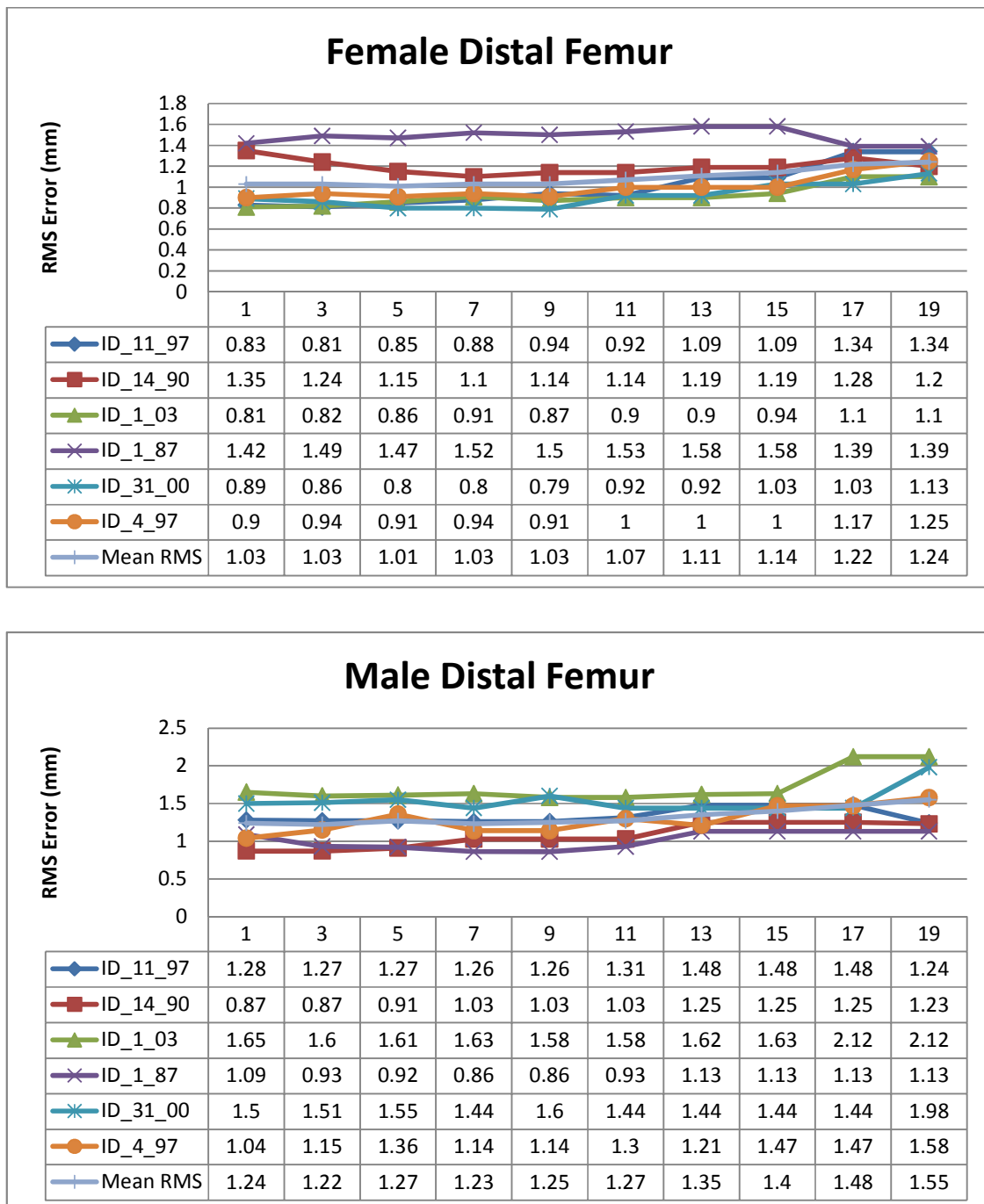


Figure 9.119 Reconstruction RMS errors vs. point cloud density (in mm) for the female (top), and male (bottom) distalfemur phantoms using the linear least squares method

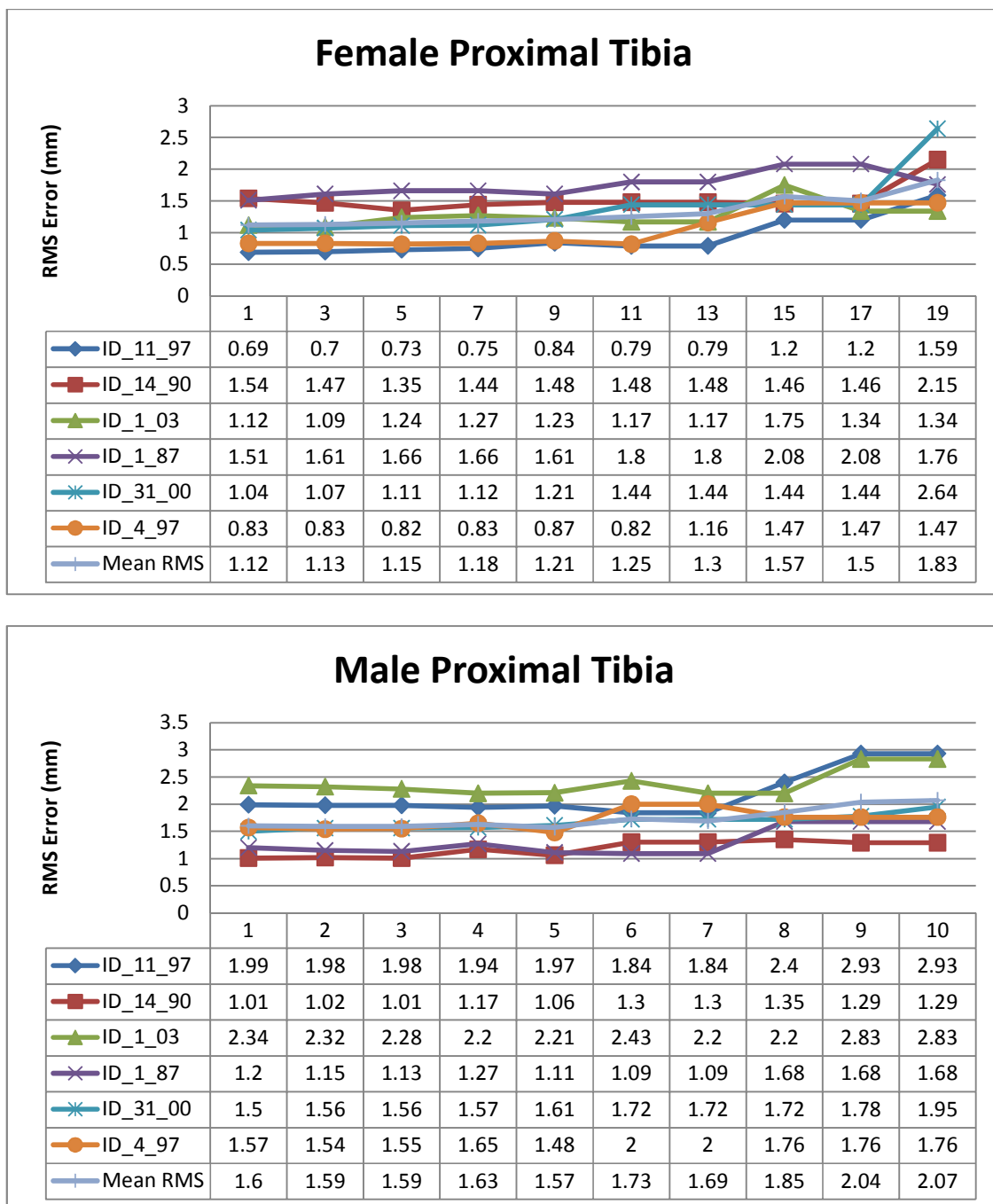


Figure 9.120 Reconstruction RMS errors vs. point cloud density (in mm) for the female (top), and male (bottom) proximal tibia phantoms using the linear least squares method

9.3.2.3 Hybrid Method (32, and 64 Principal Components)

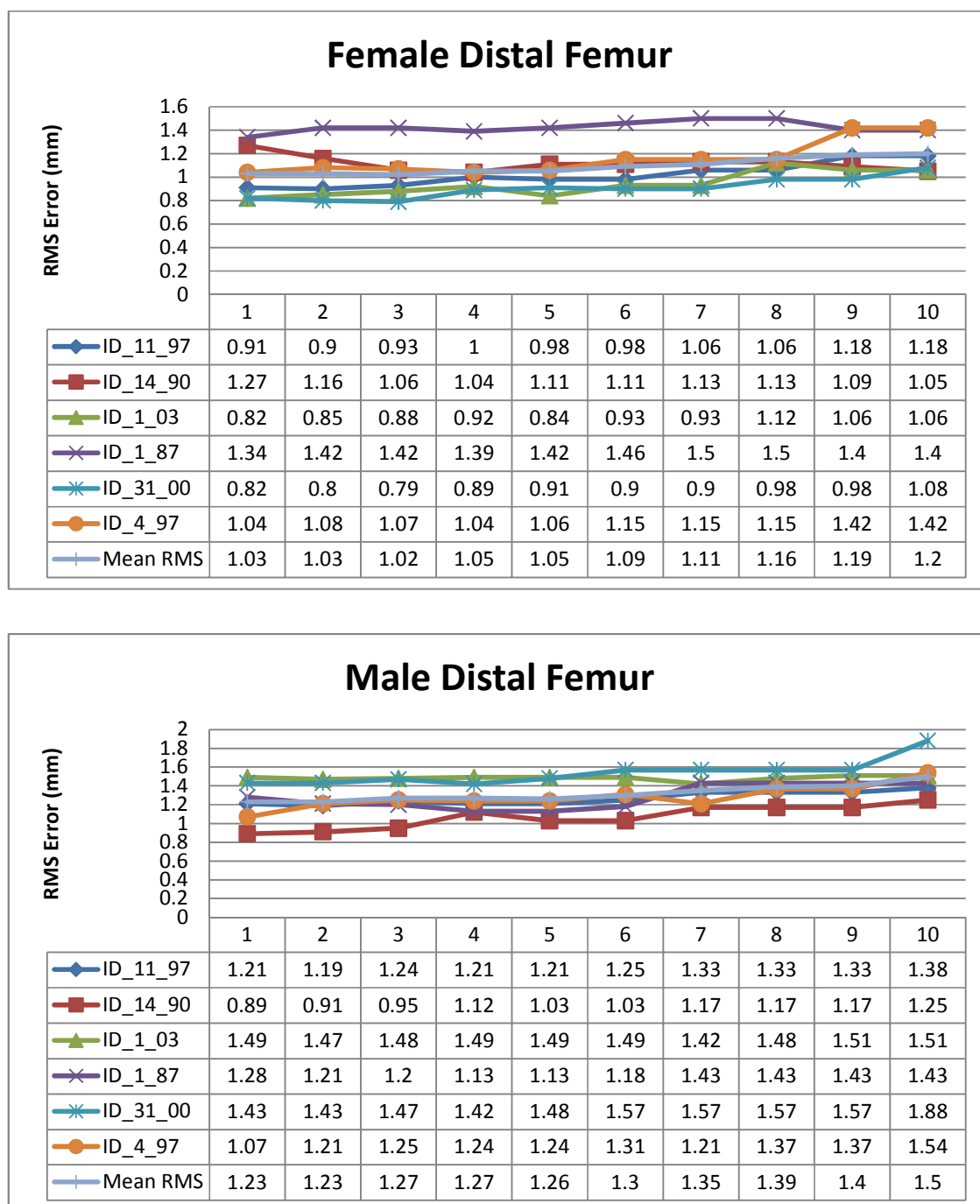


Figure 9.121 Reconstruction RMS errors vs. point cloud density (in mm) for the female (top), and male (bottom) distal femur phantoms using the hybrid morphing method

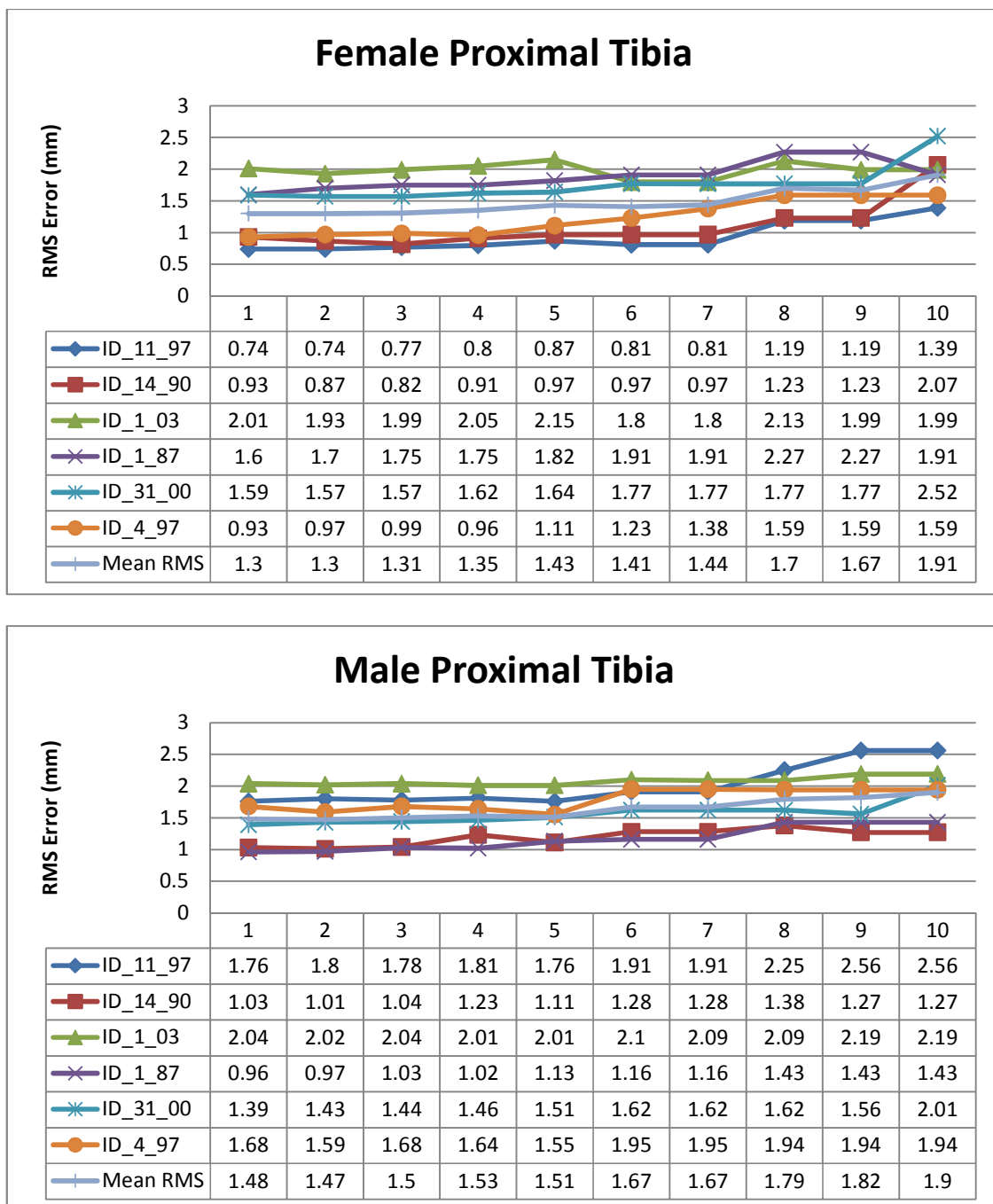


Figure 9.122 Reconstruction RMS errors vs. point cloud density (in mm) for the female (top), and male (bottom) proximal tibia phantoms using the hybrid morphing method

9.4 Ultrasound RF Data System Cadavers' Experiments Results

9.4.1 First Cadaver's Distal Femur

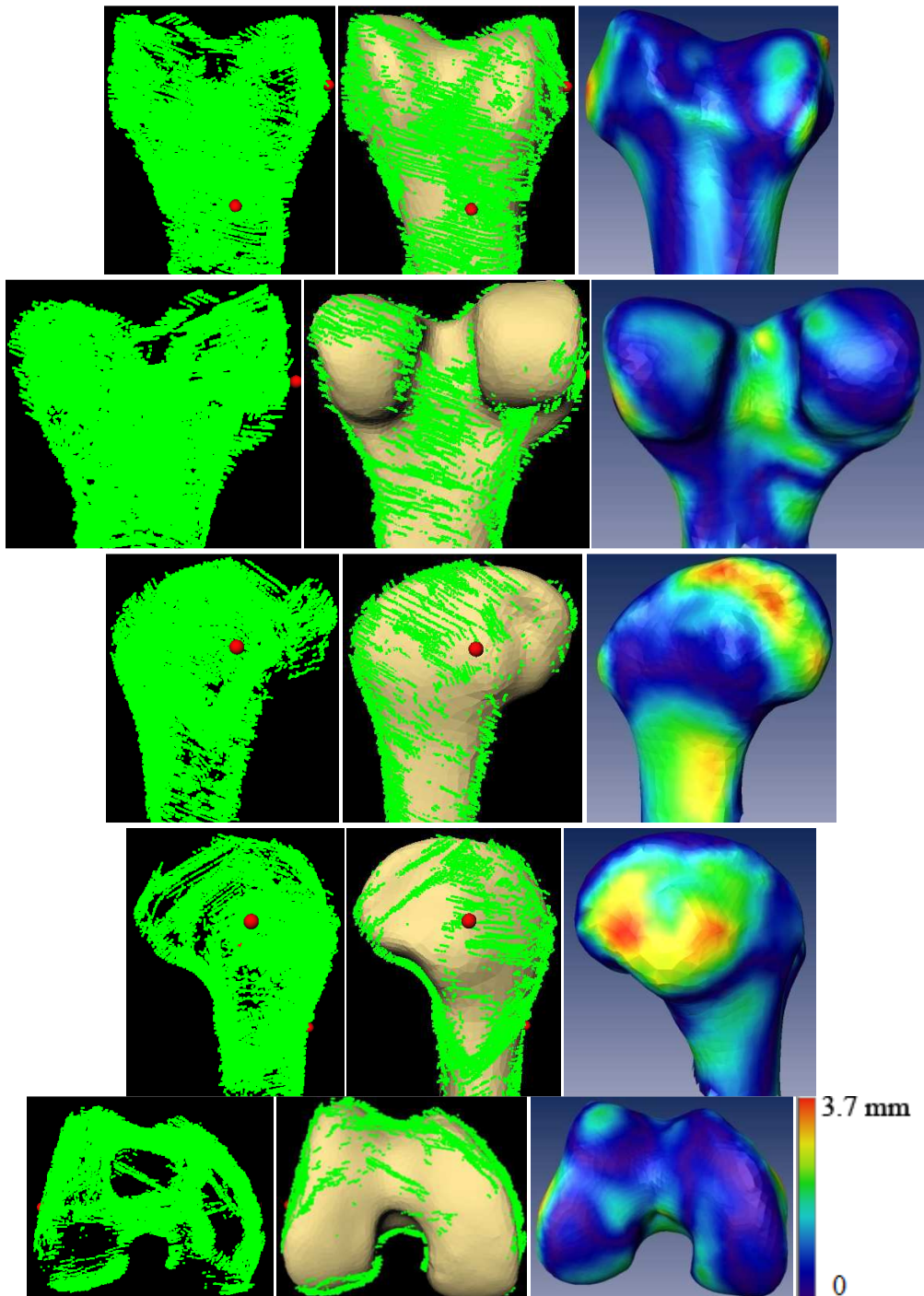


Figure 9.123 Point cloud (left), point cloud overlaid on reconstructed model (middle), and reconstruction error color map (right) for the first cadaver's distal femur

9.4.2 First Cadaver's Proximal Tibia

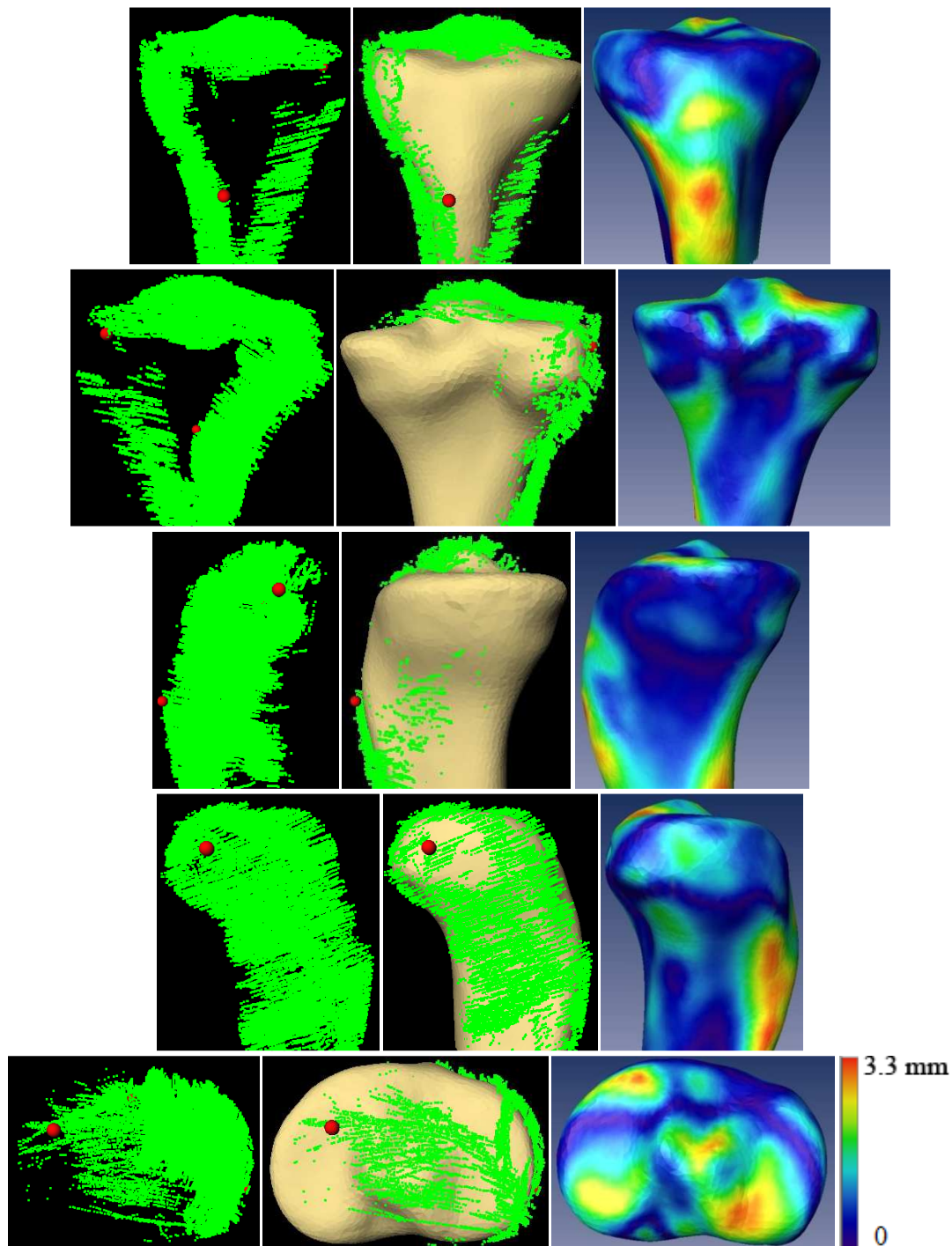


Figure 9.124 Point cloud (left), point cloud overlaid on reconstructed model (middle), and reconstruction error color map (right) for the first cadaver's proximal tibia

9.4.3 Second Cadaver's Distal Femur

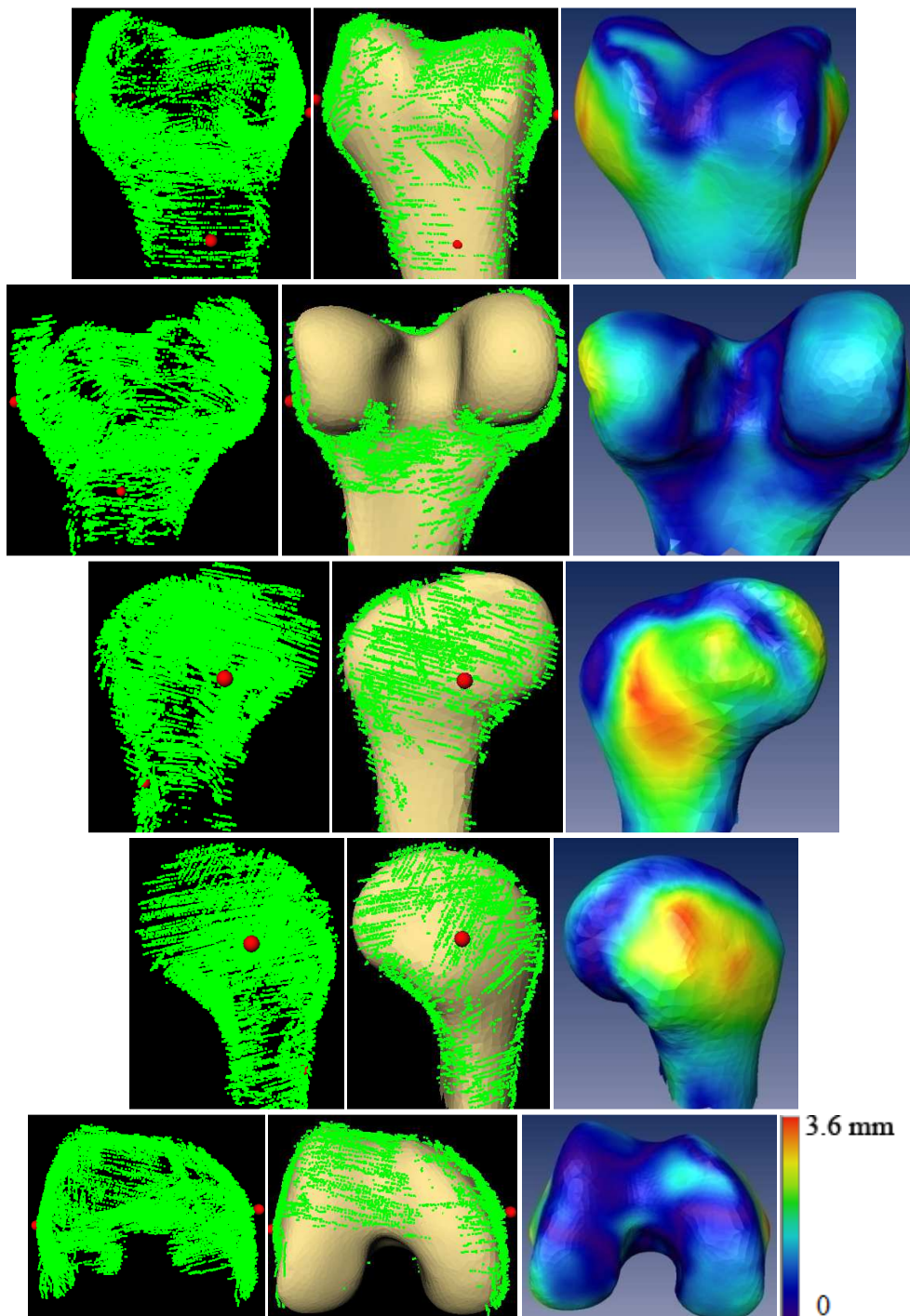


Figure 9.125 Point cloud (left), point cloud overlaid on reconstructed model (middle), and reconstruction error color map (right) for the second cadaver's distal femur

9.5 Ultrasound RF Data Imaging System's Clinical Study Results

This section presents the clinical study results for the three trials for each of the six knees scanned in the study. The reconstructed 3D point clouds are shown as well as the reconstructed 3D models (with the point clouds overlaid on them) for each of the distal femurs and proximal tibias scanned in each of the three trials for every volunteer's knee. The color maps, of the distance errors between the reconstructed 3D bone models and the golden reference 3D bone models manually segmented from the MRI scans of the volunteers knees, are shown along with the point clouds and the reconstructed models in different anatomical views (medial, lateral, anterior, posterior, superior (for the proximal tibia), and inferior (for the distal femur)). Sections 9.5.1 to 9.5.6 contains the model reconstruction results for the six knees. The results for each knee consists of the results for the three trials of distal femur 3D model reconstruction, and three trials of proximal tibia 3D model reconstruction.

Examining the reconstruction error color maps for the reconstructed 3D models for the three trials for each bone (distal femur, or proximal tibia), it can be shown that the reconstruction error is low and has similar distribution along the bone's surface for the three trials with few areas having higher error than the rest of the bone's surface. The source of high error areas (yellow, and red colors in the color map) in the reconstruction error color map for any reconstructed 3D bone model is one or combination of the following sources:

- **Missing point cloud area:** This is the case when the reconstructed point cloud is missing the point cloud part covering this area. This occurs at the areas that can't be

accessible by the ultrasound for scanning and point cloud reconstruction. These areas are the lateral condyle of the femur, the interior surface of the femoral condyles (the opposite surface to the epicondyles), and tibial plateau. In addition to these inaccessible areas of the bones, some other areas of the bones can be missed in the scanning which creates gaps in the point cloud, which causes high model reconstruction errors at these areas. If the missing point cloud area is due to incomplete scanning, then this error will most likely not be existing in different scanning trials for the same knee. While the errors, caused by the gaps in the point cloud due to inaccessible parts of the bone, will be existing in all scanning trials of the same knee.

- **High error in the point cloud at the area:** This case occurs when the part of the point cloud at that area (with high reconstruction error) having high error (low accuracy). This can happen due motion artifact from the motion of the patient's leg, or the motion tracking system (the magnet of the electromagnetic tracking system) during any of the region scanning sessions. The high error areas of the point cloud can also occur in areas where the bone depth is large (in high BMI patients) which increases the distance travelled by the ultrasound pulse, and thus increases the error in the bone depth estimation due to the inexact ultrasound speed used as described in section 7.3. This source of error will most likely not exist in all of the scanning trials of the same knee if it is due to motion artifact because of its randomness in occurrence. While, if the source of this error large bone depth, the error will exist in all of the scanning trials of the same knee.

- Lack of area's anatomical morphology representation in the atlas: This case occurs when an area of the bone's surface is having a morphology not existing in the statistical atlas used, and can't be extrapolated from the morphology variations encoded in the atlas used. This error occurs in all of the scanning trials for the same knee.

9.5.1 Volunteer's Knee 1

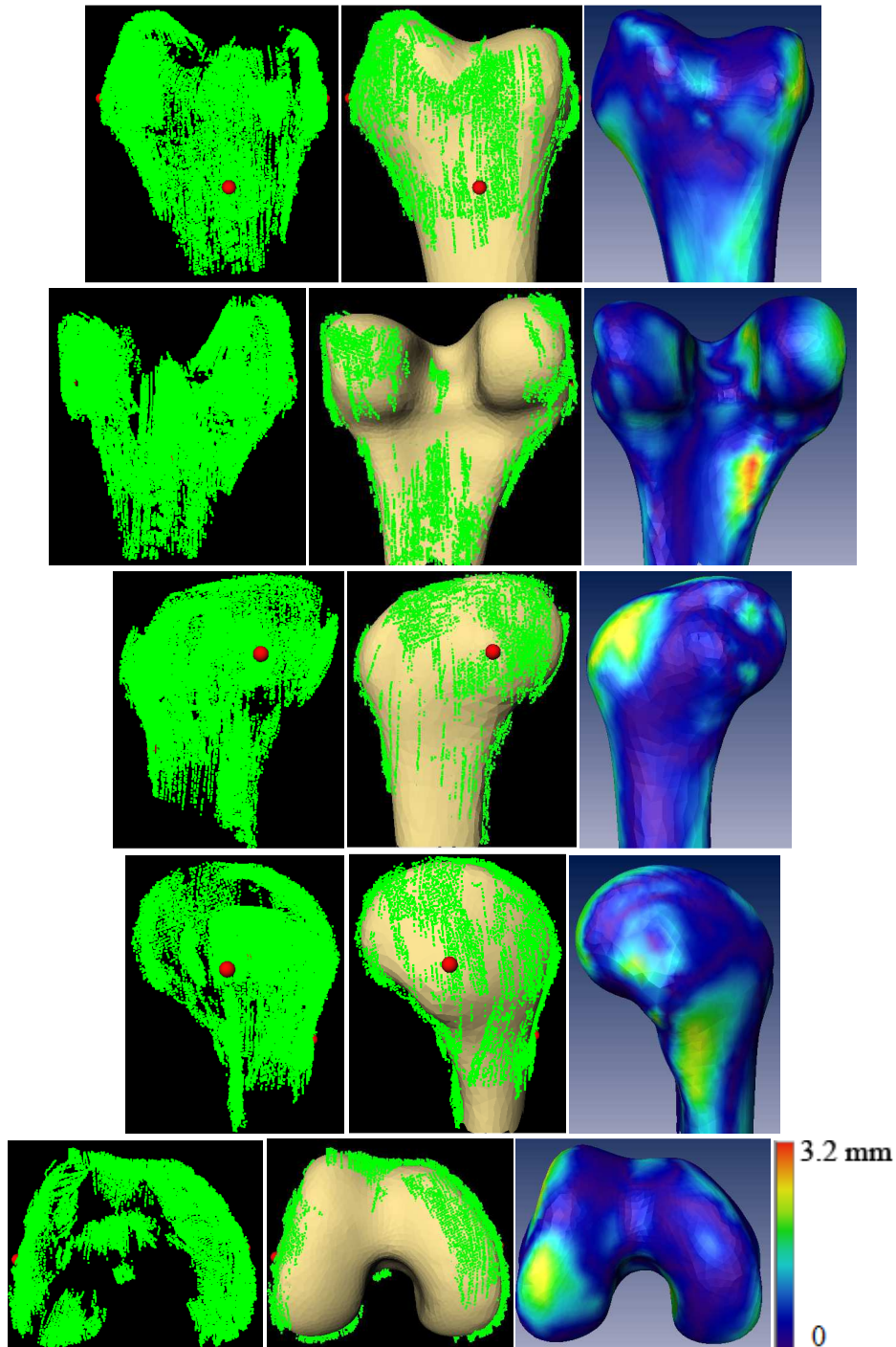


Figure 9.126 Point cloud (left), reconstructed model (middle), and error map (right) for volunteer's knee 1 distal femur, trial 1, with RMS of 0.84 mm and Avg. error of 0.64 mm

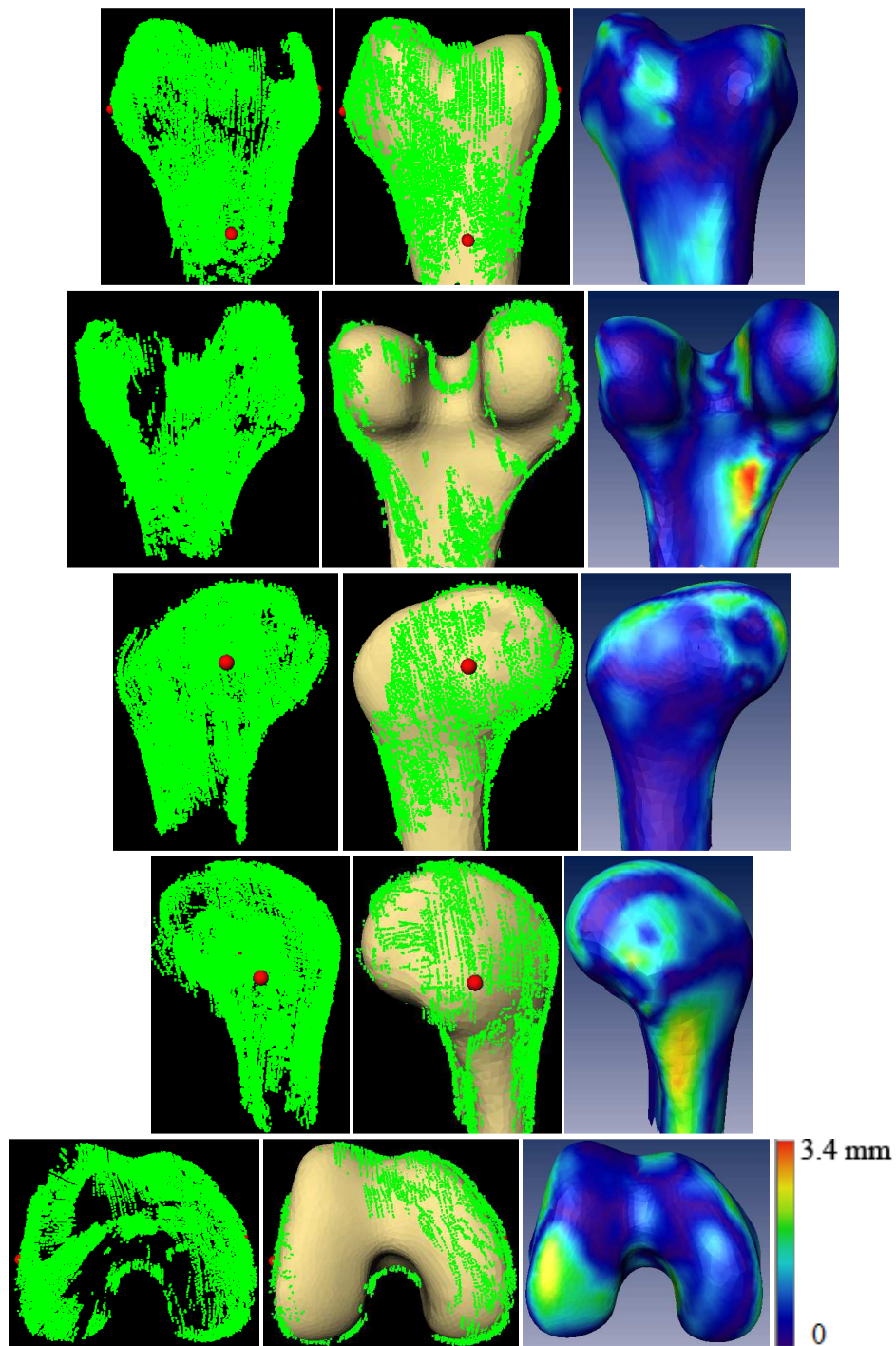


Figure 9.127 Point cloud (left), reconstructed 3D model (middle), and reconstruction error color map (right) for volunteer's knee 1 distal femur, trial 2, with RMS of 0.94 mm and Avg. error of 0.74 mm

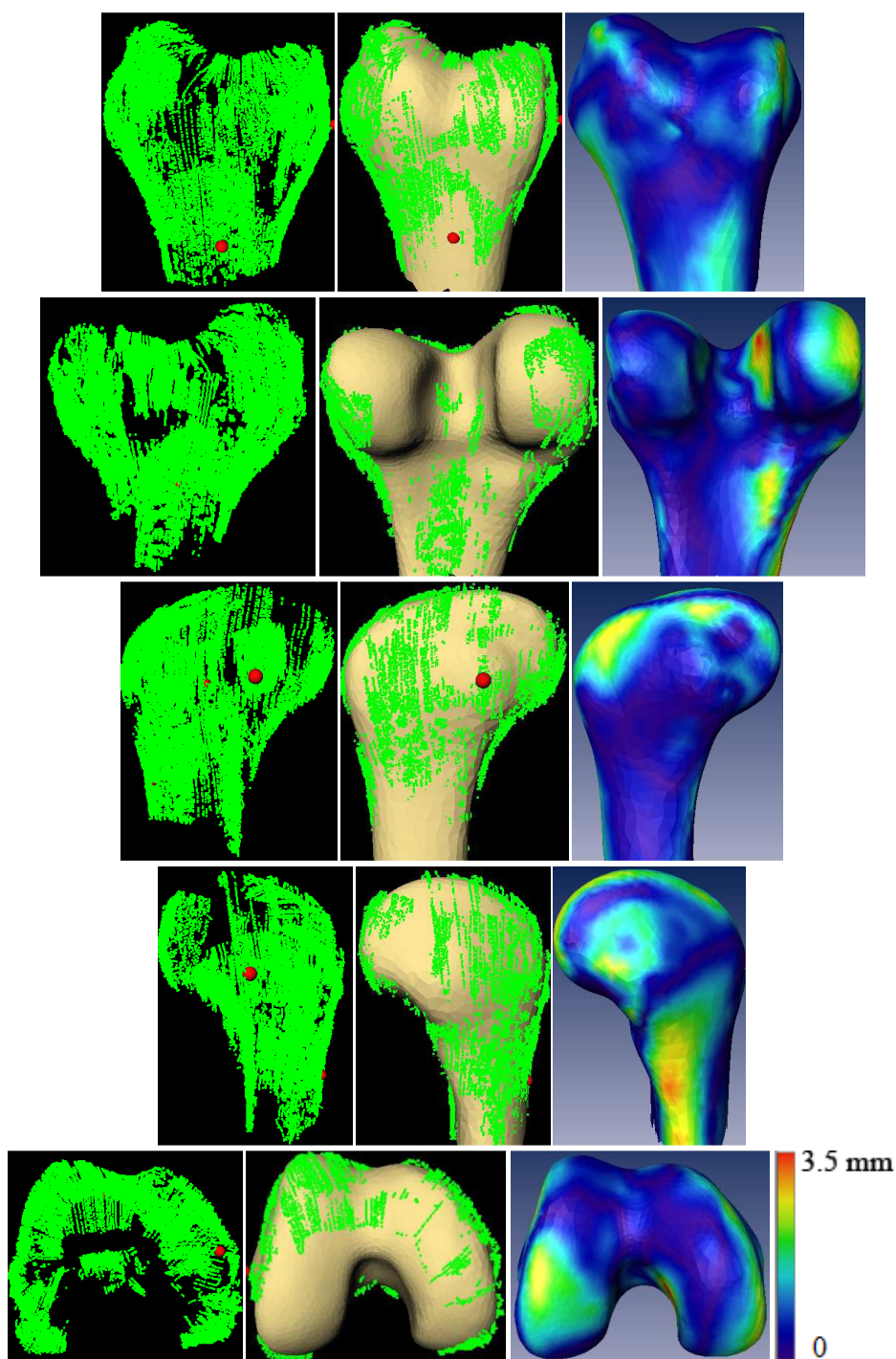


Figure 9.128 Point cloud (left), reconstructed 3D model (middle), and reconstruction error color map (right) for volunteer's knee 1 distal femur, trial 3, with RMS of 1.04 mm and Avg. error of 0.8 mm

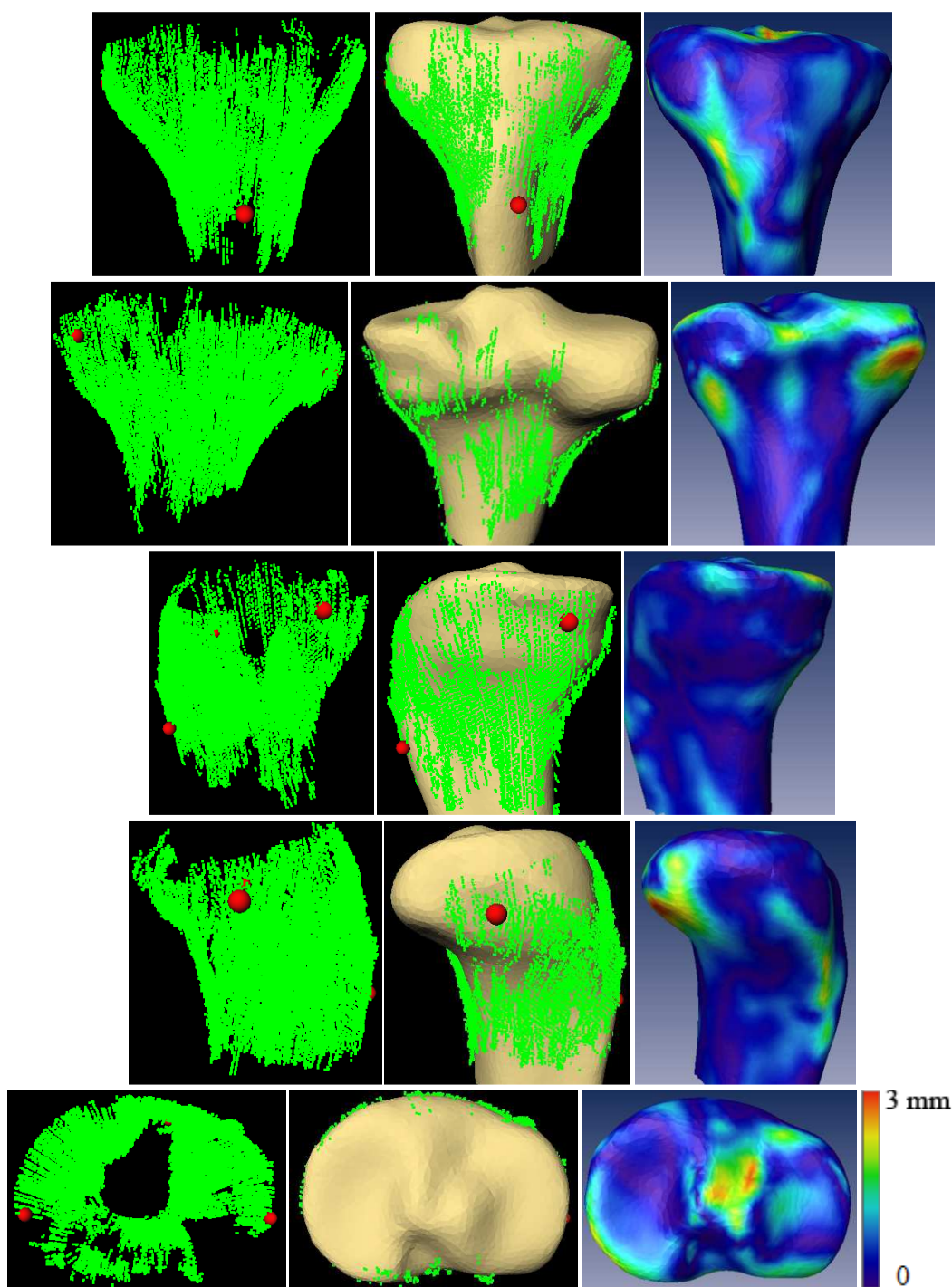


Figure 9.129 Point cloud (left), reconstructed 3D model (middle), and reconstruction error map (right) for volunteer's knee 1 proximal tibia, trial 1, with RMS of 0.78 mm and Avg. error of 0.6 mm

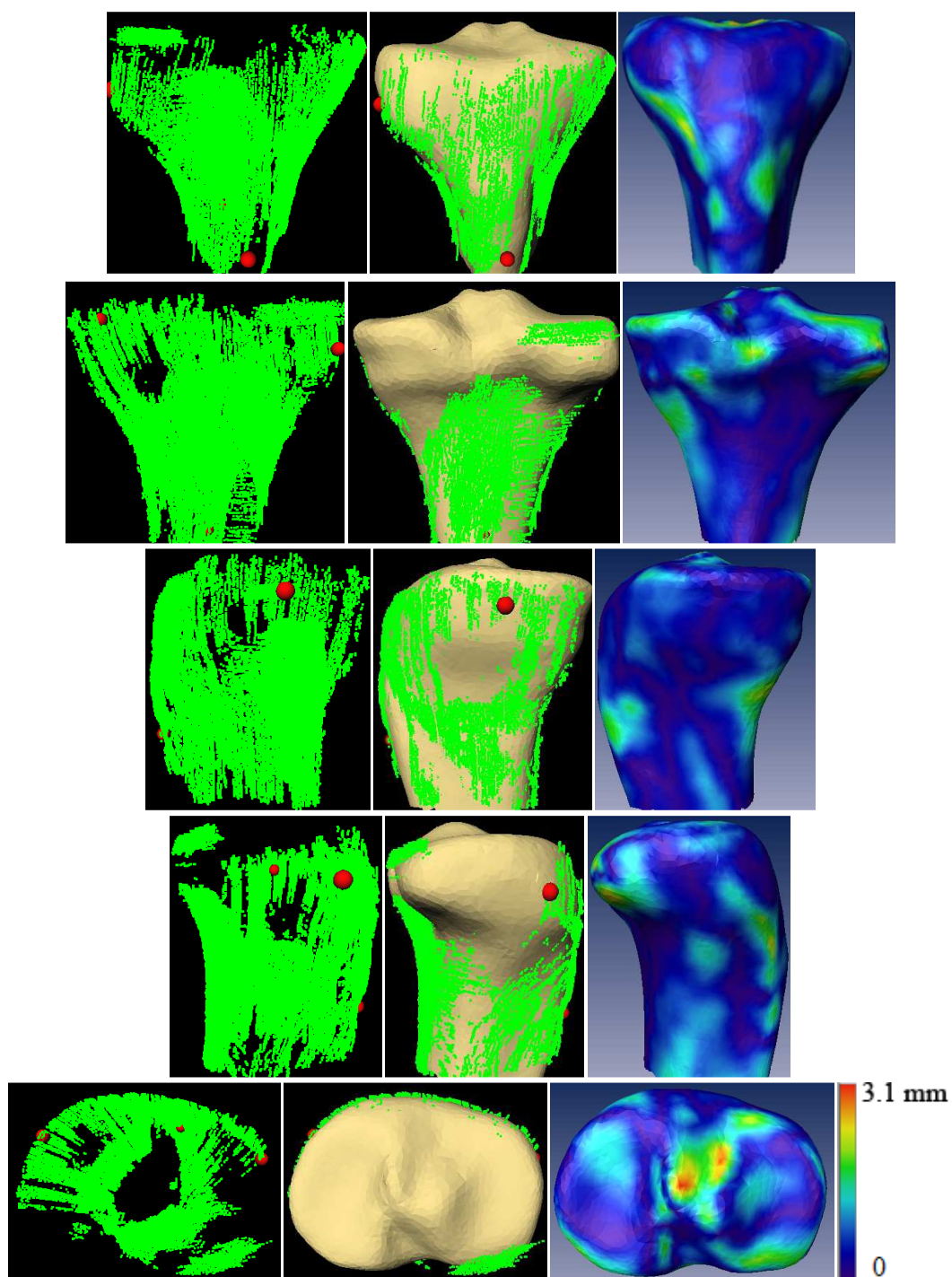


Figure 9.130 Point cloud (left), reconstructed 3D model (middle), and reconstruction error color map (right) for volunteer 1 proximal tibia, trial 2, with RMS of 0.79 mm and Avg. error of 0.62 mm

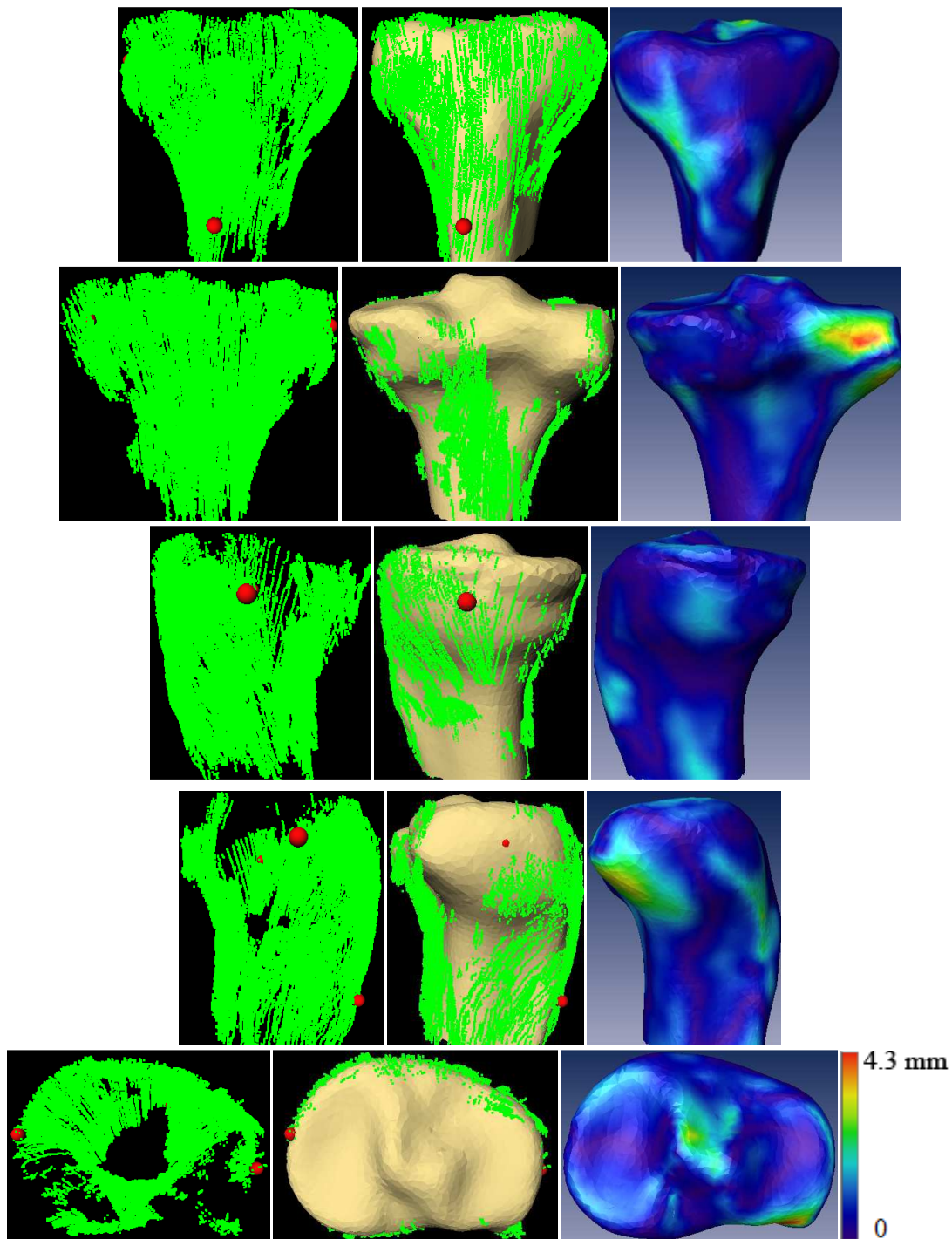


Figure 9.131 Point cloud (left), reconstructed 3D model (middle), and reconstruction error color map (right) for volunteer's knee 1 proximal tibia, trial 3, with RMS of 0.96 mm and Avg. error of 0.75 mm

9.5.2 Volunteer's Knee 2

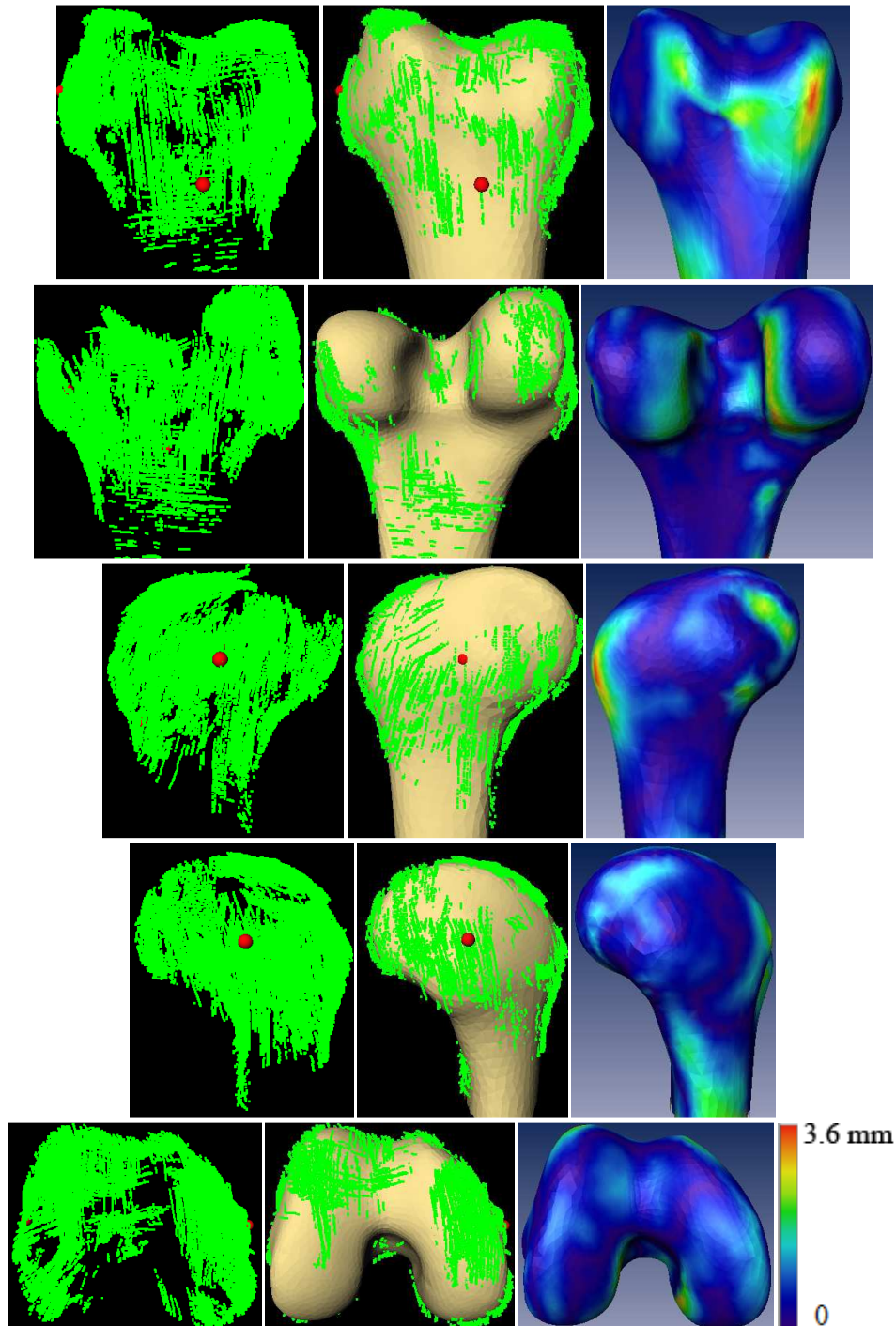


Figure 9.132 Point cloud (left), reconstructed 3D model (middle), and error map (right) for volunteer's knee 2 distal femur, trial 1, with RMS of 1 mm and Avg. error of 0.78 mm

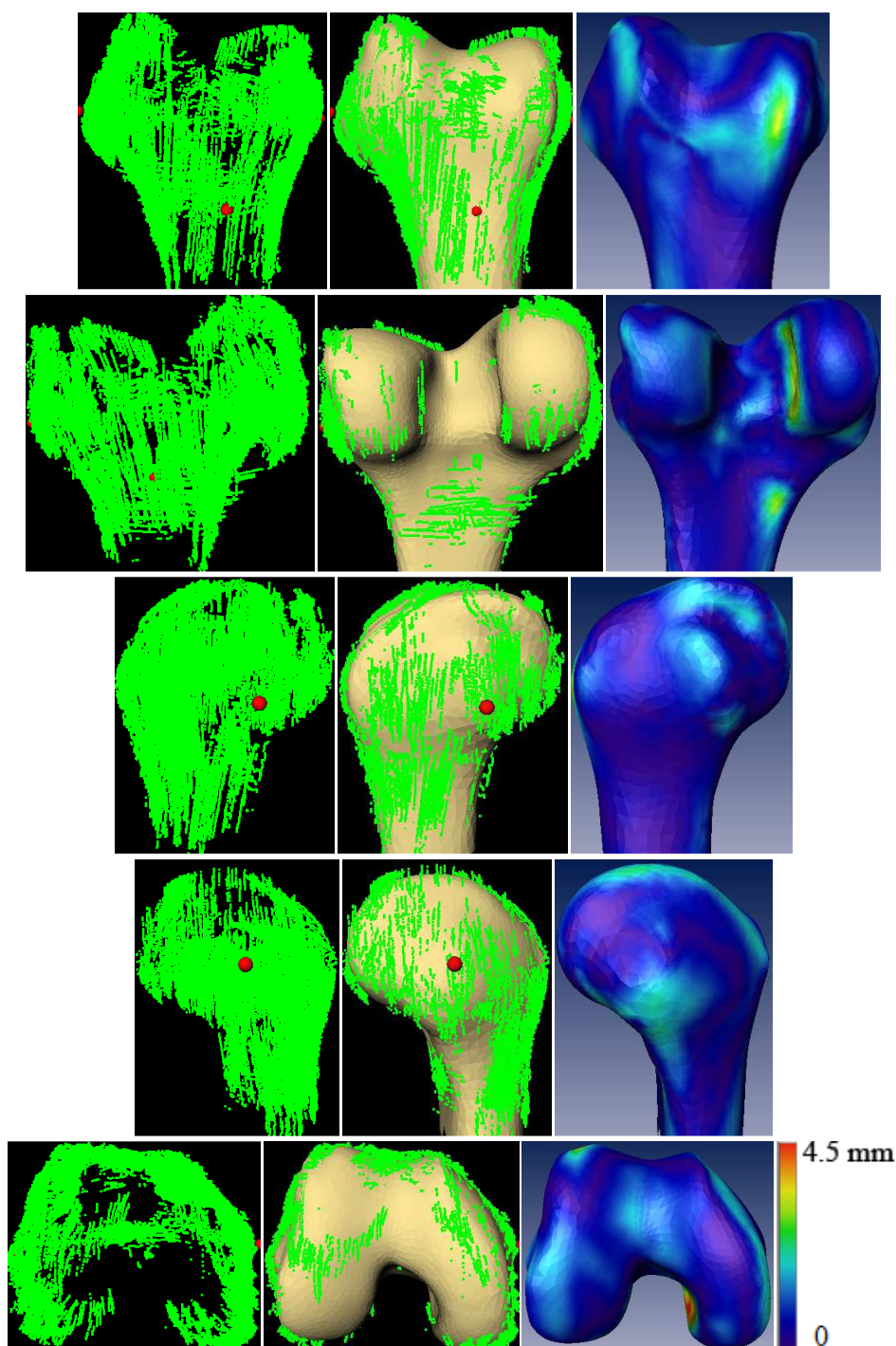


Figure 9.133 Point cloud (left), reconstructed 3D model (middle), and reconstruction error color map (right) for volunteer's knee 2 distal femur, trial 2, with RMS of 1.09 mm and Avg. error of 0.85 mm

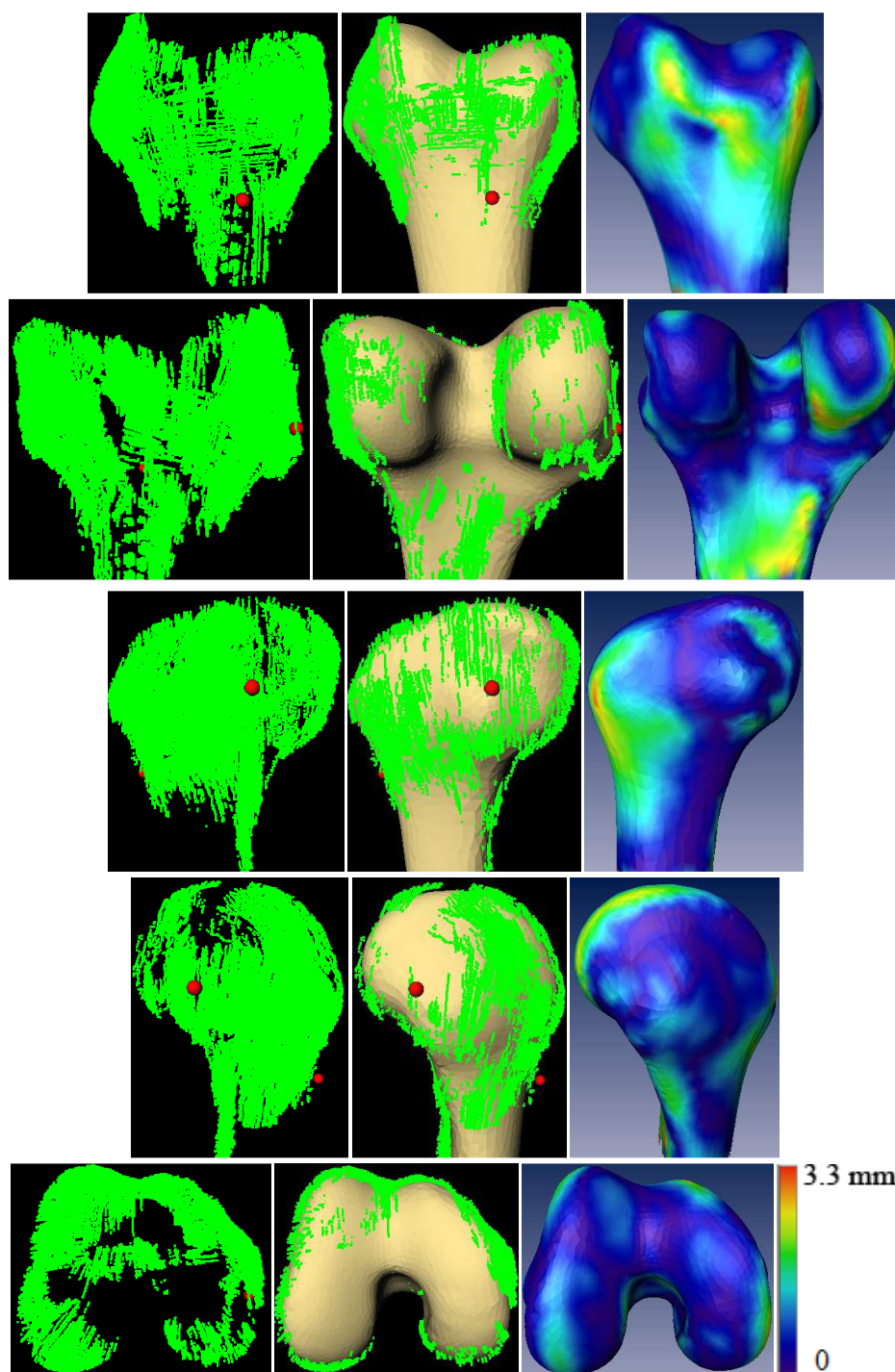


Figure 9.134 Point cloud (left), reconstructed 3D model (middle), and reconstruction error color map (right) for volunteer 2 distal femur, trial 3, with RMS of 0.95 mm and Avg. error of 0.72 mm

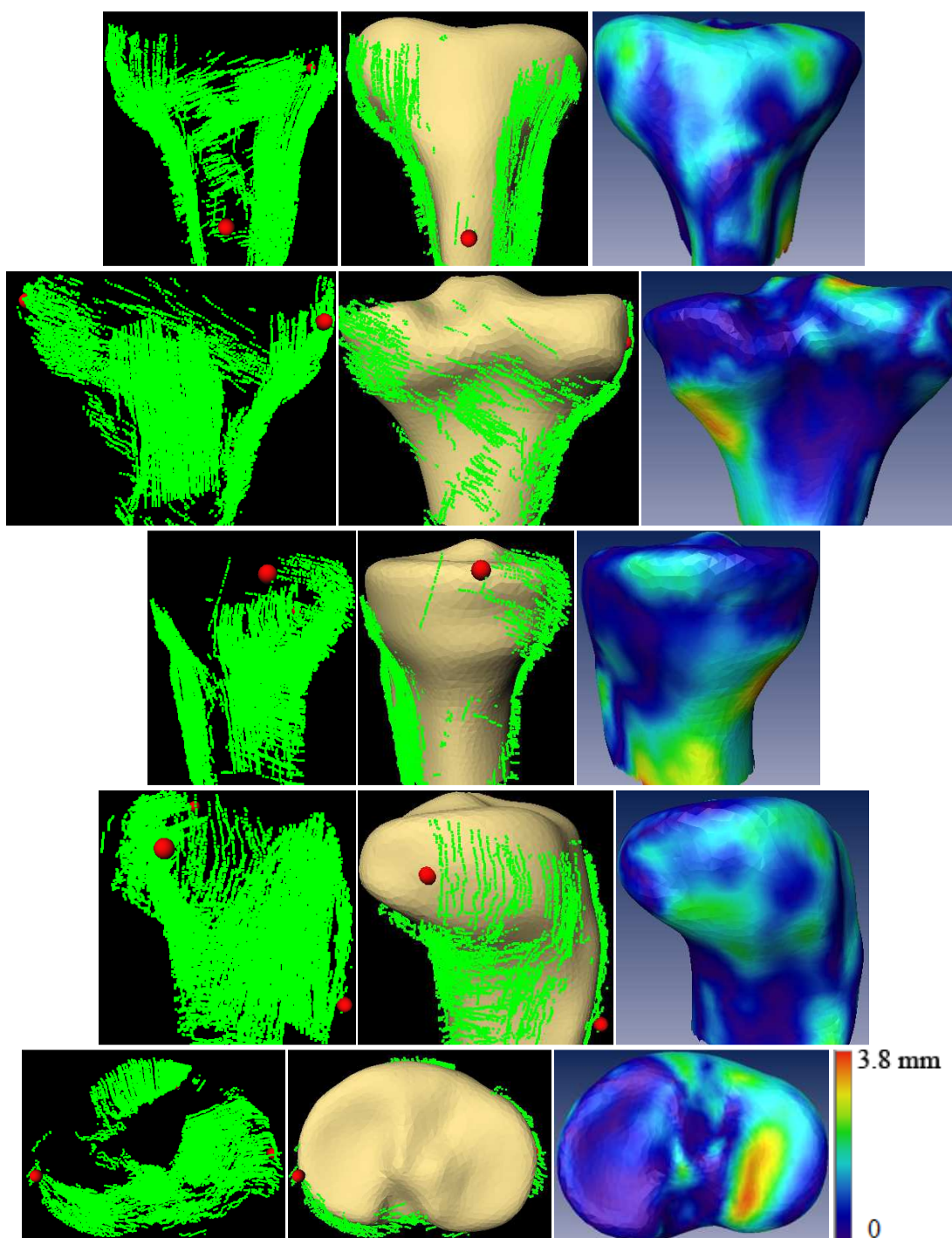


Figure 9.135 Point cloud (left), reconstructed 3D model (middle), and reconstruction error color map (right) for volunteer 2 proximal tibia, trial 1, with RMS of 1.2 mm and Avg. error of 0.98 mm

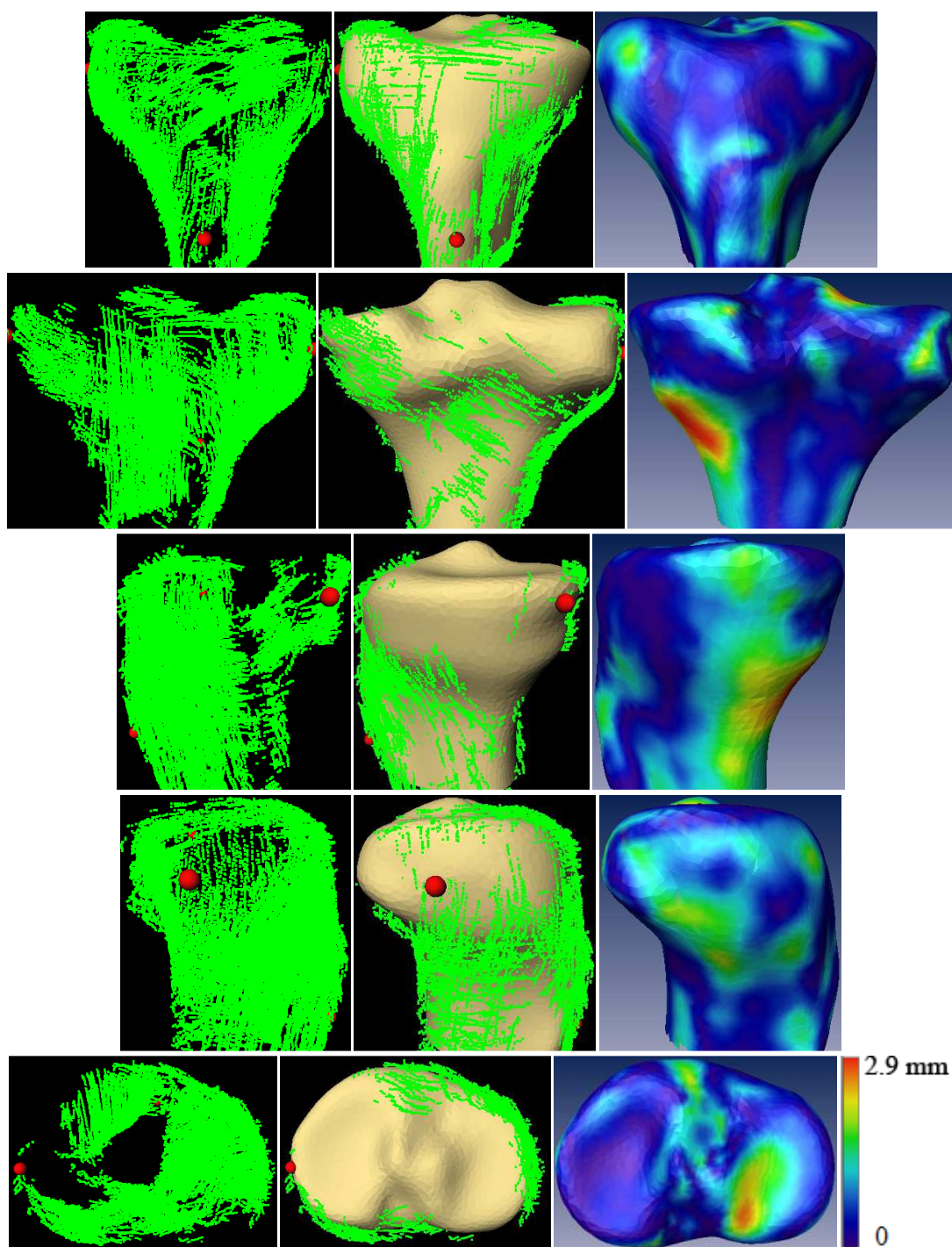


Figure 9.136 Point cloud (left), reconstructed 3D model (middle), and reconstruction error color map (right) for volunteer 2 proximal tibia, trial 2, with RMS of 0.91 mm and Avg. error of 0.71 mm

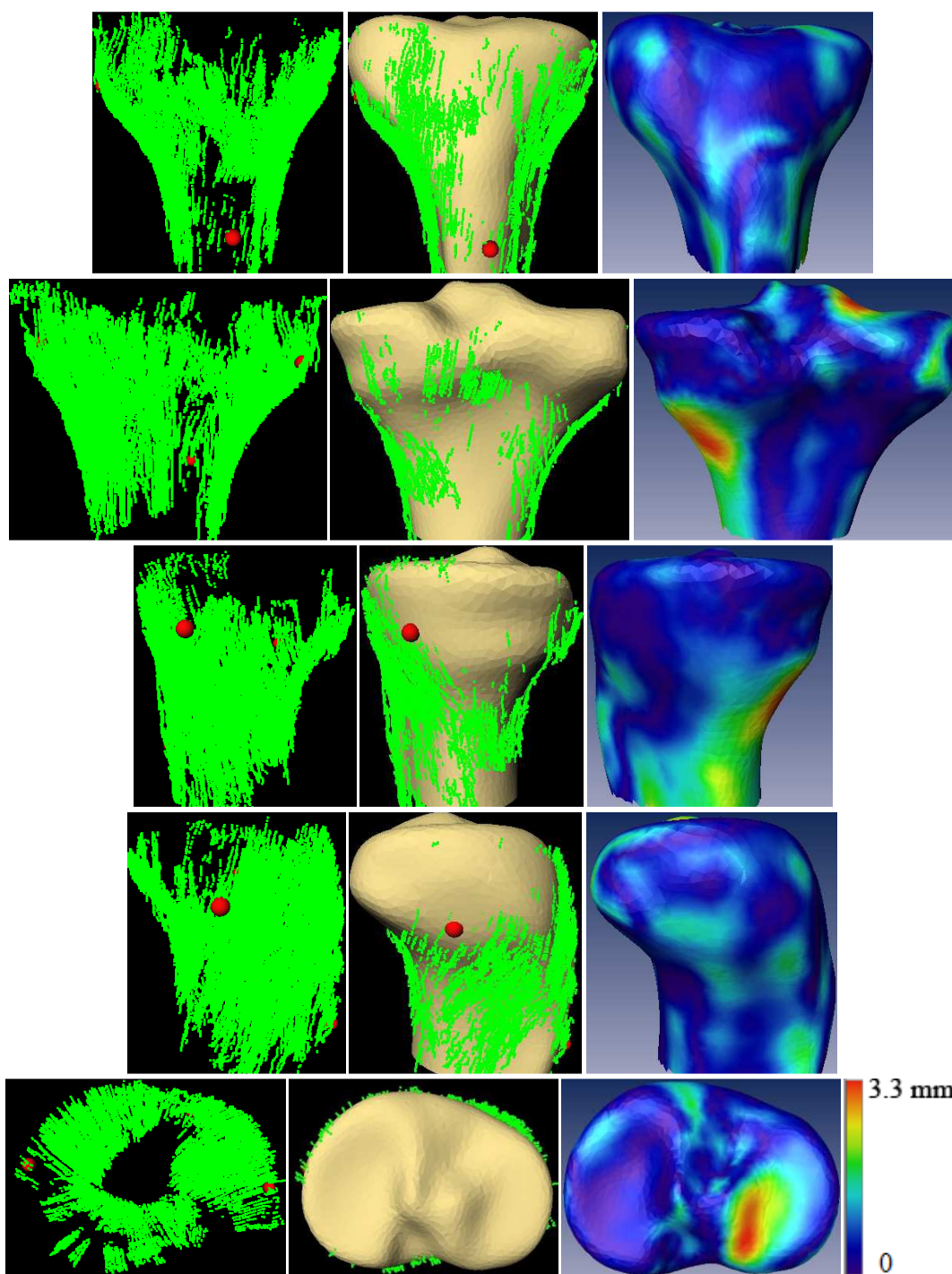


Figure 9.137 Point cloud (left), reconstructed 3D model (middle), and reconstruction error color map (right) for volunteer 2 proximal tibia, trial 1, with RMS of 0.95 mm and Avg. error of 0.72 mm

9.5.3 Volunteer's Knee 3

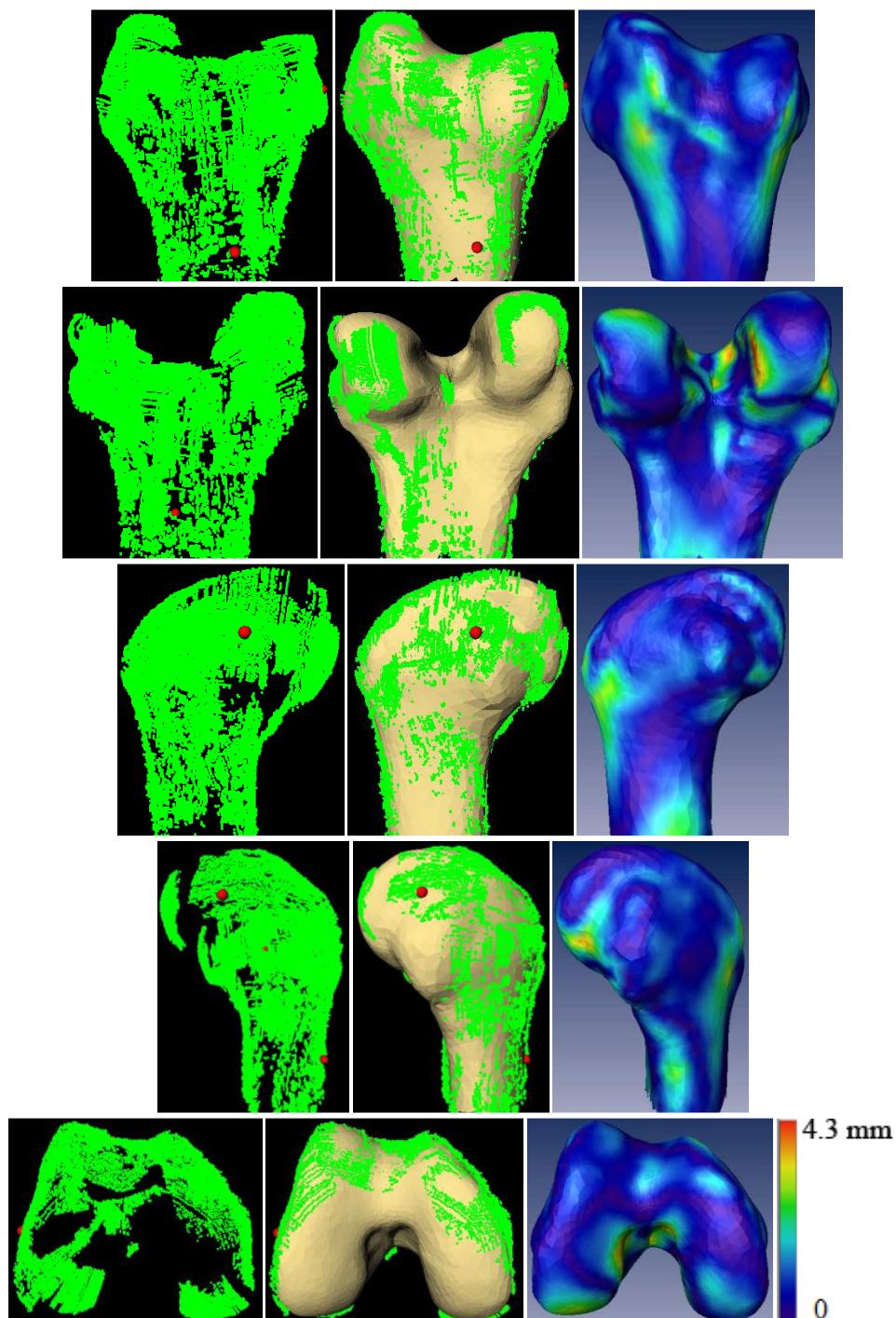


Figure 9.138 Point cloud (left), reconstructed model (middle), and error map (right) for volunteer's knee 3 distal femur, trial 1, with RMS of 1.18 mm and Avg. error of 0.93 mm

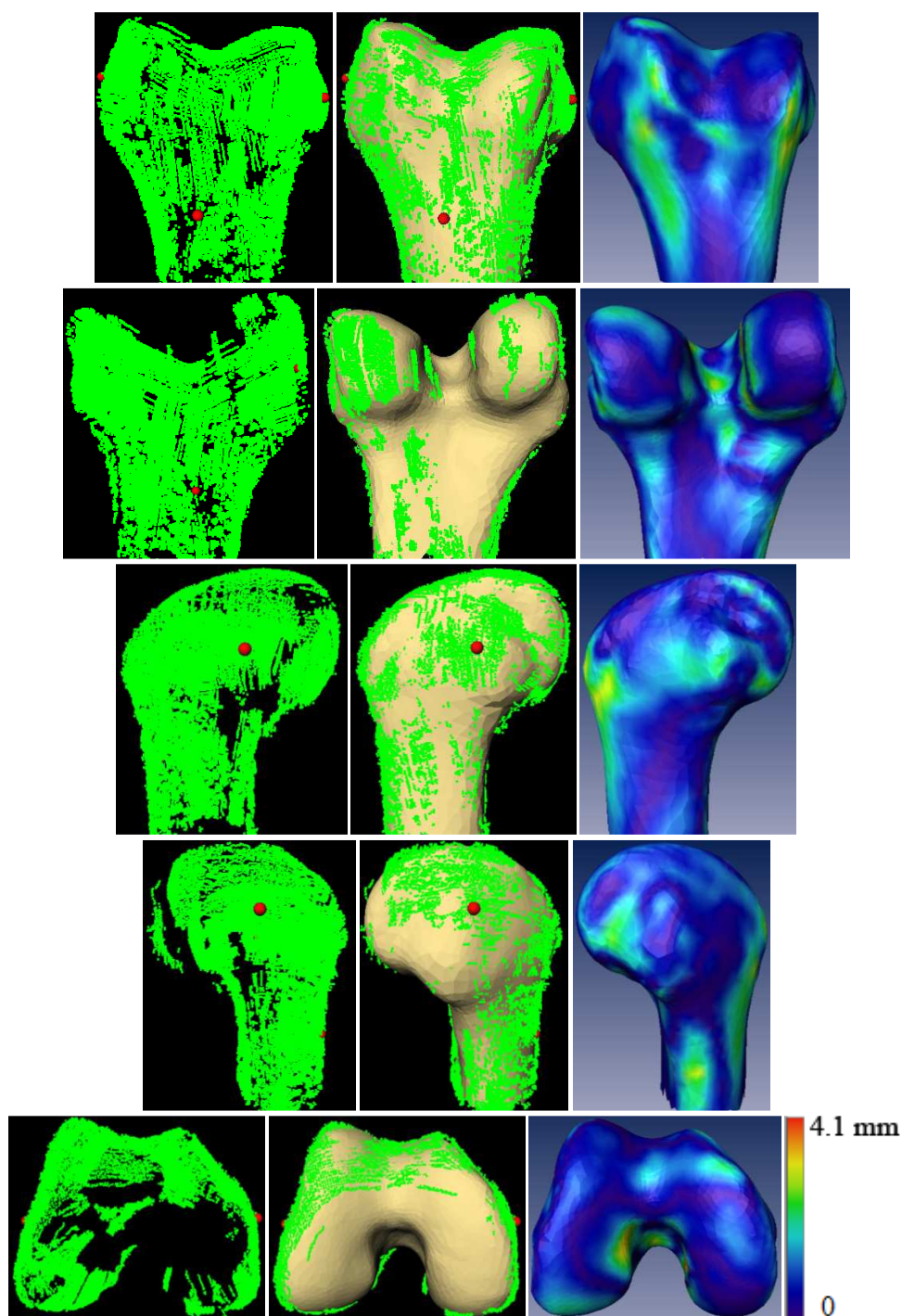


Figure 9.139 Point cloud (left), reconstructed 3D model (middle), and reconstruction error color map (right) for volunteer's knee3 distal femur, trial 2, with RMS of 1.05 mm and Avg. error of 0.83 mm

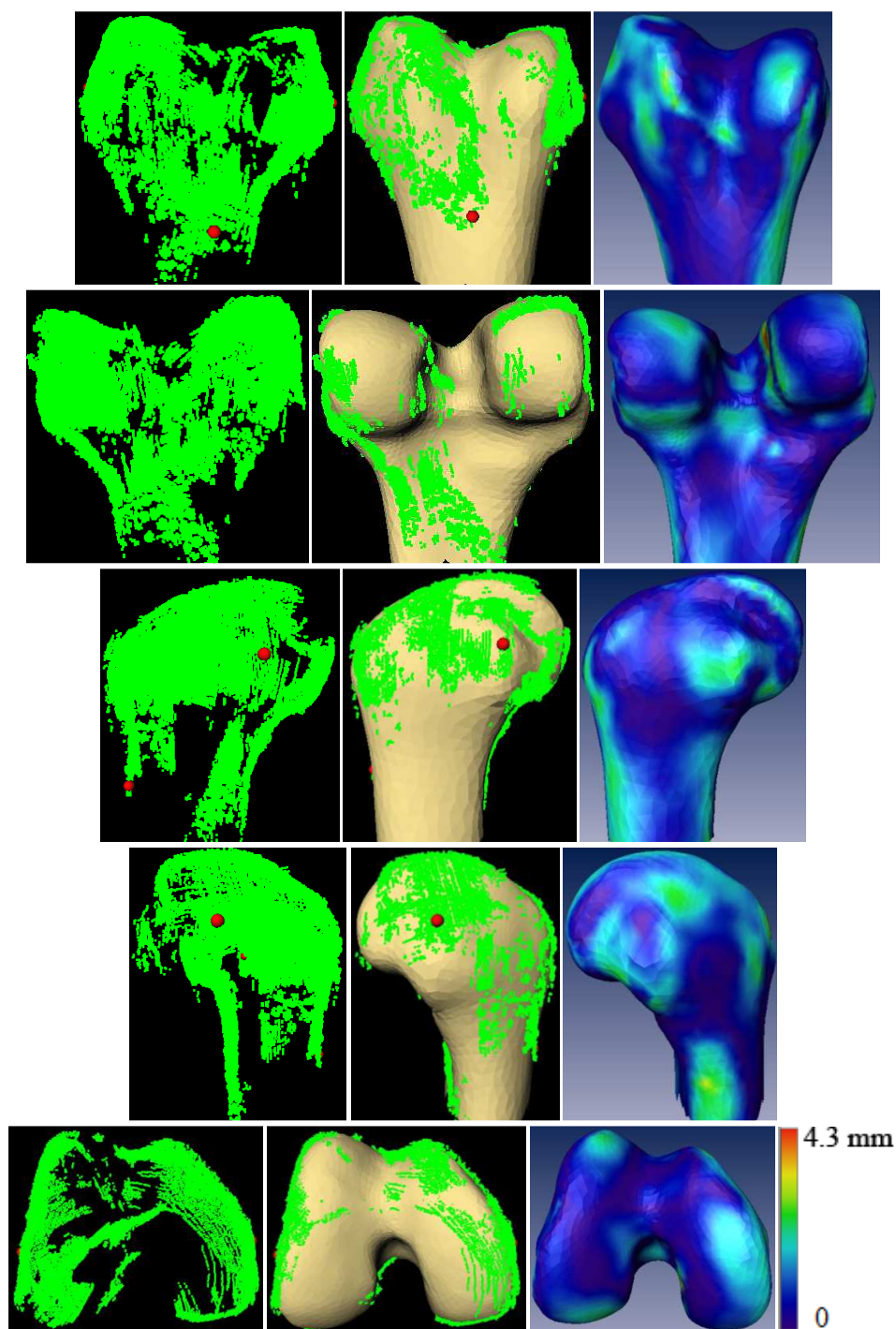


Figure 9.140 Point cloud (left), reconstructed 3D model (middle), and reconstruction error color map (right) for volunteer's knee 3 distal femur, trial 3, with RMS of 1.01 mm and Avg. error of 0.81 mm

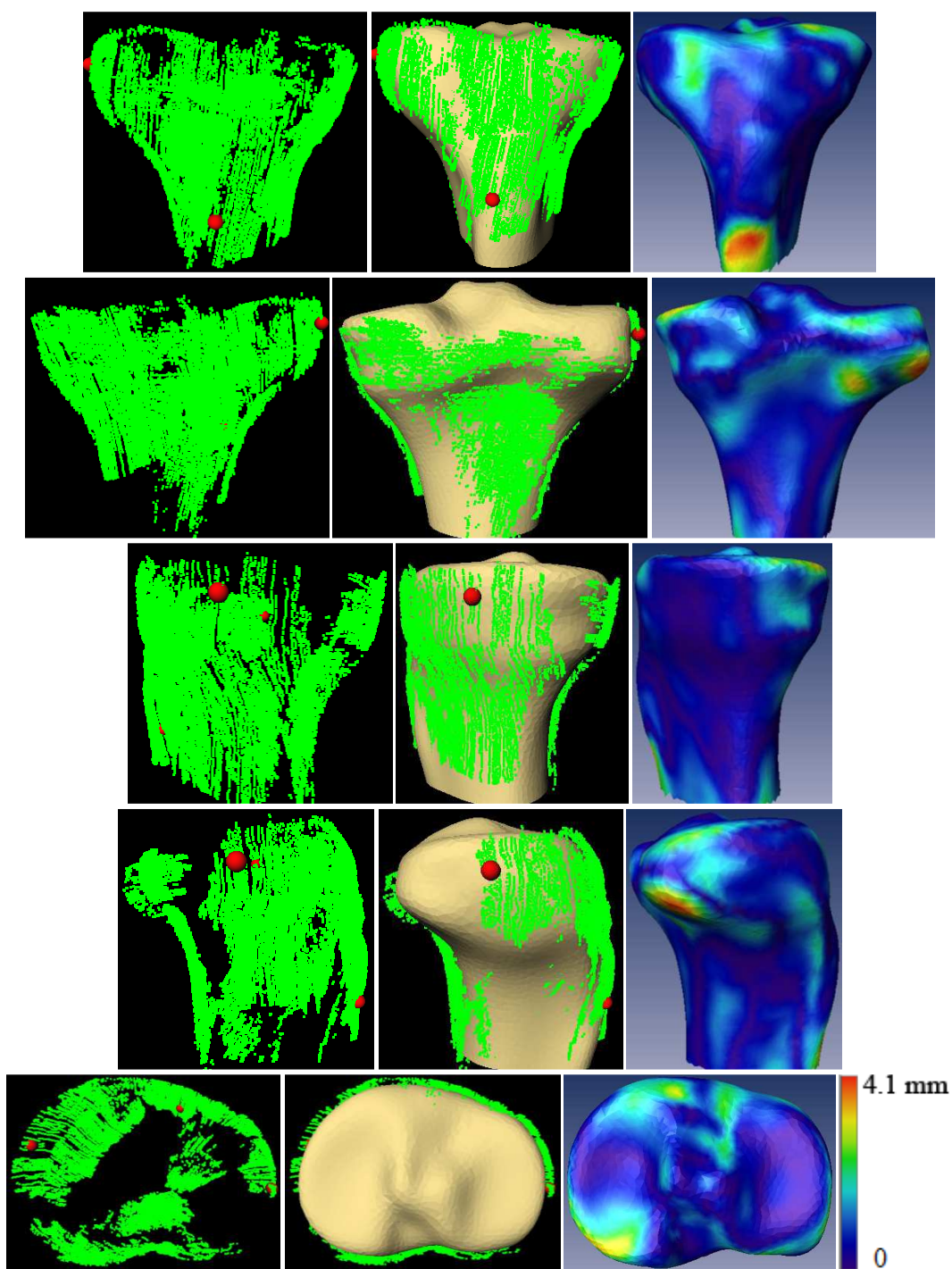


Figure 9.141 Point cloud (left), reconstructed 3D model (middle), and reconstruction error color map (right) for volunteer's knee 3 proximal tibia, trial 1, with RMS of 1.05 mm and Avg. error of 0.8 mm

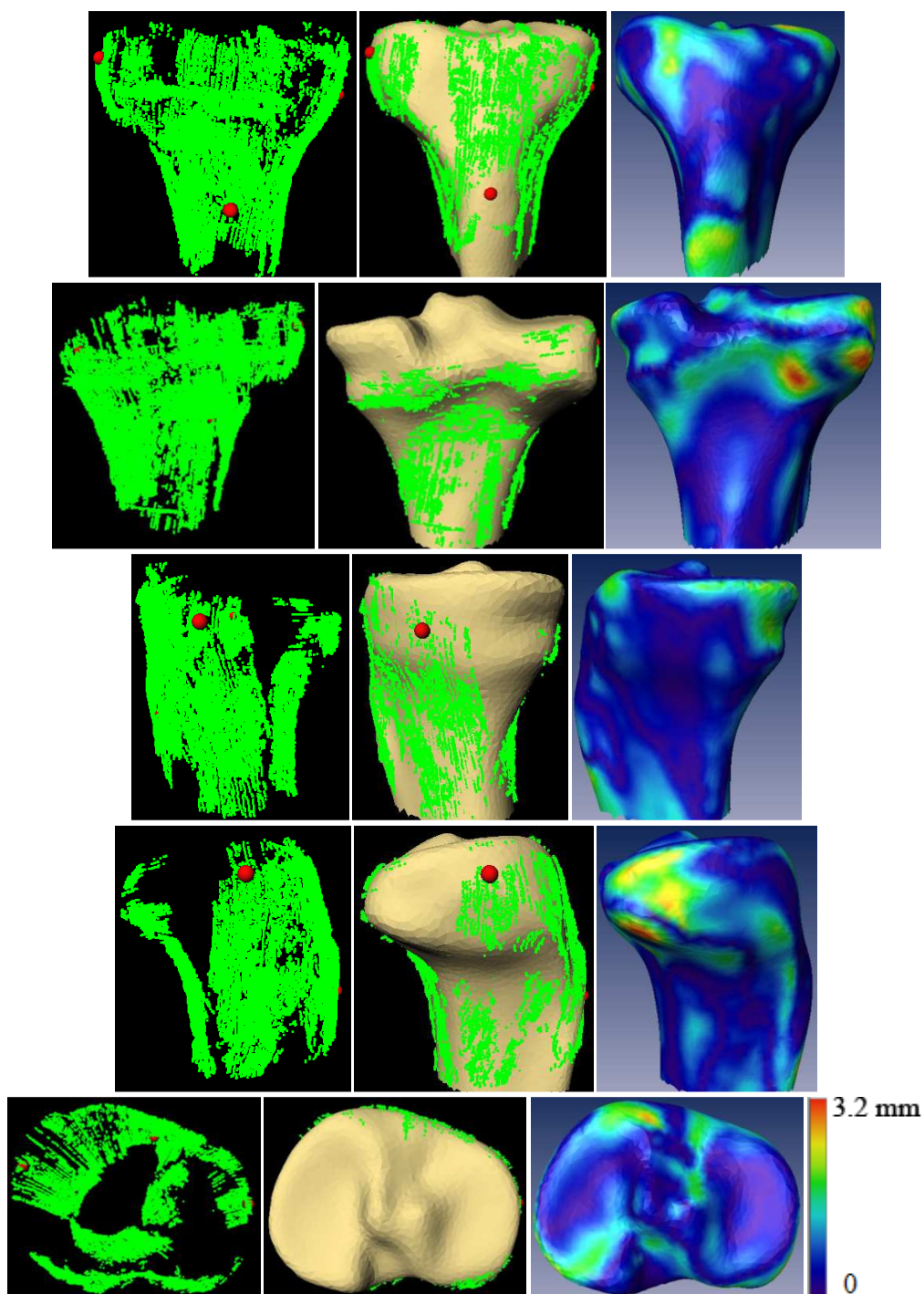


Figure 9.142 Point cloud (left), reconstructed 3D model (middle), and reconstruction error color map (right) for volunteer's knee 3 proximal tibia, trial 2, with RMS of 0.88 mm and Avg. error of 0.69 mm

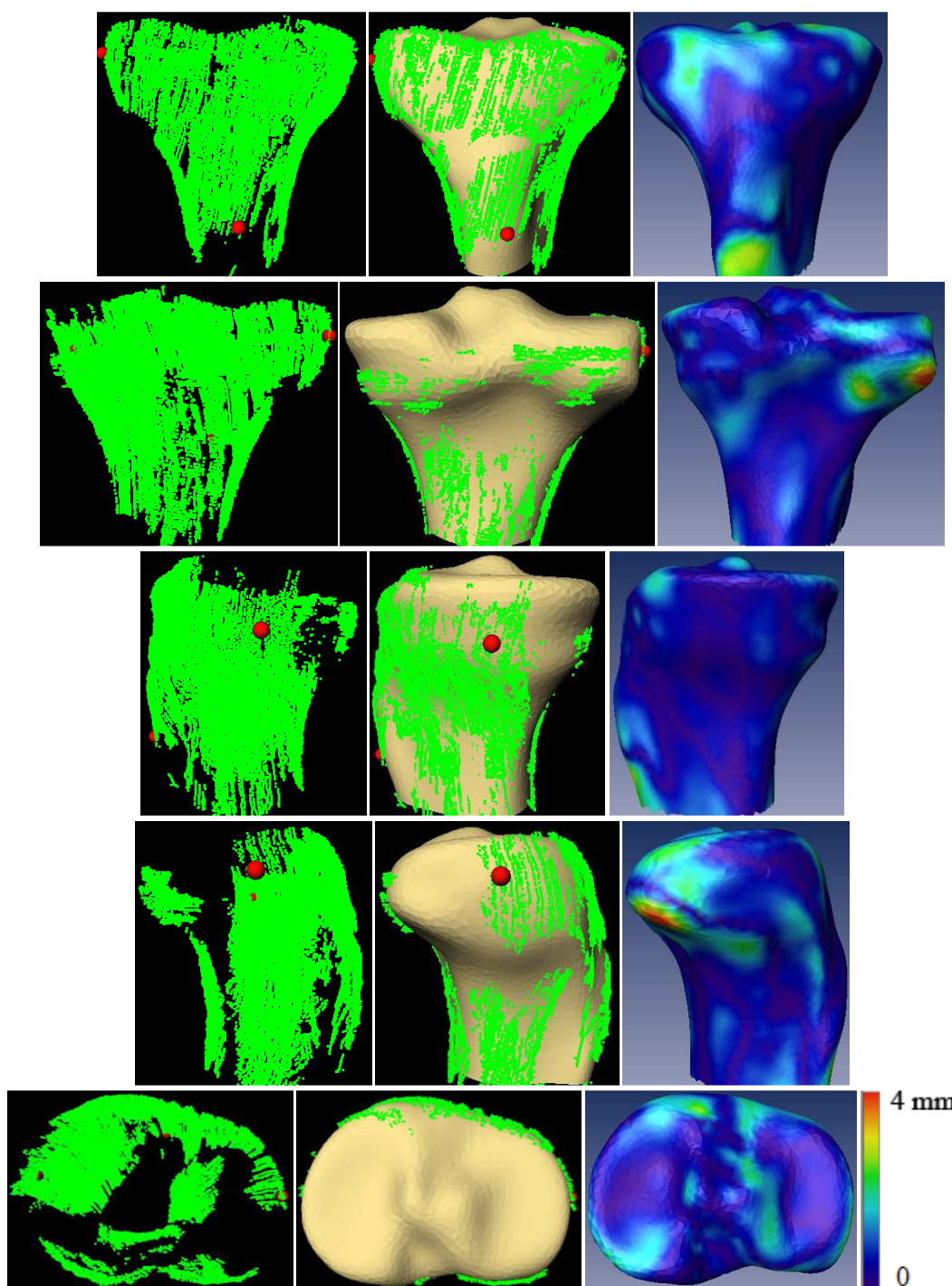


Figure 9.143 Point cloud (left), reconstructed 3D model (middle), and reconstruction error color map (right) for volunteer's knee 3 proximal tibia, trial 3, with RMS of 0.89 mm and Avg. error of 0.68 mm

9.5.4 Volunteer's Knee 4

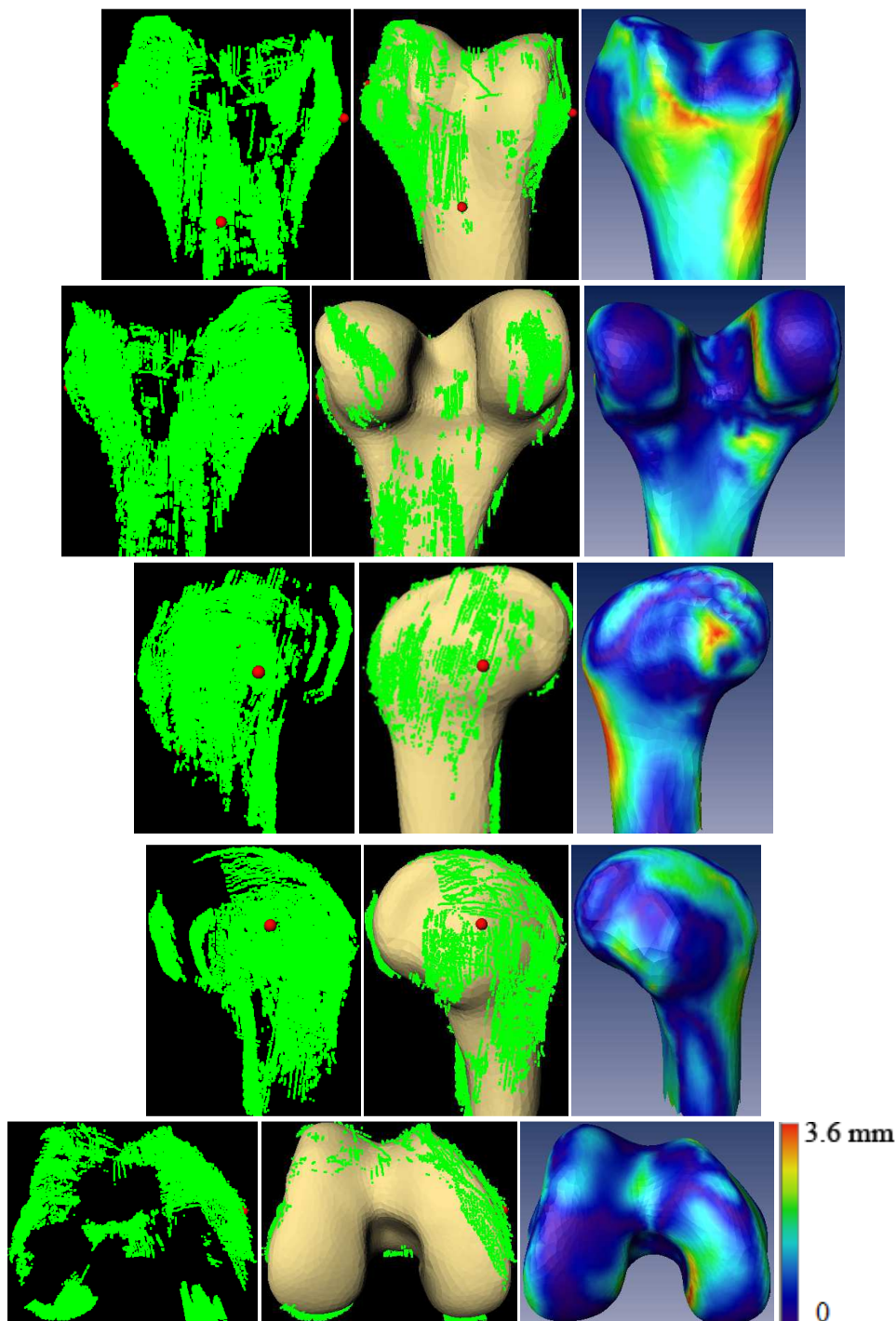


Figure 9.144 Point cloud (left), reconstructed model (middle), and error map (right) for volunteer's knee 4 distal femur, trial 1, with RMS of 1.14 mm and Avg. error of 0.89 mm

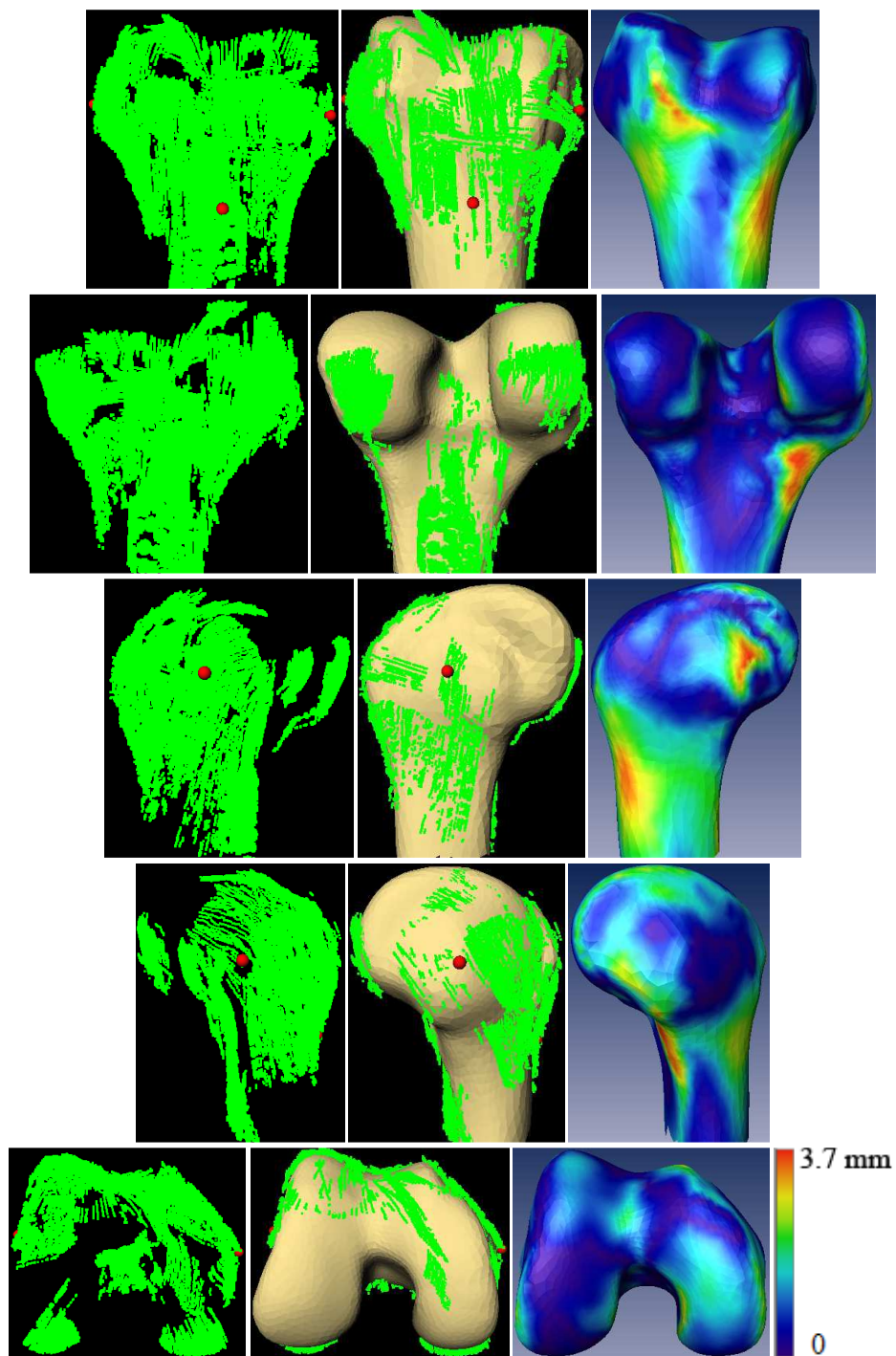


Figure 9.145 Point cloud (left), reconstructed 3D model (middle), and reconstruction error color map (right) for volunteer's knee 4, trial 2, distal femur with RMS of 1.17 mm and Avg. error of 0.92 mm

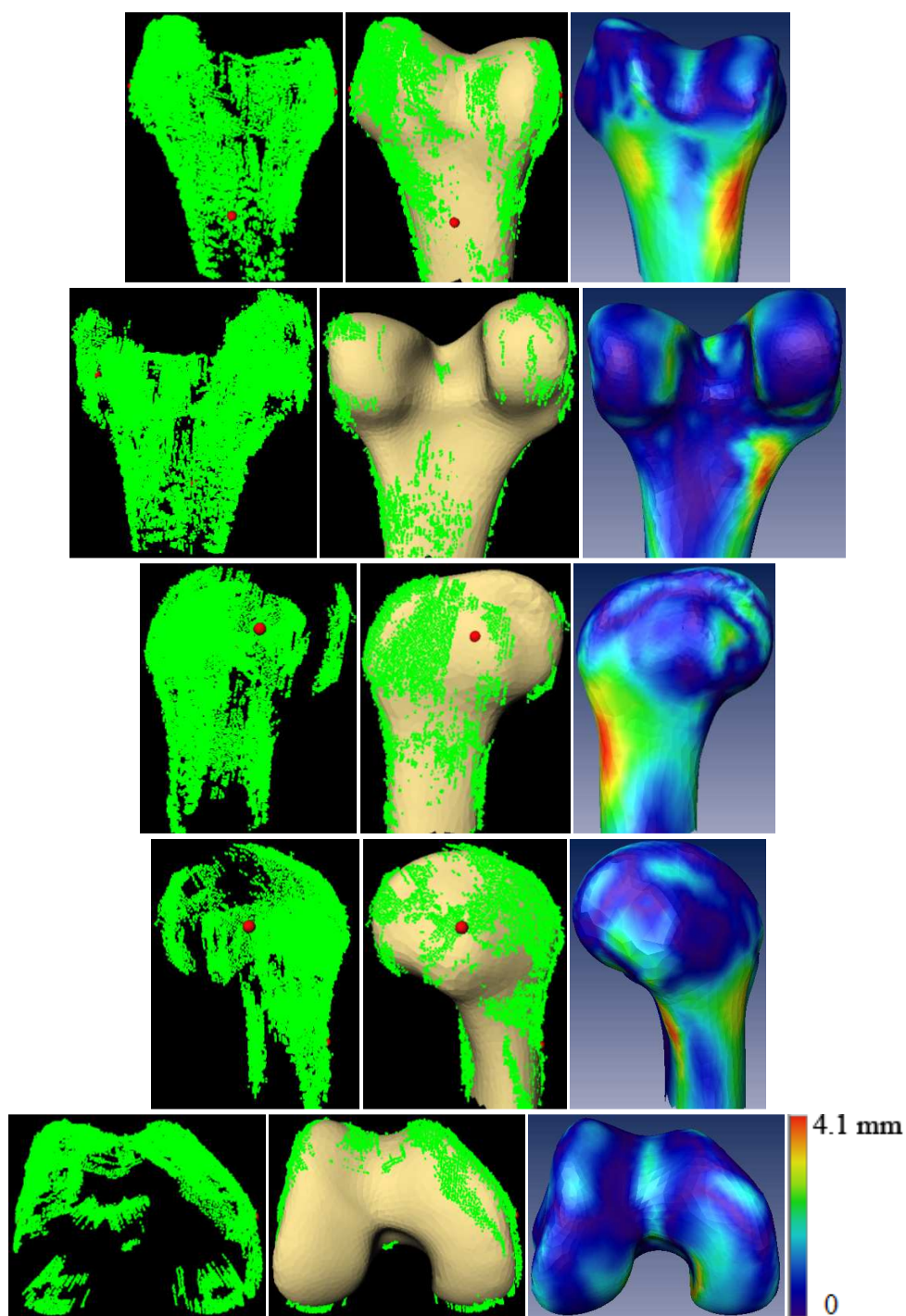


Figure 9.146 Point cloud (left), reconstructed 3D model (middle), and reconstruction error color map (right) for volunteer's knee 4 distal femur, trial 3, with RMS of 1.2 mm and Avg. error of 0.95 mm

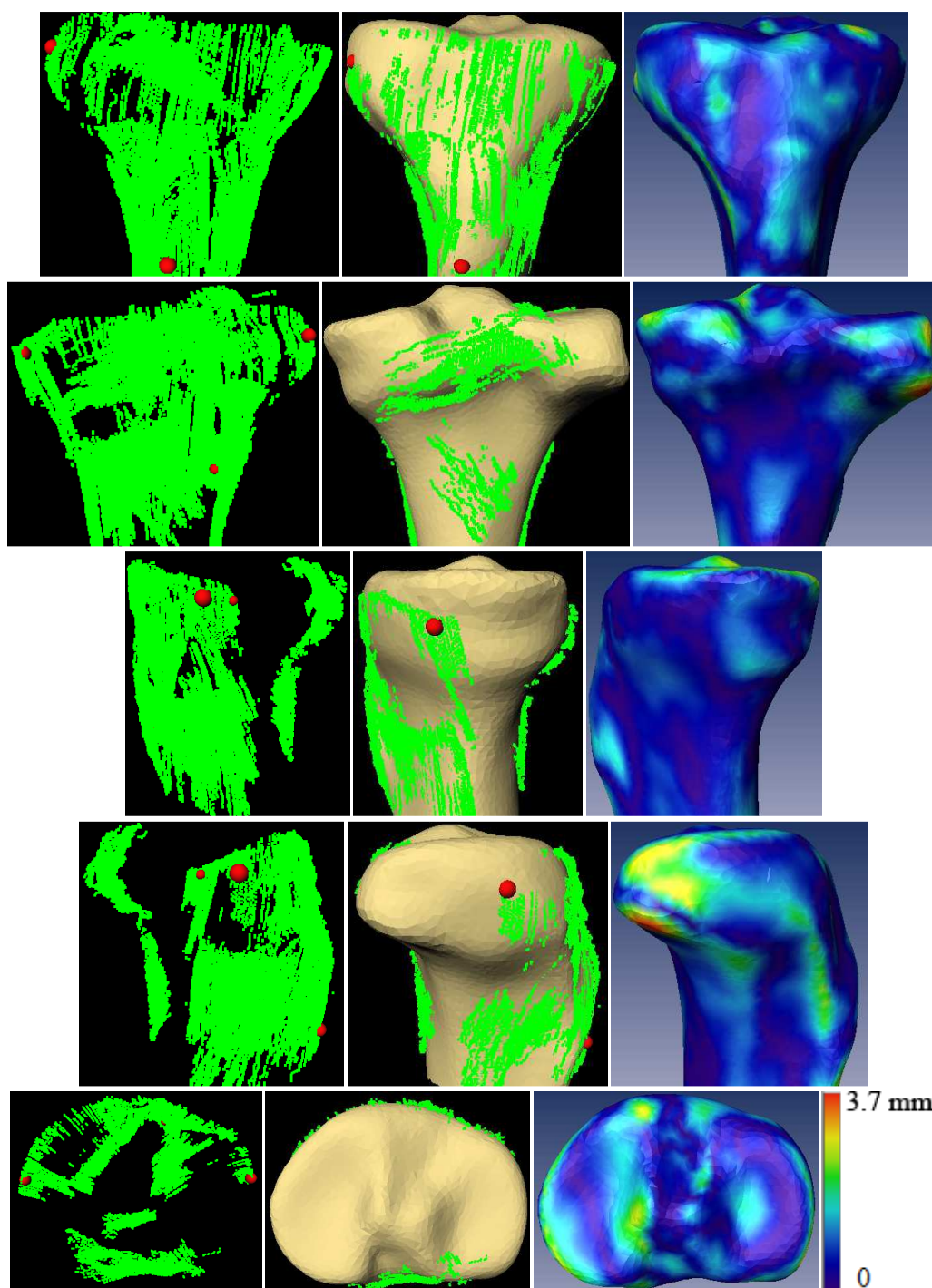


Figure 9.147 Point cloud (left), reconstructed 3D model (middle), and reconstruction error color map (right) for volunteer's knee 4 proximal tibia, trial 1, with RMS of 0.94 mm and Avg. error of 0.75 mm

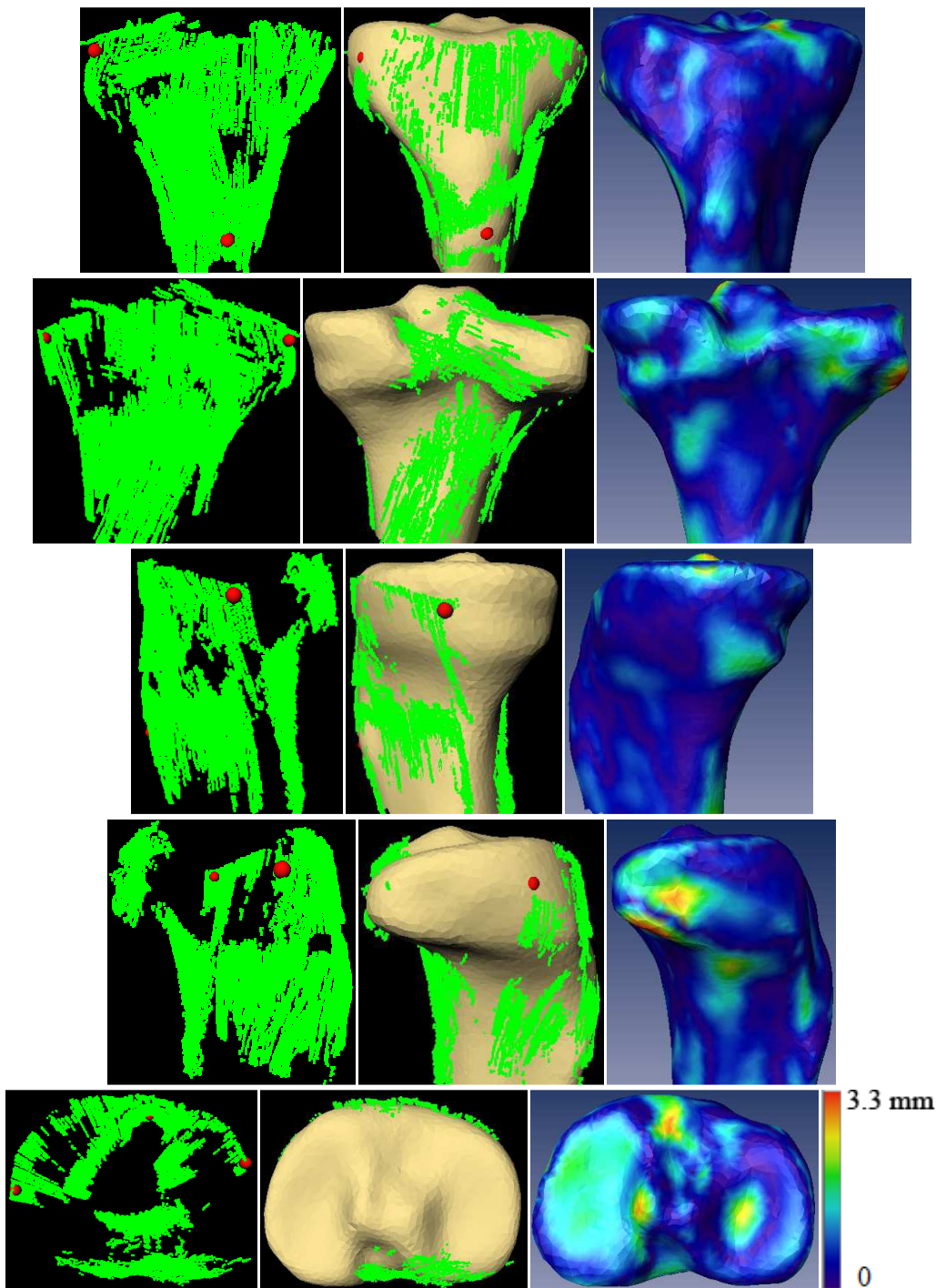


Figure 9.148 Point cloud (left), reconstructed 3D model (middle), and reconstruction error color map (right) for volunteer's knee4 proximal tibia, trial 2, with RMS of 0.87 mm and Avg. error of 0.68 mm

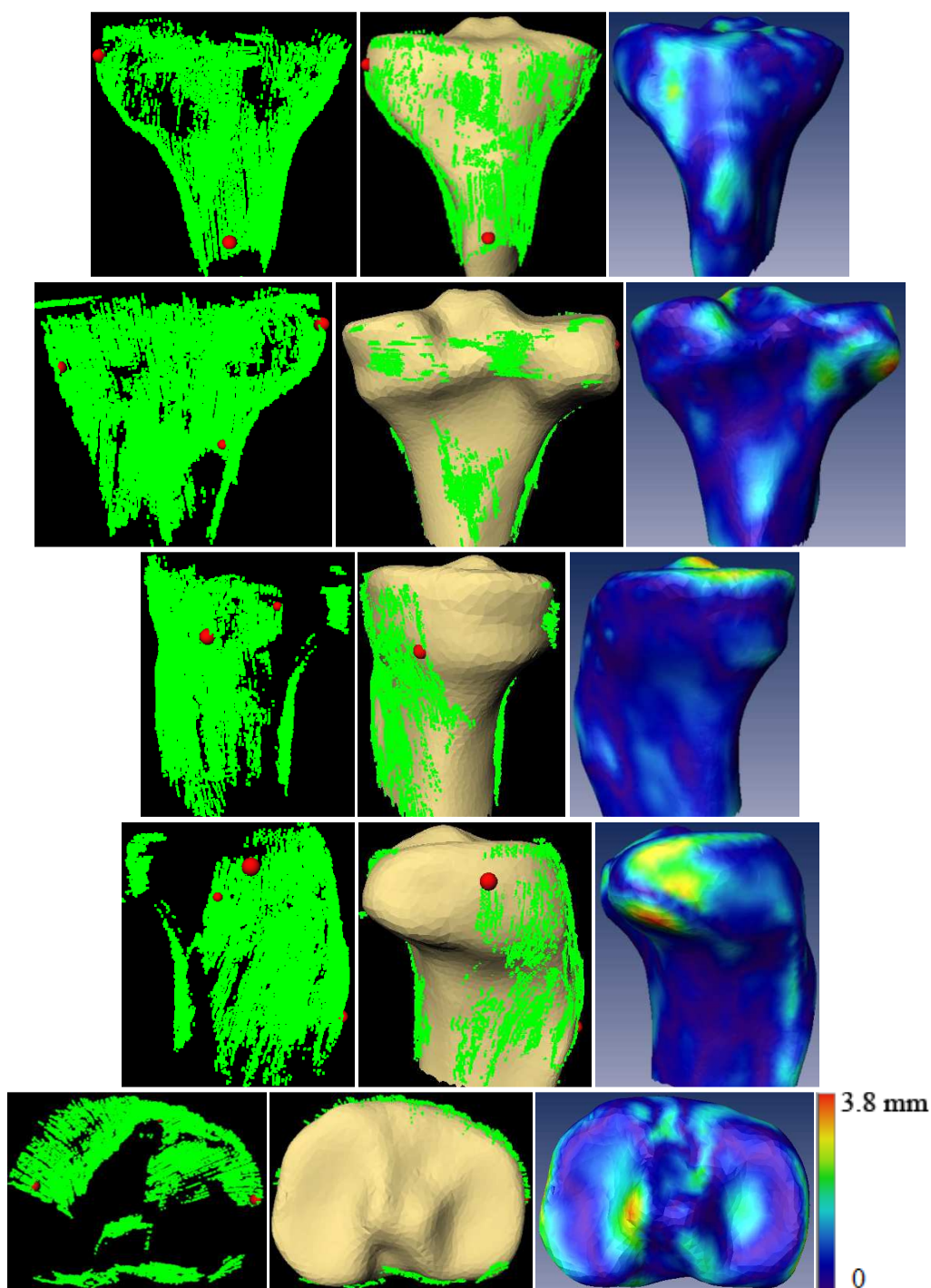


Figure 9.149 Point cloud (left), reconstructed 3D model (middle), and reconstruction error color map (right) for volunteer's knee 4 proximal tibia, trial 3, with RMS of 0.86 mm and Avg. error of 0.66 mm

9.5.5 Volunteer's Knee 5

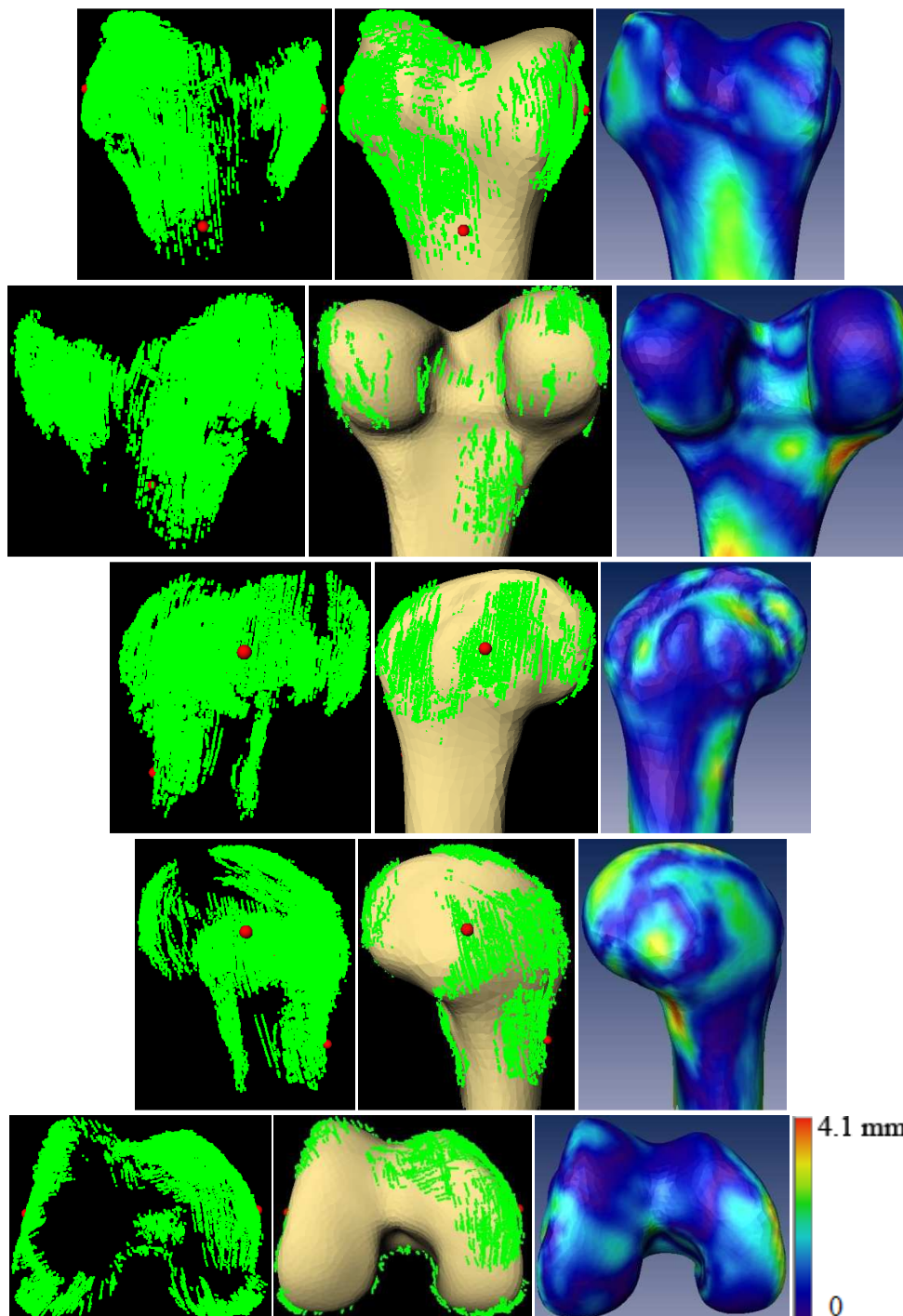


Figure 9.150 Point cloud (left), reconstructed model (middle), and error map (right) for volunteer's knee5 distal femur, trial 1, with RMS of 1.19 mm and Avg. error of 0.96 mm

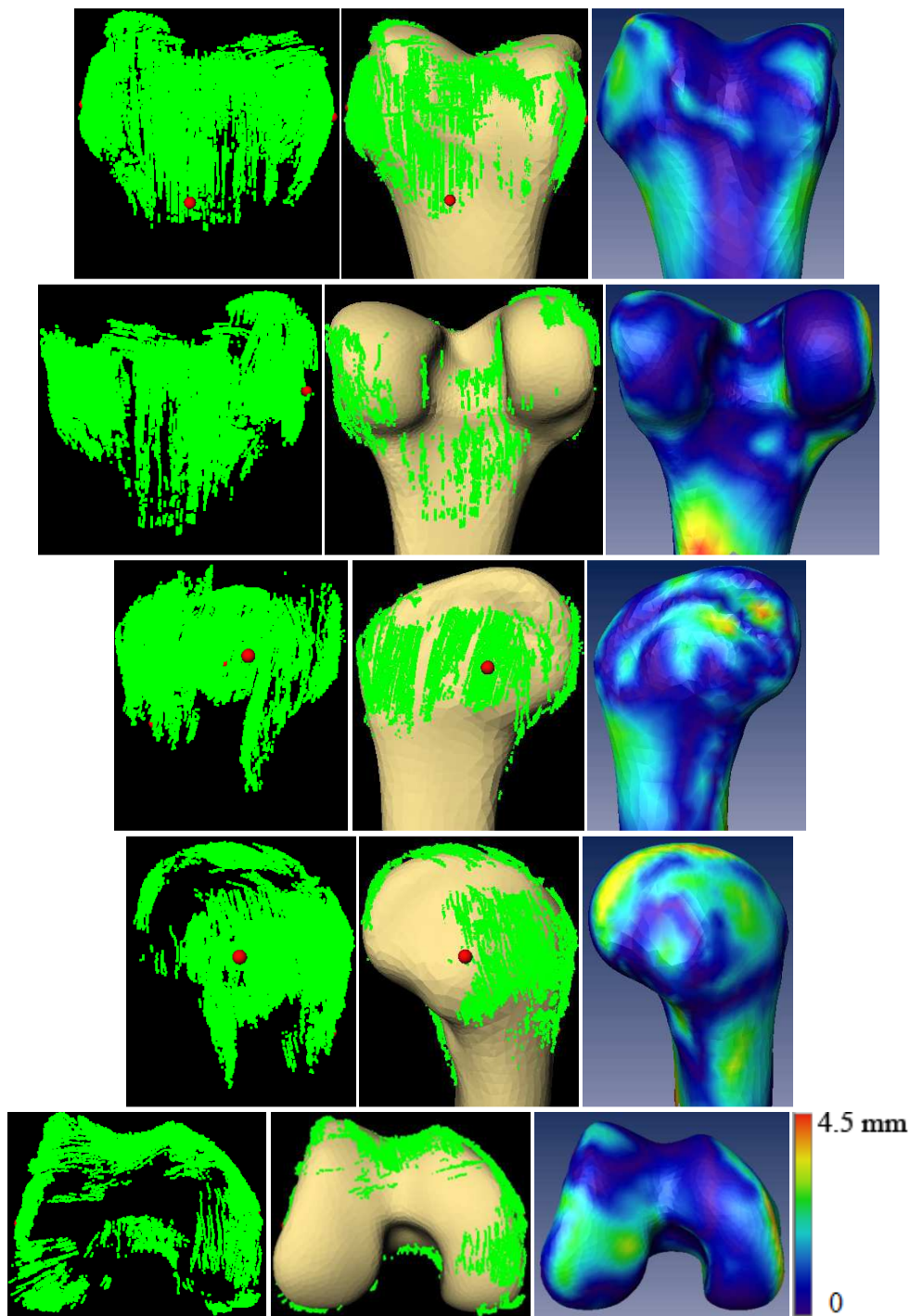


Figure 9.151 Point cloud (left), reconstructed 3D model (middle), and reconstruction error color map (right) for volunteer's knee 5 distal femur, trial 2, with RMS of 1.28 mm and Avg. error of 1.01 mm

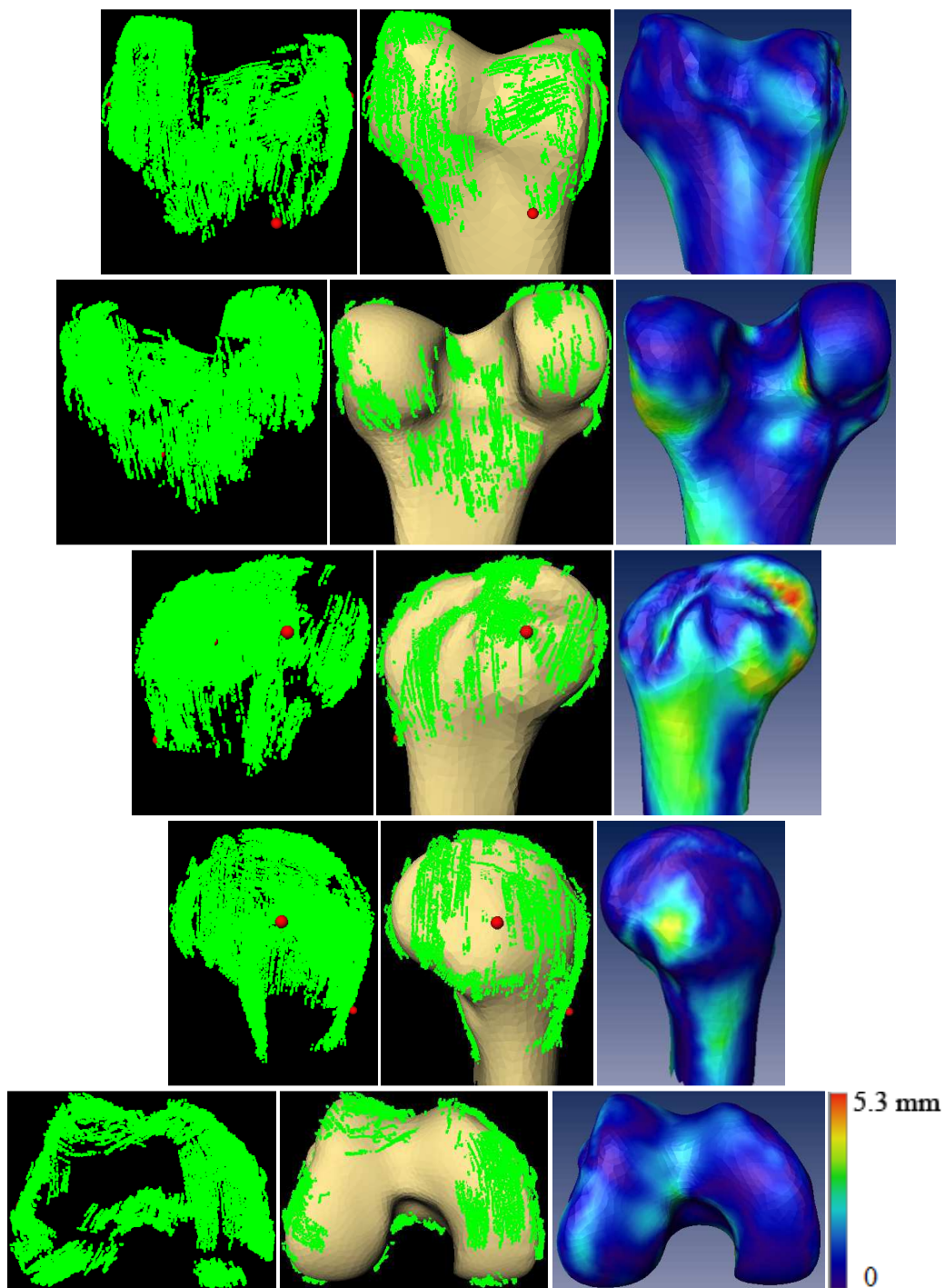


Figure 9.152 Point cloud (left), reconstructed 3D model (middle), and reconstruction error color map (right) for volunteer's knee 5, trial 3, distal femur with RMS of 1.3 mm and Avg. error of 1.04 mm

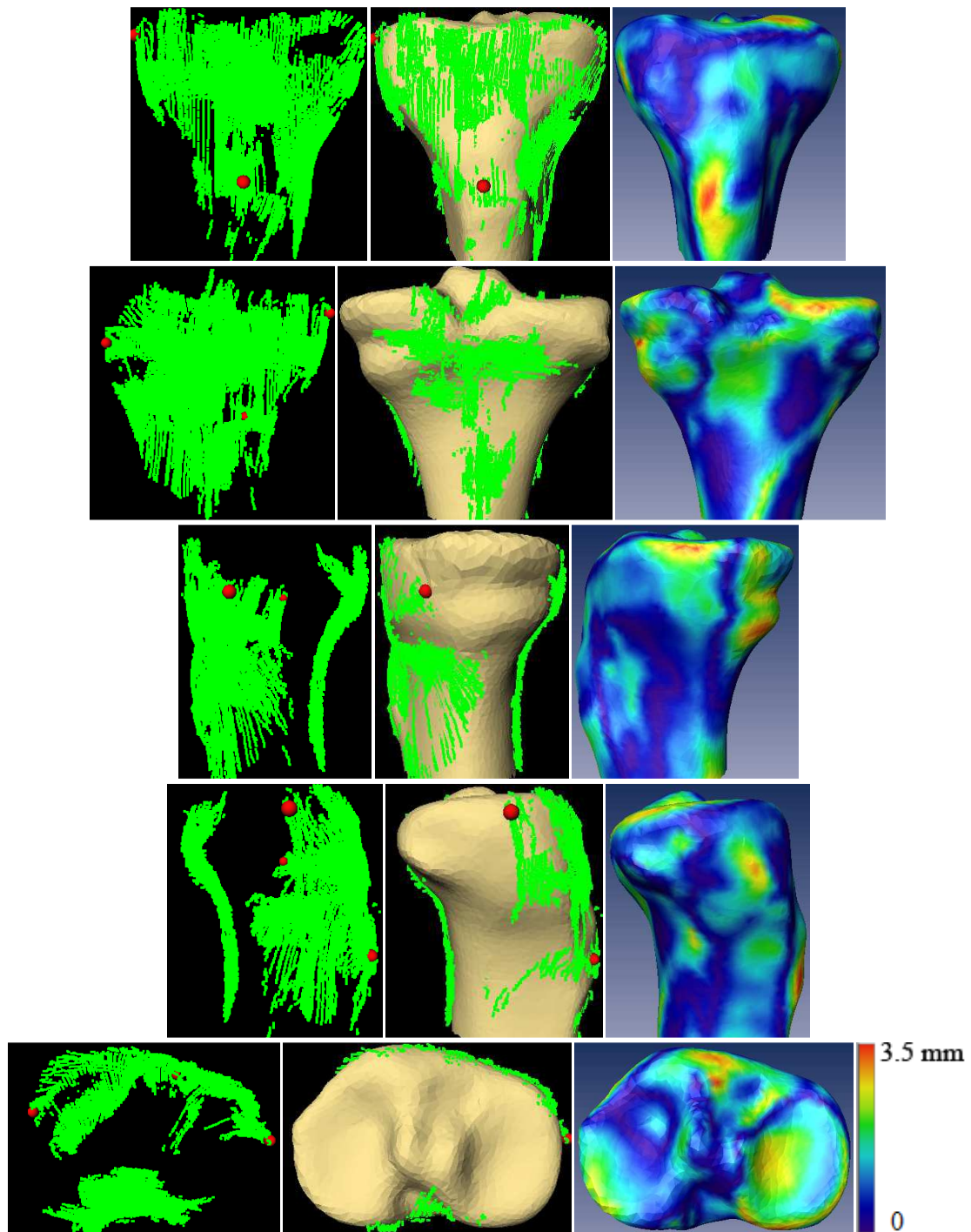


Figure 9.153 Point cloud (left), reconstructed 3D model (middle), and reconstruction error color map (right) for volunteer's knee 5 proximal tibia, trial 1, with RMS of 1.3 mm and Avg. error of 1.08 mm

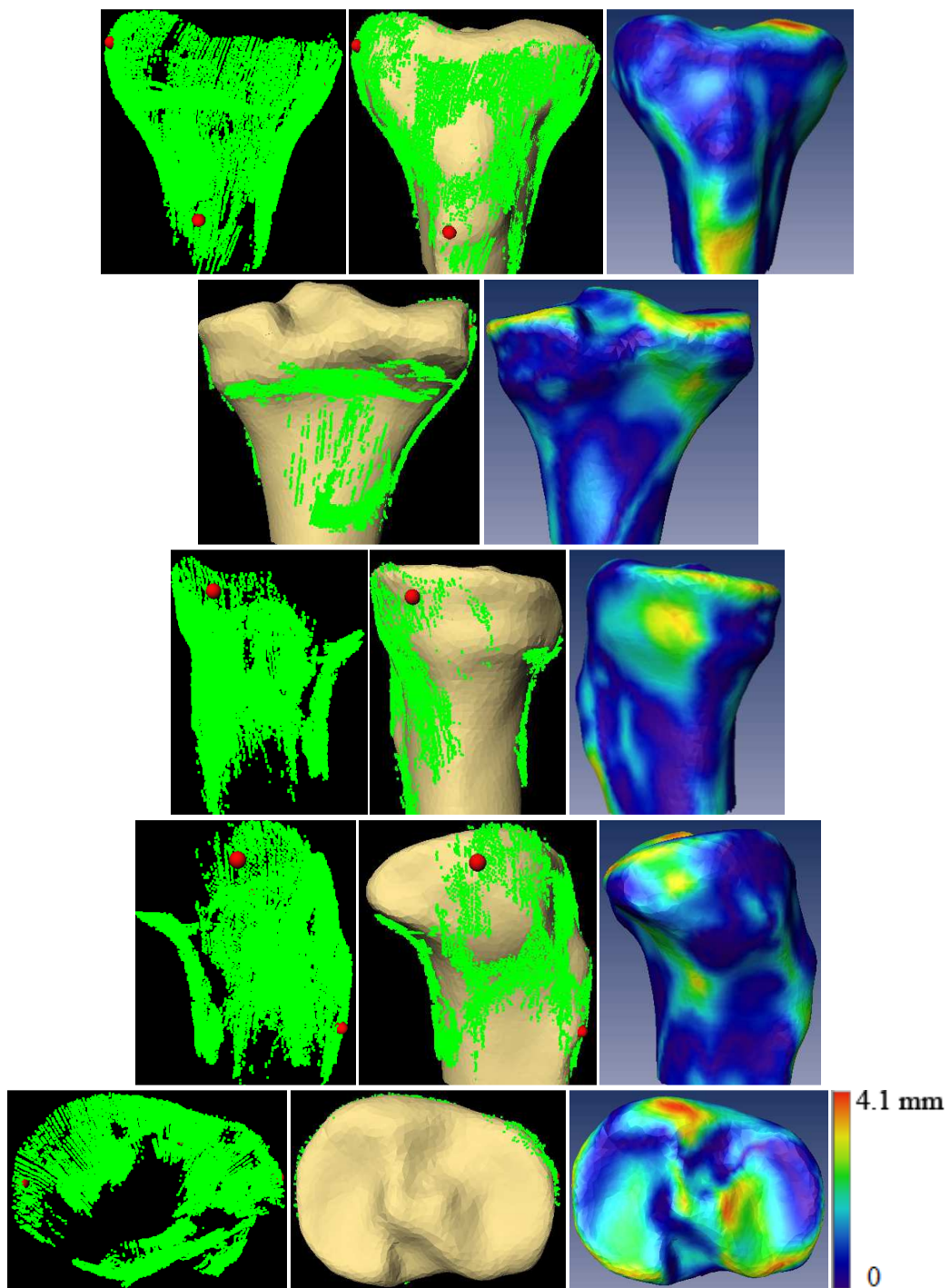


Figure 9.154 Point cloud (left), reconstructed 3D model (middle), and reconstruction error color map (right) for volunteer's knee 5 proximal tibia, trial 2, with RMS of 1.42 mm and Avg. error of 1.13 mm

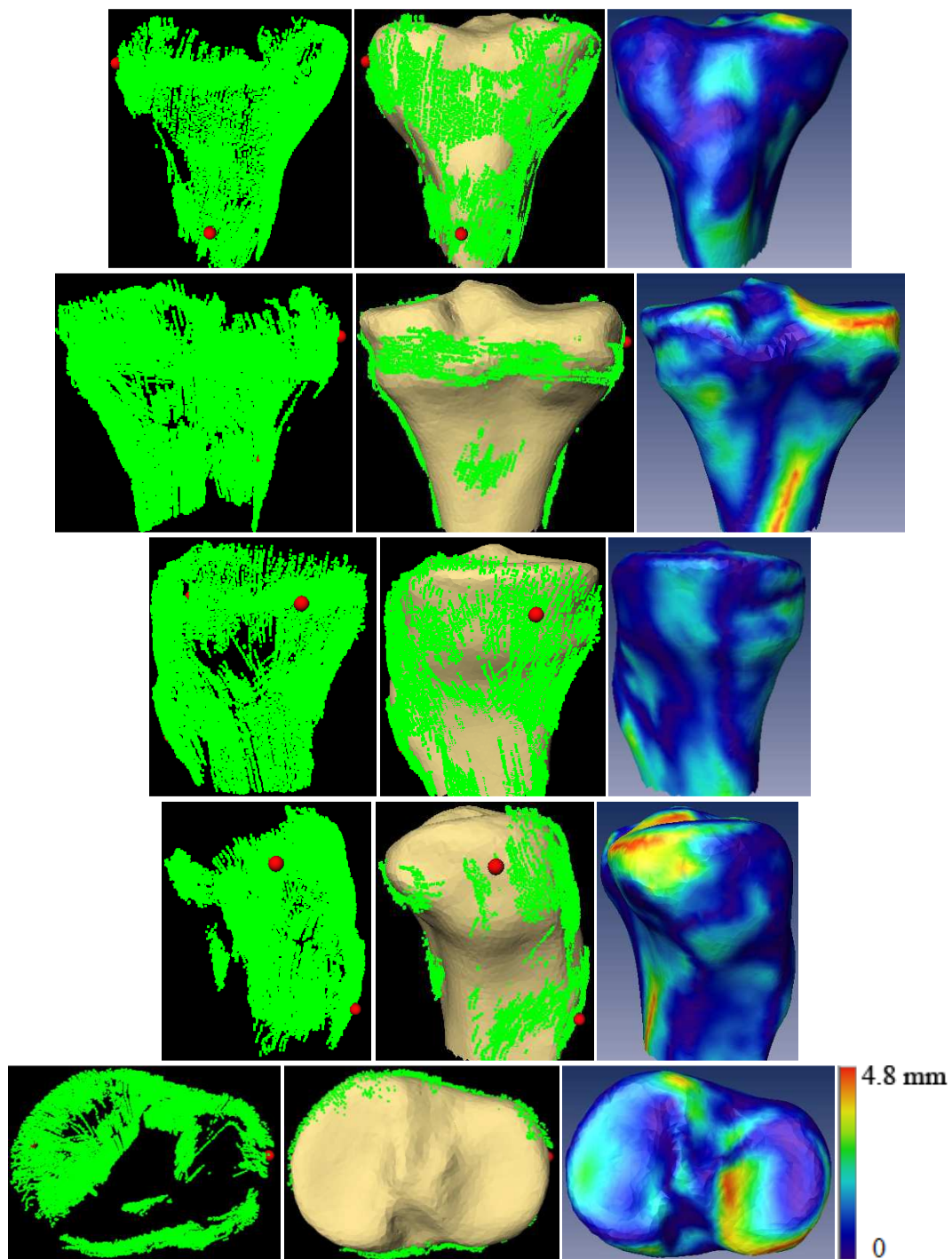


Figure 9.155 Point cloud (left), reconstructed 3D model (middle), and reconstruction error color map (right) for volunteer's knee 5 proximal tibia, trial 3, with RMS of 1.49 mm and Avg. error of 1.2 mm

9.5.6 Volunteer's Knee 6

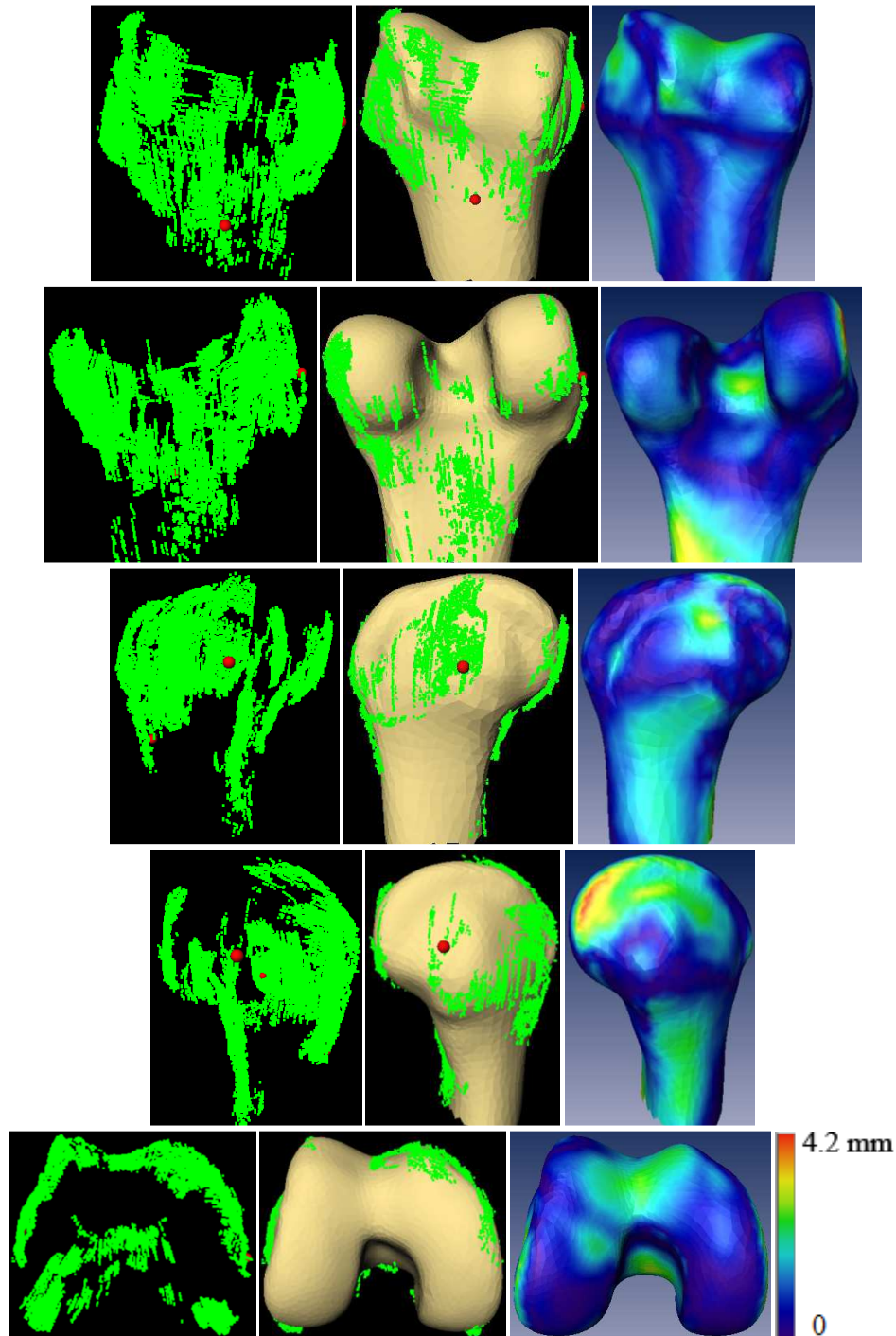


Figure 9.156 Point cloud (left), reconstructed model (middle), and error color map (right) for volunteer's knee 6 distal femur, trial 1, with RMS of 1.27 mm and Avg. error of 1 mm

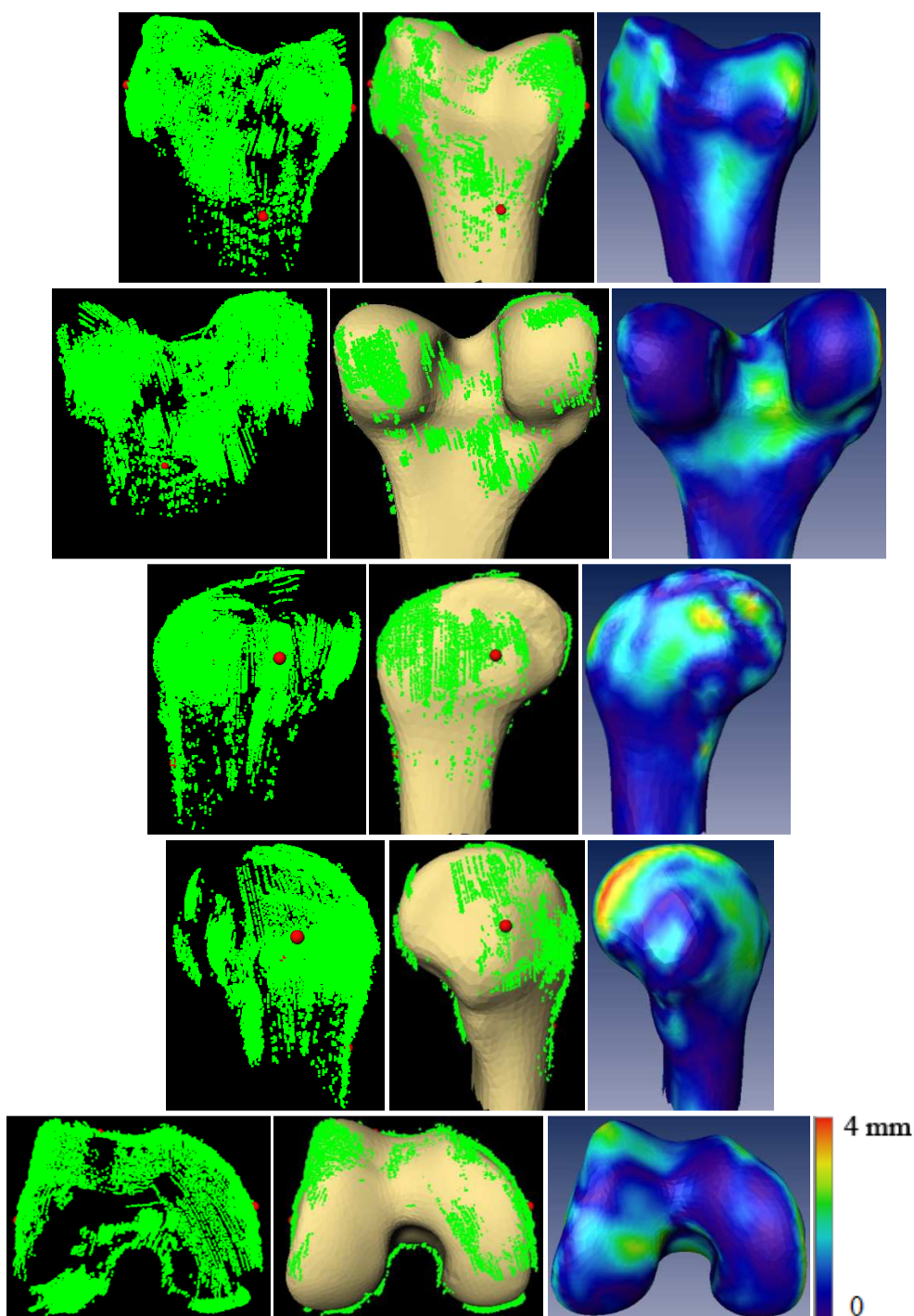


Figure 9.157 Point cloud (left), reconstructed 3D model (middle), and reconstruction error color map (right) for volunteer's knee 6 distal femur, trial 2, with RMS of 1.17 mm and Avg. error of 0.92 mm

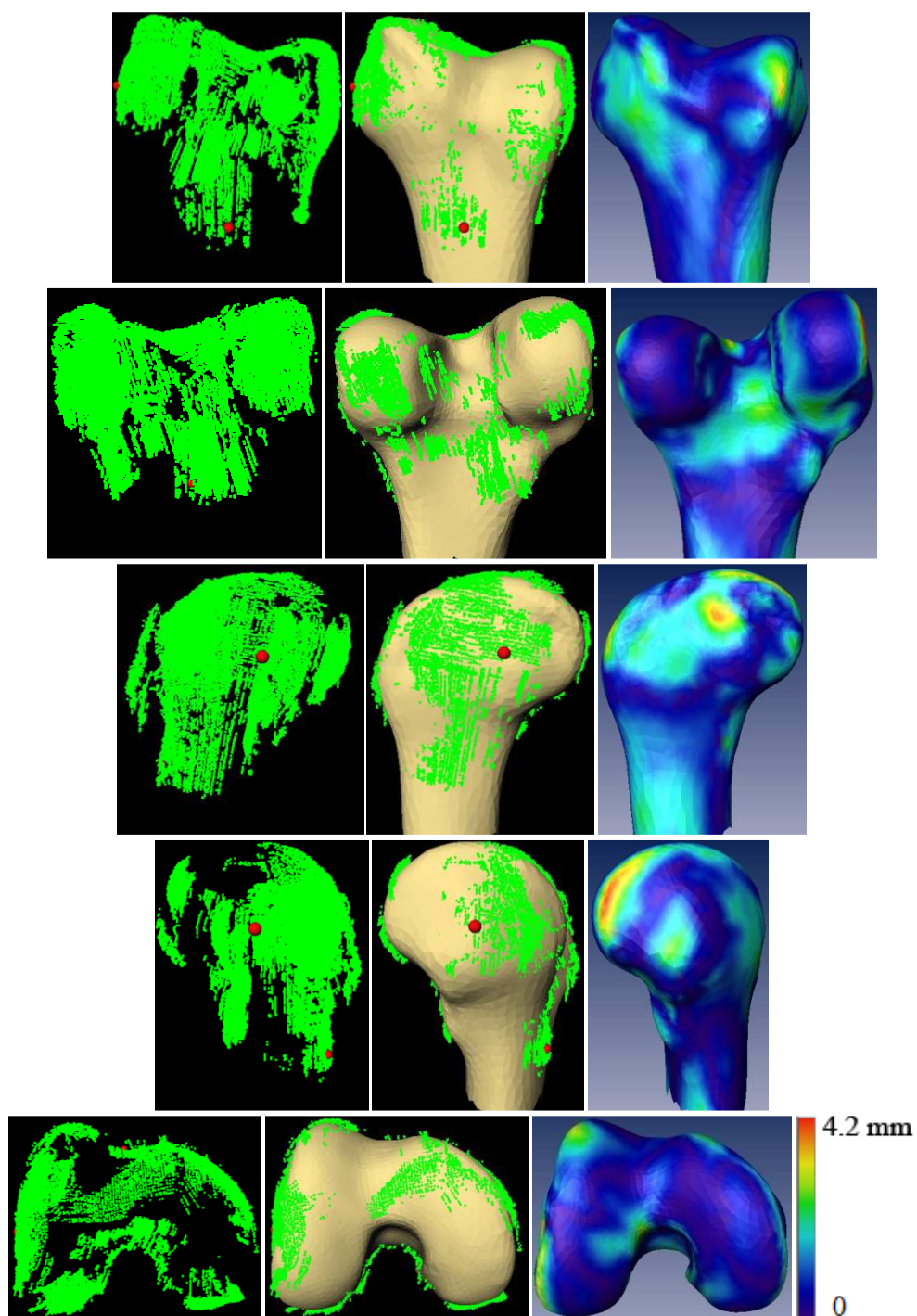


Figure 9.158 Point cloud (left), reconstructed 3D model (middle), and reconstruction error color map (right) for volunteer's knee 6 distal femur, trial 3, with RMS of 1.21 mm and Avg. error of 0.97 mm

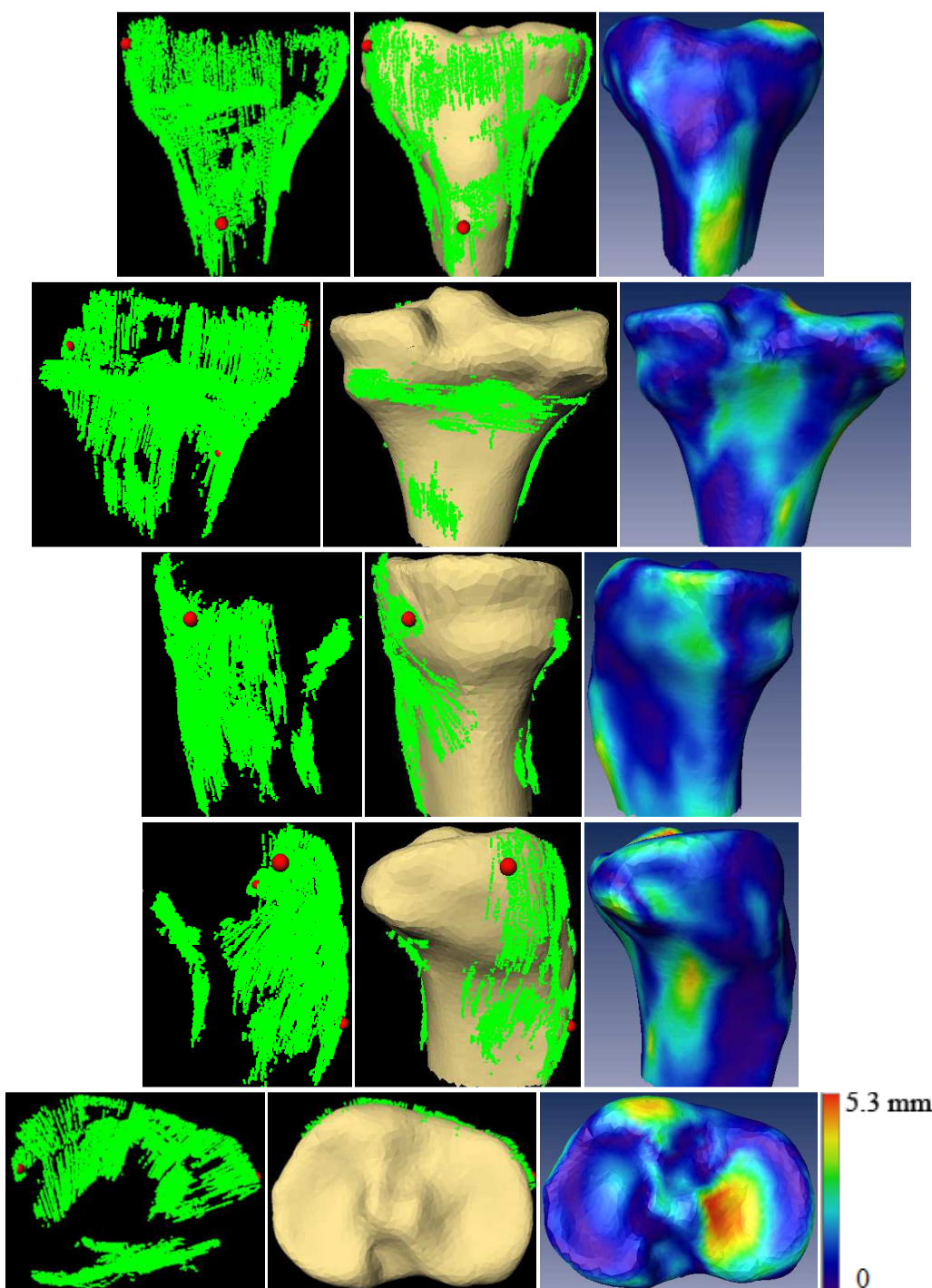


Figure 9.159 Point cloud (left), reconstructed 3D model (middle), and reconstruction error color map (right) for volunteer's knee 6 proximal tibia, trial 1, with RMS of 1.61 mm and Avg. error of 1.27 mm

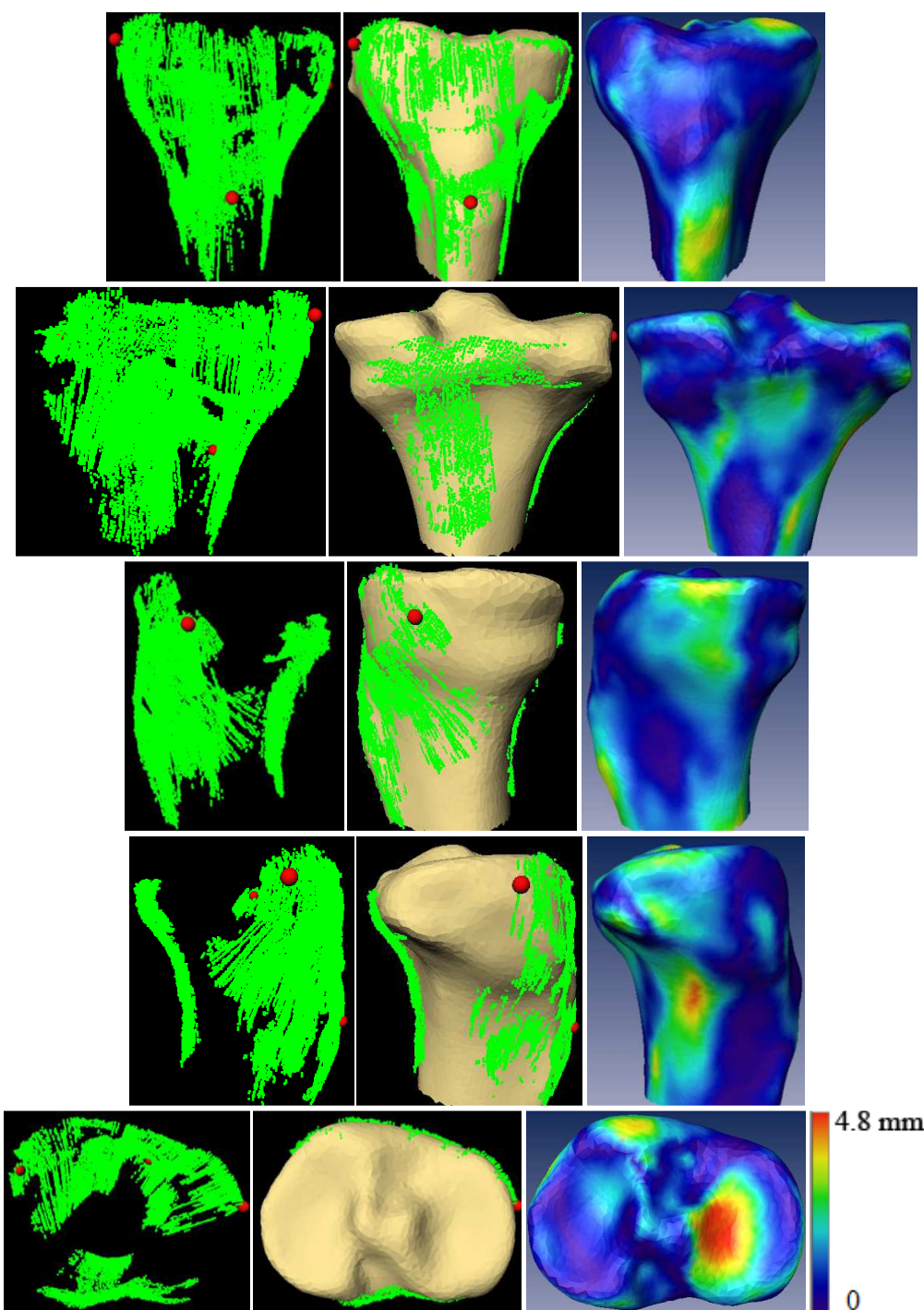


Figure 9.160 Point cloud (left), reconstructed 3D model (middle), and reconstruction error color map (right) for volunteer's knee 6 proximal tibia, trial 2, with RMS of 1.54 mm and Avg. error of 1.23 mm

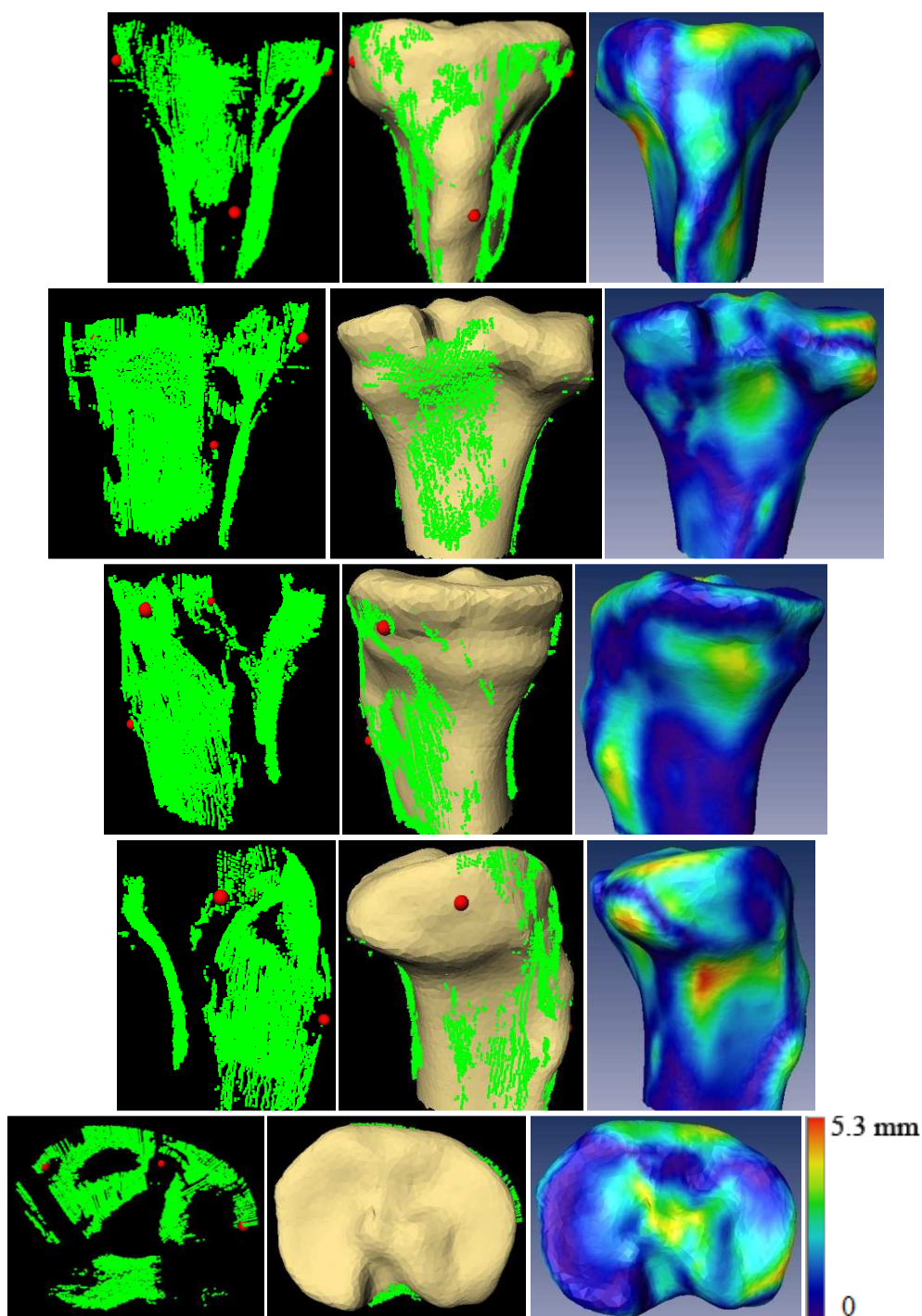


Figure 9.161 Point cloud (left), reconstructed 3D model (middle), and reconstruction error color map (right) for volunteer's knee 6 proximal tibia, trial 3, with RMS of 1.75 mm and Avg. error of 1.43 mm

References

- [1] United States Bone and Joint Decade: The Burden of Musculoskeletal Diseases in the United States. Rosemont, IL: American Academy of Orthopaedic Surgeons; 2008.
- [2] Wilmer L Sibbitt Jr, Andres Peisajovich, Adrian A Michael, Kye S Park, Randy R Sibbitt, Philip A Band, Arthur D Bankhurst, "Does Sonographic Needle Guidance Affect the Clinical Outcome of Intraarticular Injections?," *Journal of Rheumatology*, vol. 39, no. 6, pp. 1892-1902, 2009.
- [3] Joanna Cunningham, Nicola Marshall, Geoff Hide, Claire Bracewell, John Isaacs, Philip Platt, David Kane, "A Randomized, Double-Blind, Controlled Study of Ultrasound-Guided Corticosteroid Injection Into the Joint of Patients With Inflammatory Arthritis," *Arthritis and Rheumatism*, vol. 62, no. 7, pp. 1862-1869, 2010.
- [4] Douglas W Jackson, Nicholas A Evans, Bradley M Thomas, "Accuracy of Needle Placement into the Intra-Articular Space of the Knee," *Journal of Bone and Joint Surgery*, vol. 84-A, no. 9, pp. 1522-1527, 2002.
- [5] Erika L Daley, Sarvottam Bajaj, Leslie J Bisson, Brian J Cole, "Improving Injection Accuracy of the Elbow, Knee, and Shoulder," *American Journal of Sports Medicine*, vol. 39, no. 3, pp. 656-662, 2011.
- [6] A Jones, M Regan, J Ledingham, M Patrick, A Manhire, M Doherty, "Importance of Placement of Intra-Articular Steroid Injections," *British Medical Journal*, vol. 307, no. 6915, pp. 1329-1330, 1993.
- [7] Bisbinas, M Belthur, HG Said, M Green, DJA Learmonth, "Accuracy of Needle Placement in ACJ Injections," *Knee Surgery Sports Traumatology Arthroscopy*, vol. 14, no. 8, pp. 762-765, 2006.

- [8] JA Eustace, DP Brophy, RP Gibney, B Bresnihan, O FitzGerald, "Comparison of the Accuracy of Steroid Placement with Clinical Outcome in Patients with Shoulder Symptoms," *Annals of the Rheumatic Diseases*, vol. 56, no. 1, pp. 59-63, 1997.
- [9] D. J. Brenner, and E. J. Hall, "Computed tomography - an increasing source of radiation exposure," *New England J. Medicine*, vol. 357, pp.2277-2284, 2007.
- [10] L. W. Goldman, "Principles of CT: Radiation dose and image quality," *J. Nuclear Medicine Technology*, vol. 35, no. 4, pp. 213-225, 2007.
- [11] A. B. de Gonzalez, and S. Darby, "Risk of cancer from diagnostic X-rays: Estimates for the UK and 14 other countries," *The Lancet J.*, vol. 363, pp. 345-351, 2004.
- [12] E. Ron, "Ionizing radiation and cancer risk: evidence from epidemiology" *J. Pediatric Radiology*, vol. 32, no. 4, pp. 232-237, 2002.
- [13] D. C. Barratt, C. S. K. Chan, P. J. Edwards, G. P. Penney, M. Slomczykowski, T. J. Carter, D. J. Hawkes, "Instantiation and registration of statistical shape models of the femur and pelvis using 3D ultrasound imaging" *J. Medical Image Analysis*, vol. 12, pp. 358–374, 2008.
- [14] C. S. K. Chan, D. C. Barratt, P.J. Edwards, G.P. Penney, M. Slomczykowski, T. J. Carter, and D.J. Hawkes, "Cadaver validation of the use of ultrasound for 3D model instantiation of bony anatomy in image guided orthopaedic surgery," in *Proc. 7th Int. Conf. Medical Image Computing and Computer-Assisted Intervention*, Saint Malo, France, 2004, pp. 157-167.

- [15] P. Kilian, C. Plaskos, S. Parratte, J.-N. A. Argenson, E. Stindel, J. Tonetti, and S. Lavalée, “New visualization tools: computer vision and ultrasound for MIS navigation,” *Int. J. Medical Robotics and Computer Assisted Surgery* 2008; 4: 23–31.
- [16] Ameet Kumar Jain, Russell H. Taylor “Understanding Bone responses in B-mode Ultrasound Images and Automatic Bone Surface extraction using a Bayesian Probabilistic Framework” in *Proc. of SPIE Vol. 5373*, SPIE, Bellingham, WA, 2004
- [17] P.J.S. Gonçalves, P.M.B. Torres , “Extracting Bone Contours in Ultrasound Images: Energetic versus Probabilistic Methods” *International Conference on Innovations, Recent Trends and Challenges in Mechatronics, Mechanical Engineering and New High-Tech Products*
- [18] J. T. Lewis, R. L. Galloway, and S. Schreiner, “An ultrasonic approach to localization of fiducial markers for interactive, image-guided neurosurgery—part I: principles,” *IEEE Trans. Biomedical Engineering*, vol. 45, no. 5, pp. 620-630, May 1998.
- [19] S. Schreiner, R. L. Galloway, J. T. Lewis, W. A. Bass, and D. M. Muratore, “An ultrasonic approach to localization of fiducial markers for interactive, image-guided neurosurgery—part II: Implementation and automation,” *IEEE Trans. Biomedical Engineering*, vol. 45, no. 5, pp. 631-641, May 1998
- [20] C. R. Maurer, R. P. Gaston, D. L. G. Hill, M. J. Gleeson, M. G. Taylor, M. R. Fenlon, P. J. Edwards, and D. J. Hawkes. “AcouStick: A tracked A-mode ultrasonography system for registration in image-guided surgery,” in *Proc. 2nd Int.*

- Conf. Medical Image Computing and Computer-Assisted Intervention, Cambridge, U.K., 1999, pp. 953-963.
- [21] C. Amstutz, M. Caversaccio, J. Kowal, R. Bachler, L. P. Nolte, and R. Hausler, "A-mode ultrasound-based registration in computer-aided surgery of the skull," *J. Arch. Otolaryngology. Head and Neck Surgery*, vol. 129, pp. 1310–1316, 2003.
- [22] A. Mozes, T. C. Chang, L. Arata, and W. Zhao, "Three-dimensional A-mode ultrasound calibration and registration for robotic orthopaedic knee surgery," *Int. J. Medical Robotics, and Computer Assisted Surgery*, vol. 6, pp. 91-101, 2010.
- [23] W. R. Hedrick, D. L. Hykes, D. E. Starchman, "Ultrasound physics and instrumentation," 4th ed, 1995
- [24] <http://www.ndigital.com/optotrak-techspecs.php>
- [25] D. R. Gauldie, "Calibration and registration with 3d a-mode ultrasound," M.S. thesis, Queen's Univ., Ontario, Canada. 2002.
- [26] F. Leszko, K. R. Hovinga, A. L. Lerner, R.D. Komistek, M. R. Mahfouz "In vivo normal knee kinematics: is ethnicity or gender an influencing factor?," *J. Clinical Orthopedics Related Research*. 2011;469:95–106.
- [27] D. L. Benoit, D. K. Ramsey, M. Lamontagne, L. Xuf, P. Wretenberg, and P. Renström, "Effect of skin movement artifact on knee kinematics during gait and cutting motions measured in vivo," *J. Gait and Posture*, vol. 24, pp. 152–164, 2006.
- [28] C. Reinschmidt, A. J. van den Bogert, B. M. Nigg, A. Lundberg, and N. Murphy, "Effect of skin movement on the analysis of skeletal knee joint motion during running," *J. Biomechanics*, vol. 30, no. 7, pp. 729-732, 1997.

- [29] L.H. Staib and J.S. Duncan, "Deformable Fourier models for surface finding in 3D images," Proc. VBC'92 Conf., pp.90-194, 1992
- [30] R. Szekely, A. Kelemen, C. Brechbuler, and G. Gerig. "Segmentation of 2D and 3D objects from MRI volume data using constrained elastic deformations of flexible Fourier surface models," Medical Image Analysis, 1(1):19-34,1996.
- [31] T.F. Cootes, C.J. Taylor, D.H. Cooper, and J. Graham. "Active shape models - Their training and application. Computer Vision and Image Understanding, 61(1):38{59, 1995.
- [32] M. Fleute, and S. Lavallee, "Nonrigid 3-D/2-D registration of images using statistical models" in Proc. 2nd Int. Conf. Medical Image Computing and Computer-Assisted Intervention, Cambridge, U.K., 1999, pp. 138-147.
- [33] S. Laporte, W. Skalli, J. A. De Guise, F. Lavaste, and D. Mitton, "A biplanar reconstruction method based on 2D and 3D contours: application to the distal femur," J. Computer Methods in Biomechanics and Biomedical Engineering, vol. 6, no. 1, pp. 1-6, 2003.
- [34] G. Zheng, and L. P. Nolte, "Surface reconstruction of bone from X-ray images and point distribution model incorporating a novel method for 2D-3D correspondence," in Proc. IEEE Conf. Computer Vision and Pattern Recognition, 2006, pp. 2237-2244.
- [35] K. T. Rajamani, M. A. Styner, H. Talib, G. Zheng, L.-P. Nolte, and M. A. Gonzalez Ballester, "Statistical deformable bone models for robust 3D surface extrapolation from sparse data" J. Medical Image Analysis, vol. 11, pp. 99-109, 2007.

- [36] M. Fleute, and S. Lavallee, "Building a complete surface model from sparse data using statistical shape models: application to computer assisted knee surgery," in Proc. 1st Int. Conf. Medical Image Computing and Computer-Assisted Intervention, Cambridge, MA, 1998, pp. 879-887.
- [37] M. Fleute, S. Lavallee, and R. Julliard, "Incorporating a statistically based shape model into a system for computer-assisted anterior cruciate ligament surgery," *J. Medical Image Analysis*, vol. 3, no. 3, pp 209–222, 1999.
- [38] Mahfouz, Badawi, Merkl, Abdel Fatah, Pritchard, Kesler, Moore, Jantz, Jantz, "Patella Sex Determination by 3D Statistical Shape Models and Nonlinear Classifiers," *Forensic Science International*, vol. 173, no. 2-3, pp. 161-170, 2007.
- [39] Mahfouz, Merkl, Abdel Fatah, "Automatic Methods for Characterizing of Sexual Dimorphism of Adult Femora: Distal Femur," *Computer Methods in Biomechanics and Biomedical Engineering CMMBE Journal*, vol. 10, no. 6, pp. 447-456, 2007.
- [40] Mahfouz, Abdel Fatah, Bowers, Scuderi, "Three-dimensional Morphology of the Knee Reveals Ethnic Differences Reveals Ethnic Differences", *J. Clinical Orthopaedics, and Related Research*, Volume 470, Issue 1, January , 2011
- [41] W. H. Press, S. A. Teukolsky, W. T. Vetterling, B. P. Flannery, "Numerical recipes in C: the art of scientific computing," 2nd ed. Cambridge University Press, Cambridge, 1992.
- [42] Dennis, Komistek, Scuderi, Argenson, Insall, and Mahfouz: 'In Vivo Three Dimensional Determination of Kinematics for Subjects with a Normal Knee or a

Unicompartmental or Total Knee Replacement' J Bone Joint Surgery 83:S104-S115, 2001.

- [43] Komistek, Dennis, Mahfouz, "In Vivo Fluoroscopic Analysis of the Normal Human Knee,' Clinical Orthopedics 410: 69-81, 2003.
- [44] Dennis, Komistek, Mahfouz: 'In Vivo Fluoroscopic Analysis of Fixed-Bearing Total Knee Replacements.' Clinical Orthopedics, 410:114-130, 2003.
- [45] Mahfouz, Traina, Komistek, Dennis, Oster, "An In Vivo Determination of Knee Kinematics for Subjects Having either a Hamstring or Patellar Tendon ACL Graft," The Journal of Knee Surgery, Vol. 16, No. 4, October 2003
- [46] Mahfouz, Hoff, Komistek, Dennis "A Robust Method for Registration of Three-Dimensional Knee Implant Models to Two-Dimensional Fluoroscopy Images," IEEE Transactions on Medical Imaging, Vol. 22, No. 12, December 2003
- [47] Mahfouz, Hoff, Komistek, Dennis: "Effect of Segmentation Errors on 3D-to-2D Registration of Implant Models in X-ray Images." J Biomechanics, February 2005.

Vita

Rimon has received his bachelor of science degree in systems and biomedical engineering from the Cairo University, Egypt. He then joined the University of Tennessee to pursue his master of science and doctorate of philosophy in biomedical engineering. He worked in the center for musculoskeletal research laboratory at the University of Tennessee as a graduate research assistant throughout his course of study and research for the master's and doctorate degrees. His research interests are ultrasound imaging, 3D modeling, medical image processing, and pattern recognition,